Conference Proceedings of the Society for Experimental Mechanics Series

Matthew Allen
Walter D'Ambrogio
Dan Roettgen *Editors*

Dynamic Substructures, Volume 4

Proceedings of the 41st IMAC, A Conference and Exposition on Structural Dynamics 2023

SEM

Springer

Conference Proceedings of the Society for Experimental Mechanics Series

Series Editor

Kristin B. Zimmerman
Society for Experimental Mechanics, Inc.,
Bethel, CT, USA

The Conference Proceedings of the Society for Experimental Mechanics Series presents early findings and case studies from a wide range of fundamental and applied work across the broad range of fields that comprise Experimental Mechanics. Series volumes follow the principle tracks or focus topics featured in each of the Society's two annual conferences: IMAC, A Conference and Exposition on Structural Dynamics, and the Society's Annual Conference & Exposition and will address critical areas of interest to researchers and design engineers working in all areas of Structural Dynamics, Solid Mechanics and Materials Research.

Matthew Allen • Walter D'Ambrogio • Dan Roettgen
Editors

Dynamic Substructures, Volume 4

Proceedings of the 41st IMAC, A Conference and Exposition on Structural Dynamics 2023

Springer

Editors
Matthew Allen
Brigham Young University
Provo, UT, USA

Dan Roettgen
Sandia National Laboratories
Albuquerque, NM, USA

Walter D'Ambrogio
DIIIE
University of L'Aquila
L'AQUILA, L'Aquila, Italy

ISSN 2191-5644 ISSN 2191-5652 (electronic)
Conference Proceedings of the Society for Experimental Mechanics Series
ISBN 978-3-031-36693-2 ISBN 978-3-031-36694-9 (eBook)
https://doi.org/10.1007/978-3-031-36694-9

This Springer imprint is published by the registered company Springer Nature Switzerland AG
The registered company address is: Gewerbestrasse 11, 6330 Cham, Switzerland

Paper in this product is recyclable.

Preface

Dynamic Substructures represents one of ten volumes of technical papers presented at the 41st IMAC, A Conference and Exposition on Structural Dynamics, organized by the Society for Experimental Mechanics, held February 13–16, 2023. The full proceedings also include volumes on Nonlinear Structures and Systems; Dynamics of Civil Structures; Model Validation and Uncertainty Quantification; Special Topics in Structural Dynamics and Experimental Techniques; Computer Vision and Laser Vibrometry; Dynamic Environments Testing; Sensors and Instrumentation and Aircraft/Aerospace Testing Techniques; Topics in Modal Analysis and Parameter Identification; and Data Science in Engineering.

Each collection presents early findings from experimental and computational investigations on an important area within Structural Dynamics. Coupled structures or, substructuring, is one of these areas.

Substructuring is a general paradigm in engineering dynamics where a complicated system is analyzed by considering the dynamic interactions between subcomponents. In numerical simulations, substructuring allows one to reduce the complexity of parts of the system in order to construct a computationally efficient model of the assembled system. A subcomponent model can also be derived experimentally, allowing one to predict the dynamic behavior of an assembly by combining experimentally and/or analytically derived models. This can be advantageous for subcomponents that are expensive or difficult to model analytically. Substructuring can also be used to couple numerical simulation with real-time testing of components. Such approaches are known as hardware-in-the-loop or hybrid testing.

Whether experimental or numerical, all substructuring approaches have a common basis, namely the equilibrium of the substructures under the action of the applied and interface forces and the compatibility of displacements at the interfaces of the subcomponents. Experimental substructuring requires special care in the way the measurements are obtained and processed in order to assure that measurement inaccuracies and noise do not invalidate the results. In numerical approaches, the fundamental quest is the efficient computation of reduced order models describing the substructure's dynamic motion. For hardware-in-the-loop applications, difficulties include the fast computation of the numerical components and the proper sensing and actuation of the hardware component. Recent advances in experimental techniques, sensor/actuator technologies, novel numerical methods, and parallel computing have rekindled interest in substructuring in recent years leading to new insights and improved experimental and analytical techniques.

The organizers would like to thank the authors, presenters, session organizers, and session chairs for their participation in this track.

Provo, UT, USA — Matthew Allen
L'Aquila, Italy — Walter D'Ambrogio
Albuquerque, NM, USA — Dan Roettgen

Contents

Chapter 1
A Genetic Algorithm-Based Optimization Approach for Fixture Design that Preserves Desired Dynamic Response Characteristics

Janette J. Meyer, David J. Koester, Ray Joshua, and Douglas E. Adams

Abstract Aerospace vehicles are complex systems comprised of interconnected components that must perform reliably together as an assembly. However, reliability tests are often performed at the component level, which can lead to poor results if the interconnections between components are not accurately represented during testing. In the ideal case, a system's components would be tested in situ such that the boundary conditions of the components during testing would be the same as in operation. However, having access to the connecting components of a part can be difficult due to barriers such as inaccessible proprietary design specifications and different design timelines. Therefore, there is a need to simulate the boundary conditions provided by a connecting component without having direct access to the component. In this chapter, a process for designing a test fixture that accurately simulates the boundary conditions of a connecting component is proposed. It is assumed that the response of the connecting component is known, and the goal of the process is to design a fixture that replicates that response, without specific knowledge about the original component's geometric dimensions or material properties. The design is determined using a genetic algorithm-based optimization process that chooses combinations of bounded design parameters until the response of the fixture matches the desired response. The optimization starts by subdividing a design volume, where each partition can be assigned a different density and Young's modulus value. At each iteration, a different combination of parameter values, determined by a genetic algorithm, is chosen. The natural frequencies and mode shapes of the current design are determined and compared to the target values. Once a sufficient match is achieved, the design is complete.

To demonstrate the viability of the proposed approach, a simple component was designed and modeled. The component's first five natural frequencies and mode shapes were determined and used as the basis for the objective function. The optimization algorithm was run and a component design was determined without assuming any a priori knowledge of the target component's material properties or geometry, with the exception of its overall dimensions. The resulting component's first five natural frequencies were within 16% of the target values and the Modal Assurance Criterion values for the first five mode shapes were all greater than 0.79.

Keywords Dynamics · Fixture design · Optimization · Genetic algorithm · BARC

1.1 Introduction

It is well known that the boundary conditions of a structure affect its dynamic response and, therefore, changes in a structure's boundary condition will result in changes in its dynamic response [1, 2]. This effect is particularly important when considering common practices in durability/reliability testing. Components are often tested outside of their intended operating configuration because of the difficulty of testing them while installed in a full assembly. Inaccessible proprietary design specifications, different design timelines, cost, and practicality of testing are potential barriers to testing a component using the expected operational boundary conditions. Component-level testing is a standard substitution for assembly-level testing, but these tests do not always replicate the assembly-level dynamics, resulting in different failure modes of the parts

J. J. Meyer (✉) · D. J. Koester · D. E. Adams
Laboratory for Systems Integrity and Reliability (LASIR), Vanderbilt University, Nashville, TN, USA
e-mail: janette.j.meyer@vanderbilt.edu; david.koester@vanderbilt.edu; douglas.adams@vanderbilt.edu

R. Joshua
Honeywell, Kansas City National Security Campus, Kansas City, MO, USA
e-mail: rjoshua@kcnsc.doe.gov

M. Allen et al. (eds.), *Dynamic Substructures, Volume 4*, Conference Proceedings of the Society for Experimental Mechanics Series, https://doi.org/10.1007/978-3-031-36694-9_1

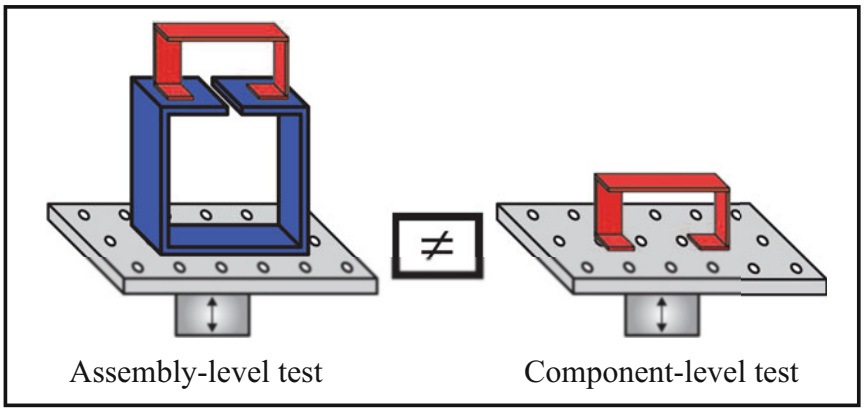

Fig. 1.1 Durability testing is often performed at the component level, which does not always sufficiently replicate the dynamics of the part while it is in operation in the full assembly

and rendering the tests ineffective, as illustrated in Fig. 1.1. There is a need to simulate the boundary conditions provided by a connecting component without having direct access to the component.

Recently, the Boundary Condition Challenge Problem [3] was introduced to address this need. A Box Assembly with Removable Component (BARC), shown in Fig. 1.1, was designed as a representative structure, and the goal is to design a test or a test fixture to replace the box portion of the assembly such that the dynamic response of the small component is preserved. Several different approaches have been taken thus far. In [4], a control strategy was developed to adjust shaker inputs such that the levels measured at select points on the BARC are comparable to those measured at the same locations during normal operating conditions. This approach attempts to compensate for changes in boundary conditions by changing the input excitation used in the test. A control-based compensation strategy was also developed in [5], but changes to the fixture design were also investigated. Topology optimization was used to create several modified support for the small component that was then 3D-printed and tested. It was found that using an optimization process based on part stiffness or static deformation was not effective, and the authors recommended that the focus of the fixture design should instead be based on the dynamic response of the fixture. Finite element models of the BARC have also been developed [2, 6]. In [6], a model was used in a gradient-based optimization scheme with a cost function based on the modal projection error (MPE). The box portion of the BARC was parameterized and the MPE-based optimization successfully converged to the original parameter values. After this proof of concept, the parameter space was restricted to force a nontrivial solution. The optimization approach was still able to produce a fixture that adequately preserved the dynamics of the small component.

In this chapter, a genetic algorithm-based optimization approach is developed to determine a fixture design. Like in [3], it is assumed that the mode shapes and natural frequencies of the target fixture are known and can therefore be used in the cost function. The optimization starts by subdividing a design volume, where each partition can be assigned a different density and Young's modulus value. At each iteration, a different combination of parameter values, determined by a genetic algorithm, is chosen. The natural frequencies and mode shapes of the current design are determined and compared to the target values. Once a sufficient match is achieved, the design is complete. It is assumed that if the dynamics of the fixture match the dynamics of the target, then the dynamics of the connecting component will also be preserved. The details of this approach will be presented next, followed by a proof-of-concept demonstration of its potential effectiveness. Conclusions and a discussion of how the method can be generalized for cases when the mode shapes and frequencies of the fixture are not known are given last.

1.2 Approach

Figure 1.2 illustrates the proposed approach. The goal of this work is to develop an optimization procedure that designs a fixture for a component (shown in red) that replaces its connecting component (shown in blue) in an assembly. The fixture should preserve the dynamics of the remaining component. The starting point for the fixture design is a generic design volume, as shown in the center image of Fig. 1.2. The design volume is subdivided into smaller subvolumes, each of which

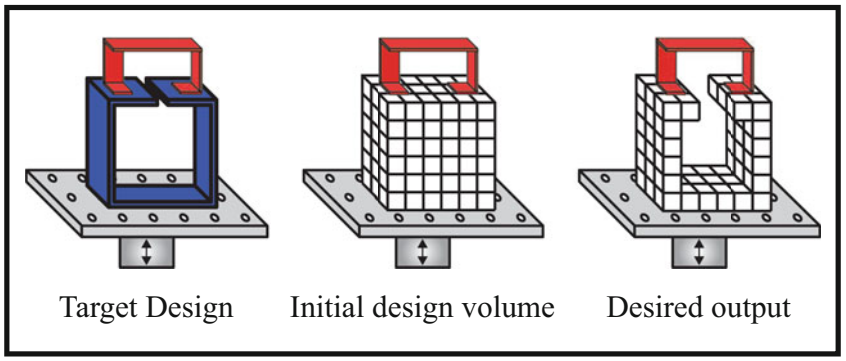

Fig. 1.2 The goal of the optimization process is to design a fixture that can replace the connecting component in the assembly

can be independently assigned density and modulus values. This approach is similar to topology optimization with one significant difference. Instead of the material property values assuming a value of zero or 100%, the properties can assume values from 0 to 100% of a nominal value. It is assumed that this continuous range is possible because of the flexibility that additive manufacturing, such as 3D printing, offers. The density and modulus of a part, or sections of a part, can be changed by changing the fill density, pattern, and/or other printing parameters [7].

A genetic algorithm-based optimization approach was selected to iterate on the material property values to find an optimum design. The genetic algorithm was chosen because it does not require a gradient calculation. Instead, a genetic algorithm chooses a "population" of parameters and evaluates their suitability based on a cost function. After each iteration, a new population is chosen from both past, low-cost parameter values and new parameter values that can be either a combination of good performing parameters or other parameter values that explore the bounded parameter space. Over time, the algorithm converges on a locally optimum solution to the problem. It is important to note that the solution produced by a genetic algorithm is not guaranteed to be a global minimum. Furthermore, the algorithm is not guaranteed to converge to the same solution if a problem is solved twice. The convergence depends on the initial population and the evolution of the subsequent generations.

To begin the optimization process, material properties are assigned to each subvolume. Then, the linear dynamics are simulated and the natural frequencies and mode shapes of the part are identified. These parameters are then compared to the parameters of the target design by calculating the cost function, C, using

$$C = \sum_{n=1}^{N} \frac{|\omega_{T,n} - \omega_n|}{\omega_{T,n}} + (1 - MAC_n) \tag{1.1}$$

where $\omega_{T,n}$ is the target natural frequency of the nth mode, ω_n is the natural frequency of the nth mode for the current design iteration, MAC_n is the Modal Assurance Criterion (MAC) value calculated using the nth mode shape of the target part and the current design iteration, and N is the number of modes used for comparison. The MAC provides a measure of the degree of linearity between two modal vectors and is calculated using [8]

$$MAC = \frac{\left|\{\psi_1\}^H \{\psi_2\}\right|^2}{\{\psi_1\}^H \{\psi_1\} \{\psi_2\}^H \{\psi_2\}} \tag{1.2}$$

where ψ_1 is a modal vector from data set 1, ψ_2 is a modal vector from data set 2, and H indicates the complex (i.e., Hermitian) transpose. MAC values are always in the interval [0, 1], where values close to 1 indicate that two mode shapes are very similar. In this work, it is assumed that the mode shapes and natural frequencies of the target design are known. Later, the case in which these values are not known will be discussed.

After the cost for each of the parameter combinations in the first population of parameter values is determined, the genetic algorithm chooses a new population of parameters and the process repeats. When the value of the cost function goes below a threshold or the change in the minimum cost between successive populations stays below a threshold, the process is stopped and the best combination of parameter values is chosen as the solution.

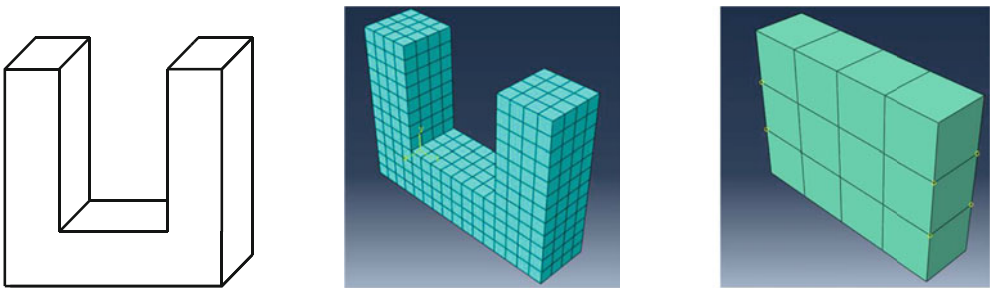

(a) (b) (c)

Fig. 1.3 (**a**) Target part; (**b**) finite element model of the target part; and (**c**) initial design volume used in the optimization

Table 1.1 Results of the design optimization

	Frequency			MAC value
Mode	Target (Hz)	Opt. result (Hz)	% Diff.	Opt. result
1	21.1	24.6	16.6	0.9045
2	25.3	25.1	−0.5	0.8366
3	46.2	46.8	1.1	0.9262
4	56.7	50.4	−11.1	0.9691
5	84.5	77.5	−8.3	0.7877

1.3 Problem Setup and Analysis

To demonstrate the effectiveness of the genetic algorithm-based optimization approach, the target design, similar to the base of the BARC and shown in Fig. 1.3a, was modeled using finite element software (Abaqus). Figure 1.3b shows the finite element model of the target part that was used to generate the target mode shapes and natural frequencies. The initial design volume, shown in Fig. 1.3c, was chosen with dimensions that match the outer dimensions of the target part, which were chosen arbitrarily. The design volume was subdivided into 12 subvolumes and sectioned in Abaqus such that each subvolume could be assigned different material properties.

The analysis procedure was implemented using a combination of MATLAB and Abaqus software. The genetic algorithm-based optimization was set up in MATLAB in order to take advantage of its optimization tools. The finite element model analysis was run in Abaqus. To easily interface the two software programs, code to programmatically create the finite element model was developed. Python code, based on Abaqus API, was generated in MATLAB and written to a file that was then accessed by Abaqus. This approach allowed the material property values, which are generated by MATLAB's genetic algorithm tools, to be input into the model. A system command issued from MATLAB began the Abaqus analysis process. Once the analysis was complete, the results were written to a text file and then read into MATLAB in order to evaluate the cost function.

The material properties of each of the 12 subvolumes were defined as a percentage of a nominal value. The nominal density and Young's modulus values were chosen to match those of the target part, which were chosen arbitrarily. In order to prevent unrealizable combinations, for example, 0% density and 100% modulus, density and modulus values were scaled with the same percentage within each subvolume. The initial values of each of these 12 parameters were assigned randomly by MATLAB's genetic algorithm.

1.4 Results

The optimization was run using the first five modes and a population size of 200. After 40 generations, a solution was identified. Table 1.1 shows a comparison of the natural frequencies and mode shapes of the optimization result and the target part. There is good agreement in the first five natural frequencies, with absolute differences ranging between 0.5% and 16.6%. The mode shapes also showed strong correlation with MAC values ranging from 0.79 to 0.97. Figure 1.4a shows the MAC comparisons graphically. Figure 1.4b shows the 12 parameter values for the design solution. The percentages show how the nominal material property values were scaled to achieve the solution. The expected values are 100% for all sections along the left, bottom, and right edges and 0% for the inner four sections. The values in the inner four sections are relatively

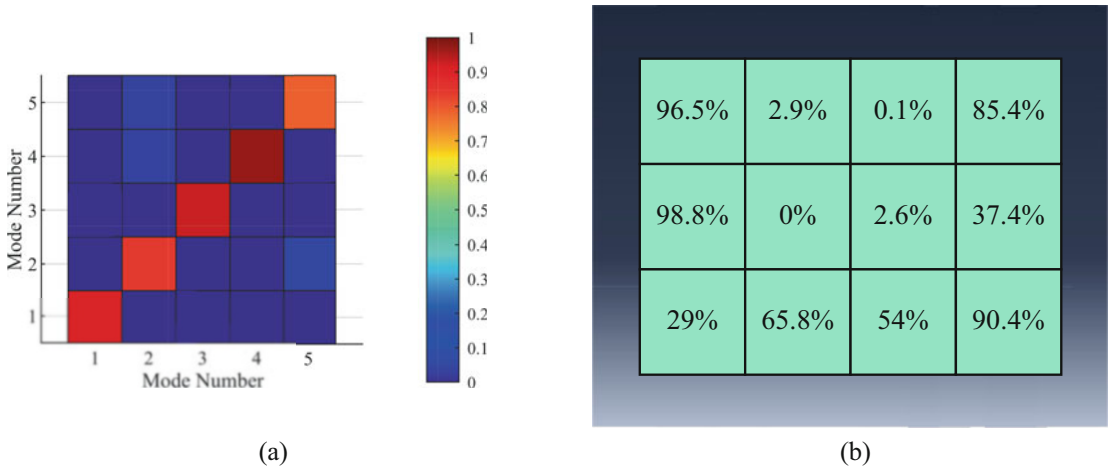

Fig. 1.4 (**a**) Target part; (**b**) finite element model of the target part; and (**c**) initial design volume used in the optimization

close to 0%, but several of the outer values are much less than the expected 100%. It is not clear why the algorithm could not tune these parameters closer to the expected values. It is possible that if a stricter stopping criterion was used, the algorithm would have kept searching for a better solution and these values would have eventually converged to the expected values. Despite these differences, the results indicate the potential of this method to identify a design that has preselected dynamics.

To develop this approach further and make its application more generalizable, several refinements will be considered in future work. First, the geometry of the target part used in the above analysis was simple and allowed a small number of partitions to be used to divide the initial design volume. As the complexity of the target part increases, the number of partitions used to divide the initial design volume will likely need to be increased. A larger number of partitions will allow the optimized part to realize more complex mode shapes, which would likely lead to a better dynamic match to the target part. However, increasing the number of partitions means more parameter values in the optimization problem and longer analysis times. Determining how to select the number of partitions to balance this trade-off will be the subject of future work. Another consideration is how to create the fixture design without needing the mode shapes and natural frequencies of the target part. The cost function (Eq. 1.1) used in this analysis required these modal parameters. However, this detailed information may not be available in a more realistic, industry setting. To address this challenge, the cost function used in the optimization can be reformulated to only consider the response characteristics of the small component. This will allow the optimization process to refine the fixture design until the connecting component responds as if it was mounted in the assembly. The next steps of this work will be to determine which response characteristics (linear, nonlinear, etc.) to include in the reformulated cost function.

1.5 Conclusions

The purpose of this work was to demonstrate a genetic algorithm-based optimization process that identifies a fixture design whose dynamics match those of a target part. The process starts with a generic design volume that is subdivided into subvolumes, each of which can be assigned different material properties. During the optimization, combinations of these material properties are interrogated until the linear dynamics of the design sufficiently match those of a target part. This process was demonstrated for a box-like fixture similar to the one used in the BARC from the Boundary Condition Challenge Problem. The first five modes of the resulting fixture design matched well with the target design. Natural frequencies were all within 16% of the target values, and the MAC values for the first five mode shapes were all greater than 0.79. Future work will address the need to generalize the method such that the natural frequencies and modes shapes of the target part do not need to be included in the analysis.

Acknowledgments This work was funded by Honeywell Federal Manufacturing & Technologies, LLC under Contract No. DE-NA-0002839 with the US Department of Energy/National Nuclear Security Administration. The US government retains and the publisher, by accepting the article for publication, acknowledges that the US government retains a nonexclusive, paid-up, irrevocable, worldwide license to publish or reproduce the

Honeywell Federal Manufacturing & Technologies is operated for the US Department of Energy under Contract Number DE-NA-0002839.

This work is funded by the Department of Energy's Kansas City National Security Campus, operated by Honeywell Federal Manufacturing & Technologies, LLC under contract number DE-NA0002839.

References

1. Avitabile, P.: Why you can't ignore those vibration fixture resonances. Sound Vib. **33**, 20–27 (1999)
2. Takeshita, A., Sedillo, H., Jankowski, K., Barba, J., Bouma, A., Billingsley, E., Abdelkefi, A.: Effects of test fixture connections and interference of the barc structure on its dynamical responses. I. J. Mech. Sci. **221**, 107186 (2022)
3. Soine, D.E., Jones, R.J., Harvie, J.M., Skousen, T.J., Schoenherr, T.F.: Designing hardware for the boundary condition round robin challenge. In: Topics in Modal Analysis & Testing, vol. 9, pp. 119–126. Springer, Berlin (2019)
4. Musella, U., Blanco, M.A., Mastrodicasa, D., Monco, G., Emilio, D.L., Simone, M., Peeters, B., Mucchi, E., Guillaume, P.: Combining test and simulation to tackle the challenges derived from boundary conditions mismatches in environmental testing. In: Sensors and Instrumentation, Aircraft/Aerospace, Energy Harvesting & Dynamic Environments Testing, vol. 7, pp. 259–269. Springer, Berlin (2020)
5. Rohe, D.P., Schultz, R.A., Schoenherr, T.F., Skousen, T.J., Jones, R.J.: Comparison of multi-axis testing of the barc structure with varying boundary conditions. In: Sensors and Instrumentation, Aircraft/Aerospace, Energy Harvesting & Dynamic Environments Testing, vol. 7, pp. 179–193. Springer, Berlin (2020)
6. Schoenherr, T.F.: Designing an optimized fixture for the barc hardware using a parameterized model. Technical report, Sandia National Lab. (SNL-NM), Albuquerque, NM (2019)
7. Dudescu, C., Racz, L.: Effects of raster orientation, infill rate and infill pattern on the mechanical properties of 3d printed materials. ACTA Univ. Cibiniensis **69**(1), 23–30 (2017)
8. Allemang, R.J.: The modal assurance criterion–twenty years of use and abuse. Sound Vib. **37**(8), 14–23 (2003)

Chapter 2
Substructure Modeling and Interface Characterization of Lap-Joint Beam

Gabrielle Graves, Michael Ross, and Abdessattar Abdelkefi

Abstract The purpose of this work is to model the interface behavior of a bolted lap joint with dynamic substructuring techniques. Assembled structures are notable for their nonlinearities, energy dissipation, and uncertainties due to sliding and slapping of the substructures at the joint interface. The consequential linear and nonlinear effects make it imperative to accurately model the complex joint interface physics. A dual-assembly method is used to couple linear beam substructures and a nonlinear interface subdomain with Lagrange multipliers. Coupling methodologies that employ Lagrange multipliers allow the solvers to be tuned to the physics of each domain and subsequently increase the efficiency of the solution. Furthermore, this methodology enables the implementation of various joint models. The linear joint model employed in this work simulates the joint dynamics with springs and dampers, which are inserted between coincident nodes of the substructures. These elements inhibit the interface degrees of freedom from rigid coupling and define the contact stiffness and contact damping.

Keywords Substructuring · Lagrange multipliers · Bolted joint · Nonlinear dynamics

2.1 Introduction

Bolted connections are a versatile and reliable means to assemble structures. The implementation of bolted connections is simple, but the physical behavior of assembled structures is complex due to the dynamics of the joint interfaces. The interface slip–stick behavior under loading causes nonlinear stiffness and frictional energy dissipation. These joint nonlinearities are difficult to predict and may vary between identical structures due to the uncertainty in micro-geometry [1]. Domain decomposition (DD) methods are a numerical way to dynamically couple partitions of an assembled structure at interface boundaries or internally. All DD methods fall into either the overlapping or nonoverlapping categories [2]. Both DD methodologies use coupled time-stepping algorithms to iteratively solve for dynamic response of each subdomain. However, overlapping methods partition a structure in a way such that parts of subdomains intersect each other. Nonoverlapping methods, often referred to as dynamic substructuring, have subdomains that only intersect at a single interface. Some nonoverlapping methods such as FETI create continuity between the partitions at the interface with Lagrange multipliers [3]. Dynamic substructuring (DS) is a valuable tool for large-scale system modeling given its ability to capture component dynamics and reduce computational time [4]. DS methods conduct a primal assembly by assuming linear interface behavior and coupling and assembling the substructures with fixed interface modes [5]. Dual-assembly techniques also employ compatibility equations to equalize the interface displacement; however, the structure is assembled with equilibrium forces, which generates weak interface compatibility [4]. There are many investigations involving physical domain dynamic substructuring on large systems. However, the implementation of DS with finite rigid coupling for interface modeling has not

G. Graves (✉)
Sandia National Laboratories, Albuquerque, NM, USA

Department of Mechanical and Aerospace Engineering, New Mexico State University, Las Cruces, NM, USA
e-mail: gabyg98@nmsu.edu

M. Ross
Sandia National Laboratories, Albuquerque, NM, USA

A. Abdelkefi
Department of Mechanical and Aerospace Engineering, New Mexico State University, Las Cruces, NM, USA

M. Allen et al. (eds.), *Dynamic Substructures, Volume 4*, Conference Proceedings of the Society for Experimental Mechanics Series, https://doi.org/10.1007/978-3-031-36694-9_2

received as much attention. This study hopes to gain insight into alternative linear contact modeling techniques by simulating interface displacement discontinuities of a lap-joint beam with springs connected to coincident nodes. In addition, it is desired to partition the solvers based on the physics of the subdomains. Therefore, the structure is partitioned into three subdomains where the two linear subdomains are the beam plates and the third is the interface domain that has linear and nonlinear properties.

2.2 Lap-Joint Beam and Substructure Modeling

The exemplary problem modeled in this study is a lap-jointed beam assembly with cantilever boundary conditions and a tip mass at the right end. The substructure plates and tip mass are composed of 1080 steel alloy. The SAE grade 2 bolt, which is located at the center of the assembled plates, has a 5/16 inch nominal diameter. The interface overlap of the assembly is 60 mm while the overall length excluding the tip mass is 500 mm. Figure 2.1 depicts the lap-jointed structure while Table 2.1 lists the material and geometric properties.

The modeled structure in this study is a simple cantilever lap-joint beam with a tip mass on the free end. The structure is partitioned into three subdomains, which includes the two plates and the interface. Traditionally the interface is not considered a separate domain and therefore does not have any independent stiffness and damping properties. However, specifying an interface domain allows the linear and nonlinear joint characteristics to be explicitly defined [6]. Furthermore, a separate interface domain with independent degrees of freedom (dof) enables all subdomains to be rigidly coupled with two interfacial boundaries and avoids complex compatibility equations. All subdomains are coupled in the physical domain with an equilibrium force at the shared boundary, g. These equilibrium forces at each coupled dof can be expressed with signed Boolean matrices and Lagrange multipliers:

$$g_1 = -B_{i1}^T \lambda_1 = -B_1^T \lambda_1 \tag{2.1}$$

$$g_2 = B_{i2}^T \lambda_2 = -B_2^T \lambda_2 \tag{2.2}$$

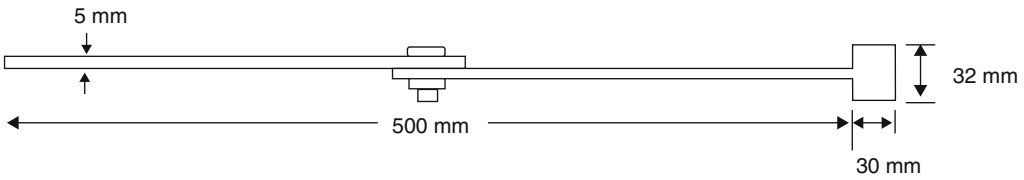

Fig. 2.1 Lap-jointed beam schematic

Table 2.1 Material properties and dimensions of lap-joint beam

Structure properties	Description	Values	Units
E	Young's modulus	210	GPa
ρ	Density	7720	Kg/m^3
L	Total length of beam plates	500	mm
t	Thickness of beam plates	5	mm
w	Width of beam plates	25	mm
L_t	Length of tip mass	30	mm
h_t	Height of tip mass	32	mm

The above equilibrium forces apply for all dof for each coincident node pair and are only valid if the meshes of the subdomains at the boundaries are identical. Equations (2.3) and (2.4) express the two compatibility equations that tie all degrees of freedom at the interfacial boundaries. The mesh of each subdomain at the interfacial boundaries is identical so that the degrees of freedom of coincident nodes are constrained.

$$B_1 u_1 + B_{i1} u_i = 0 \tag{2.3}$$

$$B_2 u_2 + B_{i2} u_i = 0 \tag{2.4}$$

The coupling between the three subdomains brought by the equilibrium and compatibility equations results in the following equations of motion:

$$M_1 \ddot{u}_1 + C \dot{u}_1 + K_1 u_1 + B_1^T \lambda_1 = F_1 \tag{2.5}$$

$$M_2 \ddot{u}_2 + C_2 \dot{u}_2 + K_2 u_2 + B_2^T \lambda_1 = F_2 \tag{2.6}$$

$$M_i \ddot{u}_i + C_i \dot{u}_i + K_i u_i + B_{i1}^T \lambda_1 + B_{i2}^T \lambda_2 = 0 \tag{2.7}$$

2.3 Eigenvalue Problem Validation

Before examining the dynamics of the modeled structure with boundary displacement discontinuities, a rigid joint must be modeled and validated. The partitioned model can obtain a rigid joint by increasing all spring stiffness values across the entire interface to 1×10^8 N/m, such that all tangential and axial relative movements are negligible. This is comparable to a tied constraint for all three dof at each node in Sierra SD. In Table 2.2, the first three natural frequencies of the substructured and tied model are compared.

$$\left(\begin{bmatrix} K_1 & \overline{0} & \overline{0} & B_1^T & \overline{0} \\ \overline{0} & K_2 & \overline{0} & \overline{0} & B_2^T \\ \overline{0} & \overline{0} & K_i & B_1^T & B_2^T \\ B_1 & \overline{0} & B_{1i} & \overline{0} & \overline{0} \\ \overline{0} & B_2 & B_{2i} & \overline{0} & \overline{0} \end{bmatrix} - \omega^2 \begin{bmatrix} M_1 & \overline{0} & \overline{0} & \overline{0} & \overline{0} \\ \overline{0} & M_2 & \overline{0} & \overline{0} & \overline{0} \\ \overline{0} & \overline{0} & M_i & \overline{0} & \overline{0} \\ \overline{0} & \overline{0} & \overline{0} & \overline{0} & \overline{0} \\ \overline{0} & \overline{0} & \overline{0} & \overline{0} & \overline{0} \end{bmatrix} \right) \overline{X} = \overline{0} \tag{2.8}$$

The natural frequencies' errors are mainly attributed to the pseudo mass of the interface domain, M_i. A pseudo mass matrix is applied to recondition the analysis and allow for convergence of transient analyses. For the above eigenvalue problem described by Eq. (2.8) and other transient analyses, M_i is a diagonal matrix with all nonzero values equivalent to 0.001 kg. The small quantity of interface mass decreases the natural frequency of the substructured model. If the interface domain was not considered a separate domain, a pseudo mass matrix would not be necessary since the interface stiffness and damping would be implemented into the beam plate subdomains.

Table 2.2 Natural frequencies of substructured and tied models

Natural frequency	Substructured model	Tied model	Error (%)
ω_1	17.761	17.932	0.95
ω_2	52.945	53.429	0.91
ω_3	124.282	131.124	5.20

2.4 Conclusions

In this work, the dynamic effects of the linear properties of a bolted joint interface were modeled with linear translational springs coupling the dof of each coincident node pair of the finite element model. It was found that the substructured model behaves as a continuous beam with a tied contact definition at the interface when the spring stiffness is above 1×10^8 N/m. However, due to the conditioning of the substructuring approach, a pseudo mass was added to the interface domain. This created slight errors in the natural frequencies between the tied and substructured models. A deeper investigation will be conducted to model the nonlinear and linear with magnitudes dependent on the radial distance from the bolt. The area that the joint forces will reside will be dependent on the bolt preload and the frustum zone. Furthermore, the nonlinear softening and damping must be captured by implementing Jenkin's elements. The Jenkin's elements will also model the dynamics of the interface by defining the stick or slip state of each node pair at the interface.

Acknowledgments This article has been authored by an employee of the National Technology & Engineering Solutions of Sandia, LLC under Contract No. DE-NA0003525 with the U.S. Department of Energy (DOE). The employee owns all rights, title, and interest in and to the article and is solely responsible for its contents. The US government retains and the publisher, by accepting the article for publication, acknowledges that the US government retains a nonexclusive, paid-up, irrevocable, worldwide license to publish or reproduce the published form of this article or allow others to do so for US government purposes. The DOE will provide public access to these results of federally sponsored research in accordance with the DOE Public Access Plan.

References

1. Brake, M.R.: The mechanics of jointed structures: recent research and open challenges for developing predictive models for structural dynamics. AIAA J. **5**, 1169–1181 (2017)
2. Dolean, V., Jolivet, P., Nataf, F.: An introduction to domain decomposition methods: algorithms, theory, and parallel implementation. Soc. Ind. Appl. Math. (2015)
3. Gosselet, P., Rey, C.: Non-overlapping domain decomposition methods in structural mechanics. Arch. Comput. Meth. Eng. **13**, 515–572 (2006)
4. de Klerk, D., Rixen, D.J., Voormeeren, S.N.: General framework of dynamic substructuring: history, review and classification of techniques. AIAA J. **46**, 1169–1181 (2008)
5. Rixen, D.J., Gruber, F.M.: Evaluation of substructure reduction techniques with fixed and free interfaces. Strojniški vestnik-J. Mech. Eng. **62**, 452–462 (2016)
6. Rixen, D.J., Klassen, S.W.B.: Using SEMM to identify the joint dynamics in multiple degrees of freedom without measuring interfaces. Dyn. Substruct. **4**, 87–99 (2020)

Chapter 3
Characterization of Rubber Mounts Through Virtual Point Transformation Using Different Boundary Conditions in the Context of Dynamic Substructuring

Alessandro Zucchini, Frank Naets, and Arthur Hülsmann

Abstract Nowadays, especially in the electric mobility field, noise and vibrations is becoming day by day a more important topic that requires accurate prediction. In the context of dynamic substructuring applied to the automotive field, a crucial aspect for determining the noise property of a vehicle is the evaluation of the transfer behavior of the rubber elements connecting the different components of a car. The goal of this research is to extract the frequency-dependent dynamic stiffness for different models of rubber bushings presenting a similar architecture and belonging to the rear drivetrain of a BMW i4 and iX. In particular, we will compare two different methods for characterizing the dynamic behavior of nonlinear elements. Firstly, for each type of bushings, a free-free measurement procedure will be considered. In comparison to literature, this approach will be adapted with a third metal bracket to account for the current bushing's architecture. In this procedure, the dynamic properties are determined from triaxial accelerometers measurements with impact hammer excitation. The output results in terms of dynamic stiffness will be compared with dedicated measurements conducted on a Hydropulse machine inside a test bench of the BMW Group. Secondly, on the same bushings, an experiment will be performed by clamping the rubber mounts to the ground and creating fixed boundary conditions. This second approach should allow to directly extract dynamic stiffness properties, without first performing a system inversion. Since this approach is suitable both for hammer impacts or shaker excitations, both approaches will be explored and further analyzed. Both the free-free and the fixed boundary condition experiment implement the technique of virtual point transformation. Therefore, further attention will be given to error evaluations coming from such technique and how to improve the transformation in terms of accuracy and numerical stability. Future research will focus on how the extracted dynamic stiffness models can be integrated into a system-level simulation framework for electrical vehicle noise generation.

Keywords Virtual point transformation · Dynamic substructuring · Transfer path analysis · Rubber mount characterization · Error evaluation

3.1 introduction

Dynamic substructuring (DS) has proven to be a powerful engineering tool for a wide variety of industries. It allows a complex dynamic system to be modeled and analyzed as separate components or "substructures',' building a bridge between the efforts of different suppliers and design groups. Also, components coming from numerical models may be coupled with experimental data. Substructuring methods associated with these models are numerous and have been well accepted over the

A. Zucchini (✉)
BMW Group, München, Germany

KU Leuven, Department of Mechanical Engineering, Heverlee, Belgium
e-mail: alessandro.zucchini@bmw.de

F. Naets
KU Leuven, Department of Mechanical Engineering, Heverlee, Belgium

DMMS Core Lab, Flanders Make, Leuven, Belgium
e-mail: frank.naets@kuleuven.be

A. Hülsmann
BMW Group, München, Germany
e-mail: arthur.huelsmann@bmw.de

M. Allen et al. (eds.), *Dynamic Substructures, Volume 4*, Conference Proceedings of the Society for Experimental Mechanics Series, https://doi.org/10.1007/978-3-031-36694-9_3

last decades [1, 2]. In the automotive field, the most common domain for DS is the frequency domain because of two main reasons:

- Firstly, it is easy to express differential equations of a dynamical system by means of its frequency response functions (FRFs).
- Secondly, this domain is the most convenient for combining experimental models with numerical obtained ones.

However, with increasing product complexity, the question arises of how truthful some models represent the actual behavior of the components. Experimental identification of components is therefore often desired for the purpose of model validation. Although the substructuring techniques themselves are formulated in a rather straightforward way (see, for instance, [3]), the largest challenges exist in the coupling of the measured components. This work follows and expands some previous experimental campaigns available in [4] and in [5].

3.2 Virtual Point Transformation

For the evaluation of the transfer function through dynamic substructuring, we need to connect different components on some connection points instead of using a discrete interface. These points are said to be virtual because very often are difficult to access or it is even impossible to apply a sensor on them. In our case, rubber bushings connect those structures. The general layout of such rubber elements is shown in Fig. 3.1; the geometry can be slightly different. However, they all consist of an external rubber cylinder and an internal aluminum core.

The virtual point transformation helps us since we can reduce those two discrete interfaces to two points. The VPT is nothing more than a geometrical reduction: we will measure displacements and excitations in the proximity of the coupling point to obtain its six degrees of freedom and its six moments under the assumption that the system is behaving rigidly.

Here, we briefly recall the VPT; for more details, we advise to read [6–8]. The virtual point transformation relies on a reduction in a modal sense, namely, reducing the interface connectivity using a set of interface deformation modes (IDMs) specified by a matrix $\boldsymbol{R}$.

A virtual point v is surrounded by N_k triaxial acceleration sensors, registering translational displacements in the local $(x; y; z)$ frame of the sensors. Then N_h local impacts are applied to the structure. The relation between the six IDMs and the number of responses coming from the sensors is given by

$$\boldsymbol{u} = \boldsymbol{R}_u \boldsymbol{q} + \boldsymbol{\mu} \tag{3.1}$$

The matrix $\boldsymbol{R}_u$ is responsible for translating the actual displacements $\boldsymbol{u}$ detected by the accelerometers into the three displacements and three rotations $\boldsymbol{q}$ of the virtual point. Since the number of IDMs of the virtual point is smaller than the number of DOF, we add a residual on the displacements $\boldsymbol{\mu}$. Expanding the previous equation for the single virtual point v and the single sensor k:

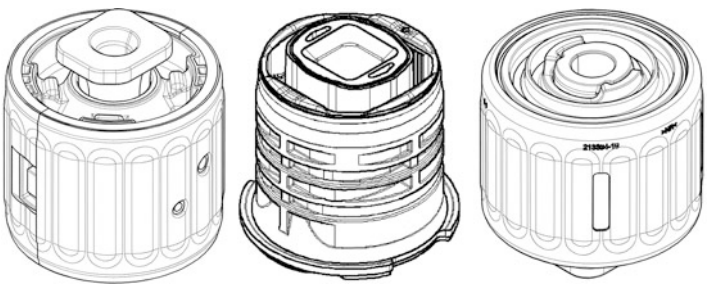

Fig. 3.1 Drawing of the different architectures of rubber bushings

$$\begin{Bmatrix} u_x^k \\ u_y^k \\ u_z^k \end{Bmatrix} = \boldsymbol{R}^{kv}\boldsymbol{q}^v + \boldsymbol{\mu}^v = \boldsymbol{E}^{k^T}\bar{\boldsymbol{R}}^{kv} + \boldsymbol{q}^v + \boldsymbol{\mu}^v = \begin{bmatrix} e_{x,X}^k & e_{x,Y}^k & e_{x,Z}^k \\ e_{y,X}^k & e_{y,Y}^k & e_{y,Z}^k \\ e_{z,X}^k & e_{z,Y}^k & e_{z,Z}^k \end{bmatrix} \begin{bmatrix} 1 & 0 & 0 & 0 & r_Z^k & -r_Y^k \\ 0 & 1 & 0 & -r_Z^k & 0 & r_X^k \\ 0 & 0 & 1 & r_Y^k & -r_X^k & 0 \end{bmatrix} \begin{Bmatrix} q_X^v \\ q_Y^v \\ q_Z^v \\ q_{\theta_X}^v \\ q_{\theta_Y}^v \\ q_{\theta_Z}^v \end{Bmatrix} + \begin{Bmatrix} \mu_x^k \\ \mu_y^k \\ \mu_z^k \end{Bmatrix} \tag{3.2}$$

where $\bar{\boldsymbol{R}}^{kv}$ is the 3×6, global frame matrix associated with the sensor k and the virtual point v and contains an identity matrix and the position vector of the sensor k in matrix form with respect to the global system of coordinates. $\boldsymbol{E}^k$ is the rotation matrix from the global to the local coordinate system of the sensor k. For a certain number of sensors N_k and virtual points N_v, we define $\boldsymbol{R}_u$ with

$$\boldsymbol{R}_u = \begin{bmatrix} \boldsymbol{R}^{1,1} & & & & \\ \boldsymbol{R}^{2,1} & \boldsymbol{0} & \boldsymbol{0} \cdots & \boldsymbol{0} & \\ \boldsymbol{R}^{3,1} & & & & \\ & \boldsymbol{R}^{4,2} & & & \\ \boldsymbol{0} & \boldsymbol{R}^{5,2} & \boldsymbol{0} & \boldsymbol{0} & \vdots \\ & \boldsymbol{R}^{6,2} & & & \\ \vdots & \boldsymbol{0} & \boldsymbol{0} & \ddots & \\ & & & & \boldsymbol{R}^{N_{k-2},N_v} \\ \boldsymbol{0} & \boldsymbol{0} & \boldsymbol{0} & \cdots & \boldsymbol{R}^{N_{k-1},N_v} \\ & & & & \boldsymbol{R}^{N_k,N_v} \end{bmatrix} \tag{3.3}$$

In case of a single spare channel c in the local direction e_i^c, it is possible to write

$$u_i^c = \boldsymbol{R}_i^{cv}\boldsymbol{q}^v + \mu_i^c = \left[e_i^{c^T} \ (r_i^c \times e_i^c)^T\right]\boldsymbol{q}^v + \mu_i^c \tag{3.4}$$

Finally, the resulting IDMs matrix $\boldsymbol{R}_u$ shall be block diagonal, or at least have IDMs that are uncoupled over the various virtual points and sensor groups (if a different ordering was used). Note that in any case one should take care that $\boldsymbol{R}_u$ is at least full rank (but preferably overdetermined) such that a (generalized) pseudo-inverse $\boldsymbol{T}_u$ can be computed by applying

$$\boldsymbol{q} = \left(\boldsymbol{R}_u{}^T \boldsymbol{W}_u \boldsymbol{R}_u\right)^{-1} \boldsymbol{R}_u{}^T \boldsymbol{W}_u \boldsymbol{u} = \boldsymbol{T}_u \boldsymbol{u} \tag{3.5}$$

Here, the matrix $\boldsymbol{W}_u$ is a $N_r \times N_r$ weighting matrix.

In a complete similar way, it is possible to transport the $m > n$ forces applied to the structure to obtain the $n = 6$ moments around the virtual point. For the forces, we can write

$$\boldsymbol{m} = \boldsymbol{R}_f \boldsymbol{f} \tag{3.6}$$

Expanding that equation for a single impact h for the virtual point v:

$$\begin{Bmatrix} m_X^v \\ m_Y^v \\ m_Z^v \\ m_{\theta_X}^v \\ m_{\theta_Y}^v \\ m_{\theta_Z}^v \end{Bmatrix} = \boldsymbol{R}^{hv^T} f^h = \begin{bmatrix} \boldsymbol{e}^h \\ \boldsymbol{r}^h \times \boldsymbol{e}^h \end{bmatrix} f^h = \begin{bmatrix} 1 & 0 & 0 \\ 0 & 1 & 0 \\ 0 & 0 & 1 \\ 0 & -r_Z^h & r_Y^h \\ r_Z^h & 0 & -r_X^h \\ -r_Y^h & r_X^h & 0 \end{bmatrix} \begin{Bmatrix} e_X^h \\ e_Y^h \\ e_Z^h \end{Bmatrix} f^h \tag{3.7}$$

where $\boldsymbol{R}^{hv}$ is defined by an identity matrix and the position vector of the impact in matrix form with respect to the global system of coordinates. $\boldsymbol{e}^h$ is the direction vector of the impact in the global coordinates of system. Once again, we build the block diagonal matrix $\boldsymbol{R}_f$ for the number of impacts N_h and number of virtual points N_v find by using a generalized inverse:

$$\boldsymbol{f} = \boldsymbol{W}_f{}^T \boldsymbol{R}_f (\boldsymbol{R}_f{}^T \boldsymbol{W}_f \boldsymbol{R}_f)^{-1} \boldsymbol{m} = \boldsymbol{T}_f{}^T \boldsymbol{m} \tag{3.8}$$

where $\boldsymbol{W}_f$ is an $N_h \times N_h$ weighting matrix for the impacts.

From those two transformation matrices $\boldsymbol{T}_u$ and $\boldsymbol{T}_f{}^T$, it is possible to reduce the $N_r \times N_h$ FRF matrix to a $6N_v \times 6N_v$ of the IDMs of our virtual point(s):

$$\boldsymbol{Y}_{qm} = \boldsymbol{T}_u \boldsymbol{Y}_{uf} \boldsymbol{T}_f{}^T \tag{3.9}$$

Here, $\boldsymbol{Y}_{uf}$ is the $N_r \times N_h$ accelerance matrix determined by the number of responses $N_r = 3N_k + N_c$ and the number of impacts N_h.

3.3 System of Study

As mentioned, the goal of this chapter is to extract the dynamic stiffness of some rubber isolators (see Fig. 3.1 for instance). Schematically, we can represent those elements as a spring connecting the 6 DOFs of two points that are said to be "virtual.' (Fig. 3.2).

To apply the virtual point transformation to those bushings, we will attach to them some aluminum brackets so that we can place sensors and impacts to the structure. Figure 3.3 briefly shows the four main structures that compose our full system:

- Two crosses $A1$ and $A2$ are attached respectively to the upper and the lower side of the internal aluminum core of the mount. We will reduce those components with the aluminum core to the first virtual point $VP1$ of the system.
- On the other side of the "spring," we will reduce to the second virtual point $VP2$ the cross B attached to the outer cylinder of the rubber isolator I.

It is important to remember that in our system the two virtual points are not located in two different positions in space (like schematically shown in Fig. 3.2), but occupy the same location at the center of the rubber mount.

Fig. 3.2 Schematic diagram of a rubber bushing through the virtual point representation

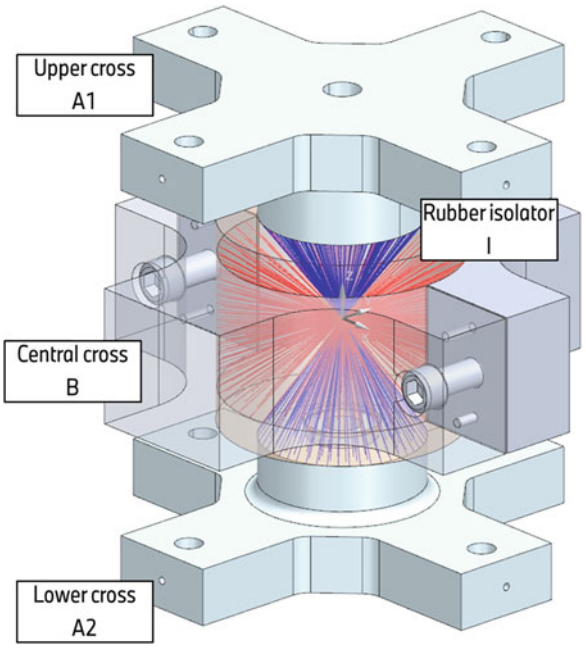

Fig. 3.3 Experiment setup in free-free conditions

Knowing our system and how the different parts are connected to each other, we can start writing the uncoupled system configuration dynamic stiffness like

$$\begin{bmatrix} \boldsymbol{Z}_{11}^{A1} & \mathbf{0} & \mathbf{0} & \mathbf{0} & \mathbf{0} \\ \mathbf{0} & \boldsymbol{Z}_{11}^{A2} & \mathbf{0} & \mathbf{0} & \mathbf{0} \\ \mathbf{0} & \mathbf{0} & \boldsymbol{Z}_{11}^{I} & \boldsymbol{Z}_{12}^{I} & \mathbf{0} \\ \mathbf{0} & \mathbf{0} & \boldsymbol{Z}_{21}^{I} & \boldsymbol{Z}_{22}^{I} & \mathbf{0} \\ \mathbf{0} & \mathbf{0} & \mathbf{0} & \mathbf{0} & \boldsymbol{Z}_{22}^{B} \end{bmatrix} \begin{Bmatrix} \boldsymbol{q}_1^{A1} \\ \boldsymbol{q}_1^{A2} \\ \boldsymbol{q}_1^{I} \\ \boldsymbol{q}_2^{I} \\ \boldsymbol{q}_2^{B} \end{Bmatrix} = \begin{Bmatrix} \boldsymbol{m}_1^{A1} + \boldsymbol{g}_1^{A1-I} + \boldsymbol{g}_1^{A1-A2} \\ \boldsymbol{m}_1^{A2} + \boldsymbol{g}_1^{A2-I} + \boldsymbol{g}_1^{A2-A1} \\ \boldsymbol{m}_1^{I} + \boldsymbol{g}_1^{I-A1} + \boldsymbol{g}_1^{I-A2} \\ \boldsymbol{m}_2^{I} + \boldsymbol{g}_2^{I-B} \\ \boldsymbol{m}_2^{B} + \boldsymbol{g}_2^{B-I} \end{Bmatrix} \tag{3.10}$$

where $\boldsymbol{Z}$ are the dynamic stiffnesses obtained after integrating and inverting the accelerances $\boldsymbol{Y}$, $\boldsymbol{q}$ are the 6 DOF of a structure reduced to its virtual point, $\boldsymbol{m}$ are the 6 moments of the structure around its virtual point, and $\boldsymbol{g}$ are the internal forces between two different substructures.
By imposing the displacements compatibility and the force equilibrium between the interfaces, we obtain the final form of the system $A1A2BI$:

$$\begin{bmatrix} \boldsymbol{Z}_{11}^{A1} + \boldsymbol{Z}_{11}^{A2} + \boldsymbol{Z}_{11}^{I} & \boldsymbol{Z}_{12}^{I} \\ \boldsymbol{Z}_{21}^{I} & \boldsymbol{Z}_{22}^{B} + \boldsymbol{Z}_{22}^{I} \end{bmatrix} \begin{Bmatrix} \boldsymbol{q}_1 \\ \boldsymbol{q}_2 \end{Bmatrix} = \begin{Bmatrix} \boldsymbol{m}_1^{A1} + \boldsymbol{m}_1^{A2} + \boldsymbol{m}_1^{I} \\ \boldsymbol{m}_2^{B} + \boldsymbol{m}_2^{I} \end{Bmatrix} \tag{3.11}$$

3.4 Error Evaluation

Much work has been done to evaluate performance indicators for the virtual point transformation [7, 9]. Here, we will propose a new idea for evaluating the sensor consistency during the displacement reduction. To do that, we will consider the simpler system $A1$ and apply this VPT check only to that structure instead of the entire assembly. This will provide us an indication of how reliable such transformation is and if, therefore, we are allowed to extend our assumptions to the main system $A1A2BI$. For the reason that we conducted the experiment using triaxial accelerometers, we are considering a redundant number of information for our displacement reduction. Theoretically six independent displacements $\boldsymbol{u}$ are needed to obtain the six IDMs displacements $\boldsymbol{q}$; this would be possible by using six unidirectional sensors. Since we are using triaxial accelerometers, there is a linear dependency between the acquired signals, and, therefore, we have the need of acquiring at least seven displacements. Because we have three sensors and we also have $N_r = 9$ responses and our information contain a redundancy. Here, also the number of hammer impact is redundant, but such information is not relevant for the sensor consistency evaluation.

Figure 3.4 gives an idea of the system of study: on the cross $A1$, we can identify four main points where hammer impacts (in red arrow) were performed and responses (in blue) were acquired.

The idea behind this method is, for each impact, to perform the displacement reduction by removing some of the redundant information from the displacement vector $\boldsymbol{u}$ and obtain the reduced displacement $\boldsymbol{q}^*$ at the virtual point. From that point, it is theoretically possible to transform back and reconstruct the removed displacements $u_{removed}$.

From Eq. 3.5, we can remove the rth redundant information of the ith sensor and the rth line of the transformation matrix $\boldsymbol{T}_u$ to obtain the new displacement IDMs like

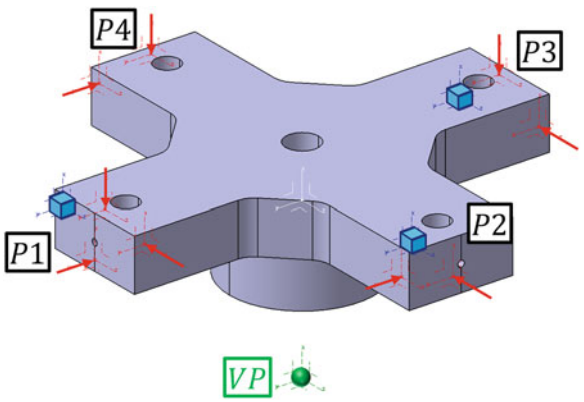

Fig. 3.4 Schematic representation of the virtual point transformation applied to the system $A1$

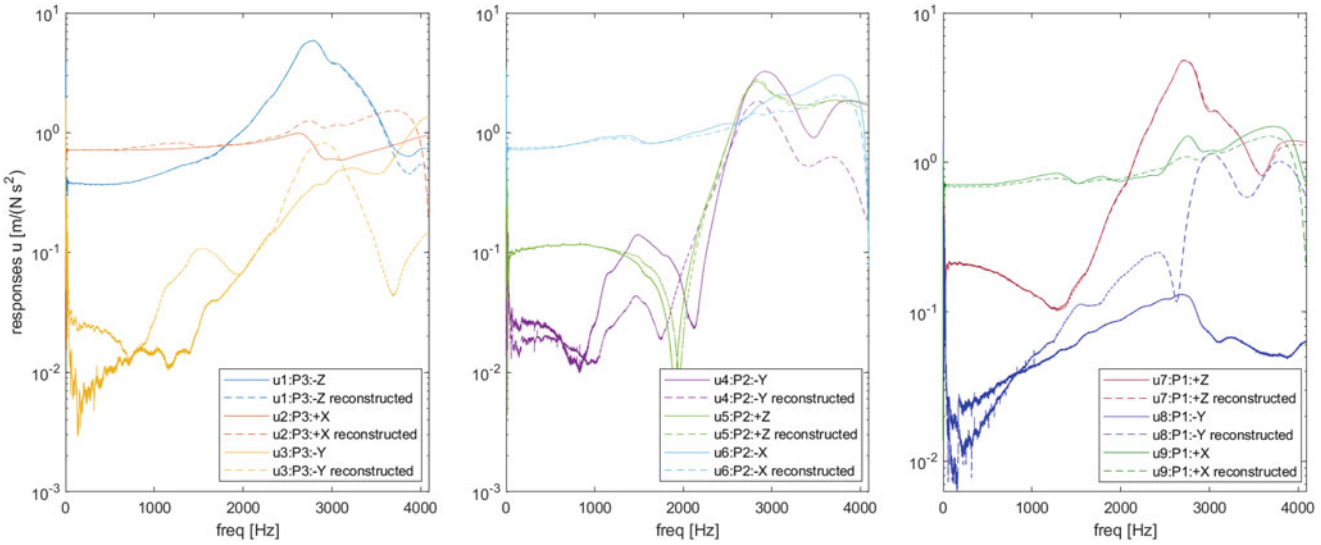

Fig. 3.5 Sensors reconstructed displacements vs. measured displacements

$$\boldsymbol{q}^* = \boldsymbol{T}_u{}^* \boldsymbol{u} = \boldsymbol{R}_u^{\sim 1*} \begin{Bmatrix} u_{1,1} \\ u_{2,1} \\ u_{3,1} \\ \vdots \\ \cancel{u_{r,i}} \\ \vdots \\ u_{3,k} \end{Bmatrix} \tag{3.12}$$

Note that here $\boldsymbol{T}_u{}^*$ is a 6×8 matrix since we removed one row. From Eq. 3.12, it is then possible to transform back to the original measured displacement and reconstruct the removed information.

$$\boldsymbol{u}^* = \boldsymbol{R}_u \boldsymbol{q}^* \tag{3.13}$$

Here, $\boldsymbol{u}^*$ is the 9×1 reconstructed displacements vector from the 6×1 IDMs $\boldsymbol{q}^*$. Figure 3.5 shows in three graphs the comparison between the measured displacement (with a solid line) and the reconstructed ones (with a dashed line), respectively, from the sensor placed in positions $P3$, $P2$, and $P1$ (see Fig. 3.4) of the system $A1$ in the full frequency range of acquisition.

What can we note here is that the measured displacement and the reconstructed one are matching quite well for almost the entire frequency range. The two curves separate only at very high frequency or at very low amplitude.

After performing the VPT with the reduced displacements vector and reconstructing the missing removed displacement for each rth response of all the $k = 3$ sensors, we evaluated the difference between the measured $\boldsymbol{u}$ and the reconstructed $\boldsymbol{u}^*$ through the modal assurance criterion MAC.

$$MAC(\boldsymbol{u}, \boldsymbol{u}^*) = \frac{(\tilde{\boldsymbol{u}}^* \boldsymbol{u})(\tilde{\boldsymbol{u}} \boldsymbol{u}^*)}{(\tilde{\boldsymbol{u}}^* \boldsymbol{u}^*)(\tilde{\boldsymbol{u}} \boldsymbol{u})} \tag{3.14}$$

Figure 3.6 shows the MAC value over the frequency range of acquisition for the impact in $+X$ global direction of the location $P1$. We repeated such operation for every impact applied on the system $A1$ and always obtained similar results. We can immediately note that $MAC > 0.95$ until 2500 Hz and begins to decrease only at higher frequencies. Being our frequency range of interest until 1500 Hz, we can hence always assume the virtual point transformation valid.

We conducted that study for the displacement IDMs reduction by considering as our displacement vector $\boldsymbol{u}$ the hth column of the accelerance matrix $\boldsymbol{Y}_{uf}$ corresponding to the the hth impact. The same operation can be done for the force reduction by considering the rth row of $\boldsymbol{Y}_{uf}$ and by removing, during the reduction in Eq. 3.8, the $1 < j\text{th} < N_h$ redundant information

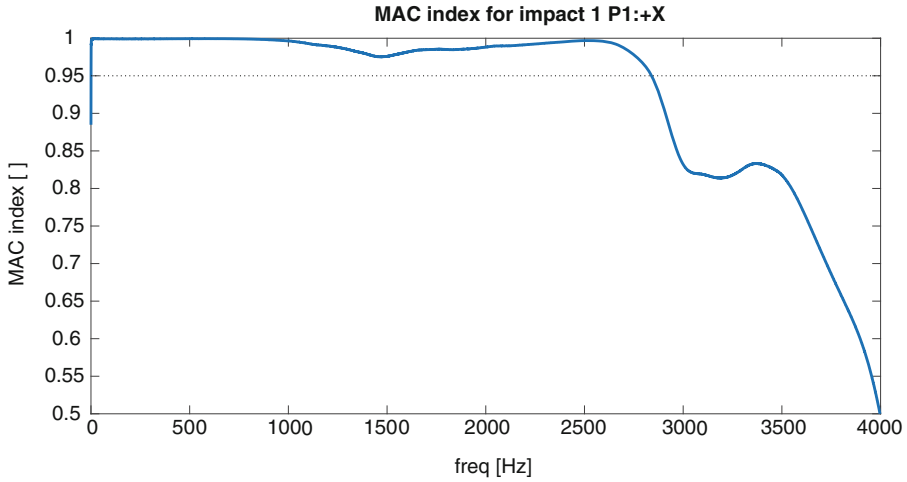

Fig. 3.6 Modal assurance criterion between $\boldsymbol{u}$ and $\boldsymbol{u}^*$ over the frequency range of acquisition

as well as the jth column from $\boldsymbol{T}_f{}^T$. From the 6 IDMs $\boldsymbol{n}^*$, it is again possible to reconstruct back and obtain the $1 \times N_h$ vector $\boldsymbol{f}^*$ and then compare it with $\boldsymbol{f}$ using Eq. 3.14. Again, this can be repeated for all the N_r response channels.

3.5 Measurements in Free-Free Boundary Conditions

The measurement in free-free boundary conditions has a schematic representation like the one in Fig. 3.2, where impacts and responses are respectively applied and measured on both sides of the spring. From the N_r number of responses and the N_h number of impacts that will create an $N_r \times N_h$ accelerance matrix, the virtual point transformation is then performed and will generate a $6N_v \times 6N_v = 12 \times 12$ accelerance matrix (we have 2 virtual points). Such 12×12 matrix will look like

$$\boldsymbol{Y}^{A1A2BI} = \begin{bmatrix} \boldsymbol{Y}_{11}^{A1} + \boldsymbol{Y}_{11}^{A2} + \boldsymbol{Y}_{11}^{I} & \boldsymbol{Y}_{12}^{I} \\ \boldsymbol{Y}_{21}^{I} & \boldsymbol{Y}_{22}^{B} + \boldsymbol{Y}_{22}^{I} \end{bmatrix} \tag{3.15}$$

The most relevant information is the dynamic transfer accelerance between the 6 DOFs of the virtual point $VP1$ with the 6 DOFs of the virtual point $VP2$. Here, it is interesting to note that the accelerances of the aluminum crosses (systems $A1$, $A2$, and B) are located on the diagonal block of the matrix and for that reason do not influence the transfer stiffness term of the rubber isolator that is located on the off-diagonal block. In theory, inside Eq. 3.15 and because of the reciprocity property, the two terms $\boldsymbol{Y}_{12}^I$ and $\boldsymbol{Y}_{21}^I$ should be equal and one the transpose of the other.

By integrating and inverting this matrix, it is possible to obtain the dynamic stiffness with

$$\boldsymbol{Z} = -\omega^2 \boldsymbol{Y}^{-1} \tag{3.16}$$

In this chapter, we will however put our focus just on the transfer stiffness $\boldsymbol{Z}_{12}^I = \boldsymbol{Z}_{21}^I{}^T$. Such a term is also the one that most matters for DS purposes when connecting two different structures through their virtual points.

After hanging the system $A1A2BI$ with some rubber bands (see Fig. 3.7), we acquired the measurement, performed Eq. 3.9, and produced a graphic output of the two transfer stiffnesses of Eq. 3.11.

Inside those 6×6 matrices, for an industrial context, the most important information is contained in the first three elements of the diagonal: those curves represent the dynamic transfer stiffnesses between the DOFs of the two VP respectively in X, Y, and Z global direction. Figure 3.8 shows X and Y-global directions (coinciding with the radial directions of the mount) in the range of the first 1000 Hz in blue and red color plotted respectively from $\boldsymbol{Z}_{12}^I$ and $\boldsymbol{Z}_{12}^I{}^T$. For the sake of simplicity and readability, all the 36 curves will not be illustrated in the chapter; however, there is a good matching between all the corresponding terms inside 1500 Hz.

Here, in Fig. 3.8, one can immediately note that the blue and red curves are coincident and are also following a dashed black line. This line represents the reference stiffness for that particular rubber mount. Such curves were measured internally

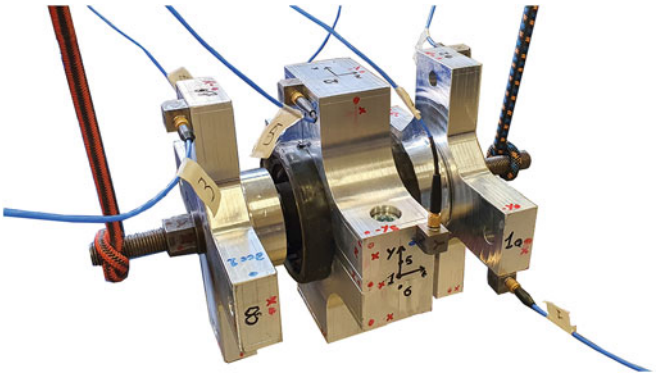

Fig. 3.7 Test setup: measurement in free-free boundary conditions

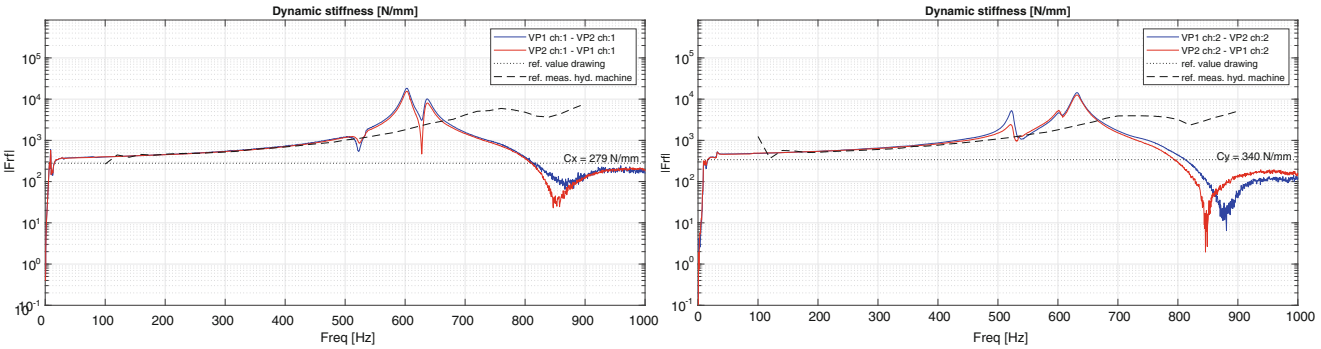

(a) Dynamic transfer stiffness in X-global direction

(b) Dynamic transfer stiffness in Y-global direction

Fig. 3.8 Measured dynamic transfer stiffnesses over frequency compared with reference values

inside the test bench of the BMW Group with the use of a hydraulic machine. Shown more in detail in Fig. 3.8, the trend is very well matching in the first 500 Hz. In the graphs, one can note a double peak around 600 and 640 Hz: this behavior is not measured by that hydraulic machine but it is actually expected due to the design of this specific rubber mount composed of a double rubber cylinder, one inside the other. We can therefore consider those results until 1000–1500 Hz is very reliable.

3.6 Measurements in Fixed Boundary Conditions

When measuring in fixed boundary conditions, the information contained inside the accelerance matrix will be different since an extra-stiffening is introduced by the constraints [10]. So far, the admittance matrix of our system looked like the following:

$$\begin{Bmatrix} \boldsymbol{u}_1 \\ \boldsymbol{u}_2 \end{Bmatrix} = \boldsymbol{Y}\boldsymbol{f} = \begin{bmatrix} \boldsymbol{Y}_{11} & \boldsymbol{Y}_{12} \\ \boldsymbol{Y}_{21} & \boldsymbol{Y}_{22} \end{bmatrix} \begin{Bmatrix} \boldsymbol{f}_1 \\ \boldsymbol{f}_2 \end{Bmatrix} \tag{3.17}$$

On our system, we decided to clamp one of the two sides and fix the side of the virtual point $VP1$ (see Fig. 3.9). By doing so, we obtained that the displacements on the fixed side were obviously zero ($\boldsymbol{u}_1 = \boldsymbol{0}$) and the only contributions were the forces and the measured responses on the nonfixed side. Knowing that fact, we can extract the unknown forces acting on the fixed side $\boldsymbol{f}_1 = -{\boldsymbol{Y}_{11}}^{-1}\boldsymbol{Y}_{12}\boldsymbol{f}_2$ from the first row of the system in Eq. 3.17. By plugging this expression inside the second row of Eq. 3.17, we then get

$$\boldsymbol{u}_2 = \boldsymbol{Y}_{21}\boldsymbol{f}_1 + \boldsymbol{Y}_{22}\boldsymbol{f}_2 = (-\boldsymbol{Y}_{21}{\boldsymbol{Y}_{11}}^{-1}\boldsymbol{Y}_{12} + \boldsymbol{Y}_{22})\boldsymbol{f}_2 = \boldsymbol{Y}^*\boldsymbol{f}_2 \tag{3.18}$$

Fig. 3.9 Schematic representation of the performed measurements in fixed boundary conditions

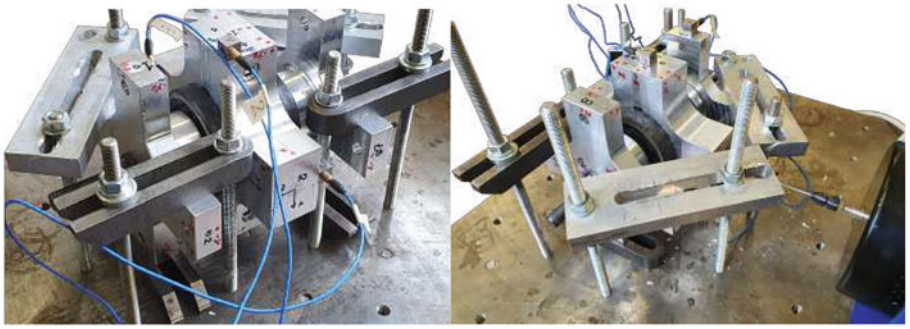

(a) Hammer impacts and virtual point transformation (b) Shaker measurements

Fig. 3.10 Experiment setup in fixed boundary conditions

where $\boldsymbol{u}_2$ and $\boldsymbol{f}_2$ are respectively the measured displacement and forces of the nonclamped side of the system and $\boldsymbol{Y}^*$ is the admittance matrix obtained from that experiment setup. It is important to note, inside Eq. 3.18, that the 6×6 matrix $\boldsymbol{Y}^*$ takes into account the "stiffening" introduced with the fixed boundary conditions and that the transfer admittances $\boldsymbol{Y}_{12}$ and $\boldsymbol{Y}_{21}$ appear inside the expression of $\boldsymbol{Y}^*$. However, it is not directly possible to extract that information since the forces on the clamped side $\boldsymbol{f}_1$ are unknowns. For that reason, it will be necessary to manipulate the admittance measured in free-free condition to have a comparable expression with $\boldsymbol{Y}^*$ in fixed boundary conditions.

In fixed boundary conditions, two different types of experiments have been conducted and will be further discussed:

- We measured the dynamic stiffness with hammer impacts and then performed the abovementioned virtual point transformation.
- We measured the direct dynamic stiffness with a shaker in X and Y radial direction corresponding respectively with the X and Y direction of the virtual point.

In both experiments, the upper $A1$ and the lower cross $A2$ were clamped to the ground, while the third central cross B was left free and later excited. We conducted the first measurement by applying hammer impacts on the structure B and by measuring the responses sensors on the same structure.

The second experiment with the shakers was slightly different: thanks to a stinger, the shaker could excite the central cross B in one specific direction coinciding with the same radial directions of the virtual point. Physically this corresponds to measuring the first and second terms in the diagonal of $\boldsymbol{Y}^*$. Those experiments in FBC have two main validating purposes:

- Firstly, by comparing those two experiments in the same boundary conditions, we could validate the VPT and see if the obtained stiffness in one particular DOF of the virtual point is coinciding with what is directly measured in the same direction with the shaker.
- Secondly, we can compare the free-free boundary condition experiment and see if, after manipulating its accelerance matrix of Eq. 3.17 according to Eq. 3.18, the results are matching (Fig. 3.10).

Figure 3.11 shows the comparison between the shaker measurements, the VPT in fixed boundary conditions, and the VPT in free-free conditions. One can immediately observe that the trend of those three different experiments is quite well matching, more specifically for both graphs we can identify

- The first three curves belonging to the direct measurement with the shaker. Between those curves:
  - The yellow one is belonging to the impedance head and, very probably, due to some dynamics of the impedance head itself, is not matching anymore with the others after 500 Hz.
  - The other two are belonging to two accelerometers positioned on the system B. The so-called *accelerometer 1* is positioned in the same direction of the excitation but opposite to the impedance head, while the *accelerometer 2* is

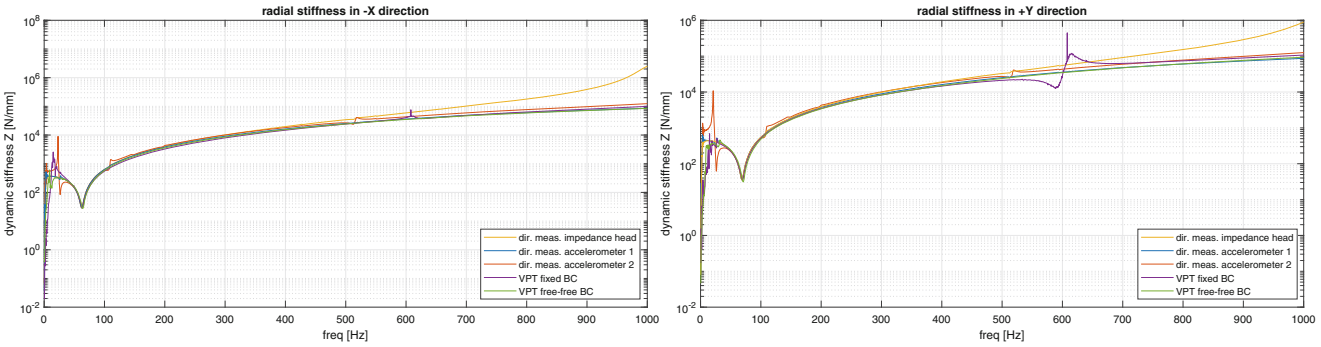

(a) Dynamic stiffness in X-global direction

(b) Dynamic stiffness in Y-global direction

Fig. 3.11 Comparison of results in fixed boundary conditions

positioned as far as possible to the direction of excitation to detect, in case it would occur, a possible torsion of the system B.

- The fourth purple curve is the stiffness in X and Y direction corresponding respectively with the first and the second element of the diagonal of the matrix $\boldsymbol{Y}^*$.
- The last green curve shows the dynamic stiffness in X and Y direction after manipulating the 12×12 FRF matrix $\boldsymbol{Y}^{A1A2BI}$ of Eq. 3.15 to obtain the 6×6 $\boldsymbol{Y}^*$ matrix representative for the fixed boundary conditions according to Eq. 3.18.

Since the trend of all curves is a very well matching, one can consider valid the virtual point transformation procedure as well as the measurements performed in free-free conditions.

3.7 Conclusions

In this chapter, we investigated the dynamic behavior of rubber elements with varying frequencies and using three different approaches: measurements in free-free boundary conditions and in fixed boundary conditions using the VPT and direct measurements in fixed boundary condition using a shaker. Firstly, we explain our particular system of study and how to perform the virtual point transformation on such system. The VPT has the major benefit that takes into account the 6 DOFs (three translations and three rotations) of the virtual points, and therefore, we can extract not only the transfer stiffness in one particular direction but also the stiffness between any other DOF. Such correlations, for example, between 2 rotational DOFs, could be really hard or even impossible to measure directly.

In the context of the virtual point transformation, we investigated the consistency of the transformation. The consistency check that we performed relies on the fact that during our experiment we were using a redundant number of information to obtain the IDMs at the virtual point. Because of that, we removed some of the information and verified that the IDMs and the reconstructed signals were not changing. Here, both sensor and impact consistencies have been checked in the entire frequency range of acquisition to see if, in the frequency range of interest, the VPT could be assumed as valid. The conclusion of this first investigation was that we could consider valid the VPT in the range between 0 and 2500 Hz.

Knowing that, we conducted the measurements in free-free conditions for different rubber mounts, and, after the VPT, we juxtaposed the dynamic stiffness in the main two radial directions with some reference values obtained on some hydraulic machines inside the BMW Group labs. The result showed the dynamic behavior that was actually expected and an excellent correlation with the abovementioned reference values, at least until 1000 Hz. After 1500 Hz, the curves on the two off-diagonal blocks of the dynamic stiffness were not matching so accurately anymore, which is probably due to some dynamic behavior of the aluminum crosses that can no longer be considered rigid bodies.

After this experiment, we performed a measurement in fixed boundary conditions by clamping one of the two sides of the assembly. To compare the results with the previous measurements, some mathematical operations were necessary. The second experiment in fixed conditions was a direct measurement in the two radial directions with a shaker, and it was also used to assure the reliability of the VPT.

After all we can conclude that, at least between 0 and 1000 Hz, we have a robust method for extracting the dynamic stiffness behavior of the rubber mounts and that we could use that information for dynamic substructuring purposes.

Acknowledgments The author gratefully acknowledges the support and contribution of the European Commission with the Marie Sklodowska Curie program through ETN ECO DRIVE project n. GA 858018.

References

1. Klerk, D., Rixen, D., Voormeeren, S.: General framework for dynamic substructuring: history, review, and classification of techniques. AIAA J. AIAA J **46**, 1169–1181 (2008)
2. Van der Seijs, M., Klerk, D., Rixen, D.: General framework for transfer path analysis: history, theory and classification of techniques. Mech. Syst. Signal Proces. **68–69**, 217–244 (2015)
3. Allen, M.S., Rixen, D., van der Seijs, M., Tiso, P., Abrahamsson, T., Mayes, R.L.: Substructuring in Engineering Dynamics: Emerging Numerical and Experimental Techniques. CISM International Centre for Mechanical Sciences. Springer International Publishing, Berlin (2019)
4. Zucchini, A., Naets, F., Hülsmann, A.: Comparison of free-free and fixed boundary conditions for non-linear rubber mount characterization. In: ISMA - 30th International Conference on Noise and Vibration Engineering and USD - International Conference on Uncertainty in Structural Dynamics, Leuven, Belgium, pp. 1698–1711 (2022)
5. Zucchini, A., Naets, F., Hülsmann, A., Desmet, W.: Characterizing non-linear elements with free-free and fixed boundary conditions for dynamic substructuring. In: NOVEM - 7th International Conference on Noise and Vibration emerging methods, Auckland, New Zealand (2023)
6. Haeussler, M., Klaassen, S., Rixen, D.: Experimental twelve degree of freedom rubber isolator models for use in substructuring assemblies. J. Sound Vib. **474**, 115253 (2020)
7. Van der Seijs, M., van den Bosch, D., Rixen, D., Klerk, D.: An improved methodology for the virtual point transformation of measured frequency response functions in dynamic substructuring. In: 4th International Conference on Computational Methods in Structural Dynamics and Earthquake Engineering, Kos Island, pp. 4334–4347 (2013)
8. Haeussler, M., Rixen, D.: Optimal transformation of frequency response functions on interface deformation modes. In: IMAC 2017 – International Modal Analysis Conference, Bethel, CT 06801-1405 (2017)
9. Haeussler, M.: Modular Sound & Vibration Engineering by Substructuring. Dissertation, Technische Universität München, München (2021)
10. Ewins, D.J. : Modal Testing: Theory, Practice, and Application. Mechanical engineering research studies. Research Studies Press, Baldock (2000)

Chapter 4
Investigation of Multiple Branches in Nonlinear Oscillators Using Real-Time Hybrid Testing

A. Mario Puhwein and Markus J. Hochrainer

Abstract The phenomenon of multiple branches of nonlinear structures occurs due to complex nonlinear interactions. They are difficult to detect and mainly investigated by numerical simulation. Commonly, path-following strategies are applied to gradually lead the nonlinear system into the desired branch. Once steady-state conditions have been determined, phenomena like isolated branches can be reproduced in dynamic simulations. However, neither the path-following strategy nor the specification of arbitrary initial conditions is generally possible in experimental dynamic testing. Nevertheless, if the effect of a nonlinear absorber on a nonlinear host structure is studied, the concept of real-time hybrid testing allows separating absorber and host structure. In this work, the absorber is tested experimentally, whereas the host structure is simulated in real time. Assuming proper coupling, the absorber can be tested under very realistic conditions, and stable states on arbitrary branches can be obtained following a two-step approach. First, the experimental subsystem is driven very close to the expected steady-state oscillation, then the real-type hybrid testing loop is closed by coupling the absorber with the simulation model, again with proper initial conditions. If the configuration of the overall system is adjacent to a desired stable branch, the system will converge to the branch within several oscillations. Once a desired configuration is reached, neighboring points can be studied by adapting the excitation frequency or amplitude. So far, the real-time hybrid testing results agree well with theoretical predictions and confirm that stable branches of nonlinear dynamic systems can be investigated using the proposed method.

Keywords Real-time hybrid simulation · Nonlinear oscillation · Multiple branches · Dynamic vibration absorber · Harmonic balance

4.1 Introduction

Real-time hybrid simulation (RTHS) allows realistic testing of physical components. This testing methodology has become widespread due to advances in simulation techniques and the availability of real-time hardware. RTHS couples a virtual simulation model to a physical model using appropriate interfaces. Those interfaces largely define the reliability of RTHS experiments because at physical system boundaries the potential and flow conditions must be satisfied. For proper coupling of mechanical components a feedback-controlled transfer system is required, which typically transfers prescribed accelerations to the physical model, and returns measured forces to the virtual model. The dynamics of the transfer system often limits the frequency range of the RTHS experiment. Another important component is the quality of the virtual simulation model, which must contain all relevant environmental factors not included in the physical model. Because of the advances in simulation technology, modeling complex dynamic systems has become very convenient, and the main challenge remaining is the real-time demand. If a complex numerical model has to react in real time, fixed-step integration schemes are used, which often induce numerical errors. Those inaccuracies are commonly categorized as either systematic or random [1, 2]. The former are repeatable, appear with regular pattern, and are found in almost any element of the RTHS loop. The latter are usually due to measurement and quantization noise and can partly be eliminated by proper filtering.

A. M. Puhwein
Technical University of Vienna, Vienna, Austria

M. J. Hochrainer (✉)
University of Applied Sciences, Wiener Neustadt, Austria
e-mail: markus.hochrainer@fhwn.ac.at

M. Allen et al. (eds.), *Dynamic Substructures, Volume 4*, Conference Proceedings of the Society for Experimental Mechanics Series, https://doi.org/10.1007/978-3-031-36694-9_4

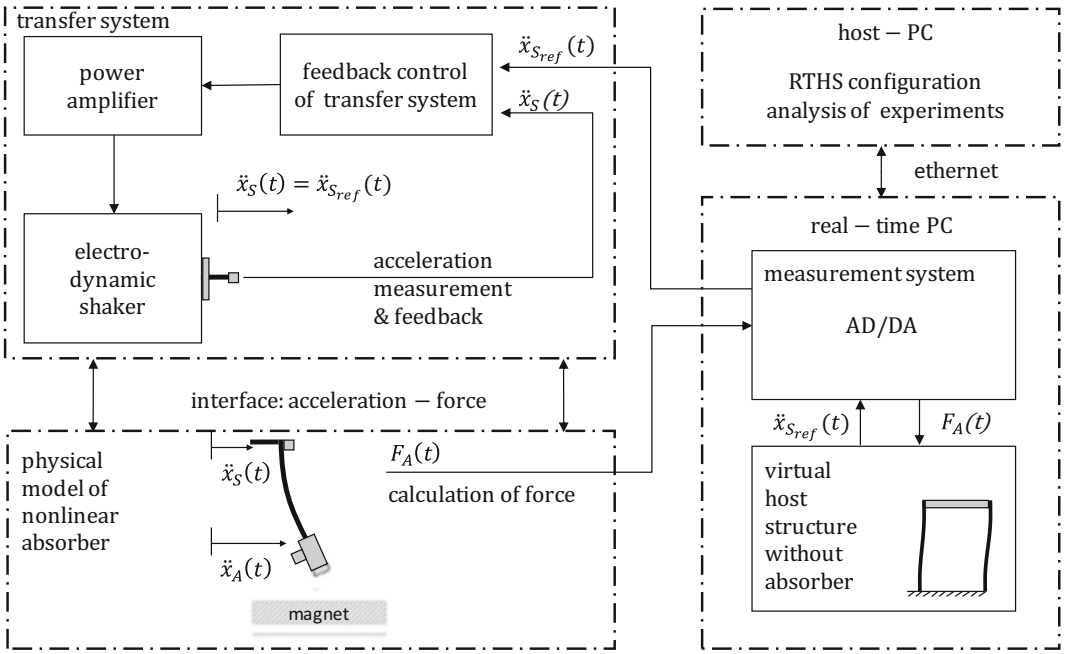

Fig. 4.1 Schematic of the RTHS setup with relevant interface quantities

A major source of systematic errors is the transfer system, which might even cause system instabilities if the required feedback control is not designed carefully enough. To date, the control of the transfer system is still a challenge; see, for example, [3–6]. Since the dynamics of physical model and actuator is not known exactly, effects like damping, friction, and other nonlinearities make a correct coupling difficult. Therefore, many different control schemes have been proposed, for example, compensation of phase shift [7, 8], inverse compensation [9, 10], or adaptive control using real-time actuator identification [11–14]. Recently, successful applications of artificial neural networks have been reported [15].

Another strategy to improve the accuracy of the transfer system is focusing on repetitive processes. This can either be done by repeating an experiment several times [16], thereby adapting the interface conditions until the coupling error is negligible. A different approach assumes repetitive processes whose period is small compared to the testing time. If the physical system is nonlinear elastic, the "iterative learning control" (ILC) or "repetitive control" (RC) [17–21] can be applied successfully. It can be used in addition to classic feedback control and leads to a flexible and precise adaptive control strategy. ILC schemes have many salient features, for example, the compensation of time delays in the transfer system or the correction of phase shifts when filtering measured signals. In the work presented, the transfer systems apply ILC, which has proven to work very accurately and robustly. For the proposed application, it is ideally suited because the steady-state response of a nonlinear elastic physical absorber is studied. During the experiment, the accelerations of the absorber base and mass are measured and used to determine the driving force of the absorber. This force is subsequently transferred to the virtual model of the nonlinear host structure that is simulated on a real-time system. Using the simulated structural acceleration as reference signal for the transfer system finally closes the RTHS loop (see Fig. 4.1 for the schematic of the RTHS setup). The RTHS configuration as well as the analysis of the measurements is performed on a standard PC (host-PC) without the need for real-time capabilities.

Since the work presented can be used to study nonlinear dynamic absorption, the physical oscillator is of Duffing type. The nonlinear restoring forces are obtained by magnetic forces resulting from the interaction of a strong base magnet and a small magnet attached to the moving mass (see Fig. 4.2a).

4.2 Analytical Model and Approximate Solution

Typically, complex dynamic systems are simplified by modal decomposition, thereby reducing the dynamics to dominant degrees of freedom. If both virtual and physical models are reduced to a nonlinear single degree of freedom system (see Fig. 4.2b), the coupled dynamics becomes

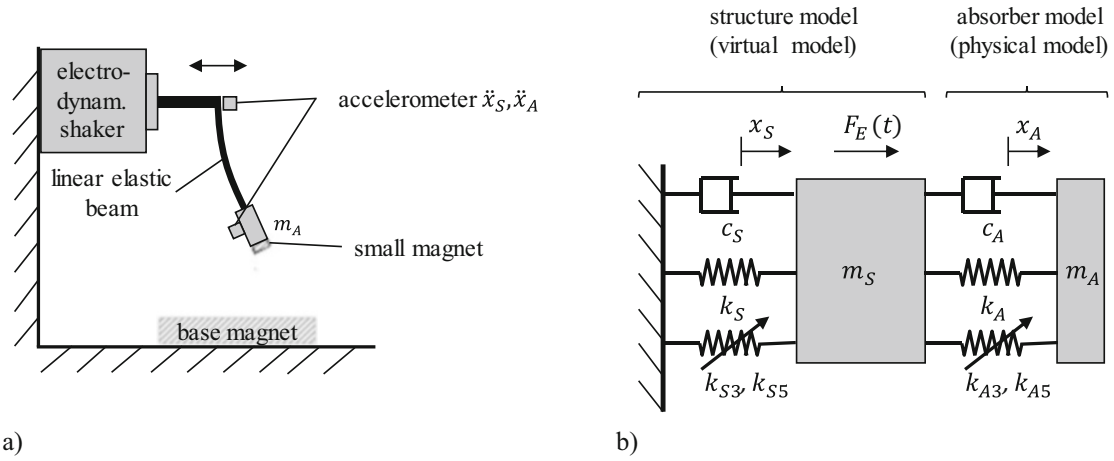

Fig. 4.2 (**a**) Model of the dynamic absorber with nonlinear restoring forces caused by repelling or attracting magnets; (**b**) Representation of a nonlinear oscillator with a nonlinear dynamic absorber attached

$$
\begin{aligned}
&m_S\ddot{x}_S + c_S\dot{x}_S + k_S x_S + k_{S3}x_S{}^3 + k_{S5}x_S{}^5 - c_A\,(\dot{x}_A - \dot{x}_S)\\
&\quad - k_A\,(x_A - x_S) - k_{A3}(x_A - x_S)^3 - k_{A5}(x_A - x_S)^5 = F_E\,\cos(\omega t)\\
&m_A\ddot{x}_A + c_A\,(\dot{x}_A - \dot{x}_S) + k_A\,(x_A - x_S) + k_{A3}(x_A - x_S)^3 + k_{A5}(x_A - x_S)^5 = 0.
\end{aligned}
\tag{4.1}
$$

This is an extended representation of Duffing-type oscillators with cubic and quintic stiffness terms, where m_S, c_S, k_S, k_{S3}, k_{S5}, F_E describe the mass, damping coefficient, linear, cubic, and quintic stiffness, as well as the excitation force of the host structure and m_A, c_A, k_A, k_{A3}, k_{A5} denote the mass, damping coefficient, linear, cubic, and quintic stiffness of the absorber. For analytical processing, it is convenient to transform the equations of motion to a dimensionless representation by introducing the normalized displacements $q_S = x_S/x_{S,\,stat}$, $q_A = (x_S - x_A)/x_{S,\,stat}$, with the equivalent static deformation $x_{S,\,stat} = F_E/k_S$. Commonly, the linear dynamic behavior is characterized by the natural frequencies $\omega_{nS} = \sqrt{k_S/m_S}$, $\omega_{nA} = \sqrt{k_A/m_A}$, and the damping ratios of $\zeta_S = c_S/(2m_S\omega_{nS})$, $\zeta_A = c_A/(2m_A\omega_{nA})$ of host structure and absorber.

Defining the mass and frequency ratio $\mu = m_A/m_S$, $\lambda = \omega_{nA}/\omega_{nS}$, the normalized excitation frequency $\gamma = \omega/\omega_{nS}$ as well as the dimensionless time and its derivative $\tau = \omega_{nS}t$, $dg/d\tau = g'$, the coupled equations of motion become

$$
\begin{aligned}
&q_S'' + 2\zeta_S q_S' + q_S + \tfrac{4}{3}\alpha_3 q_S{}^3 + \tfrac{8}{5}\alpha_5 q_S{}^5 + 2\zeta_A\lambda\mu q_A' + \lambda^2\mu q_A + \tfrac{4}{3}\mu\beta_3 q_A{}^3 + \tfrac{8}{5}\mu\beta_5 q_A{}^5 = \cos(\gamma\tau)\\
&q_A'' + 2\zeta_S q_S' + q_S + \tfrac{4}{3}\alpha_3 q_S{}^3 + \tfrac{8}{5}\alpha_5 q_S{}^5 + 2\zeta_A\lambda\,(\mu+1)\,q_A' + \lambda^2\,(\mu+1)\,q_A\\
&\quad + \tfrac{4}{3}\,(\mu+1)\,\beta_3 q_A{}^3 + \tfrac{8}{5}\,(\mu+1)\,\beta_5 q_A{}^5 = \cos(\gamma\tau)\,.
\end{aligned}
\tag{4.2}
$$

where $\alpha_3 = 3k_{S3}x_{S,\,stat}{}^2/4k_S$, $\beta_3 = a(\mu)\alpha_3$ describe the normalized cubic and quintic stiffness of the host structure. Following the generalization of Den Hartog's equal-peak method [22] for an optimal absorption, the normalized cubic and quintic absorber stiffness become $\alpha_5 = 5k_{S5}x_{S,\,stat}{}^4/8k_S$, $\beta_5 = b(\mu)\alpha_5$, where $a(\mu)$, $b(\mu)$ are system-dependent functions of the mass ratio μ. These equations generalize the results of systems with cubic nonlinearities (see again [22]).

To obtain analytical expressions for estimate solutions of Eq. 4.2, the method of harmonic balance is used. Applying the approximations $q_A = A_A\cos\gamma\tau + B_A\sin\gamma\tau$, $q_S = A_S\cos\gamma\tau + B_S\sin\gamma\tau$ and substituting $\cos^3\gamma\tau \approx 3/4\cos\gamma\tau$, $\sin^3\gamma\tau \approx 3/4\sin\gamma\tau$ and $\cos^5\gamma\tau \approx 5/8\cos\gamma\tau$, $\sin^5\gamma\tau \approx 5/8\sin\gamma\tau$ with subsequent comparison of sine and cosine coefficients renders a set of four coupled nonlinear algebraic equations:

$$
\begin{aligned}
&\alpha_5 {A_\mathrm{S}}^5 + \alpha_5 2 {A_\mathrm{S}}^3 {B_\mathrm{S}}^2 + \alpha_5 A_S {B_S}^4 + \alpha_3 {A_\mathrm{S}}^3 + \alpha_3 A_\mathrm{S} {B_\mathrm{S}}^2 + \beta_5 \mu {A_\mathrm{A}}^5 + \beta_5 \mu 2 {A_\mathrm{A}}^3 {B_\mathrm{A}}^2 \\
&\quad + \beta_5 \mu A_\mathrm{A} {B_\mathrm{A}}^4 + \beta_3 \mu {A_\mathrm{A}}^3 + \beta_3 \mu A_\mathrm{A} {B_\mathrm{A}}^2 + \left(1-\gamma^2\right) A_\mathrm{S} + 2\zeta_\mathrm{S}\gamma B_\mathrm{S} + \lambda^2 \mu A_\mathrm{A} + 2\zeta_\mathrm{A}\lambda\mu\gamma B_\mathrm{A} = 1 \\
&\alpha_5 {A_\mathrm{S}}^5 + \alpha_5 2 {A_\mathrm{S}}^3 {B_\mathrm{S}}^2 + \alpha_5 A_\mathrm{S} {B_\mathrm{S}}^4 + \alpha_3 {A_\mathrm{S}}^3 + \alpha_3 A_\mathrm{S} {B_\mathrm{S}}^2 + \beta_5 \left(\mu+1\right) {A_\mathrm{A}}^5 + \beta_5 \left(\mu+1\right) 2 {A_\mathrm{A}}^3 {B_\mathrm{A}}^2 \\
&\quad + \beta_5 \left(\mu+1\right) A_\mathrm{A} {B_\mathrm{A}}^4 + \beta_3 \left(\mu+1\right) {A_\mathrm{A}}^3 + \beta_3 \left(\mu+1\right) A_\mathrm{A} {B_\mathrm{A}}^2 + A_\mathrm{S} \\
&\quad + 2\zeta_\mathrm{S}\gamma B_\mathrm{S} + \left(\lambda^2 \left(\mu+1\right) - \gamma^2\right) A_\mathrm{A} + 2\zeta_\mathrm{A}\lambda \left(\mu+1\right) \gamma B_\mathrm{A} = 1 \\
&\alpha_5 {B_\mathrm{S}}^5 + \alpha_5 2 {A_\mathrm{S}}^2 {B_\mathrm{S}}^3 + \alpha_5 {A_\mathrm{S}}^4 B_\mathrm{S} + \alpha_3 {A_\mathrm{S}}^2 B_\mathrm{S} + \alpha_3 {B_\mathrm{S}}^3 + \beta_5 \mu {B_\mathrm{A}}^5 + \beta_5 \mu 2 {A_\mathrm{A}}^2 {B_\mathrm{A}}^3 \\
&\quad + \beta_5 \mu {A_\mathrm{A}}^4 B_\mathrm{A} + \beta_3 \mu {A_\mathrm{A}}^2 B_\mathrm{A} + \beta_3 \mu {B_\mathrm{A}}^3 - 2\zeta_\mathrm{S}\gamma A_\mathrm{S} + \left(1-\gamma^2\right) B_\mathrm{S} \\
&\quad - 2\zeta_\mathrm{A}\lambda\mu\gamma A_\mathrm{A} + \lambda^2 \mu B_\mathrm{A} = 0 \\
&\alpha_5 {B_\mathrm{S}}^5 + \alpha_5 2 {A_\mathrm{S}}^2 {B_\mathrm{S}}^3 + \alpha_5 {A_\mathrm{S}}^4 B_\mathrm{S} + \alpha_3 {A_\mathrm{S}}^2 B_\mathrm{S} + \alpha_3 {B_\mathrm{S}}^3 + \beta_5 \left(\mu+1\right) {B_\mathrm{A}}^5 \\
&\quad + \beta_5 \left(\mu+1\right) 2 {A_\mathrm{A}}^2 {B_\mathrm{A}}^3 + \beta_5 \left(\mu+1\right) {A_\mathrm{A}}^4 B_\mathrm{A} + \beta_3 \left(\mu+1\right) {A_\mathrm{A}}^2 B_\mathrm{A} \\
&\quad + \beta_3 \left(\mu+1\right) {B_\mathrm{A}}^3 - 2\zeta_\mathrm{S}\gamma A_\mathrm{S} + B_\mathrm{S} - 2\zeta_\mathrm{A}\lambda \left(\mu+1\right) \gamma A_\mathrm{A} + \left(\lambda^2 \left(\mu+1\right) - \gamma^2\right) B_\mathrm{A} = 0.
\end{aligned}
\tag{4.3}
$$

These equations must be solved numerically for a given harmonic excitation. Starting from a known initial configuration, a path-following method (see [23, 24]) renders A_S, A_A, B_S, B_A, and γ, which can be used to generate FRF diagrams for the illustration of the complex system dynamics (see Fig. 4.3a, b).

If those frequency response curves are evaluated for varying excitation amplitudes, the characteristic stationary behavior is captured by three-dimensional surfaces (see Fig. 4.3c, d). Consideration of this extended representation is essential to understand nonlinear phenomena of the system like multiple and isolated branches. Apparently both excitation frequency f and amplitude $a_\mathrm{F} = F_\mathrm{E}/m_\mathrm{S}$ must be adapted to follow the turning points along the surface.

4.3 Variable System Configuration

Although the numerical solution presented allows determining all stationary equilibrium conditions, an experimental confirmation of those points on multiple branches is almost impossible. From an experimental point of view, it is firstly demanding to set up a nonlinear model with given cubic and quintic stiffness terms and secondly even more difficult to drive the system to a predefined state if multiple branches exist. However, in a real-time hybrid simulation, the situation is simplified because the virtual model and its initial conditions can be chosen arbitrarily. This allows focusing on the behavior of the physical absorber as experimental challenge. If the absorber is guided to a desired configuration, and it is furthermore possible to calculate the corresponding system states of the virtual model, then coupling of both oscillators becomes possible. When implementing this basic idea, the critical part is a smooth transition from the simulated to the physical interaction forces. Therefore, the proposed approach starts with proper excitation of the physical absorber by an electrodynamic shaker until a predefined stationary oscillation is reached. Because the absorber base acceleration equals the structural acceleration $\ddot{x}_\mathrm{S}$ (see Fig. 4.2b), the corresponding host structure forcing is given by

$$
F_\mathrm{A} + F_\mathrm{E} = m_\mathrm{S}\ddot{x}_\mathrm{S} + c_\mathrm{S}\dot{x}_\mathrm{S} + k_\mathrm{S}x_\mathrm{S} + k_{\mathrm{S}3}{x_\mathrm{S}}^3 + k_{\mathrm{S}5}{x_\mathrm{S}}^5 \tag{4.4}
$$

if x_S and its derivatives are known. This inverse host structure dynamics determines the sum of all applied forces, and if $\ddot{x}_\mathrm{S}$ is given and F_A is measured, F_E can be determined from Eq. 4.4. Once $F_\mathrm{A} + F_\mathrm{E}$ is determined, the virtual host structural model can be simulated in a starting configuration, which is maintained until absorber and structure reach stationary conditions. For moderate-to-large vibration amplitudes, the nonlinear response terms become significant, and $F_\mathrm{E} + F_\mathrm{A}$ can no longer be described by a single-frequency oscillation. However, since the final excitation in the RTHS configuration is assumed harmonic, the estimated external force excitation $\hat{F}_\mathrm{E}$ can be approximated by

$$
\hat{F}_\mathrm{E} = A_\mathrm{E}\cos\omega t + B_\mathrm{E}\sin\omega t. \tag{4.5}
$$

Using a recursive least-squares estimation method, the unknown coefficients A_E and B_E can be determined (see [25, 26]). Once these excitation coefficients remain constant, stationary conditions are reached, and at time t_S the system configuration

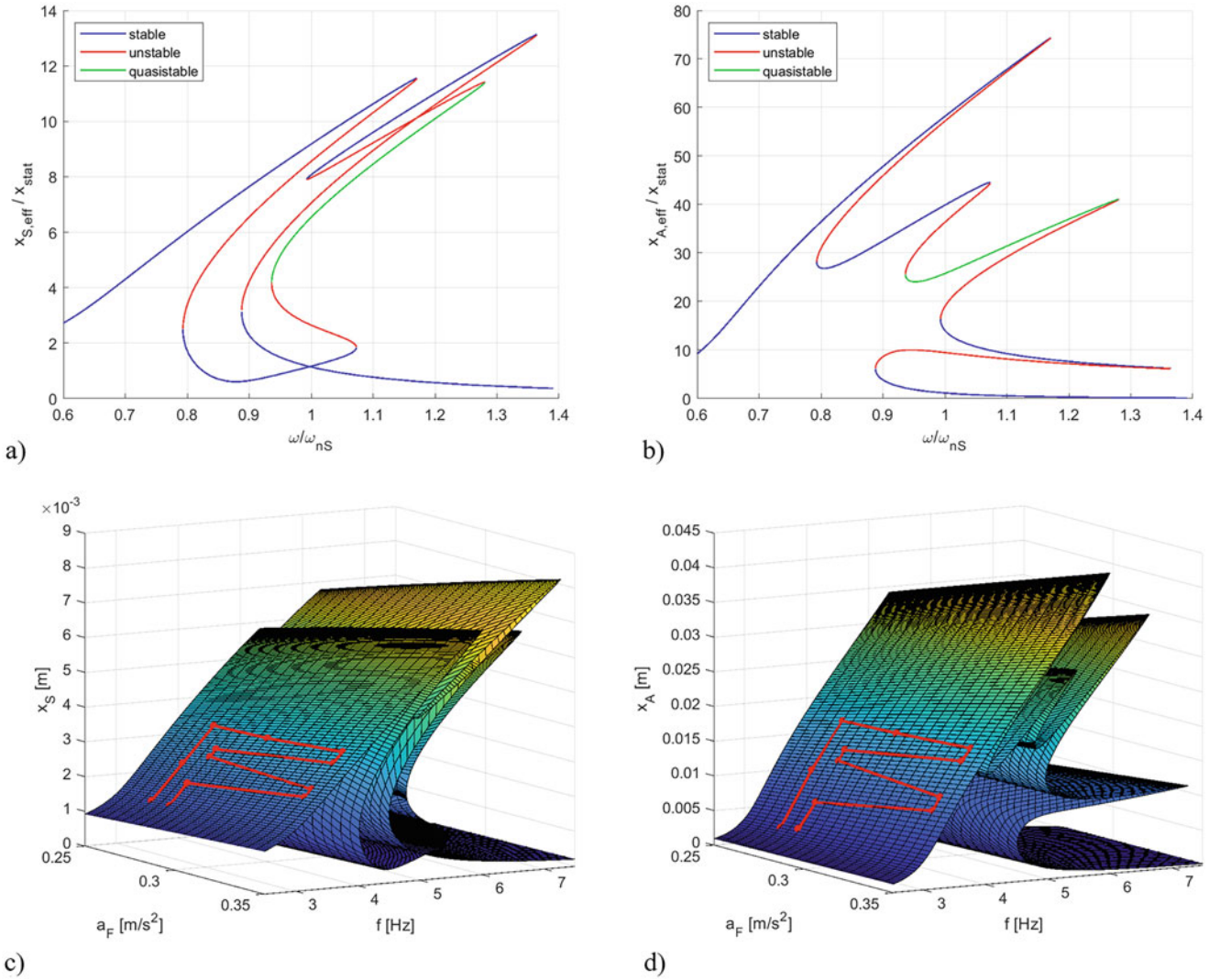

Fig. 4.3 Simulation of nonlinear 2DOF system: (**a**) typical FRF of host structure with multiple branches; (**b**) FRF of absorber; (**c**) response surface of structure; (**d**) response surface of absorber

can be switched from a controlled absorber excitation to the desired real-time hybrid simulation. In this new configuration, absorber and virtual host structure are directly coupled by feeding back the simulated floor acceleration $\hat{a}_S$ to the physical absorber using the transfer system.

If all tasks are carried out correctly, the switching will be smooth, and the system states and forces do not change abruptly. However, the stability of the coupled system cannot be determined from the stability of the individual oscillators. If the stationary point of the two DOF system is not in a stable region, the coupling causes a transition from stable to instable vibrations. In such a situation, even a smooth transition will not maintain the system states, but drives them to a new stable equilibrium. It is important to note that the initially applied absorber base acceleration a_S is different from the equivalent external force excitation $a_F = \hat{F}_E/m_S$. All major steps of the proposed variable system configuration with smooth transitions are illustrated in the flowchart in Fig. 4.4.

4.4 Experimental Results

As described in [27], all parameters of the Duffing-type absorber used in the experimental setup can be prescribed and set individually. Nevertheless, a final dynamic identification run is recommended to determine ω_A, ζ_A, k_A, k_{A3}, and k_{A5} for numerical simulations. Therefore, the shaker is excited with a harmonic time sweep signal of amplitude $\ddot{x}_S = 0.3$ m/s^2 in

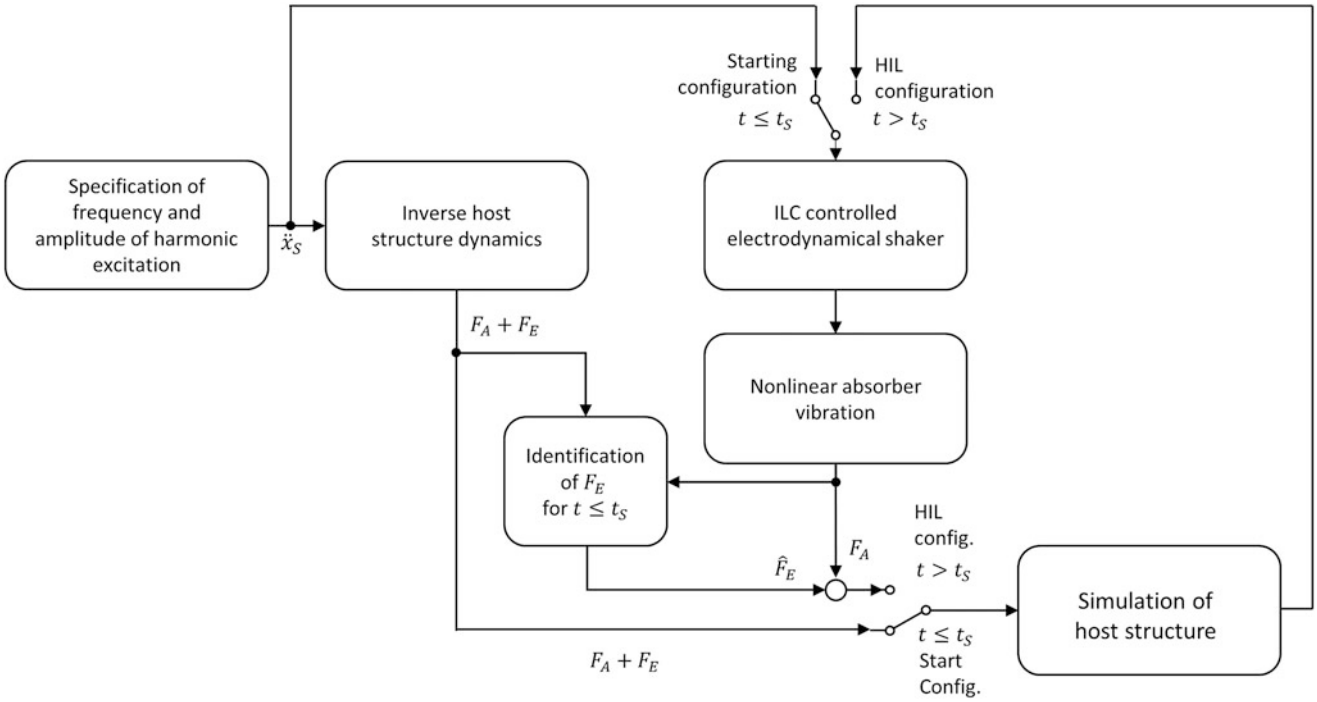

Fig. 4.4 Variable system configuration to drive absorber to desired stationary state with subsequent smooth switching to the RTHS configuration at time t_S

the frequency range $6\pi \leq \omega \leq 10\pi$ rad/s (see Fig. 4.5a). The measured acceleration a_A must be integrated to obtain the absorber velocity v_A as well as the displacement x_A. A direct least-squares identification in time domain renders the desired linear and nonlinear parameters:

$$\boldsymbol{w} = \left(\boldsymbol{X}^T \boldsymbol{X}\right)^{-1} \boldsymbol{X}^T \boldsymbol{a}_A \tag{4.6}$$

where the N measurements are collected in the data matrix $\boldsymbol{X} = \left(\boldsymbol{x}_1^T, \ldots \boldsymbol{x}_i^T, \ldots \boldsymbol{x}_N^T\right)^T$ with $\boldsymbol{x}_i = \left(v_{A,i}\ x_{A,i}\ x_{A,i}^3\ x_{A,i}^5\right)$ and the acceleration vector is defined by $\boldsymbol{a}_A = (a_{A,1}, \ldots, a_{A,N})^T$. All identified parameter are elements of $\boldsymbol{w} = (c_A, k_A, k_{A3}, k_{A5})^T$. If the absorber is base excited, its mass m_A cannot be identified and must be weighted instead.

Assuming that the absorber remains close to steady state during the sine-sweep excitation, the envelope of the absorber displacement approximates the frequency response function (see Fig. 4.5a). The estimated absorber's frequency response (see Fig. 4.5b) indicates the desired behavior, but in the vicinity of amplitude jumps transient oscillations occur. Although those variations are undesired, they do not influence the dynamic identification since the equation of motion captures all transient effects correctly. Alternatively, it is possible to measure individual points of the FRF by exciting the absorber at distinct frequencies and extract the vibration amplitude from the steady-state response. For the parameter identification, however, this time-consuming method has not proven advantageous when compared to the sine-sweep excitation.

From an experimental point of view, it is essential that the identified model describes the dynamics of the resonance branch correctly. A close inspection of the FRF in Fig. 4.5b reveals a positive curvature at increasing amplitudes indicating a fifth-order nonlinearity, which is included in the parameter identification of the absorber model. This nonlinearity is due to the construction of the absorber. It results from the magnetic field of the base magnet if the absorber moves into regions with an inhomogeneous field at moderate-to-large vibration amplitudes. In these situations, the restoring forces are described by higher order polynomials [27].

Once the absorber is identified and the parameter of the virtual model (host structure) is selected, the coupled dynamics can be simulated in time domain. However, the RTHS results can only be interpreted if the regions of stability of the coupled system are known. For a harmonic force excitation, the nonlinear system response can either be stable, quasi-stable, or instable.

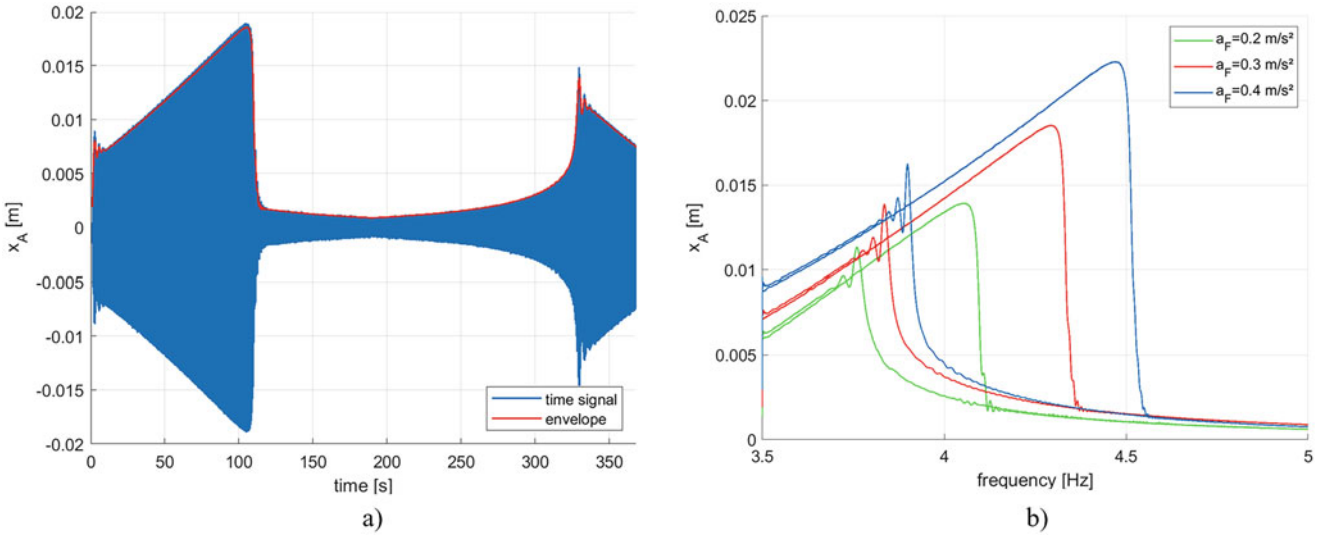

Fig. 4.5 Absorber characteristics: (**a**) displacements during sine sweep excitation for $a_F = 0.3$ m/s^2; (**b**) approximation of the FRF by extracting displacement response envelope for different excitation amplitudes

Stable and quasi-stable configurations are tested in the laboratory using the RTHS setup. A typical stable configuration is obtained for $f = 3.7$ Hz and $a_S = 1.24$ m/s^2 (see Fig. 4.6a). For $t < 18$ s, neither the excitation frequency nor the excitation amplitude is changed. Having reached a steady-state vibration response at $t_S = 18$ s, the system is switched to the required RTHS configuration and for $t > t_S$ the absorber response remains almost unaffected because of the stable configuration. The stable configuration is shown in Fig. 4.6d and marked with a red circle. The parameter configuration demonstrates the vibration-reducing effect of nonlinear absorber, and consequently, the structural response is much smaller than the absorber displacement. Occasionally, almost negligible adaptions are visible in the displacement responses, which result from inevitable noise in the acceleration measurements and minor errors in the feedback control of the electrodynamic shaker.

The behavior of the response in Fig. 4.6b is fundamentally different. For $t < 15$ s, the excitation frequency is linearly increased from $f = 3.7$ Hz to the final value of $f = 4.2$ Hz for $a_S = 0.736$ m/s^2. For 15 s $< t <$ 18 s,the excitation remains constant to allow steady-state conditions before switching to the RTHS configuration at $t = 18$ s. Again, the switching appears almost perfect, but after a short transient phase, the responses become quasi-periodic and remain in this condition for both structure and absorber. The transition is also illustrated in Fig. 4.6d, where the trajectory is marked with a red triangle. Since the transition to the quasi-periodic vibrations takes place rather slowly, in the time range 18 s $< t <$ 25 s, the quasi-periodic responses are hardly recognizable if the coupled system is driven to another setpoint too early. Such responses occur quite often in nonlinear dynamic absorption and the corresponding regimes. They are typically located in regions between Neimark–Sucker bifurcation points.

Maybe the most surprising effect occurs in the third example (see Fig. 4.6c). In the initial configuration for $t < 18$ s, the behavior is similar to Fig. 4.6b, and steady-state conditions are reached for $t > 15$ s when the excitation frequency remains constant at $f = 4.1$ Hz. After the transition to the RTHS configuration at $t_S = 18$ s, the system becomes quasi-stable and remains in this state while increasing the excitation frequency to 4.1 Hz $< f <$ 4.35 Hz in the time range 18 s $< t <$ 42 s. However, a few seconds later a new equilibrium point is reached because small variations in amplitudes and forces add up to significant quantities, resulting in considerably reduced absorber amplitudes. Consequently, the absorber structure interaction force decreases, and structural displacements increase. Those increased vibrations transfer energy to the absorber again until new steady-state conditions are obtained at $t \approx 55$ s with much higher vibration amplitudes while still increasing the excitation frequency up to 4.6 Hz. The transitions are also given in Fig. 4.6d and marked by the red stars. The time required for this transition is varying to some extent when the experiment is repeated, but the system will leaves the quasi-stable configuration in all RTHS experiments.

In summary, it can be stated that the vibration of the host structure must be known to force the coupled system into a desired state because in the initial phase of the experiment the absorber is excited with the expected structural vibration. After coupling the systems, the absorber's base excitation is no longer a known harmonic signal, but taken from the simulated structure. For further excitation, the virtual force $\hat{F}_E$ is applied to the structural model. Since the absorber's base acceleration

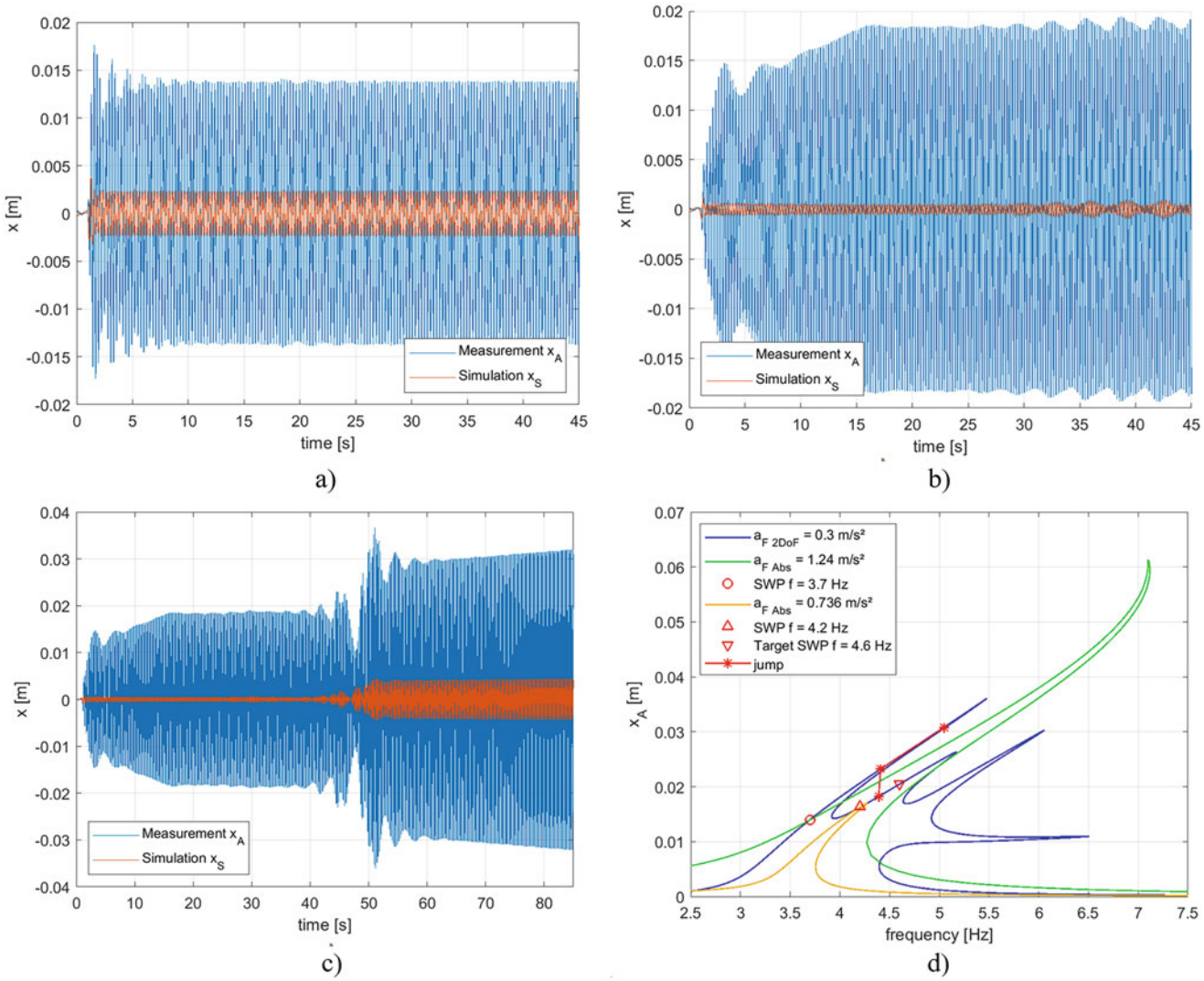

Fig. 4.6 Application of proposed algorithm: (**a**) for a stable configuration; (**b**) for a quasi-stable configuration; (**c**) transition from a quasi-periodic to a stable configuration; (**d**) frequency response of absorber and coupled system with the intersection points for subfigures (**a**)–(**c**)

remains unchanged when switching the configuration, the transition to the RTHS is generally very smooth. To be able to drive the real-time hybrid test into a desired state, the structural acceleration $\hat{a}_S$ is determined from the numerical model.

If the FRFs of the SDOF absorber and the two DOF coupled system are compared (see Fig. 4.6d), the desired intersection point can be found. However, it must be noted that only the intersection at the considered frequency renders the stable and desired configuration. Any further intersections describe equilibrium conditions with different structural accelerations a_S and thus the external forcing is different. Although there is an excellent agreement between numerical simulation and real-time hybrid testing, there might be the need for some experimental fine-tuning. In such a situation, the excitation amplitude can be adapted during the experiment to obtain results with the highest possible accuracy. For experimental fine-tuning, it is generally not necessary to perform further numerical analysis of the coupled system.

During all experiments conducted so far, the desired configuration has been reached. Even if the system reaches new, undesired stationary conditions, the RTHS experiment can be continued. In this case, it is possible to slowly change the excitation frequency ω or the excitation amplitude $\hat{F}_E$. With these adaptions, the system can be guided to arbitrary points on the response surface for studying dynamic effects as long as the stable region is not left.

4.5 Conclusion

Multiple branches of nonlinear systems are difficult to detect and mainly investigated by numerical simulations. Commonly, path-following strategies are applied to gradually lead the nonlinear system into the desired equilibrium point to study the dynamic behavior. Although this strategy is generally not possible in an experimental setup with a multiple degrees of freedom-coupled system, the proposed real-time hybrid simulation setup allows a similar approach. Since only the absorber is studied experimentally, and all remaining system parts are simulated in a virtual model with proper coupling, any stable steady-state configuration can be tested in the hybrid simulation. Firstly, the absorber is forced to a desired steady-state point of operation, and secondly it is coupled to the virtual system in a corresponding vibration state. If the configuration of the system is adjacent to a stable branch, the system will converge to the branch within several oscillations and thus the proposed method is working perfectly. If a point on an unstable trajectory is selected, the coupled system becomes instable and moves to a neighboring stable point. In case of a quasi-periodic target configuration, the real-time hybrid simulation becomes quasi-periodic too. Starting from a desired configuration, neighboring points can be studied by typically adapting the excitation frequency and amplitude. So far, the real-time hybrid testing results agree well with theoretical predictions and confirm that stable branches of nonlinear dynamic systems can be investigated using the proposed method.

Acknowledgments Parts of this work were also funded by the "Austrian COMET-Programme" (Project InTribology1, no. 872176) under the scope of K2 InTribology and were developed at the University of Applied Science Wiener Neustadt.

References

1. Mercan, O., Ricles, J.M.: Stability and accuracy analysis of outer loop dynamics in real-time pseudodynamic testing of SDOF systems. Earthq. Eng. Struct. Dyn. **36**(11), 1523–1543 (2007). https://doi.org/10.1002/eqe.701
2. Lin, F., Maghareh, A., Dyke, S.J., Lu, X.: Experimental implementation of predictive indicators for configuring a real-time hybrid simulation. Eng. Struct. **101**(15), 427–438 (2015). https://doi.org/10.1016/j.engstruct.2015.07.040
3. Hochrainer, M.J.: Real-time hybrid testing: challenges and experiences from a teaching point of view. In: Mains, M., Dilworth, B. (eds.) Topics in Modal Analysis & Testing Conference Proceedings of the Society for Experimental Mechanics Series, vol. 9. Springer (2019)
4. Hochrainer, M.J., Puhwein, A.M.: Investigation of nonlinear dynamic phenomena applying real-time hybrid simulation. In: Kerschen, G. (ed.) Nonlinear Structures and Systems Conference Proceedings of the Society for Experimental Mechanics Series, vol. 1, (2019). https://doi.org/10.1007/978-3-030-12391-8_16
5. Saouma, V., Sivaselvan, M.: Hybrid Simulation: Theory, Implementation and Applications. Taylor & Francis Ltd. London, UK (2008)
6. Bursi, O.S., Wagg, D.: Modern testing techniques for structural systems. In: Dynamics and Control, CISM International Centre for Mechanical Sciences, vol. 502. Springer Wien New York (2008)
7. Zhao, J., French, C., Shield, C., Posbergh, T.: Considerations for the development of real-time dynamic testing using servo-hydraulic actuation. Earthq. Eng. Struct. Dyn. **32**(11), 1773–1794 (2003)
8. Gawthrop, P.J., Wallace, M.I., Neild, S.A., Wagg, D.J.: Robust real-time substructuring techniques for under-damped systems. Struct. Control Health Monit. **14**(4), 591–608 (2007)
9. Bonnet, P.A., Lim, C.N., Williams, M.S., Blakeborough, A., Neild, S.A., Stoten, D.P., Taylor, C.A.: Real-time hybrid experiments with Newmark integration MCSmd outer-loop control and multi-tasking strategies. Earthq. Eng. Struct. Dyn. **36**(1), 119–141 (2007)
10. Chen, C., Ricles, J.M.: Analysis of actuator delay compensation methods for real-time testing. Eng. Struct. **31**(11), 2643–2655 (2009)
11. Chae, Y., Kazemibidokhti, K., Ricles, J.M.: Adaptive time series compensator for delay compensation of servo-hydraulic actuator systems for real-time hybrid simulation. Earthq. Eng. Struct. Dyn. **42**(11), 1697–1715 (2013)
12. Chen, P.-C., Chang, C.-M., Spencer, B.F., Tsai, K.-C.: Adaptive model-based tracking control for real-time hybrid simulation. Bull. Earthq. Eng. **13**(6), 1633–1653 (2015)
13. Najafi, A., Spencer, B.F.: Adaptive model reference control method for real-time hybrid simulation. Mech. Syst. Signal Process. **132**, 183–193 (2019)
14. Tsokanas, N., Pastorino, R., Stojadinović, B.: Adaptive model predictive control for actuation dynamics compensation in real-time hybrid simulation. Mech. Mach. Theory. **172**. https://doi.org/10.1016/j.mechmachtheory.2022.104817
15. Insam, C., Göldeli, M., Klotz, T., Rixen, D.J.: Comparison of feedforward control schemes for real-time hybrid substructuring (RTHS). Dyn. Substruct. **4**, 1–14 (2021). https://doi.org/10.1007/978-3-030-47630-4_1
16. Witteveen, W., Koller, L., Penninger, D.: Non-simultaneous real-time hybrid simulation of a numerical and experimental mechanical system with moderate nonlinearities via iterative coupling based on Frequency Response Functions. Mech. Syst. Signal Process. **163**, 108055 (2022). https://doi.org/10.1016/j.ymssp.2021.108055
17. Insam, C., Kist, A., Rixen, D.J.: High fidelity real-time hybrid substructure testing using iterative learning control. In: ISR 2020; 52th International Symposium on Robotics (2020). isbn:978-3-8007-5428-1

18. Wang, Y., Gao, F., Doyle, F.J.: Survey on iterative learning control, repetitive control, and run-to-run control. J. Process Control. **19**, 1589–1600 (2009)
19. Xu, J.-X., Tan, Y.: Linear and Nonlinear Iterative Learning Control. Springer-Verlag Berin Heidelberg New York (2003)
20. Bristow, D.A., Baron, K.L., Alleyne, A.G.: Iterative learning control. In: Levine, W.S. (ed.) The Control Handbook. CRC Press, Boca Raton, FL, USA (2011)
21. Hochrainer, M.J., Puhwein, A.M.: Investigation of nonlinear dynamic phenomena applying real-time hybrid simulation. In: Kerschen, G., Brake, M., Renson, L. (eds.) Nonlinear Structures and Systems Conference Proceedings of the Society for Experimental Mechanics Series, vol. 1. Springer (2020). https://doi.org/10.1007/978-3-030-12391-8_16
22. Habib, G., Detroux, T., Viguié, R., Kerschen, G.: Nonlinear generalization of Den Hartog's equal-peak method. Mech. Syst. Signal Process. **52–53**, 17–28 (2015). https://doi.org/10.1016/j.ymssp.2014.08.009
23. Puhwein, A.M., Hochrainer, M.J.: Real-time hybrid simulation study of a physical duffing absorber attached to a virtual nonlinear structure. In: Allen, M., D'Ambrogio, W., Roettgen, D. (eds.) Dynamic Substructures Conference Proceedings of the Society for Experimental Mechanics Series, vol. 4. Springer (2023). https://doi.org/10.1007/978-3-031-04094-8_13
24. Puhwein, A.M., Hochrainer, M.J.: Mitigation of nonlinear structural vibrations by duffing-type oscillators using real-time hybrid simulation. In: Brake, M.R., Renson, L., Kuether, R.J., Tiso, P. (eds.) Nonlinear Structures & Systems Conference Proceedings of the Society for Experimental Mechanics Series, vol. 1. Springer (2023). https://doi.org/10.1007/978-3-031-04086-3_22
25. Nelles, O.: Nonlinear System Identification. Springer (2010)
26. Eykhoff, P.: System Identification. Wiley (1974)
27. Hochrainer, M.J., Puhwein, A.M.: Design and characterization of a multi-purpose duffing oscillator with flexible parameter selection. In: Epp, D.S. (ed.) Special Topics in Structural Dynamics & Experimental Techniques Conference Proceedings of the Society for Experimental Mechanics Series, vol. 5. Springer (2021). https://doi.org/10.1007/978-3-030-47709-7_7

Chapter 5
A First Experience with Multidimensional Contact Real-Time Hybrid Substructuring: Toward Testing of Foot Prostheses

Arian Kist, Talhah Ansari, Christina Insam, and Daniel Rixen

Abstract Real-time hybrid substructuring (RTHS) is a promising approach to investigate the influence of foot prostheses on the gait pattern in versatile situations, while avoiding the necessity to model the prosthesis and its ground interaction. A numerical gait simulation is coupled in real-time to a prosthesis prototype on a test rig using sensors and actuators. However, synchronization errors make such experiments prone to instabilities. Thus, methods are required to ensure robust and stable RTHS experiments. In previous work, we developed promising methods using a one-dimensional contact RTHS experiment. In this contribution, we show our first experience with multidimensional contact RTHS in order to take the next step to enable foot prosthesis RTHS experiments. We present the design of a simplified planar foot prosthesis RTHS setup. Furthermore, we show the first results of a virtual RTHS test, where test stability is ensured through the application of normalized passivity control (NPC). From these results, we conclude that our approach is promising to extend our previously developed methods to the multidimensional case.

Keywords Real-time hybrid substructuring · Prosthesis testing · Passivity control · Hardware-in-the-loop · Hybrid simulation

5.1 Introduction

The development of prostheses for the lower human limb, which accurately reproduce the gait of able-bodied humans, has high relevance in the modern aging society. Especially, widespread diseases like diabetes mellitus and peripheral arterial disease are some of the major causes of a lower limb amputation. Even though the total number of lower limb amputations has been decreasing in recent years, still more than 60,000 lower limb amputations were registered in Germany in 2019 [1]. After such an amputation, the amputees rely on using a prosthesis in order to restore their ability to walk. Prosthetics have been used for centuries to support amputees, and, in general, prosthetics are a great help to let amputees walk again. Nonetheless, they still have major shortcomings due to the complexity of the biological counterpart. The gait of an amputee wearing the prosthesis is altered compared to the gait of an able-bodied person. A long-term imbalanced loading of the legs during walking can lead to bone and joint diseases. [2, 3] To overcome these problems, the influence of the prosthesis on the gait of the amputee must be considered from an early development stage on. Nevertheless, the investigation of lower limb prostheses together with a walking amputee is cumbersome. A pure stimulative approach is often not feasible since it requires the development and validation of an accurate numerical model of the prosthesis, which is an ambitious and time-consuming process. Another approach would consist of testing the prosthesis with human test subjects. Although this avoids the modeling and gives great insight into how the gait is altered, the test results are subjective to the specific test persons and test scenario. [4, 5] To conclude, methods are required that combine the advantages of prototype-based and simulation-based testing.

Real-time hybrid substructuring (RTHS) is a mechanical hardware-in-the-loop method to investigate complex dynamic structures economically and with high accuracy. This method originates from structural testing in earthquake engineering, but can be used for all kinds of dynamic structures. In RTHS, the dynamic system to investigate is partitioned into a numerical substructure and an experimental substructure. The former is simulated numerically, while for the latter a prototype is built and investigated on a test rig. To replicate the system dynamics of the whole system, the numerical part and the experimental

A. Kist (✉) · T. Ansari · C. Insam · D. Rixen
Chair of Applied Mechanics, School of Engineering and Design, Technical University of Munich, Garching, Germany
e-mail: arian.kist@tum.de; talhah.ansari@tum.de; rixen@tum.de

M. Allen et al. (eds.), *Dynamic Substructures, Volume 4*, Conference Proceedings of the Society for Experimental Mechanics Series, https://doi.org/10.1007/978-3-031-36694-9_5

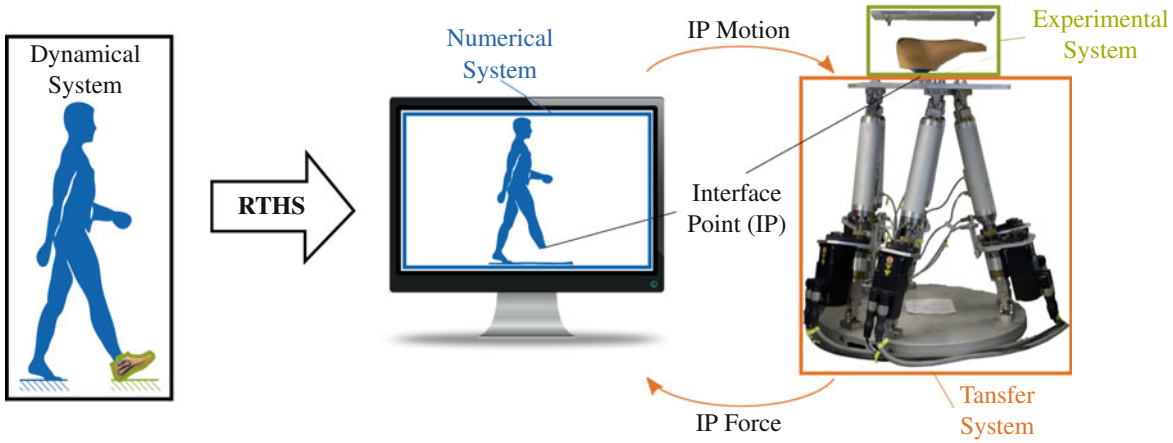

Fig. 5.1 RTHS principle visualized using the example of testing foot prostheses. Herein, the gait of an amputee is simulated numerically and coupled in real-time to a real foot prosthesis on a test rig. Thereby, the dynamic interplay between both subsystems is emulated and the influence of the prosthesis on the amputee's gait can be investigated (Image of the amputee adapted from [11]; figure adapted from [5])

part are coupled in real-time using a transfer system [6–8]. This enables to investigate systems, where some parts or effects cannot be modeled properly. By investigating only these critical parts experimentally on a test rig and coupling their response to the numerical model of the remaining structure in real-time, the systems dynamics of the whole system are preserved. By transferring this method to investigate lower limb prostheses and their influence on the gait of the amputee, the abovementioned drawback of the current test procedures can be overcome. The idea of using RTHS for the assessment of foot prostheses was proposed by *Yang et al.* [9] and further pursued by *Insam et al.* [5, 10]. The concept is visualized in Fig. 5.1. The dynamic system to investigate is a human wearing a foot prosthesis. Since the prosthesis is the critical structure, it is investigated experimentally. The remainder, which is the walking amputee, is simulated numerically. Note that, even though the modeling of the amputee is highly complex, this approach offers the advantage that the dynamic interaction between the amputee and the prosthesis can be investigated without putting a person at risk. Furthermore, several physical quantities, like hip torque, muscle activation, etc., can be measured from the numerical simulation, which would not be easily possible in a human. The motion of the interface point (IP), which is the point where the prosthesis is mounted, is calculated by the numerical system and sent as a command to a controlled actuator. This actuator, which is a Stewart Platform in Fig. 5.1, executes this motion.[1] The forces and torques at the IP resulting from this motion are measured and fed back to the numerical system. Consequently, the next time integration step of the numerical simulation is performed, which results in a new value for the IP motion and is sent as the next command to the actuator. Since the whole RTHS loop runs in real-time, the true dynamic properties of the amputee walking with the prosthesis can be emulated. This enables a highly versatile investigation of the influence of the prosthesis on the human gait in many different scenarios without modeling the prosthesis.

Although this approach is promising, it involves many challenges. Testing foot prosthesis is a multidimensional contact scenario, which means it comes into contact with the ground intermittently. Hence, the system dynamics exhibit discontinuities. As reported in [9, 10], RTHS tests for such systems are prone to instabilities, which cause the test fidelity to decrease heavily and potentially damage the test rig. These instabilities can be traced back to a nonideal transfer system, that is, imperfect actuator tracking, in combination with RTHS tests including contact. Thus, in our previous work [12–15], we intensively investigated control approaches to ensure robust and stable RTHS experiments with contact. Despite showing great potential, the methods were only tested and validated using a one-dimensional RTHS scenario. Since testing of foot prostheses is a multidimensional contact scenario, we aim at the extension and validation of the developed methods using multidimensional contact RTHS scenarios. Note that, in [5], a first preliminary RTHS test using a real foot prosthesis as experimental system was performed. Despite proving the general applicability of RTHS to investigate foot prostheses, the transfer system used here was not powerful and fast enough to test our methods to improve the interface tracking and guarantee stability.

In this contribution, we present our first experience with multidimensional contact RTHS experiments. We design a simplified planar foot prosthesis model to be investigated with RTHS. This model provides the advantage that in contrast to real foot prosthesis the dynamic response of the simplified system can be fully modeled. Thus, we can compare our RTHS

[1] Note that the prosthesis is mounted upside down on the actuator, which must be compensated for.

results to a reference simulation. Furthermore, we show the first results of a virtual RTHS test (that is the transfer system and the experimental system are simulated numerically as well), including the application of normalized passivity control (NPC).

5.2 System Design

In order to take a step further to the testing of foot prostheses with RTHS, a simplified planar foot model shown in Fig. 5.2 was developed. It consists of two rigid bodies with the masses m_{NUM} and m_{EXP}, respectively. The lower body is a thin beam with the length l_{EXP} representing a foot prosthesis. The upper body is a disc with radius r_{NUM} and represents the remaining part of an amputated leg. The upper body is excited in the x- and y-direction via spring-damper couplings ($k_{\mathrm{p,x}}$, $k_{\mathrm{d,x}}$ and $k_{\mathrm{p,y}}$, $k_{\mathrm{d,y}}$) to an exciting motion $x_{\mathrm{ex}}(t)$ and $y_{\mathrm{ex}}(t)$. The disc can rotate with the angle ϕ_{NUM} and a rotation $\phi_{\mathrm{ex}}(t)$ is imposed at the basis of a rotational spring-damper-system ($k_{\mathrm{p},\phi}$, $k_{\mathrm{d},\phi}$). This corresponds to controlling the disk to a desired motion using PD controllers. To connect the disk to the lower body, again spring-damper couplings are used. Both spring-damper-systems rotate with ϕ_{NUM}. One spring-damper-system ($k_{\mathrm{p,par}}$, $k_{\mathrm{d,par}}$) is parallel to the axis connecting the interface points on both masses. This spring has the undeformed length l_0. The other spring-damper-system ($k_{\mathrm{p,per}}$ and $k_{\mathrm{d,per}}$) is perpendicular to this connecting axis and is undeformed if there is no relative perpendicular displacement of the interface points. The beam can rotate with ϕ_{EXP}. Thus, the beam is additionally connected to the disc via a rotational spring-damper-system ($k_{\mathrm{p,rot}}$ and $k_{\mathrm{d,rot}}$). The interface point of the beam is shifted in beam direction with the distance a from the center of mass (CoM). Note that the simplicity of the system allows us to determine a reference simulation for the RTHS experiment, which would be much more challenging for a real foot prosthesis RTHS. Nevertheless, with the described system we can investigate multidimensional contact RTHS similar to a foot prosthesis RTHS. In order to model the ground contact, two distinct contact points (CP_1 and CP_2) at each end of the beam can come into contact with the ground and thus experience a ground reaction force. For the ground contact modeling, we refer to the next section.

The substructuring into the numerical part (blue) and experimental part (green) is indicated in Fig. 5.2. The upper disk, together with the exciting motion, is chosen as a numerical subsystem. The interface couplings, the beam, and the ground contact are consequently the experimental subsystem.

5.3 Simulation Setup

In order to gain a first experience with the designed model and the respective RTHS experiments, we developed a digital twin for the whole RTHS loop. In this purely virtual RTHS, in addition to the numerical subsystem also the transfer system and the experimental system are numerically simulated. The simulation was implemented using *Mathworks* MATLAB/Simulink (Version R2022a). All simulation parameters are given in Table 5.1.

The numerical mass m_{NUM} is excited using an external motion that acts on the disc via spring-damper-systems as seen in Fig. 5.2. We chose the exciting trajectories as follows:

$$x_{\mathrm{ex}}(t) = -A_{\mathrm{x}} \cos\left(2\pi \frac{f_{\mathrm{d}}}{2} t\right) + A_{\mathrm{x}} + x_{\mathrm{NUM},0} \tag{5.1}$$

$$y_{\mathrm{ex}}(t) = \frac{y_{\mathrm{EXP},0} + A_{\mathrm{y}}}{2} \cos\left(2\pi f_{\mathrm{d}} t\right) - \frac{y_{\mathrm{EXP},0} + A_{\mathrm{y}}}{2} + y_{\mathrm{NUM},0} \tag{5.2}$$

$$\phi_{\mathrm{ex}}(t) = A_{\phi} \cos\left(2\pi \frac{f_{\mathrm{d}}}{2} t\right) - A_{\phi} + \phi_{\mathrm{NUM},0} \tag{5.3}$$

Note that quantities with a $\bullet_{\bullet,0}$ as second index denote an initial value. Furthermore, it has to be mentioned that these trajectories are chosen just to ensure a planar RTHS test with ground contact and zero velocities at the beginning and end of the trajectories. We do not aim to reproduce human gait characteristics by this choice. All forces acting on m_{NUM} are due to spring-damper systems, and thus, its equations of motions can be solved in order to simulate the motion of m_{NUM}. The motion of the IP $\mathbf{q}_{\mathrm{IP}}$ is sent as motion command to our controlled actuator (see Fig. 5.2). In our setup, this actuator is an in-house-built Stewart Platform controlled using a decentralized cascaded P-PI-PI joint control with no feedforward controller. In order to simulate the dynamic response of the actuator up to 100 Hz, we use second-order transfer functions,

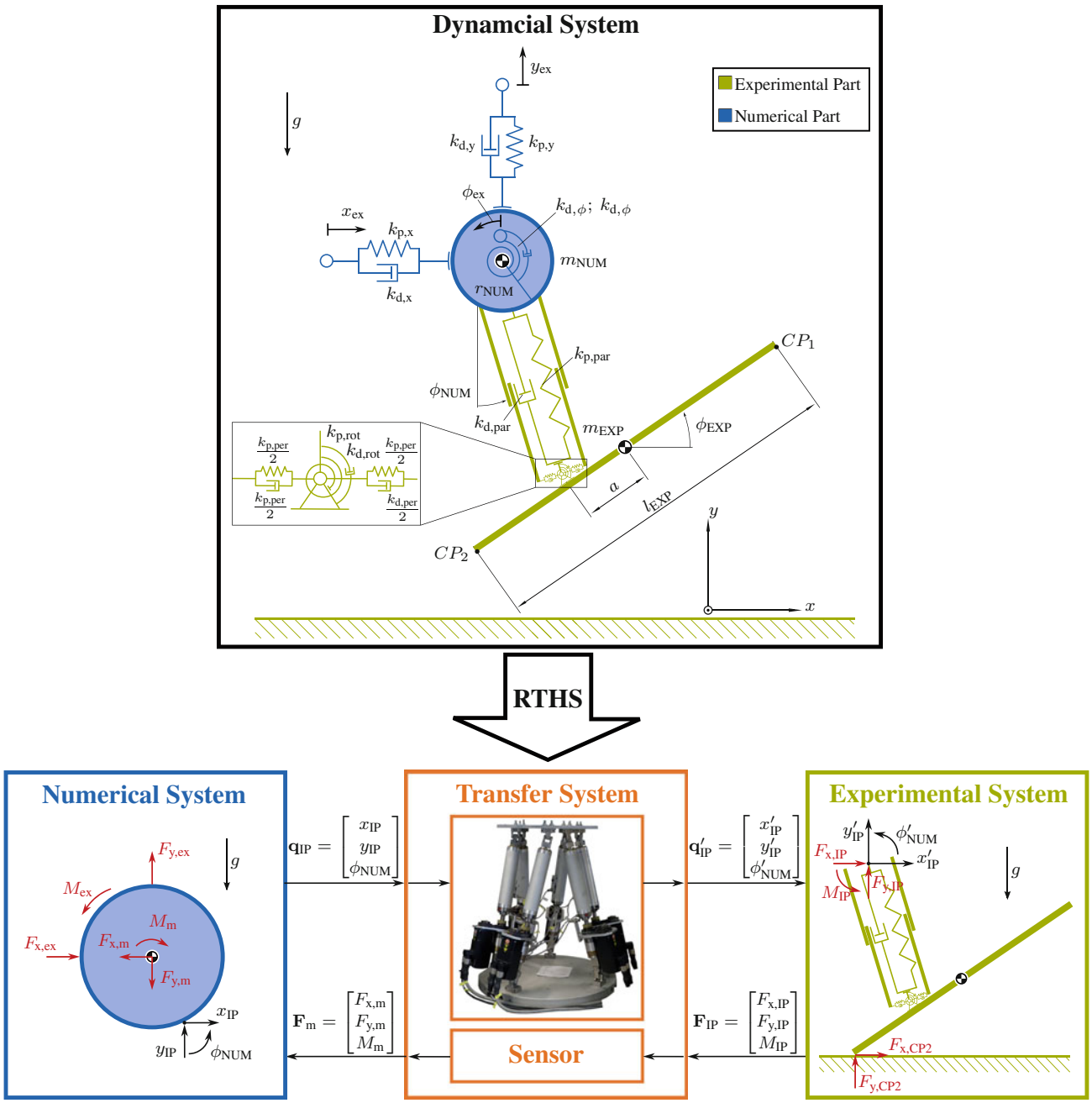

Fig. 5.2 Simplified planar foot prosthesis RTHS scenario. The upper part of this figure shows the dynamic system to be investigated using RTHS in detail. The lower part of this figure shows the RTHS setup with the respective substructures and the interface quantities

determined in previous work. For more information on the controller and the system identification, we refer to our previous publication [15]. Due to a nonideal tracking performance, the actuator executes the motion $\mathbf{q}'_{\mathrm{IP}} \neq \mathbf{q}_{\mathrm{IP}}$. The force-torque-sensor, measuring the interface force, is assumed to be ideal for our digital twin, thus $\mathbf{F}_{\mathrm{m}} = \mathbf{F}_{\mathrm{IP}}$. As mentioned, we also simulate the dynamic behavior of the experimental system in our virtual RTHS. To model the ground contact, the method by *Geyer and Herr* [16] was implemented. This model assumes two distinct contact points (CP_1 and CP_2) at the toe and the heel, where the contact to the ground occurs. The vertical (y-direction) ground reaction force is calculated based on a nonlinear spring-damper model, which is activated during ground penetration. The horizontal (x-direction) ground reaction force models static and kinetic friction. The static friction force is calculated as nonlinear spring-damper-system similar to the vertical ground reaction force. The force during kinetic friction is calculated based on the vertical ground reaction force and

Table 5.1 Parameters used for the simulation. Note that all initial values (denoted by a 0 as second index) are chosen in a way that each spring is initially in its static equilibrium.

Variable	Value	Variable	Value	Variable	Value
A_x	0.015 m	A_y	0.005 m	A_ϕ	$\frac{\pi}{16}$ rad
f_d	0.25 Hz	$k_\mathrm{p,x} = k_\mathrm{p,y}$	10^4 N/m	$k_\mathrm{d,x} = k_\mathrm{d,y}$	75 Ns/m
$k_{\mathrm{p},\phi}$	100 N/rad	$k_{\mathrm{d},\phi}$	5 Ns/rad	$k_\mathrm{p,par}$	8650 N/m
$k_\mathrm{d,par}$	10 Ns/m	$k_\mathrm{p,per}$	10^6 N/m	$k_\mathrm{d,per}$	500 Ns/m
$k_\mathrm{p,rot}$	0.5 N/rad	$k_\mathrm{d,rot}$	0.01 Ns/rad	l_0	0.071 m
a	0.005 m	r_NUM	0.01 m	l_EXP	0.03 m
g	9.81 m/s^2	m_NUM	9.6187 kg	m_EXP	0.3813 kg
$\phi_\mathrm{NUM,0}$	$\frac{\pi}{8}$ rad	$y_\mathrm{NUM,0}$	0.0835 m	$x_\mathrm{NUM,0}$	0 m
$\phi_\mathrm{EXP,0}$	0.3581 rad	$y_\mathrm{EXP,0}$	0.01 m	$x_\mathrm{EXP,0}$	0.358 m
ΔT	10^{-4} s	Solver	ode1 (Euler)	t_stop	4 s
G_p	800	T_LP	0.05 s	–	–

a sliding friction coefficient. Note that compared to the implementation by *Geyer and Herr*, we increased the vertical ground stiffness by a factor of ten in order to decrease ground penetration (all other parameters for the ground contact modeling were chosen as published in [16]). Based on the actual IP motion $\mathbf{q}'_\mathrm{IP}$ and the ground contact, all forces acting on m_EXP are determined and its dynamic behavior can be simulated.

5.4 Normalized Passivity Control (NPC)

NPC is a control approach to ensure stability of RTHS experiments, countering the abovementioned stability problems. This approach was originally proposed by *Peiris et al.* [17] and applied to one-dimensional RTHS experiments. *Insam et al.* [13, 14] further investigated this approach using one-dimensional RTHS experiments with contact, where it proved to be a very promising and versatile approach to ensure robustness and stability even in the presence of discontinuities and large tracking errors.

In NPC, a passivity observer monitors the power flow in and out of the transfer system. If the transfer system generates more power on the interface to the experimental system than on the interface to the numerical system, it is said to be active and thus unstable. In this case, an artificial damping force is added to the force feedback to the numerical system in order to restore the passivity, hence the stability. In case of a one-dimensional RTHS experiment with the interface degree of freedom (DoF) z_IP and interface force F_IP (F_m as measured interface force, respectively), the power flow between the subsystems is calculated as follows:

$$P^\mathrm{NUM} = \dot{z}_\mathrm{IP} \cdot F_\mathrm{m}^\mathrm{NPC} \tag{5.4}$$

$$P^\mathrm{EXP} = \dot{z}'_\mathrm{IP} \cdot F_\mathrm{IP} \approx \dot{z}'_\mathrm{IP} \cdot F_\mathrm{m} \tag{5.5}$$

Note that in Eq. 5.4, which calculates the power flow between the numerical system and the transfer system, the force $F_\mathrm{m}^\mathrm{NPC}$ also includes the added artificial damping, that is, $F_\mathrm{m}^\mathrm{NPC} = F_\mathrm{m} + F_\mathrm{d}$. Furthermore, in Eq. 5.5, which calculates the power flow between the experimental and the transfer system, it is assumed that $F_\mathrm{IP} \approx F_\mathrm{m}$, since the actual interface force is not accessible, but only the measured force. As stated above, the transfer system is classified as active if $P^\mathrm{EXP} > P^\mathrm{NUM}$, that is, $P_\mathrm{error} = P^\mathrm{EXP} - P^\mathrm{NUM} > 0$. Based on this condition, the damping force is calculated:

$$F_\mathrm{d} = \begin{cases} G_\mathrm{d} \cdot \frac{\tilde{P}_\mathrm{error}}{P_\mathrm{tot}} \cdot \dot{z}_\mathrm{IP} & \text{if } \tilde{P}_\mathrm{error} > 0 \\ 0 & \text{if } \tilde{P}_\mathrm{error} \leq 0 \end{cases} \tag{5.6}$$

Herein, $P_\mathrm{tot} = P^\mathrm{EXP} + P^\mathrm{NUM}$, that is, the total power, is used to normalize the error power P_error, for the calculation of the damping gain. Thus, this approach is referred to as *normalized* passivity control. The tuning parameter G_p can be adjusted to adapt the damping magnitude. The artificial damping force F_d is then added to the measured interface force and the total

force F_m^{NPC} is used within the numerical system. Note that $\tilde{\bullet}$ indicates a filtering with a first-order lowpass filter with the transfer function $G_{\mathrm{LP}}(s) = (T_{\mathrm{LP}}s + 1)^{-1}$ in order to smooth out the potentially noisy signals.

In order to extend this one-dimensional NPC to our multidimensional system, we implemented an individual NPC for each interface DoF. Hence, the passivity is monitored alongside each interface DoF individually. If one of these DoFs becomes active, damping is only added in this direction and the other DoFs are not affected. In this preliminary implementation, we did not tune each NPC individually, but we use the same parameterization for each of the interface DoF based on our experience from the one-dimensional RTHS experiments. The parameters are also given in Table 5.1. As will be shown in the next section, this resulted in satisfactory behavior of the NPC, but we plan individual tuning and adaption to further improve the performance in future work. The only adaption to the one-dimensional approach described above was an additional lowpass filtering of the damping force using a filter with the transfer function $G(s) = (0.005s + 1)^{-1}$ for the artificial damping force in x- and y-direction and $G(s) = (0.05s + 1)^{-1}$ for the rotational DoF. This was done to further smooth out the damping forces in order to avoid high force peaks in $F_{\mathrm{m}}^{\mathrm{NPC}}$, which is used for the numerical time integration in the numerical subsystem.

5.5 Simulation Results

In order to investigate the behavior of the planar system shown in Fig. 5.2, we performed two virtual RTHS tests. One RTHS simulation with the use of the NPC and one without the use of NPC. Furthermore, we computed the reference solution, which corresponds to the actual behavior of the planar system we want to investigate with RTHS. Consequently, for the reference solution, the transfer system is assumed to have ideal transfer behavior, that is, $\mathbf{q}'_{\mathrm{IP}} = \mathbf{q}_{\mathrm{IP}}$ and $\mathbf{F}_{\mathrm{m}} = \mathbf{F}_{\mathrm{IP}}$. Using this reference,

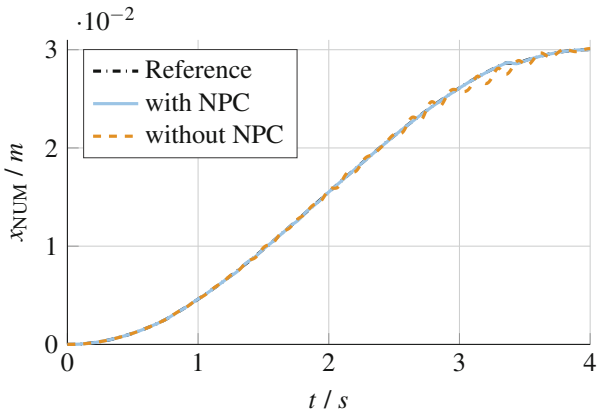

(a) x-position of the CoM of m_{NUM} over time.

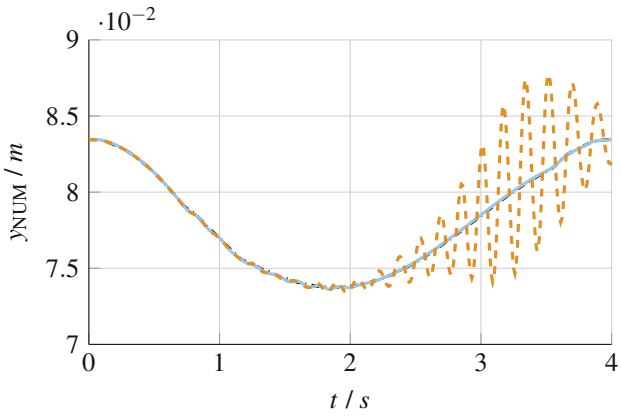

(b) y-position of the CoM of m_{NUM} over time.

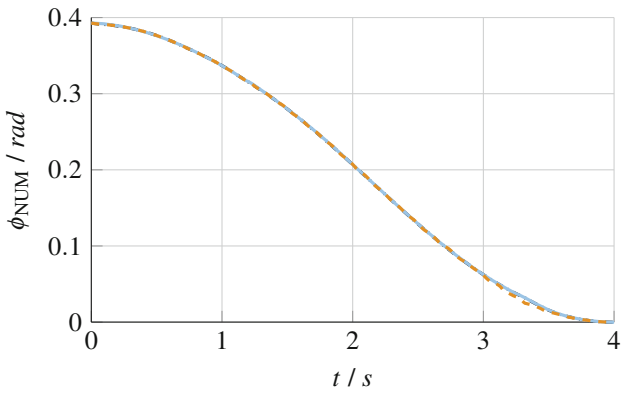

(c) Rotation of m_{NUM} over time.

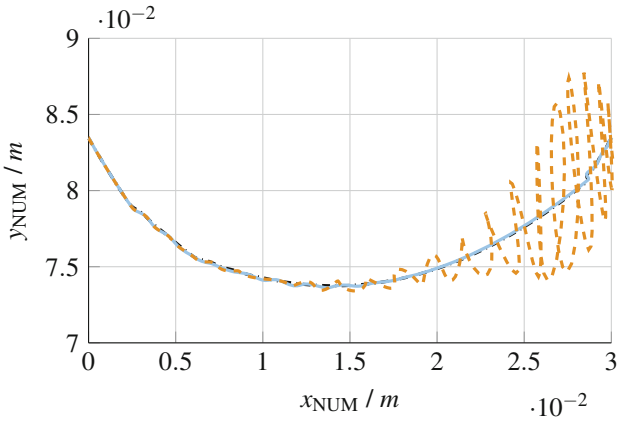

(d) y-position of the CoM of m_{NUM} over its x-position.

Fig. 5.3 Motion of the CoM of m_{NUM} with and without the use of NPC. Additionally, the reference trajectories are shown, which correspond to the actual motion of the reference system, respectively the results with an ideal transfer system. Note that the difference between the RTHS trajectories with NPC and the reference trajectories is barely visible in these figures

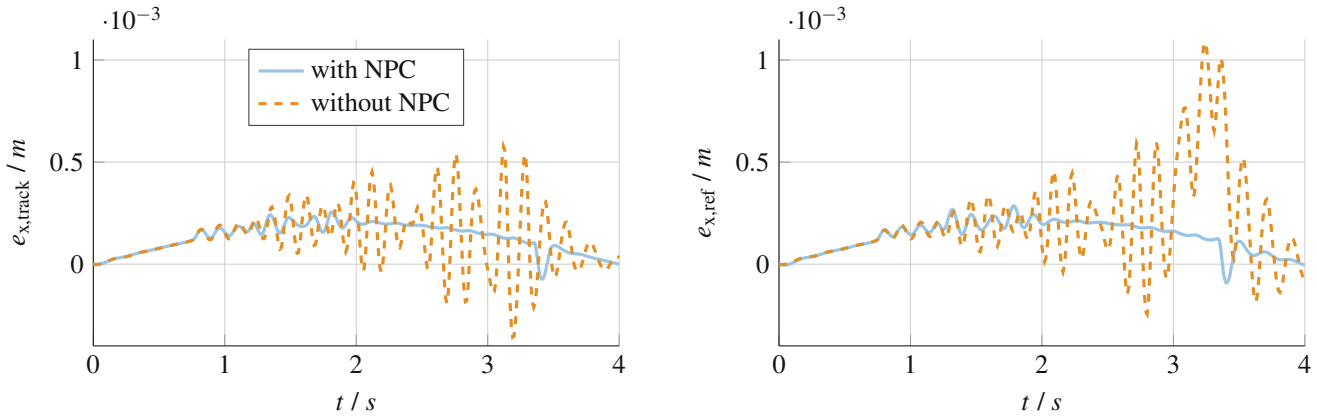

(a) Tracking error in x-direction, that is $e_{\mathrm{x,track}} = x_{\mathrm{IP}} - x'_{\mathrm{IP}}$.

(b) Reference error in x-direction, that is $e_{\mathrm{x,ref}} = x_{\mathrm{IP}}^{\mathrm{Ref}} - x'_{\mathrm{IP}}$.

Fig. 5.4 Tracking and reference error exemplary for the x-direction in the RTHS simulation with and without the use of NPC

we are able to assess the fidelity of the RTHS test outcome. In Fig. 5.3, the motion of the CoM of m_{NUM} is visualized for all three simulations. Furthermore, in the Appendix, the motion of the CoM of m_{EXP} is shown in Fig. 5.5 as well as the interface forces in Fig. 5.6.

From observing these figures, we can confirm that also in the multidimensional case, RTHS experiments with contact are prone to instabilities. Without the use of NPC, the whole system undergoes high-magnitude oscillations, especially in the y-direction. These oscillations are unwanted as they do not represent the real behavior of the reference system. Consequently, this not only heavily deteriorates the test fidelity, but also could damage the test rig, if a real nonvirtual RTHS experiment would be performed. Furthermore, we confirm our observations from the one-dimensional RTHS experiments that also in the multidimensional case the stability of the RTHS tests correlates with the damping in the numerical substructure ($k_{\mathrm{d,x}}$, $k_{\mathrm{d,y}}$ and $k_{\mathrm{d},\phi}$). As we chose rather low values for the damping in the numerical substructure (see Table 5.1), the magnitude of the unwanted oscillation increased. Conversely, for higher damping values in the numerical substructure (e.g., $k_{\mathrm{d,x}} = k_{\mathrm{d,x}} = 200$ Ns/m), no unwanted oscillation was observed and thus a stable RTHS experiment could be performed. The applicability of NPC and its ability to provide stable RTHS experiments is demonstrated in our simulations. In Fig. 5.3 (and Figs. 5.5 and 5.6, respectively), it can be seen how the unwanted oscillation observed without the NPC are damped out by the artificial damping force. Furthermore, it can be observed that each individual passivity controller damps out the unwanted oscillations in the respective directions. The heavy unwanted oscillations in y-directions are sufficiently damped as well as the rather small oscillations in x-directions, without deteriorating each other's damping performance. Additionally, the rotational DoF ϕ_{NUM}, where almost no oscillations are present, is not influenced by the artificial damping in x- and y-directions.

In Fig. 5.4, the tracking and reference errors are shown with and without NPC, exemplary for the x-direction. The tracking-error quantifies the actuator's ability to track its desired trajectories and is thus calculated as $e_{\mathrm{x,track}} = x_{\mathrm{IP}} - x'_{\mathrm{IP}}$. The reference error quantifies the ability of the RTHS test to replicate the true dynamics of the reference system. We define the following error for the motion of the interface point in the reference simulation and the actual motion of the interface point in the RTHS test: $e_{\mathrm{x,ref}} = x_{\mathrm{IP}}^{\mathrm{Ref}} - x'_{\mathrm{IP}}$. In Fig. 5.4, two important observations can be made. Firstly, that the reference error and the tracking error are correlated. Thus, the major cause for the fidelity deterioration is the imperfect actuator tracking. Secondly, it can be seen that the NPC damps out oscillations, but generally does not improve the tracking performance as a major tracking and reference error is still present, also with the use of NPC. Consequently, NPC can be used in order to maintain the stability of the RTHS experiments, but further control approaches (e.g., feedforward control like iterative learning control [12]) have to be considered to improve the tracking performance and thus the test fidelity. This extends our conclusions made in [14] to the multidimensional case.

5.6 Conclusion

In this contribution, we presented our next step toward the testing of foot prostheses using RTHS. Hereby, we aim for the extension and validation of our actuator control methods for stable and robust RTHS experiments with contact that were until now only validated for a one-dimensional RTHS experiment. In order to test our methods using a multidimensional RTHS

experiment with contact, we designed a simplified planar foot prosthesis model to be investigated with RTHS. It consists of two simple rigid bodies connected using spring-damper couplings and includes ground contact modeling in horizontal and vertical directions. The simplicity of the system allows us to obtain a reference simulation to assess the fidelity of the RTHS results. For this system, we set up a virtual RTHS experiment. In this digital twin of a real RTHS experiment, also the transfer system and the experimental system are simulated numerically. This gives us the ability to gain a first experience in the application of NPC and in future work further control methods in a multidimensional RTHS experiment. First results of virtual RTHS tests were presented, in which we show that also in the multidimensional case RTHS experiments are prone to instabilities: The system shows unwanted high-magnitude oscillations that not only deteriorate the test fidelity but also could damage the test rig. This is especially true for system configurations with low damping in the numerical substructure. This is in line with our results in previous work investigating a one-dimensional RTHS experiment. In order to counter these instabilities, we implemented NPC. In our multidimensional extension of NPC, we implemented individual passivity observers for each interface DoF and added an artificial damping force in the respective unstable direction. Our simulation results show the applicability of this approach as the unwanted oscillations were damped out and a stable RTHS experiment could be ensured. To conclude, the designed system seems to be promising to further extend our previously developed control methods for RTHS with contact to a multidimensional case. In doing so, we make these methods ready to be applied successfully for the investigation of foot prostheses with RTHS. In future work, we aim for an experimental realization of the system and its RTHS test to validate the results obtained using the virtual RTHS.

5.7 Appendix

See Figs. 5.5 and 5.6.

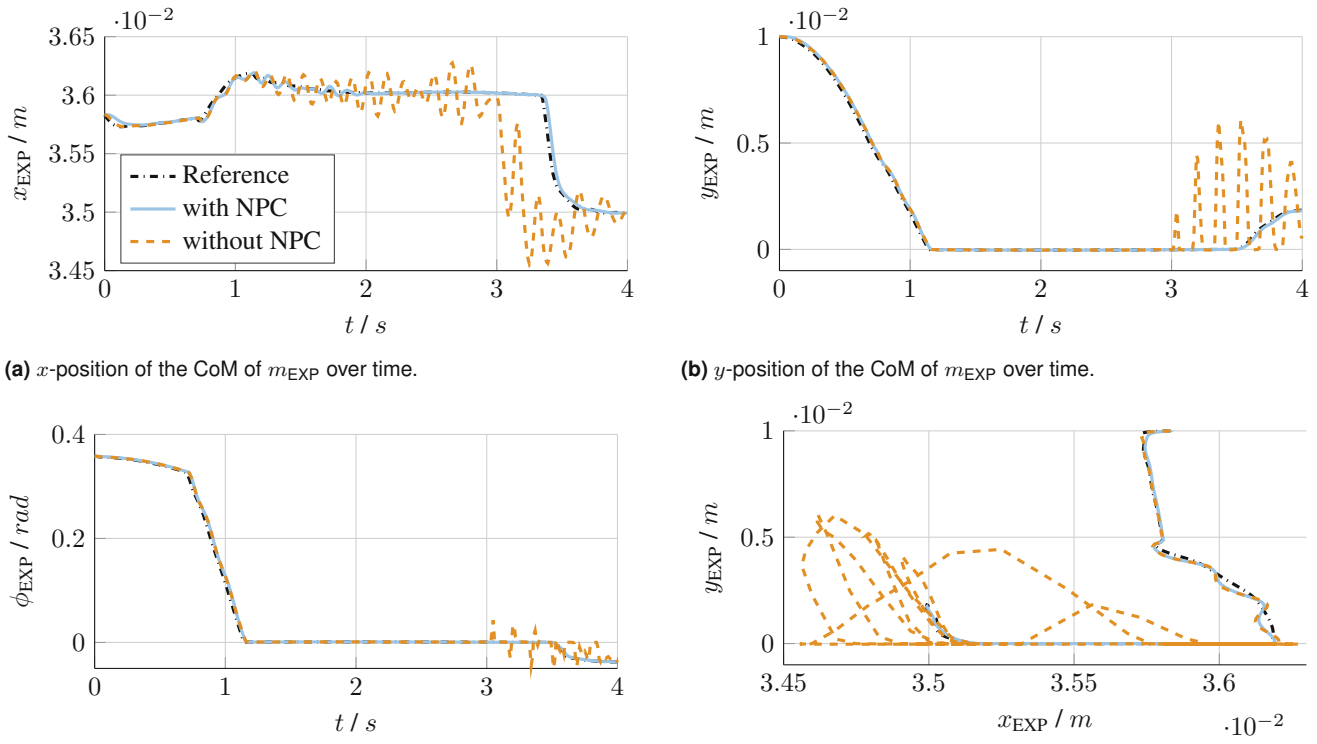

(a) x-position of the CoM of m_{EXP} over time.

(b) y-position of the CoM of m_{EXP} over time.

(c) Rotation of m_{EXP} over time.

(d) y-position of the CoM of m_{EXP} over its x-position.

Fig. 5.5 Motion of the CoM of m_{EXP} with and without the use of NPC. Additionally, the reference trajectories are shown, which correspond to the actual motion of the reference system, respectively the results with an ideal transfer system

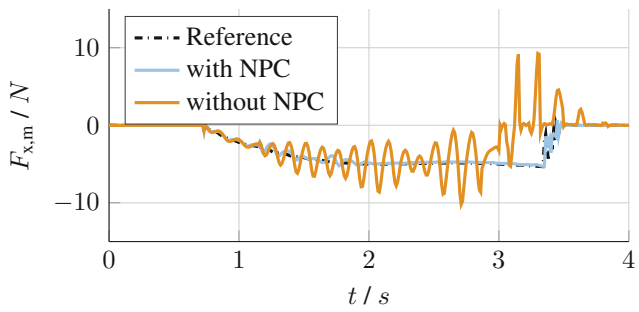

(a) Interface force between m_{NUM} and m_{EXP} in x-direction.

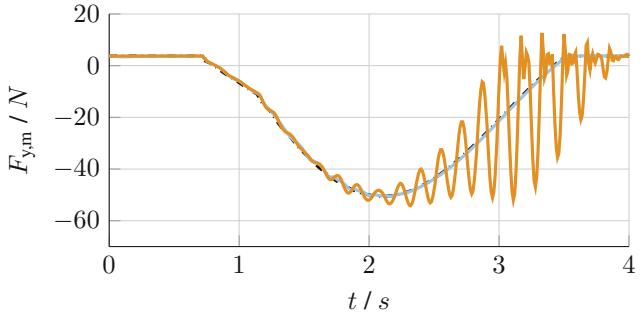

(b) Interface force between m_{NUM} and m_{EXP} in y-direction.

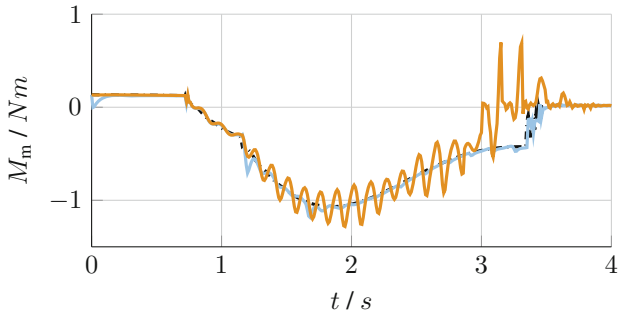

(c) Interface moment between m_{NUM} and m_{EXP}.

Fig. 5.6 Interface forces and moment between the numerical and the experimental substructure. Note that in case of NPC the displayed force is $F_{\text{m}}^{\text{NPC}}$, which includes the artificial damping force added by the NPC

Acknowledgments Part of this work was funded by the Deutsche Forschungsgemeinschaft (DFG, German Research Foundation), Project Number 450801414.

References

1. Walter, N., Alt, V., Rupp, M.: Lower limb amputation rates in Germany. Medicina **58**(1) (2022). https://doi.org/10.3390/medicina58010101
2. Gailey, R., Allen, K., Castles, J., Kucharik, J., Roeder, M.: Review of secondary physical conditions associated with lower-limb amputation and long-term prosthesis use. J. Rehab. Res. Develop. **45**, 15–29 (2008). https://doi.org/10.1682/jrrd.2006.11.0147
3. Murphy, D.: 20 - Gait Deviations after Limb Loss. In: Fundamentals of Amputation Care and Prosthetics. Demos Medical Publishing, New York City (2013)
4. Marinelli, C.: Design, Development and Engineering of a Bench for Testing Lower Limb Prosthesis, With Focus on High-Technological Solutions. PhD thesis. Politecnico di Milano (2016)
5. Insam, C., Ballat, L.-M., Lorenz, F., Rixen, D.J.: Hardware-in-the-loop test of a prosthetic foot. Appl. Sci. **11**(20) (2021). https://doi.org/10.3390/app11209492
6. Blakeborough, A., Williams, M.S., Darby, A.P., Williams, D.M.: The development of real-time substructure testing. R. Soc. **359**(1786), 1869–1891 (2001)
7. Williams, M.S.: Real-time hybrid testing in structural dynamics. In: 5th Australasian Congress on Applied Mechanics, ACAM 2007, vol. 1 (2007)
8. Plummer, A.R.: Model-in-the-loop testing. Proc. Inst. Mech. Eng. Part I J. Syst. Control Eng. **220**(3), 183–199 (2006). https://doi.org/10.1243/09596518JSCE207
9. Yang, Z., Iravani, P., Plummer, A.R., Pan, M.: Investigation of hardware-in-the-loop walking/running test with spring mass system. Towards Auton. Rob. Syst., 126–133 (2017). https://doi.org/10.1007/978-3-319-64107-2
10. Insam, C., Bartl, A., Rixen, D.J.: A step towards testing of foot prostheses using real-time substructuring (RTS). In: Special Topics in Structural Dynamics & Experimental Techniques, vol. 5, pp. 1–9. Springer International Publishing, Berlin (2020)
11. Predovic, J.: Walking Cycle Man. https://svg-clipart.com/man/YS0etCS-walking-cycle-manclipart. Accessed 05 Oct 2022
12. Insam, C., Kist, A., Rixen, D.J.: High fidelity real-time hybrid substructure testing using iterative learning control. In: ISR – 52nd International Symposium on Robotics. VDE Verlag Berlin Offenbach (2020)
13. Insam, C., Peiris, L.D.H., Rixen, D.J.: Normalized passivity control for hardware-in-the-loop with contact. Int. J. Dyn. Control **9**(4), 1471–1477 (2021). https://doi.org/10.1007/s40435-021-00790-8

14. Insam, C., Kist, A., Schwalm, H., Rixen, D.J.: Robust and high fidelity real-time hybrid substructuring. Mech. Syst. Sig. Proces. **157** (2021). https://doi.org/10.1016/j.ymssp.2021.107720
15. Insam, C., Göldeli, M., Klotz, T., Rixen, D.J.: Comparison of feedforward control schemes for real-time hybrid substructuring (RTHS). In: Dynamic Substructures, vol. 4, pp. 1–14. Springer International Publishing, New York City (2021)
16. Geyer, H., Herr, H.: A muscle-reflex model that encodes principles of legged mechanics produces human walking dynamics and muscle activities. IEEE Trans. Neural Syst. Rehab. Eng. **18**(3), 263–273 (2010). https://doi.org/10.1109/TNSRE.2010.2047592
17. Peiris, L.D.H., Plummer, A., du Bois, J.: Normalised passivity control for robust tuning in real-time hybrid tests. Int. J. Robust Nonlin. Control **32**(7), 4355–4375 (2022)

Chapter 6
Real-Time Hybrid Substructuring Using an Inertial Shaker Transfer System

David Vanasse III, Sergio Lobo-Aguilar, and Richard Christenson

Abstract Real-time hybrid substructuring (RTHS) is proposed as a cyber-physical method, combining both experimental and numerical testing, to capture the system-level dynamic interaction between numerical and physical substructures. With RTHS, a structural dynamic system can be partitioned into separate experimental and numerical components or substructures and interfaced together as a cyber-physical system similar to hardware-in-the-loop (HWIL) testing. The substructures that are well understood are simulated in real time using analytical or numerical models, while the substructures of particular interest, overly complex, or nonlinear are tested experimentally using physical specimens. In an RTHS test, the experimental and numerical substructures communicate together in real time by transferring displacement and force signals through a feedback loop using controlled actuation and sensing.

In a typical RTHS configuration, a transfer system is used to impart numerically determined displacements onto the physical substructure, and force sensors are used to measure the resulting restoring forces. The measurements are feed back into the numerical model to determine the displacement response at the next integration time step. Depending on the structural system's configuration, this traditional RTHS substructuring approach may not be desirable, and it may be required to apply forces or loads to the physical substructure through the transfer system and measure the specimen response (displacement or acceleration) for input to the numerical component. This might be the case for fluid–structure interaction problems or for physical testing of the bottom floor of a multistory building – as proposed here with use of an inertial shaker as the transfer system. In this study, an inertial shaker is utilized to transfer story shear force from the numerical substructure to the physical substructure.

Keywords Real-time hybrid substructuring · Inertial shaker

6.1 Introduction

This research will first demonstrate the successful completion of a real-time hybrid substructuring (RTHS) test in a traditional manner, then make an extension to a newly proposed method using an inertial shaker to apply force feedback. For RTHS tests with force feedback, there is certainly concern for closed-loop system stability [1–5]. Typical applications of RTHS with force applied by the transfer system utilize a hydraulic actuator attached between an inertial frame of reference and the substructure interface on the physical component [1]. The system being examined here is a two-story seismically excited building model, first investigated with the bottom story numerically modeled and top story physically tested. The closed-loop system will be shown to capture the dynamic interaction between the two stories and provide realistic system-level seismic response of the building system. The setup and procedure for physically testing the bottom story while numerically modeling the top story is then proposed. For this novel approach, the first story is subjected to a ground acceleration as it sits upon a bench-scale shake table and the calculated story shear [1] of the top floor is imparted to the top of the first story through the use of an inertial shaker as the transfer system. In turn, the absolute acceleration of the top of the first story is measured

D. Vanasse III
Department of Mechanical Engineering, University of Connecticut, Storrs, CT, USA

S. Lobo-Aguilar
Department of Civil Engineering, University of Costa Rica, San Jose, Costa Rica

R. Christenson (✉)
Department of Civil and Environmental Engineering, University of Connecticut, Storrs, CT, USA
e-mail: rchriste@engr.uconn.edu

M. Allen et al. (eds.), *Dynamic Substructures, Volume 4*, Conference Proceedings of the Society for Experimental Mechanics Series, https://doi.org/10.1007/978-3-031-36694-9_6

with an accelerometer and used as input to a numerical model of the top story of the building structure. The dynamics and procedure of the inertial shaker approach will be well defined to lay framework for future research on more advanced RTHS testing.

As RTHS continues to become more feasible due to advances in numerical computing power, digital signal processing, and high-speed actuation [6–8], innovation in the general framework and coupling of the substructures should be further explored. This research intends to promote that dialog in the substructuring community.

The structure of this chapter is as follows: Sect. 6.2 introduces the framework for this RTHS test in the two different substructuring realizations. In Sect. 6.3, the experimental setup and compensation methods are presented. The results of the testing for the traditional realization and extension to the new method are provided in Sect. 6.4. Section 6.5 is a conclusion of this research, followed by acknowledgments.

6.2 Real-Time Hybrid Substructuring (RTHS) Realizations

This section provides the conceptual substructuring of the two variations of performing an RTHS test on a two-story structure, including the interactions between the numerical and physical models. The goal of both methods is to accurately capture the full-system response to seismic excitation, without experimentally testing the full structure. This text takes a controls-based approach at RTHS as demonstrated in Fig. 6.1. Here, the numerical substructure is a linear model with measurements from the physical component as inputs, and with outputs applied to the physical substructure to close the feedback loop.

6.2.1 Realization 1

The first setup, denoted as Realization 1 herein, requires physical testing of the top story and numerically modeling the bottom story. From the physical test, the top story absolute acceleration $\ddot{x}_2^a$ is measured. The story shear V_s is calculated with Eq. (6.1), where m_2 is the second story mass. The story shear V_s is then input to a state-space model of the bottom story as a force acting on the top of the bottom story:

$$V_s = m_2 \ddot{x}_2^a \tag{6.1}$$

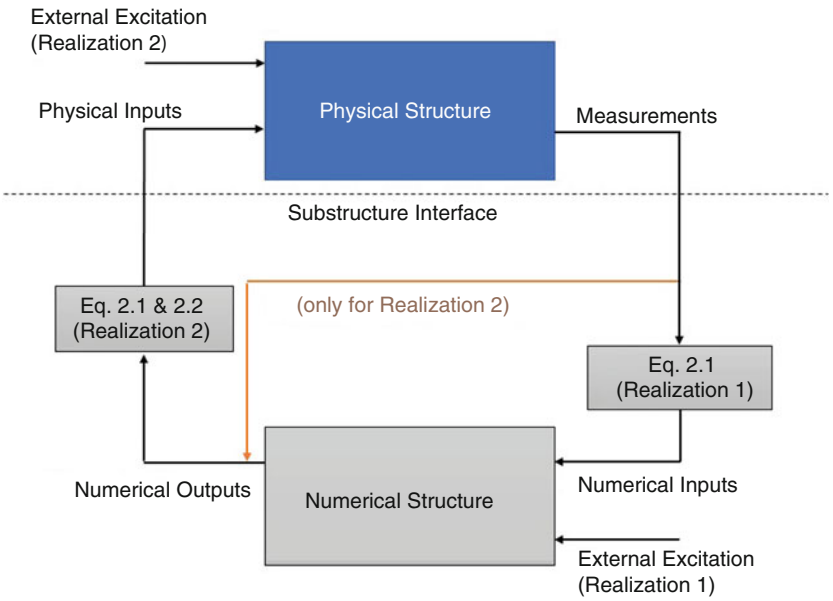

Fig. 6.1 Control-based RTHS framework

Seismic excitation of the full structure is also a numerical input. Feedback arises through application of the absolute first story displacement x_1^a as a seismic excitation at the base of the top story in the physical substructure via the shake table. The absolute first story displacement is calculated via Eq. (6.2):

$$x_1^a = x_1 + x_g \tag{6.2}$$

The value x_g is ground displacement, measured by the shake table displacement sensor for each excitation in a fully physical test. The value x_1 represents first story displacement relative to the moving base, which is computed numerically. Ground displacement is then synchronized with the measured table acceleration prior to implementation in the numerical model.

6.2.2 Realization 2

Realization 2 involves simulation of the top story, while experimentally testing the bottom story. The seismic excitation imparted by the shake table for Realization 2 is not filtered by a numerical lower story, which eliminates a potential source of error from Realization 1. However, the interaction between stories is now transferred via the inertial shaker, which is more involved due to its operation from a noninertial reference. The inertial shaker force on the first story must be equal to the story shear force that occurs at the top of floor one in the full-scale experiment. As seen by Eqs. (6.1) and (6.3), the numerical substructure requires accurate parameter values of the second story mass, and inertial shaker [active mass damper (AMD)] mass, m_2, m_{AMD} respectively to apply a force of the correct magnitude.

$$\ddot{x}_{\mathrm{AMD}} = \frac{V_s}{m_{\mathrm{AMD}}} - \ddot{x}_1^a \tag{6.3}$$

Here, $\ddot{x}_1^a$, $\ddot{x}_{\mathrm{AMD}}$, and m_{AMD} are the absolute first story acceleration, inertial shaker acceleration relative to the moving story, and inertial shaker mass, respectively. Additionally, the measurement of first story acceleration $\ddot{x}_1^a$ must have the correct magnitude with minimal delay to avoid inaccuracy and instability. Another challenge is applying the story shear from a moving reference though the inertial shaker. The inertial shaker acceleration, $\ddot{x}_{\mathrm{AMD}}$, must track the command from the numerical model in magnitude and phase. The requirements on measurement of $\ddot{x}_1^a$ and tracking of $\ddot{x}_{\mathrm{AMD}}$ are to prevent instability in the closed loop. The proposed method is more challenging due to the inertial shaker operation in a noninertial reference frame versus the traditional approach of applying story shear V_s via a hydraulic actuator from a fixed reference. However, this approach is worth investigating for extension to other systems where imparting force to the physical structure via the transfer system is of particular interest, such as fluid-loaded structures. Figure 6.2 shows the interactions between the substructures for both realizations.

6.3 Experimental Setup

This section describes the methods for each test, followed by compensation techniques. The investigated system is a reduced-scale model of a low-rise building subject to earthquake excitation. For this RTHS test, where the scaled full-system experimental test does not involve high-power consumption, is not likely to damage equipment, does not present any issues of structure size (full-scale or high-rise structure), etc., the scaled two-story physical experiment is viable for the full structure. While this is not always the case in applications when RTHS is desirable, testing the full system physically provides baseline results to evaluate the validity of the methods. In all tests, the top and bottom floor experimentally and numerically have the inertial shaker present for uniformity. In experimental tests where the inertial shaker does not play an active role, its motion is prevented by constraining its position to the end of the track. The research was performed at the National Laboratory of Structural Models and Materials at the University of Costa Rica (LanammeUCR) in San Jose, Costa Rica.

Due to the presence of feedback, actuators and sensors must be compensated to preserve stability and performance. The results are highly dependent on the tracking performance of actuators and time delay of sensors. This research implements inverse feedforward compensators designed by pole-zero placement. Section 6.3.2 shows the design process.

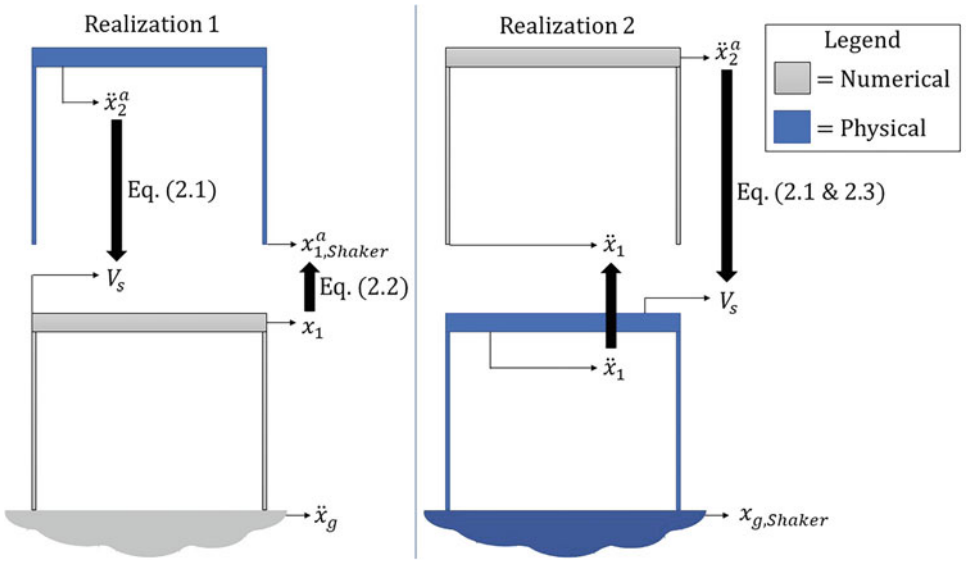

Fig. 6.2 RTHS realization diagrams

Fig. 6.3 Full structure setup

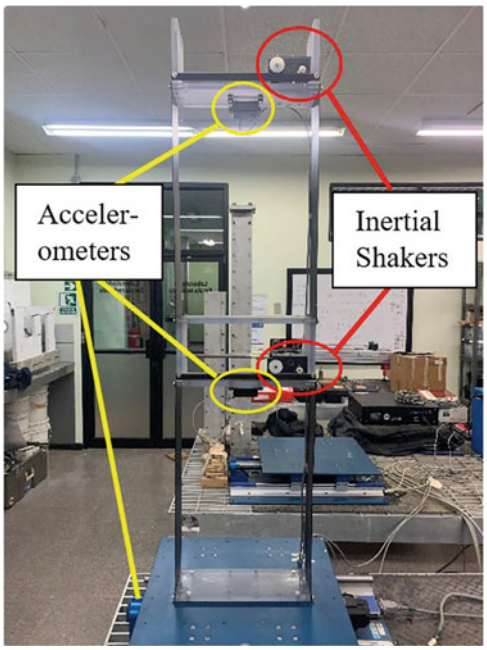

6.3.1 Fully Experimental Setup

The two-story physical structure shown in Fig. 6.3 consists of two stacked single-story sections. Each single story is constructed by mounting a Quanser AMD-2 cart with a Faulhaber Coreless DC Motor 2338S006 atop a Quanser AMD-2 structure. The inertial shakers (AMD-2 carts) use a Quanser VoltPAQ-X2 2 Channel Linear Voltage Amplifier. In the full structure test, both inertial shakers are locked in place, so they do not translate relative to the story. The structure is secured to a Quanser Shake Table II providing seismic excitation at the base of the first story. Sensors include Quanser capacitive DC accelerometers with full-scale range $\pm$ 5g, mounted to the shake table and each story of the structure. The shake table has a built-in displacement sensor. The actuators include the Quanser shake table and the two inertial shakers that remain inactive for this experiment. MATLAB/Simulink with QuaRC for Windows – Real-Time Control Software is the DAQ interface as well as control module. The Quanser Shake Table II and amplifier are powered with a Quanser UPM180-25PWM-B Universal Power Module (180 V, 25 A) – PWM-B.

To perform system identification, a band-limited white noise (BLWN) is first applied as seismic excitation to the two-story structure. The measured ground and story acceleration time histories are used to find frequency response functions (FRFs) from input (ground acceleration) to output (floor acceleration). The test structure is modeled as a two-degree-of-freedom structure with modal damping as outlined in [9]. From the measured FRF, natural frequencies and modal damping are experimentally determined.

Next, the full physical structure is subjected to various seismic excitations including both near-field and far-field earthquakes. These measurements will be used to evaluate the RTHS test performance.

6.3.2 *Fully Numerical Setup*

A numerical model of the full structure is generated as a foundation for the numerical substructures in the RTHS tests. The accuracy of the numerical model in each realization is crucial to avoid instability or inaccurate results. Equation (6.4) governs the motion for the two-degree-of-freedom lumped parameter model, adopted as a slight variation of the model used extensively for seismic vibration mitigation via MR dampers [8, 10–12].

$$\mathbf{M}\ddot{\mathbf{x}} + \mathbf{C}\dot{\mathbf{x}} + \mathbf{K}\mathbf{x} = -\mathbf{M}\boldsymbol{\Lambda}\ddot{x}_{\mathrm{g}} \tag{6.4}$$

The system matrices are.

$\mathbf{M} = \begin{bmatrix} m_1 & 0 \\ 0 & m_2 \end{bmatrix}$	$\mathbf{C} = \begin{bmatrix} c_1 + c_2 & -c_2 \\ -c_2 & c_2 \end{bmatrix}$
$\mathbf{K} = \begin{bmatrix} k_1 + k_2 & -k_2 \\ -k_2 & k_2 \end{bmatrix}$	$\boldsymbol{\Lambda} = \begin{bmatrix} -1 \\ -1 \end{bmatrix}$

Matrices **M**, **C**, and **K** are the mass, damping, and stiffness matrices, respectively, while **Λ** is a location vector as defined above. The parameters m_i, c_i, k_i are the lumped story mass, lumped flexural element damping, and lumped flexural element stiffness, respectively, for the *i*th floor. Stiffness values are determined by evaluating the steel columns as fixed-fixed beams, and modal damping is applied to determine the viscous damping coefficients. By Eq. (6.4), the continuous system has been simplified to a two-degree-of-freedom model and the vector $\mathbf{x} = [x_1\ x_2]^{\mathrm{T}}$ consists of the displacement of the bottom and top stories relative to the moving base, respectively. The command to the Quanser shake table is a displacement time history; however, the table accelerometer provides measurement of ground acceleration $\ddot{x}_{\mathrm{g}}$ to be stored for numerical application. The higher-order nonlinear effects do not significantly impede the numerical model from matching the experimental data. Equation (6.4) can be written in state-space form of Eqs. (6.5) and (6.6) by defining the state vector $\mathbf{z} = [\mathbf{x}\ \dot{\mathbf{x}}]^{\mathrm{T}}$, input scalar as $u = \ddot{x}_{\mathrm{g}}$, which is recorded prior from fully physical tests, measurement vector $\mathbf{y} = \left[\ddot{x}_1^a\ \ \ddot{x}_2^a\ \right]^{\mathrm{T}}$, and matrices A–D accordingly. For the story accelerations within the measurement vector, subscripts 1 and 2 represent first and second story, respectively, while superscripts "a" indicate an absolute measurement:

$$\dot{\mathbf{z}} = \mathbf{A}\mathbf{z} + \mathbf{B}u \tag{6.5}$$

$$\mathbf{y} = \mathbf{C}\mathbf{z} + \mathbf{D}u \tag{6.6}$$

$\mathbf{A} = \begin{bmatrix} \mathbf{0} & \mathbf{I} \\ -\mathbf{M}^{-1}\mathbf{K} & -\mathbf{M}^{-1}\mathbf{C} \end{bmatrix}$	$\mathbf{B} = \begin{bmatrix} \mathbf{0} \\ \boldsymbol{\Lambda} \end{bmatrix}$
$\mathbf{C} = [-\mathbf{M}^{-1}\mathbf{K}\ \ -\mathbf{M}^{-1}\mathbf{C}]$	$\mathbf{D} = \begin{bmatrix} 0 \\ 0 \end{bmatrix}$

6.3.3 Transfer System Compensation

In both RTHS methods, the stability and accuracy of the closed-loop test are heavily dependent on the sensors and actuators. In an RTHS test, both random error (sensor noise) and systematic error (actuator/sensor magnitude and phase disagreements) can be detrimental [8], though reduction of systematic error tends to be more important [13, 14]. An uncalibrated actuator will prevent displacement compatibility of the numerical model with the physical model; when actuators have a considerable time delay, or phase lag, this means the actuation happens slightly later than when it is commanded. The effect may be frequency dependent and is a common source of instability in RTHS tests [15]. Tracking of actuator excitation magnitude is also critical. This is more self-explanatory; the actuators should excite the structure at the commanded magnitude. Sensors have the same restrictions; if there is a phase lead/lag or high gain factor at frequencies of importance, the physical sensors will incorrectly feed data back into the numerical model. In this experiment, the first and second natural frequencies of the structure were experimentally determined to be 1.32 Hz and 3.58 Hz, respectively. The target frequency range of compensation for both actuators and sensors is thus 0–10 Hz.

Frequency response functions provide a convenient method for identifying the magnitude of input/measurement amplification and phase lead or lag. An FRF can be used to generate two plots: the first is the amplification in decibels versus frequency, and the second is the phase lead or lag versus frequency in degrees [16]. To collect FRFs for the shake table and inertial shaker, a band-limited white noise (BLWN) is individually commanded to each with no command sent to the other. The constant autospectral density function of a BLWN removes input bias from the FRF to accurately capture hardware dynamics [16].

To maintain fidelity of the substructuring, inverse feedforward compensation is employed as needed. This begins with building a transfer function (TF) that produces an FRF matching that of each sensor or actuator, then inverting the TF, ensuring it is stable, and placing it in line with the sensor [17]. If done successfully, the FRF of the collected data from the sensor/actuator with the feedforward compensator should have near-zero dB (unity) gain and a phase of zero degrees within the frequency range of 0–10 Hz. More detailed processes for transfer system compensation in RTHS tests such as minimum-phase inverse compensation and P-type iterative learning control are presented by [7].

The Quanser shake table and inertial shaker are equipped with a built-in feedback-feedforward position controllers and are experimentally proven to track commands well. A 10 Hz low-pass filter is implemented for all signals commanded to the shaker. The accelerometers are compensated as described above.

6.3.4 Realization 1 Setup

The first RTHS test, described in Sect. 6.2.1 and shown in Fig. 6.2, is a physical test of the top floor interacting with a numerically modeled bottom floor. The physical testbed is that of Sect. 6.3.1 without one structure, as shown in Fig. 6.4. The inertial is again locked in place for this test. The numerical bottom floor is seismically excited by the previously measured

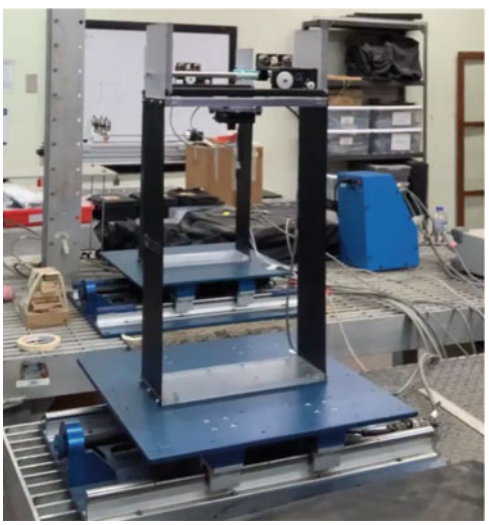

Fig. 6.4 RTHS Realization 1 experimental setup

earthquake acceleration time history, which in turn induces an acceleration to the numerical bottom floor. The only active actuator in the physical model is the shake table itself, which moves with the numerical bottom floor per Eq. (6.2). The shake table acceleration and displacement are recorded to ensure command tracking. The shake table induces motion of the physical top story, pictured in Fig. 6.4. The top story accelerometer sends a reading to the numerical model. At the next time step, this measured second story acceleration is converted to a story shear via Eq. (6.1) and input to the numerically simulated first story state-space model. The physical/numerical interface crossings can be realized by the numerical first story absolute displacement sent to the shake table command, and conversely the physical second story acceleration converted to a story shear imposed on the numerical first story.

The state-space model requires modification from its form in Sect. 6.3.1 to numerically model the bottom floor only. The equations of motion for the bottom floor can be written in the form of Eqs. (6.5) and (6.6) if the state vector is replaced by $\boldsymbol{z_1} = [x_1 \dot{x}_1]^{\mathrm{T}}$, input scalar is replaced by input vector $\mathbf{u_1} = \left[\ddot{x}_{\mathrm{g}} \;\; V_{\mathrm{s}}\right]^{\mathrm{T}}$, output vector is replaced by $y_1 = \left[x_1 \ddot{x}_1^a\right]$, and matrices **A–D** are rewritten as a new $\mathbf{A_1}$-$\mathbf{D_1}$ as follows:

$$\mathbf{A_1} = \begin{bmatrix} 0 & 1 \\ \frac{-k_1}{m_1} & \frac{-c_1}{m_1} \end{bmatrix} \qquad \mathbf{B_1} = \begin{bmatrix} 0 & 0 \\ -1 & \frac{1}{m_1} \end{bmatrix}$$

$$\mathbf{C_1} = \begin{bmatrix} 1 & 0 \\ \frac{-k_1}{m_1} & \frac{-c_1}{m_1} \end{bmatrix} \qquad \mathbf{D_1} = \begin{bmatrix} 0 & 0 \\ 0 & \frac{1}{m_1} \end{bmatrix}$$

Here, the states and outputs are all for the bottom floor, as indicated by the subscript.

6.3.5 *Realization 2 Setup*

The second RTHS test proposed by this research is a simultaneous numerical simulation of the top story and experimental test of the bottom story in real time. The physical testbed is identical to Fig. 6.1; however, the inertial shaker is no longer locked in place. Any mass above the bottom story moving along with x_1 is considered negligible. The sensors required include accelerometers on the inertial shaker, physical top floor, and shake table. Actuators in this method include the shake table and inertial shaker.

This nontraditional setup is more involved than that of Sect. 6.3.3. The ground motion is directly applied by the shake table physically, and the subsequent first story displacement is feed into the numerical model. The first story measured acceleration seismically excites the simulated top floor. The numerical top floor acceleration is then converted to a story shear via Eq. (6.1). Next, the measured bottom floor acceleration $\ddot{x}_1^a$ and calculated story shear V_{s} are input to Eq. (6.3) to determine the inertial shaker acceleration $\ddot{x}_{\mathrm{AMD}}$ required to produce that same shear force. The commanded displacement x_{AMD} is relative to the moving first story and is required to command the AMD. The measurement $\ddot{x}_1^a$ is necessary because the inertial shaker acts in a noninertial reference frame. To avoid damage, $\ddot{x}_{\mathrm{AMD}}$ is integrated twice to determine x_{AMD}, which is compared to the allowable stroke.

Again, a new state-space model must be developed with a new state vector $\boldsymbol{z_2} = [x_2 \dot{x}_2]^{\mathrm{T}}$, new input defined as scalar $u = \ddot{x}_1^a$, new output defined as scalar $y_2 = \ddot{x}_2^a$, and matrices **A–D** are rewritten as a new $\mathbf{A_2}$-$\mathbf{D_2}$ as follows:

$$\mathbf{A_2} = \begin{bmatrix} 0 & 1 \\ \frac{-k_2}{m_2} & \frac{-c_2}{m_2} \end{bmatrix} \qquad \mathbf{B_2} = \begin{bmatrix} 0 \\ -1 \end{bmatrix}$$

$$\mathbf{C_2} = \begin{bmatrix} \frac{-k_2}{m_2} & \frac{-c_2}{m_2} \end{bmatrix} \qquad \mathbf{D_2} = \begin{bmatrix} 0 \end{bmatrix}$$

With the interactions across the physical/numerical interface modeled correctly, this RTHS test will be successful with sensors and actuators that track sufficiently well.

6.4 Results

The goal of this study is to validate traditional RTHS proceedings and present a new approach via realizations 1 and 2, respectively. Realization 2 can be extended to a variety of complex tests to reduce the degree of complication. RTHS testing additionally reduces the scale of failures due to the reduction in dynamic physical components.

6.4.1 System Identification

To adjust the state-space models, a BLWN is applied as seismic excitation to the full physical 2DOF structure as outlined in Sect. 6.3.1. The BLWN is a low-pass white noise with a 10 Hz cutoff frequency, chosen per the structural natural frequencies. The resulting FRFs from ground acceleration to story acceleration are shown in Fig. 6.5.

The numerical model matches the physical model in terms of dynamics, including natural frequencies and damping ratios within the frequency range of concern. This validates the simplification to a two-degree-of-freedom model for this application.

6.4.2 RTHS Tests

Upon completion of sensor and actuator compensation, the first RTHS substructuring realization can be tested. Initially a BLWN seismic excitation is employed to ensure the single degree of freedom (SDOF) physical substructure displays two modes at the frequencies of the full physical structure (2DOF). The RTHS interactions between substructures successfully create a transformation from one natural frequency at 2.47 Hz to two natural frequencies near 1.32 and 3.58 Hz as shown in Fig. 6.6.

As shown, the RTHS test results produce a similar FRF magnitude to the full physical test; however, the second mode occurs at 3.74 Hz with 30 dB attenuation rather than 3.58 Hz with 25 dB attenuation.

Subsequently, a series of earthquake time histories are input as ground excitation to the numerical bottom floor in RTHS Realization 1 tests. Results for the 1995 Kobe, Japan, 1994 Northridge, California, and 1992 Cape Mendocino earthquakes are displayed.

As shown in Fig. 6.7, the time histories from the Kobe 1995 excitation display excellent agreement with the fully physical test performed prior, particularly for the second story, which is the physical substructure. In an RTHS test, the goal is to impart well-known dynamics to an uncertain substructure physically with the same results as a full-scale test. Therefore, the

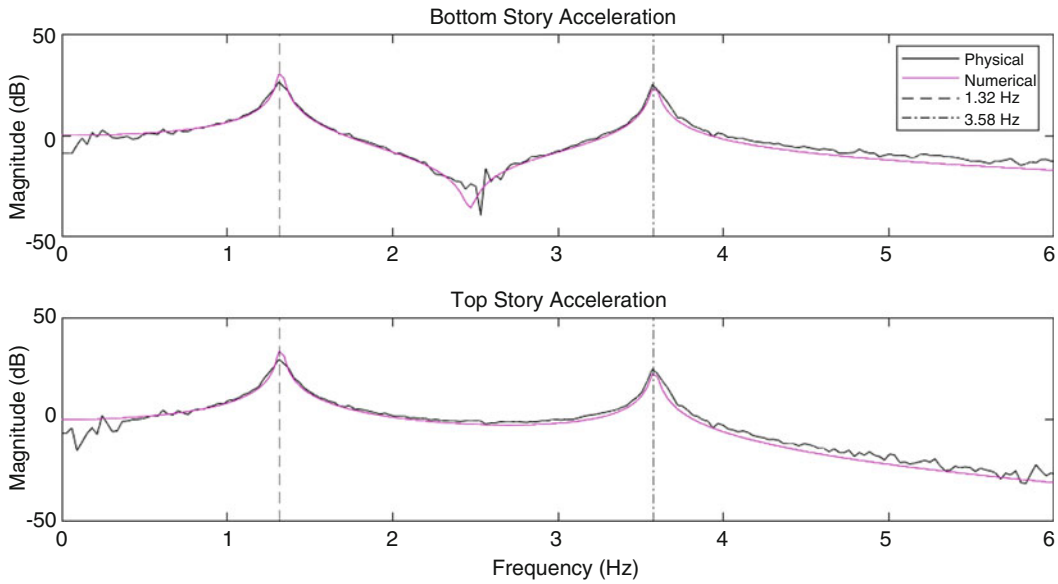

Fig. 6.5 System identification FRF magnitudes

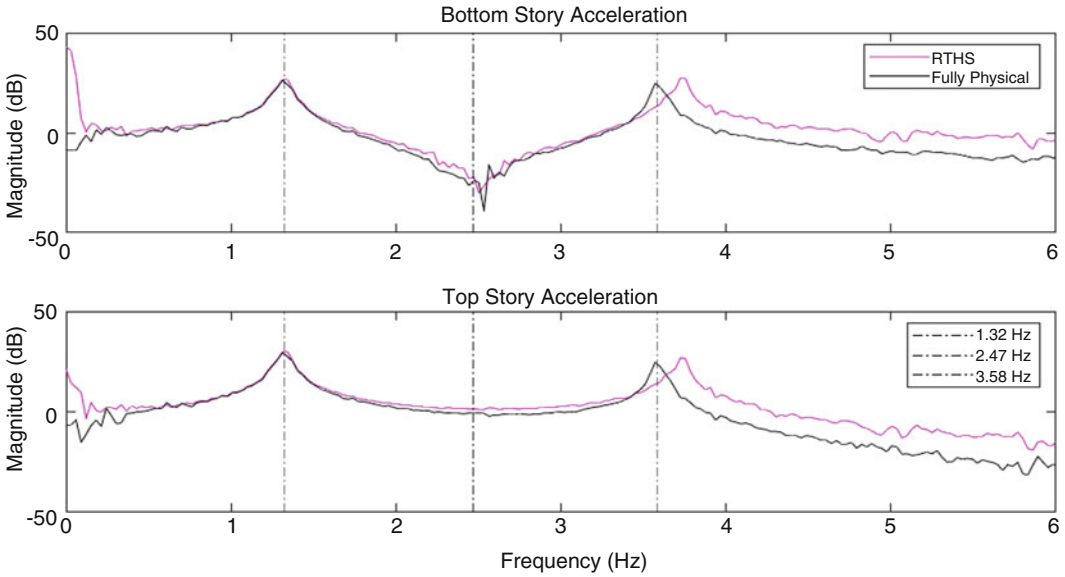

Fig. 6.6 RTHS vs. full physical FRF magnitudes

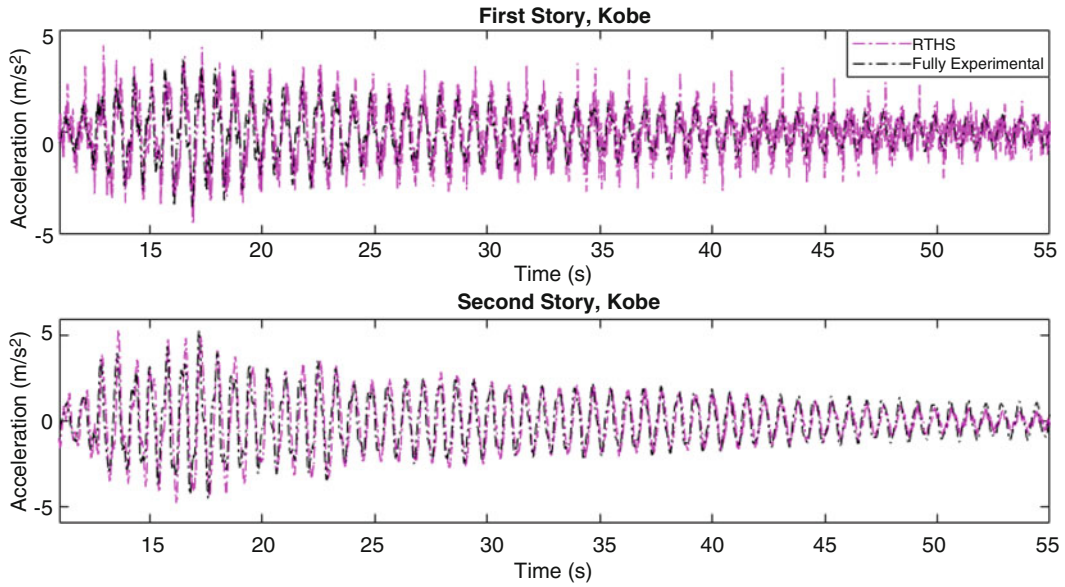

Fig. 6.7 Kobe 1995 acceleration time histories (RTHS Realization 1)

second story performance is of greater importance. Northridge and Cape Mendocino time histories exhibit better magnitude agreement for the bottom story and reduced magnitude accuracy in the second story when compared to Kobe (Fig. 6.8). All RTHS time histories are similar in nature: they underpredict first story acceleration and overpredict second story acceleration. Regardless, the frequencies and phase are in excellent agreement throughout all three tests.

Future tests will conduct RTHS Realization 2, following the procedure outlined in this chapter (Fig. 6.9).

6.5 Conclusion

This study presented the successful completion of a traditional RTHS test for a low-rise structure and proposed framework for a novel approach to investigation of the bottom floor dynamics. It has been proven that real-time hybrid substructuring provides a worthy approach to reduced-scale testing. Realization 1 has been validated by reporting closely matched FRFs

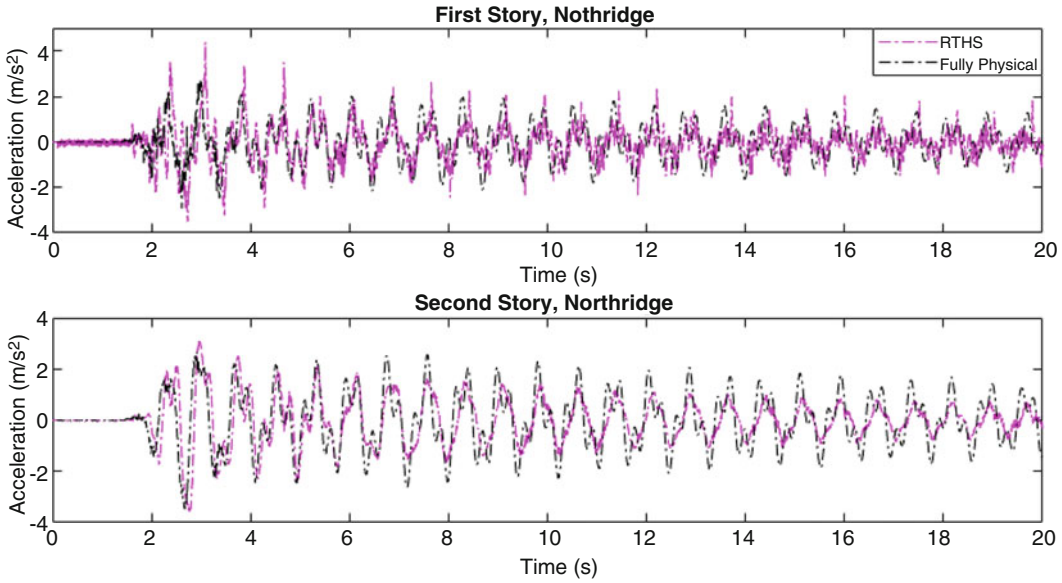

Fig. 6.8 Northridge 1995 acceleration time histories (RTHS Realization 1)

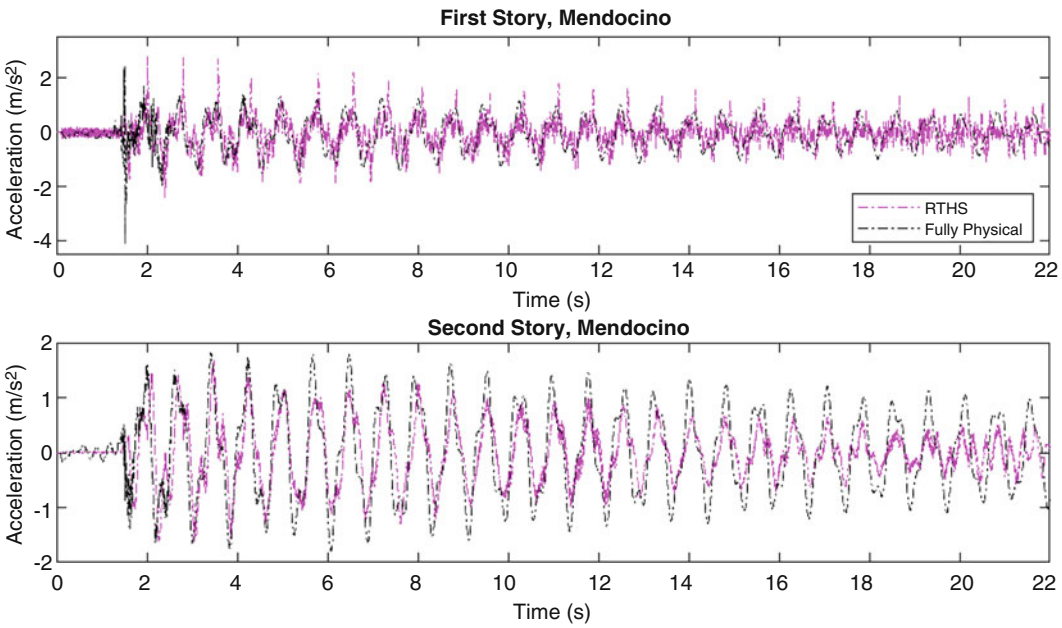

Fig. 6.9 Cape Mendocino 1992 acceleration time histories (RTHS Realization 1)

between the fully physical and RTHS tests. Furthermore, a more intuitive understanding is gained by the evidence shown in the latter portion of Sect. 6.4.2, which compares earthquake time histories between the RTHS and fully physical tests. The presence of two vibration modes in an SDOF structure further validates RTHS. The procedure for a Realization 2 setup is well defined in Sect. 6.3.3. As an extension, the numerical model for Realization 2 can be altered to represent a high-rise structure. If all interactions (story shear, seismic excitation) are transferred accurately, the method is viable. The nontraditional approach of imparting forces on the physical substructure and recording motion may be applied to a variety of complex test procedures, including wind or fluid-loaded structures.

In the Realization 1 test, the second natural frequency shown in the RTHS test attenuated more than the physical test, and it occurred at a higher value. Potentially, the system identification may have slightly overpredicted the stiffness or underpredicted mass for either structure. While both stories were the same Quanser product, one may have experienced plastic deformation due to yielding, introducing nonlinearity to the dynamics.

For future procedures conducting the Realization 2 test, it may be necessary to add a static mass to the physically tested bottom story. Justification arises through the unaccounted mass from the lower section of the top story columns that have little displacement relative to the bottom story in a fully experimental test.

Acknowledgments The authors thank the Academic Visitors Program through the Office of International Affairs and External Cooperation (OAICE) at the University of Costa Rica as well as the University of Connecticut for sponsoring travel and research, and the University of Costa Rica LanammeUCR for providing equipment and access to the lab facility to conduct the experimental testing.

References

1. Reinhorn, A., Bruneau, M., Chu, S.-Y., Shao, X., Pitman, M.: Large scale real time dynamic hybrid testing technique - shake tables substructure testing. In: The First International Conference on Advances in Experimental Structural Engineering (2005)
2. Zhao, J., French, C., Shield, C., Posberg, C.: Considerations for the development of real-time dynamic testing using servo-hydraulic actuation. Earthq. Eng. Struct. Dyn. **32**(11), 1773–1794 (2003)
3. Kyrychko, Y.N., Blyuss, K.B., Gonzalez-Buelga, A., Hogan, S.J., Wagg, D.J.: Real-time dynamic substructuring in a coupled oscillator–pendulum system. Proc. R. Soc. A. **462**, 1271 (2006)
4. Horiuchi, T., Inoue, M., Konno, T.: Development of a real-time hybrid experimental system using a shaking table (proposal of experimental concept and feasibility study with rigid secondary system). JSME Int. J. Ser. C. **42**(2), 255–264 (1999)
5. Colgate, J.E., Stanley, M.C., Brown, J.M.: Issues in the haptic display of tool use. In: Proceedings 1995 IEEE/RSJ International Conference on Intelligent Robots and Systems. Human Robot Interaction and Cooperative Robots (1995)
6. Saouma, V., Sivaselvan, M.: Hybrid Simulation: Theory, Implementation and Applications. Taylor & Francis, London (2008)
7. Insam, C., Harris, M.J., Stevens, M.R., Christenson, R.E.: Real-time hybrid substructuring for shock applications considering effective actuator control. In: IMAC-XL Sociecty for Eng. Mech. Conference, Orlando (2022)
8. Christenson, R., Lin, Y.Z., Emmons, A., Bass, B.: Large-scale experimental verification of semiactive control through real-time hybrid simulation. J. Struct. Eng. **134**(4), 522–534 (2008)
9. Inman, D.J.: Engineering Vibration. Pearson Education, Inc, Upper Saddle River (2014)
10. Dyke, S.J.: Modeling and control of magnetorheological dampers for seismic response reduction. Smart Mater. Struct. **5**, 565–575 (1996)
11. Dyke, S.J., Spencer Jr., B.F., Quast, P., Sain, M.K.: The role of control-structure interaction in protective system design. J. Eng. Mech. ASCE. **121**, 322–338 (1995)
12. Dyke, S.J., Spencer Jr., B.F., Quats, P., Kaspari Jr., D.C., Sain, M.K.: Implementation of an active mass driver using acceleration feedback control. In: Microcomputers in Civil Engineering (Special Issue on Active and Hybrid Structural Control), vol. 11, pp. 305–323 (1996)
13. Shing, P.B., Mahin, S.A.: Cumulative error effects in pseudodynamic tests. Earthq. Eng. Struct. Dyn. **15**, 409–424 (1987a)
14. Shing, P.B., Mahin, S.A.: Elimination of spurious higher-mode response in pseudodynamic tests. Earthq. Eng. Struct. Dyn. **15**(425–445), 425 (1987b)
15. Huang, L., Chen, C., Guo, T., Chen, M.: Stability analysis of real-time hybrid simulation for time-varying actuator delay using the Lyapunov-Krasovskii functional approach. J. Eng. Mech. **145**(1), 1–15 (2019)
16. Bendat, J.S., Piersol, A.G.: Random Data: Analysis and Measurement Procedures. Wiley, Hoboken (2010)
17. Franco III, J.A.: Real-time hybrid substructuring for system level vibration testing of mechanical equipment. Ph.D. Dissertation, College of Eng., Univ. of Conn., Storrs (2016). [Online]

Chapter 7
A Review of Using Transfer Path Analysis Methods to Derive Multi-axis Vibration Environments

Steven Carter

Abstract Multi-axis testing has become a popular test method because it provides a more realistic simulation of a field environment when compared to traditional vibration testing. However, field data may not be available to derive the multi-axis environment. This means that methods are needed to generate "virtual field data" that can be used in place of measured field data. Transfer path analysis (TPA) has been suggested as a method to do this since it can be used to estimate the excitation forces on a legacy system and then apply these forces to a new system to generate virtual field data. This chapter will provide a review of using TPA methods to do this. It will include a brief background on TPA, discuss the benefits of using TPA to compute virtual field data, and delve into the areas for future work that could make TPA more useful in this application.

Keywords TPA · Force reconstruction · MIMO · Vibration testing · Environments

7.1 Introduction and Motivation

Sandia National Laboratories has been investigating and using multi-axis random vibration testing for many years, developing methods and software to perform the tests [1, 2]. However, the processes for developing test specifications that are compatible with multi-axis testing are lacking. Test specifications from traditional random vibration testing cannot be used because they are generally "straight-line" enveloped spectra. These typically include smeared and amplified frequency content that encompasses all the part–part and test–test variation that may be seen in a family of source environments or parts. Additionally, the test specifications may be derived from field test hardware (such as flight test units) that have significantly different structural dynamics than the device under test (DUT). An example of this type of specification is shown in Fig. 7.1, where a straight-line spectrum is used to capture the cargo vibration exposure from a jet aircraft [3].

While these types of specifications make it easy to build in conservatism and combine data from multiple tests, they are not realizable in a multi-axis sense. This is because the multi-axis controller uses several input degrees of freedom (DOFs) to control several output DOFs. This approach contrasts with the single-input/single-output (SISO) strategy in traditional vibration testing, which presents a relatively straightforward control problem. An example of a "small" multi-axis test setup is shown in Fig. 7.2. Larger setups that use upward of 12 shakers (inputs) and 30 output DOFs have become standard at Sandia.

The key difference between SISO and multi-axis control is that a multi-axis test attempts to control the frequency, phase, and amplitude relationships of all the output DOFs, while SISO tests only control the frequency and amplitude at a single DOF. As such, the frequency, phase, and amplitude relationships between the output DOFs (the system structural dynamics)

S. Carter (✉)
Sandia National Laboratories, Albuquerque, NM, USA
e-mail: spcarter@mtu.edu

M. Allen et al. (eds.), *Dynamic Substructures, Volume 4*, Conference Proceedings of the Society for Experimental Mechanics Series, https://doi.org/10.1007/978-3-031-36694-9_7

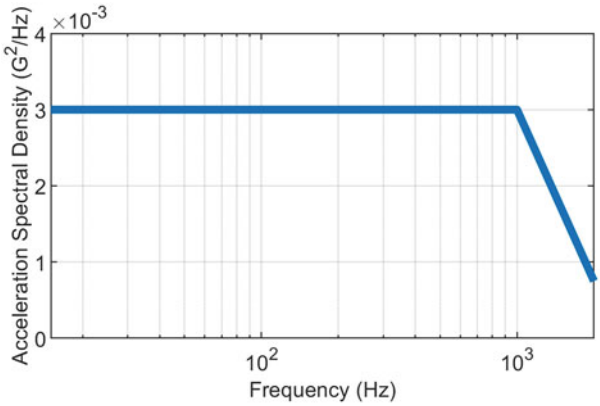

Fig. 7.1 Example enveloped spectra for jet aircraft cargo vibration exposure from MIL-STD 810H

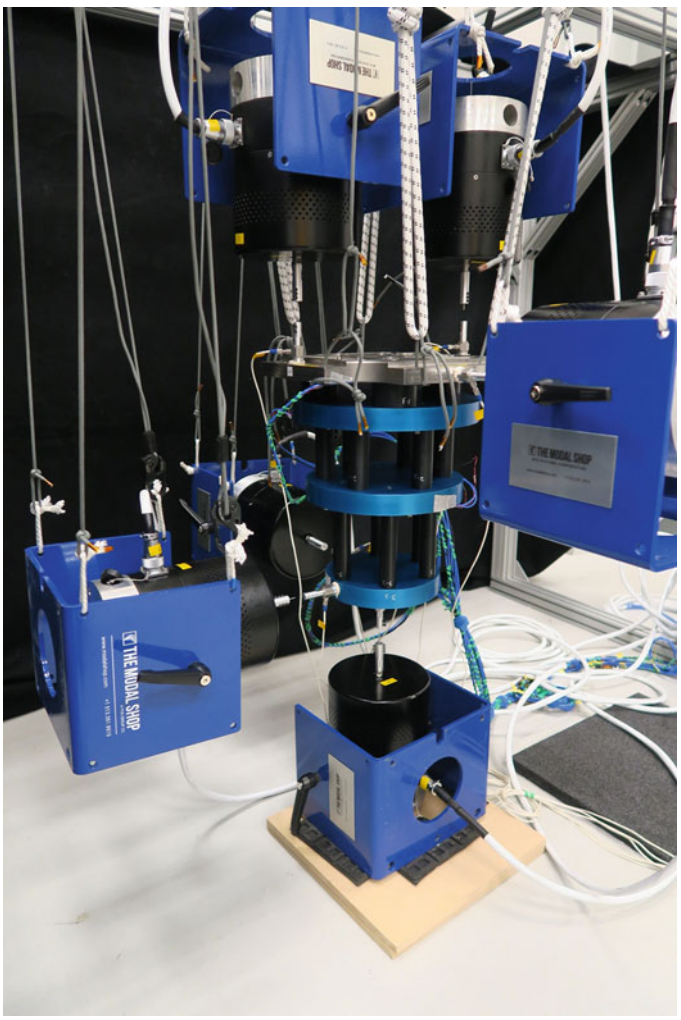

Fig. 7.2 Example multi-axis vibration test setup

should be the same for the multi-axis test specification and DUT to perform an accurate test. The reasons for this constraint can be easily understood once the multi-axis control strategy is known.

Equation 7.1 shows the basic control strategy, where $X(\omega)$ is the square cross-power spectral density (CPSD) matrix of target responses (the test specification), $H(\omega)$ is the frequency response function (FRF) matrix that describes input/output relationship between the shaker drive voltages and system responses, and $V(\omega)$ is the CPSD matrix of the shaker drive

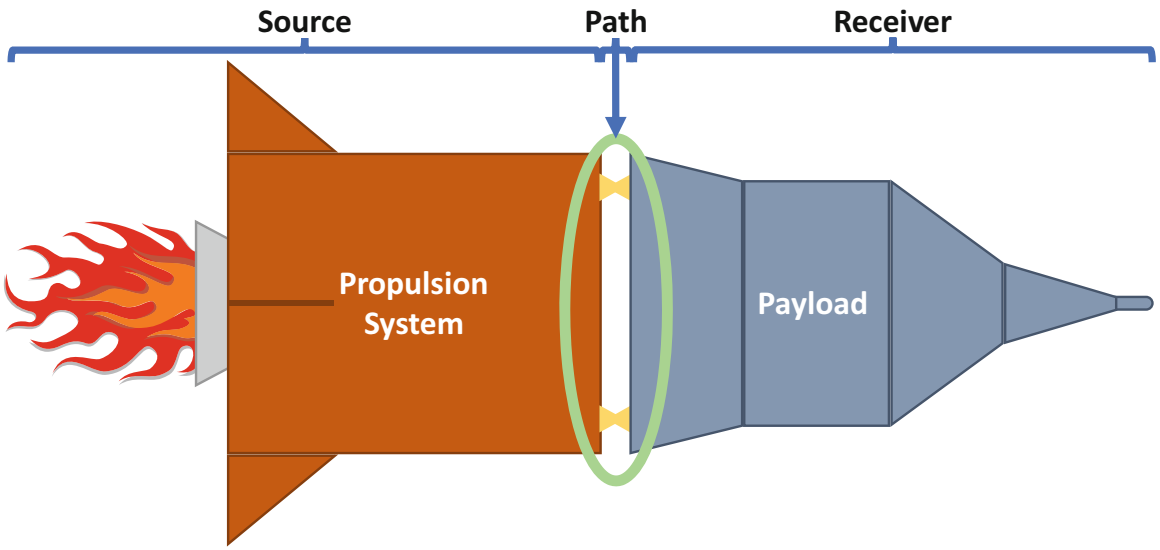

Fig. 7.3 Rocket system sketch showing the source–path–receiver descriptions

voltages. Note that the "+" indicates a pseudo-inverse and "*" indicates a conjugate transpose.

$$[V(\omega)] = [H(\omega)]^{+}[X(\omega)][H(\omega)]^{+*} \tag{7.1}$$

This equation makes it clear that there must be compatibility in the structural dynamics between $X(\omega)$ and $H(\omega)$ to find a reasonable solution for $V(\omega)$. This has typically been accomplished by computing the target CPSD matrix from field test data and applying that to the DUT. This approach does not present a complete solution though since compatibility issues may still be encountered if the field test hardware is significantly different from the DUT or if field test data is not available (e.g., when deriving environments from legacy hardware). An intuitive understanding of this problem can be gained by picturing a test specification that attempts to force operating deflection shapes to occur at frequencies that are unnatural for the DUT.

Additionally, it is obvious that the DUT must share the same nominal sensor and component configuration as the field data. Otherwise, there is currently no satisfactory technique to map field test responses to the DUT responses. Some methods have been developed to tailor test specifications to fix these compatibility issues [4, 5], and further research is underway. In the absence of a solution to fix these issues, it is easy to picture situations where the test specification is inappropriate for the DUT, resulting in a test that is difficult to control and/or does not represent the true field environment.

This introductory information suggests that it would be a clear advantage to have field data for the exact DUT when deriving multi-axis test specifications. However, the cost and time to perform a field test make it infeasible in many cases. As such, methods need to be developed to generate "virtual field data" through simulations. This chapter presents transfer path analysis (TPA) as a potential simulation method for this. It will provide a brief background on TPA, discuss the benefits and drawbacks, and discuss areas for future work. Note that this chapter represents an initial effort into using TPA this way, and several improvements are still needed to mature and build trust in the method. Nevertheless, it is felt that this chapter provides a unique perspective on the use of TPA and hopes to inspire further research.

7.2 Transfer Path Analysis Theoretical Background

This section will provide a brief background on TPA, but it is suggested that the reader refer to [6] for a more complete description of the method. The first step toward understanding TPA is to grasp the source–path–receiver model of mechanical systems. Figure 7.3 shows a sketch of a rocket system with clear boundaries for the source, path, and receiver. In this case, the propulsion system is the source, the payload is the receiver, and the attachment points between the propulsion system and payload are the paths.

The source–path–receiver system can also be described mathematically, as shown in Eq. 7.2 for linear units or Eq. 7.3 for power units. In this case, $X(\omega)$ is the payload response or receiver, $H(\omega)$ are the system FRFs (typically between the

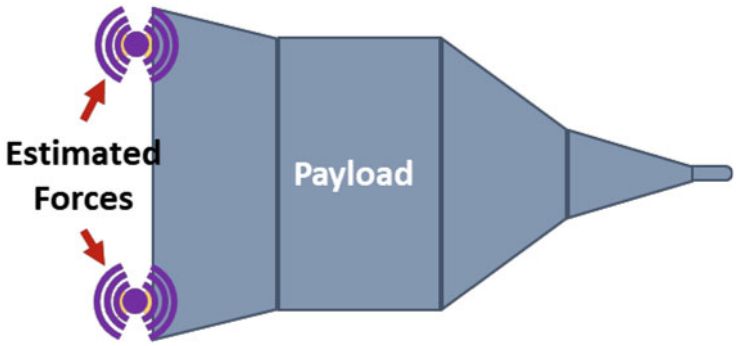

Fig. 7.4 Rocket system representation for classical TPA

source/receiver attachment points and the measurement locations on the receiver) or paths, and $F(\omega)$ are the forces acting upon the receiver or source:

$$\{X(\omega)\} = [H(\omega)]\{F(\omega)\} \tag{7.2}$$

$$[X(\omega)] = [H(\omega)][F(\omega)][H(\omega)]^{*} \tag{7.3}$$

The forces acting upon the receiver system can then be estimated via FRF matrix inversion, as shown in Eq. 7.4 for linear units or Eq. 7.5 for power units. Like Eq. 7.1, the "+" indicates a pseudo-inverse and "*" indicates a conjugate transpose. Note that this chapter will only focus on the matrix inversion method for determining the forces.

$$\{F(\omega)\} = [H(\omega)]^{+}\{F(\omega)\} \tag{7.4}$$

$$[F(\omega)] = [H(\omega)]^{+}[X(\omega)][H(\omega)]^{+*} \tag{7.5}$$

The TPA methods can be broken down into two fundamental techniques once the source–path–receiver concept is understood. These techniques are typically referred to as classical or component-based TPA [6]. Both techniques use the same fundamental math and response measurements to estimate the forces, but with different FRFs representing the paths. Classical TPA uses a representation of the system that relies on the receiver system only (i.e., the FRFs are derived from the receiver system decoupled from the source system); a sketch of this representation is shown in Fig. 7.4.

The estimated forces from classical TPA are representative of the actual loads experienced in the joint during the field test. In essence, the forces are analogous to load cells between the source and receiver system during the field test. While interesting from a diagnostic perspective, these forces are dependent on the structural dynamics of both the source and receiver systems. As such, they will change as the structural dynamics change in the receiver system. This means that the response prediction on a new receiver may be inaccurate, depending on the differences in the structural dynamics between the new and original systems.

Component-based TPA uses the coupled source–receiver representation of the system (i.e., the FRFs are derived from the coupled source–receiver system), a sketch of this representation is shown in Fig. 7.5. In this case, the estimated forces represent "equivalent sources" that cancel out the effects of the true source on the receiver system. It can be shown that these forces are a property of the true source and the FRFs between the true source and equivalent source [6]. As such, these forces can be applied to any version of the coupled source–receiver system if the source system remains the same. It is important to note that the bounding boxes that define the source and receiver systems can be somewhat arbitrary. However, practicality will generally dictate the boundary, based on what makes sense or is easy to keep the same between versions of the coupled source–receiver system.

The underlying theory means that the predicted response from the equivalent sources is theoretically the same as the true field environment. It is also important to note that the equivalent sources can be estimated anywhere on the source system and are not limited to the source/receiver interface points. Additionally, it should be noted that the equivalent sources cannot be used to predict responses on the source system. Again, the reader is referred to [6] for a derivation of the equivalent source

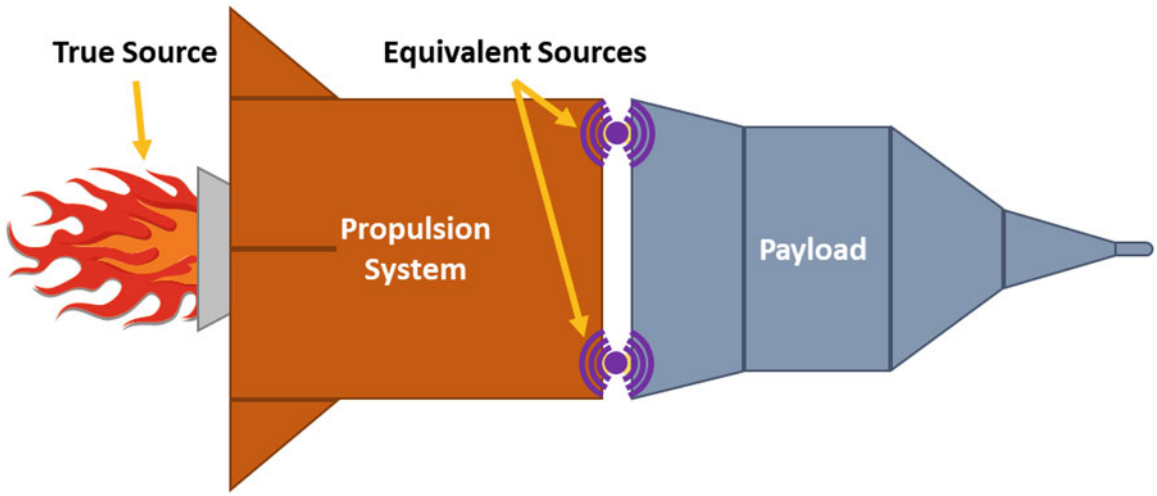

Fig. 7.5 Rocket system representation for component-based TPA

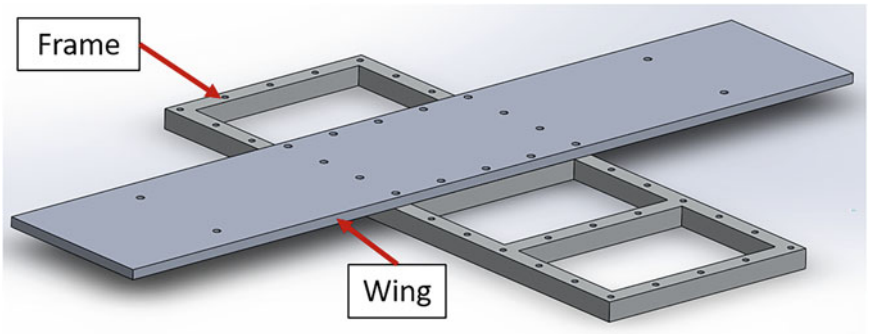

Fig. 7.6 Computer-aided design model of the round-robin system

concept that has a more detailed discussion of the assumptions and requirements. Lastly, the reader should be aware that the equivalent sources are referred to by many names, such as blocked forces, interface forces, or pseudo forces, depending on where the forces are on the source system, how they were estimated, author preferences, etc.

Both versions of TPA present value for deriving virtual field data, but component-based TPA clearly provides the most value since it results in a true estimate of the field environment. This assertion will be discussed more in the following sections.

7.3 Example of a Basic System

The TPA process to generate virtual field data will be demonstrated on finite element (FE) models of the round-robin system from the Society for Experimental Mechanics (SEM) Dynamic Substructures Technical Division, as described in [7, 8]. This system is shown in Fig. 7.6 and is composed of a frame and wing. There are "thick" wing and "thin" wing versions of the system, which provides an original (thick wing) system to estimate the forces on and a new (thin wing) system for predicting virtual field data.

The FE model was generated with Sandia's in-house finite element analysis software, Sierra/SD, and the FRFs were generated from the computed modes with a damping ratio of 0.5%. Bolted joints between the frame and wing were simulated with JOINT2G elements that were rigidly connected to the bolt holes on the frame and wing at the interface points that are highlighted in Fig. 7.7. Note that the JOINT2G elements are analogous to a Nastran CBUSH element. Additionally, the JOINT2G spring properties were chosen to represent a typical bolted connection. More information on the models can be found in [9].

The workflow for evaluating the different TPA techniques was as follows:

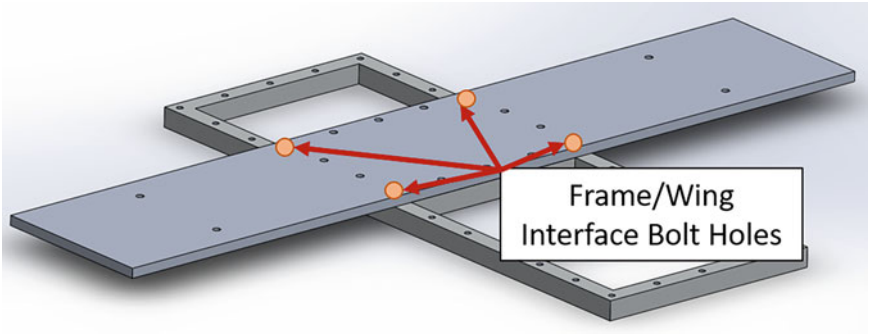

Fig. 7.7 Frame/wing interface points on the round-robin system

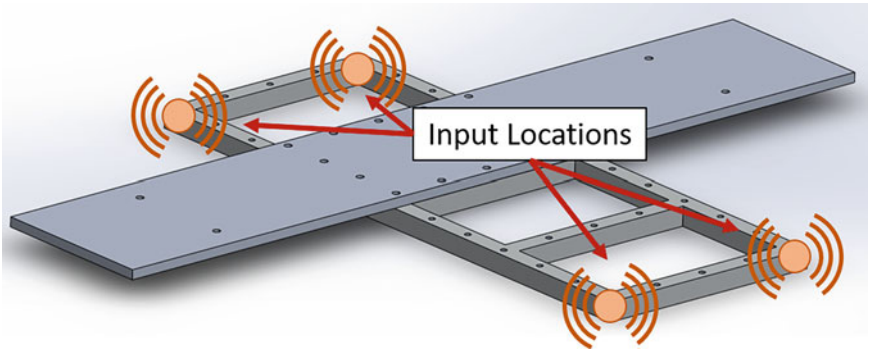

Fig. 7.8 Input locations for the virtual flight test

1. Triaxial broadband excitation was applied to the corners of the frame, as shown in Fig. 7.8, to generate truth data for both versions of the system. This was done using model-derived FRFs (from the mode shapes) at 24 triaxial response locations (72 response DOFs) that were evenly distributed over the wing using engineering judgment. Note that the number of response DOFs was chosen to have a reasonable overdetermination ratio between the responses and reference DOFs.
2. The (triaxial) forces were then estimated for the thick wing (original) system at the interface locations, as shown in Fig. 7.7. The FRFs were derived from the coupled frame/wing system for the component-based TPA technique (with the frame side interface node as the reference). The FRFs were derived from the wing-only model (at the wing side interface node) for the classical TPA technique.
3. The "virtual field data" was then generated for the thin-wing (new) system using the FRFs derived from the appropriate models (frame/wing or wing alone) for the different force estimates.

Figures 7.9, 7.10, 7.11, and 7.12 show the autopower spectral densities (APSDs) that were found from the process described above. Figures 7.9 and 7.10 show the results for the component-based and classical TPA on the thick wing (original) system (this response reconstruction is typically done as a check on the force estimation process). Figures 7.11 and 7.12 show the results for the component-based and classical TPA on the thin-wing (new) system. All the plots show the maximum enveloped spectrum, minimum enveloped spectrum, and averaged spectrum for all the response DOFs to summarize all the APSDs.

All the results are as expected. Both classical and component-based TPA appear to be accurate on the thick wing (original) system (the one that was used to estimate the forces) based on the accuracy of the virtual field data compared to the truth data. This agreement provides a minor validation of the force estimates and is primarily a check on the least-square solution for the forces (i.e., checking that the math worked as intended, *not* checking the validity of the forces). The response prediction from component-based TPA is extremely accurate for the thin-wing (new) system (which the environment is being "translated" to). However, there are significant errors in the classical TPA response predictions, as expected. In general, the classical TPA response prediction appears to overestimate the thin-wing response. This overprediction is likely due to the thin wing being lighter and more flexible than the thick wing and is not representative of a general trend in classical TPA.

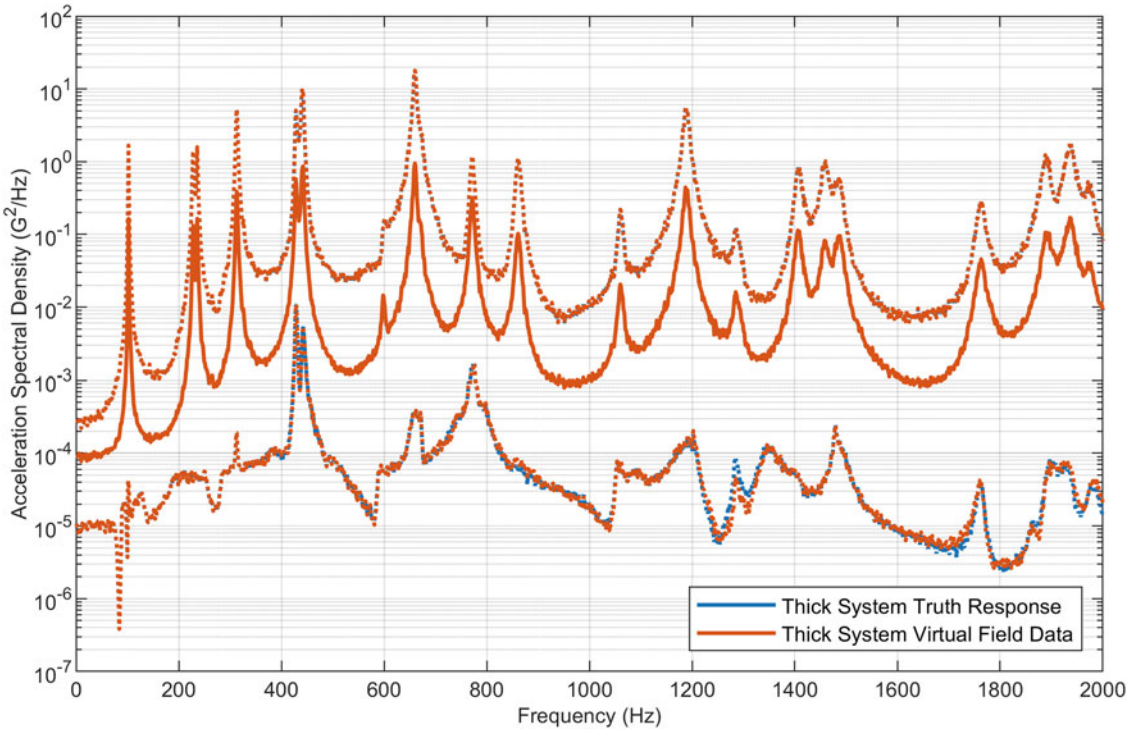

Fig. 7.9 Comparison between the truth and virtual field data for the thick wing (original) system using component-based TPA; the dashed lines represent the maximum and minimum enveloped APSD response, and the solid line represents the averaged APSD response

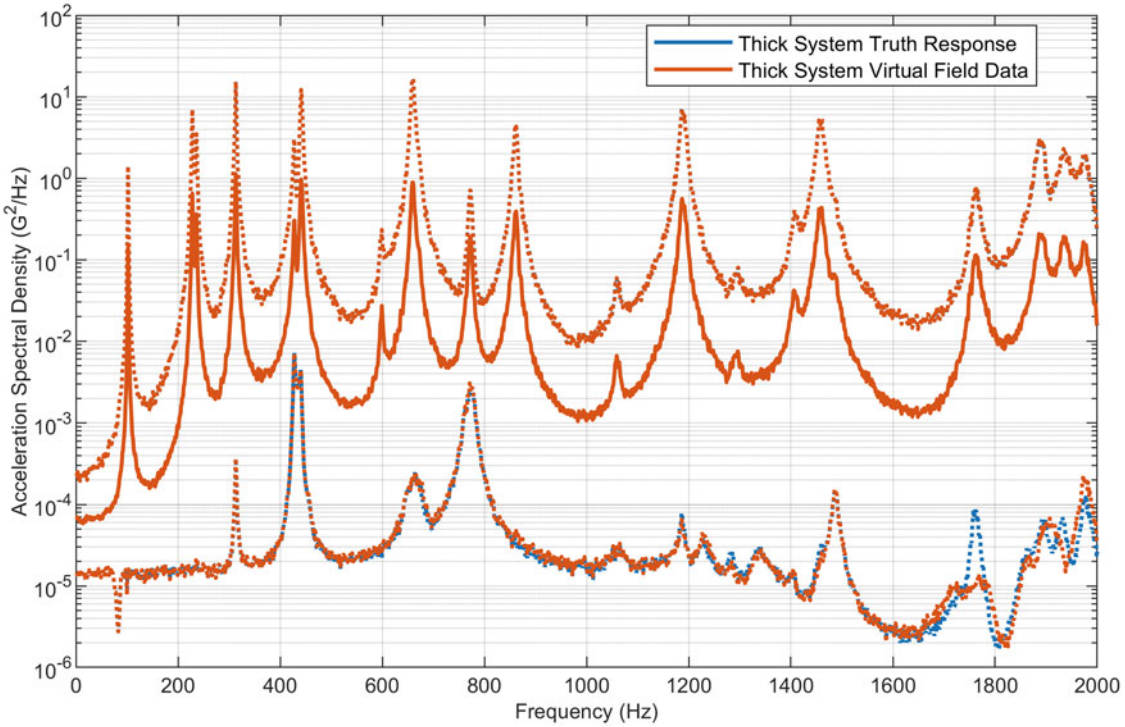

Fig. 7.10 Comparison between the truth and virtual field data for the thick wing (original) system using classical TPA; the dashed lines represent the maximum and minimum enveloped APSD response, and the solid line represents the averaged APSD response

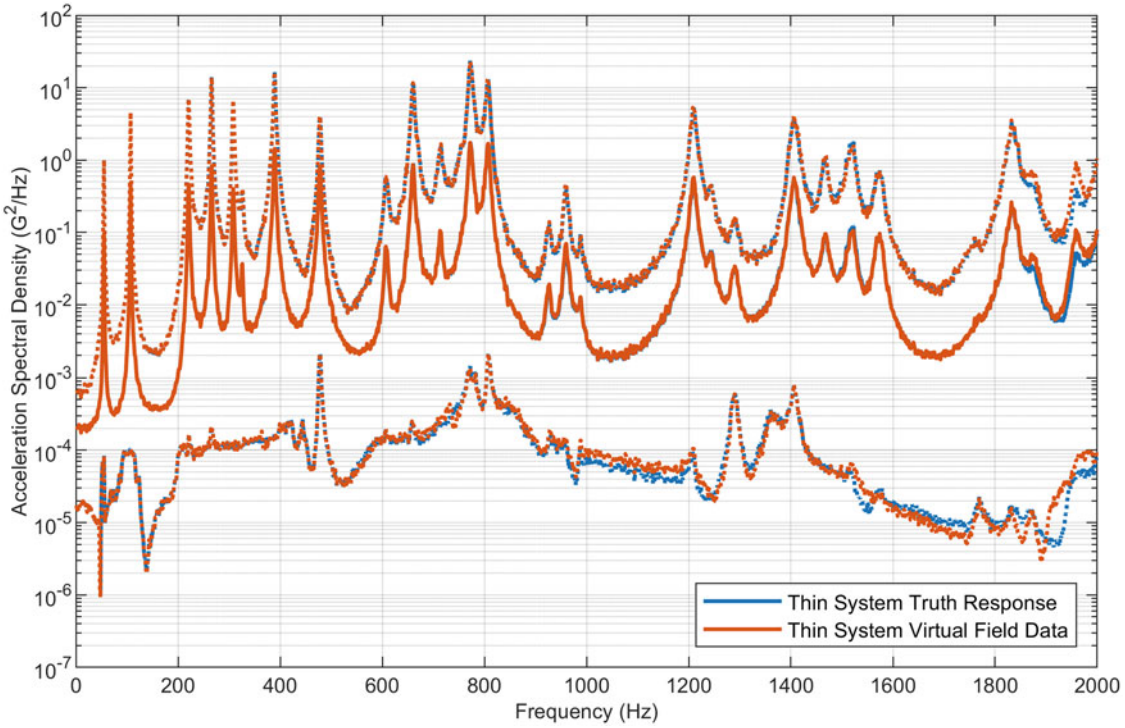

Fig. 7.11 Comparison between the truth and virtual field data for the thin-wing (new) system using component-based TPA; the dashed lines represent the maximum and minimum enveloped APSD response, and the solid line represents the averaged APSD response

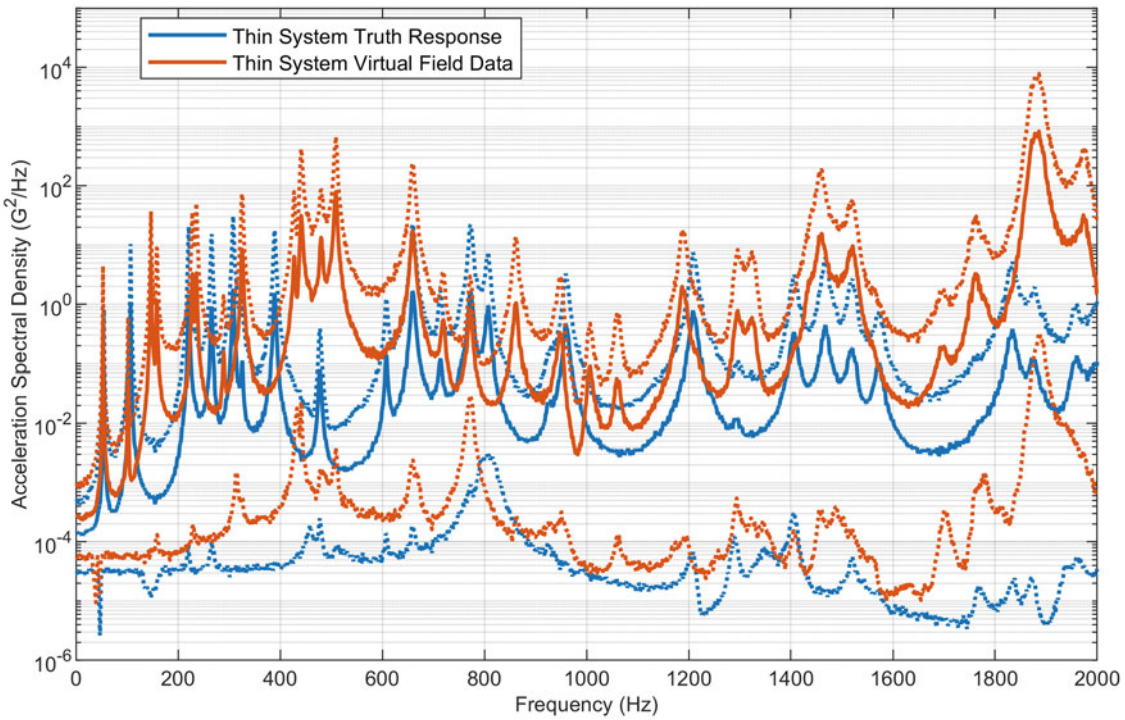

Fig. 7.12 Comparison between the truth and virtual field data for the thin-wing (new) system using classical TPA; the dashed line represents the maximum and minimum enveloped APSD response, and the solid lines represent the averaged APSD response

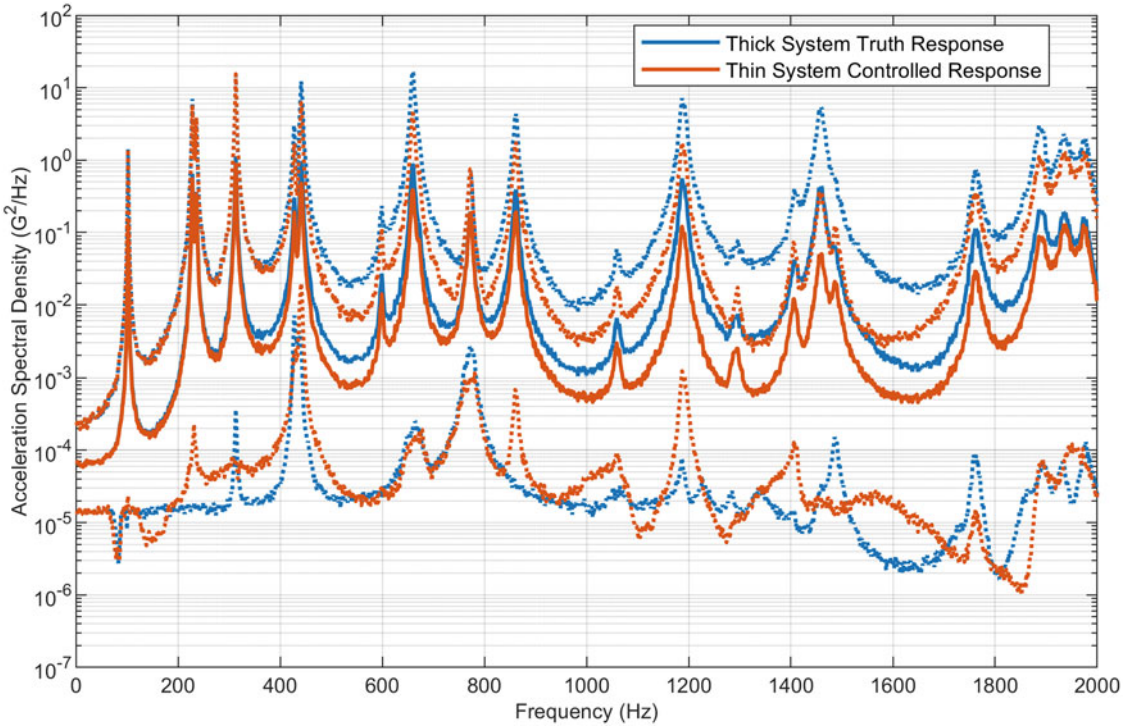

Fig. 7.13 Example of an attempt to control a multi-axis test on the thin system using the thick system CPSD as a test specification; the dashed line represents the maximum and minimum enveloped APSD response, and the solid line represents the averaged APSD response

7.4 Discussion

As expected, the above results clearly show that component-based TPA is the preferred solution for translating vibration environments from one system to another. This preference is because it provides a highly accurate prediction of the vibration response on the new system, assuming that the appropriate data is available to derive the necessary FRFs. Unfortunately, models of the source system (either FRFs, mode shapes, or FE models) may not be available, making component-based TPA impossible. Classical TPA provides an alternative in this case since it only requires a model of the receiver system.

However, there is a clear trade-off in accuracy since classical TPA shows significant errors when compared to the truth data. While this inaccuracy causes obvious problems for specification derivation, it is important to keep in mind that the alternative may be the direct application of the thick wing (original) system data to the thin-wing (new) system. In this case, the classical TPA response predictions may provide a better specification since it will generally be more realizable than the original system response. This advantage is because the classical TPA response prediction will "build in" the structural dynamics of the new system rather than trying to enforce the structural dynamics of the original system on the new system (as described above).

This outcome is clearly seen in the results of a synthesized thin-wing multi-axis test, as shown in the figures below (note that this is a "test" of the thin wing by itself). Figure 7.13 shows the "test" APSD results when the thick wing (original coupled frame/wing) system CPSD is used as a test specification. Figure 7.14 shows the test PSD results when the thin-wing (new wing) classical TPA-based CPSD is being used as a test specification. Figure 7.15 shows the test APSD results when the thin-wing (new coupled frame/wing) system truth CPSD is used as a test specification (to show that control is possible when the true response is used). Note that the multi-axis control strategy is finding forces rather than voltages in this case, but that it is still using Eq. 7.1 to estimate the sources.

Additionally, both TPA techniques can predict responses at locations that may exist in the new system but did not exist in the original system. This capability can also be used to provide a richer set of response targets for the specification, which may improve the accuracy of the inverse source estimation in the multi-axis control strategy.

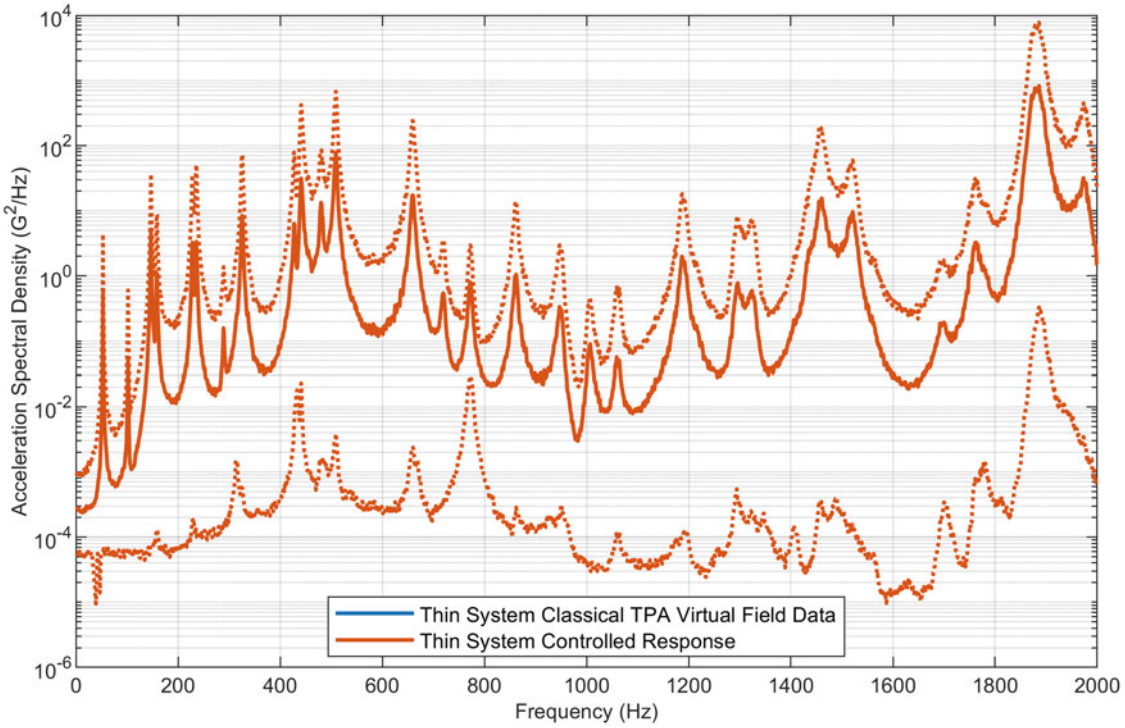

Fig. 7.14 Example of an attempt to control a multi-axis test on the thin system using the classical TPA-based response (CPSD) estimation as a test specification; the dashed line represents the maximum and minimum enveloped APSD response, and the solid line represents the averaged APSD response

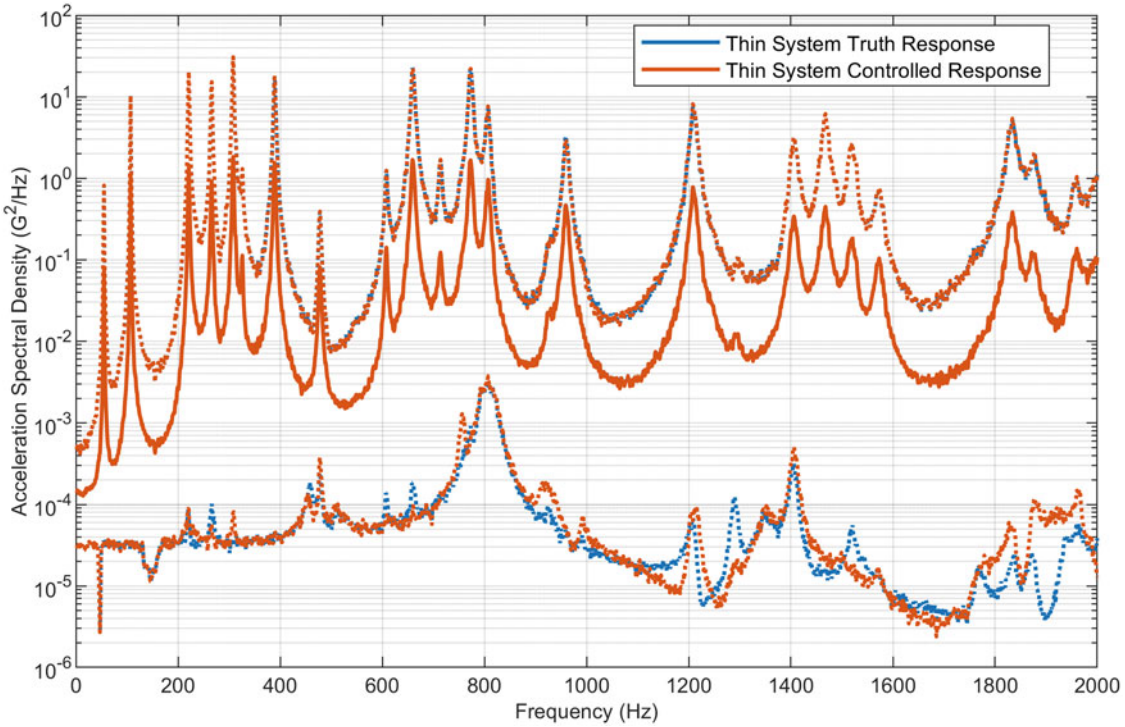

Fig. 7.15 Example of an attempt to control a multi-axis test on the thin system using the thin system truth CPSD as a test specification; the dashed line represents the maximum and minimum enveloped APSD response, and the solid line represents the averaged response

7.5 Areas for Future Work

TPA shows significant promise for generating virtual field data for developing multi-axis test specifications, but there are several areas for future work to build trust in the method. One major area of future work should be developing methods for choosing appropriate FRFs for the inverse force estimation. Satisfactory methods have been developed for the determination of the response DOFs [10], but choosing appropriate reference (or pseudo-force) DOFs seems to be an open area of research.

The importance of choosing appropriate references has been highlighted in recent work [9]. It was shown that having inappropriate references in the FRF matrix could lead to an overfit solution. This causes significant errors in the response predictions when translating the environments to a new system (with component-based TPA). Some methods have been suggested to guide the choice of FRFs and validate the estimates [11], although these methods focused on improving the numerical conditioning of the FRF matrix. Other works have suggested using Bayesian inference regression methods to estimate the forces [12, 13]. These methods can be used to simultaneously perform source selection and regularization to enhance the predictive capability of the forces and reduce the possibility of an overfit.

It is also clear that uncertainty quantification (UQ) methods should be used to provide error bounds on the response predictions so an appropriate specification can be derived from the virtual field data. This is an open area of research with significant previous work to use or build on. Some methods evaluate the uncertainty due to the FRF matrix inversion and measurement noise [14, 15]. Other methods can be used to evaluate the uncertainty when using FE models to estimate the forces or generate the FRFs. The Monte Carlo method, where repeated versions of models with randomly changing variables are used, is a straightforward approach to this problem. Perturbations of the mode frequency and damping could be a simple way to use Monte Carlo. Random matrix theory has also been proposed as a method to develop perturbed versions of the system matrices [16, 17]. Additional UQ methods would need to be factored in to quantify the error in the response prediction if classical TPA is being used.

7.6 Conclusions

TPA is being proposed as a method to generate virtual field data for deriving multi-axis vibration test specifications. Early work has shown promising results for both classical and component-based TPA. Component-based TPA is an obvious solution to this problem since the response predictions on new systems theoretically match the actual field environment. The drawback of component-based TPA is that it requires a model of the source system (either FRFs, mode shapes, or an FE model), which are not always available. Classical TPA may provide a useful alternative in these cases because it can be used to map a source environment to the structural dynamics and response DOFs on the DUT. This approach may be beneficial relative to the alternative, which is typically direct application of the original system data to the new system.

Regardless of the promise that TPA shows, future work is required to build trust in the method. The main areas (in the author's opinion) are developing better methods for choosing appropriate FRFs for the inverse force estimation and building UQ into the response predictions. There are several prior works that address these areas, giving cause for optimism on the future use of TPA to develop multi-axis vibration test specifications.

References

1. Mayes, R.P., Rohe, D.P.: Physical vibration simulation of an acoustic environment with six shakers on an industrial structure. In: Shock & Vibration, Aircraft/Aerospace, Energy Harvesting, Acoustics & Optics Conference Proceeding of the Society for Experimental Mechanics Series, vol. 9, pp. 29–41. Springer, Cham (2016)
2. Rohe, D.P., Schultz, R.: Rattlesnake: an open-source multi-axis and combined evironments vibration controller. In: Proceedings of IMAC-XL, the 40th International Modal Analysis Conference, Orlando (2022)
3. MIL-STD 810H: Military Standard, Environmental Test Methods and Engineering Guidelines. United States Department of Defense (2019)
4. Schultz, R., Nelson, G.D.: Techniques for modifying MIMO random vibration specifications. In: Proceedings of IMAC-XL, the 40th International Modal Analysis Conference, Orlando (2022)
5. Daborn, P.M.: Smarter Dynamic Testing of Critical Structures. University of Bristol (2014)
6. van der Seijs, M.V., de Klerk, D., Rixen, D.J.: General framework for transfer path analysis: history, theory, and classification of techniques. Mech. Syst. Signal Process. **68–69**, 217–244 (2016)
7. Roettgen, D., Lopp, G., Jaramillo, A., Moldenhauer, B.: Experimental substructuring of the dynamic substructures round Robin testbed. In: Proceedings of IMAC-XL, the 40th International Modal Analysis Conference, Orlando (2022)

8. Linderholt, A., Roettgen, D.: Substructuring on combinations of steel and aluminum components of the benchmark structure of the technical division on dynamic substructures. In: Proceedings of IMAC-XL, the 40th International Modal Analysis Conference, Orlando (2022)
9. Carter, S.P., Owens, B.C.: Errors using six degree of freedom force estimates to translate environments system-to-system. In: ISMA 2022, Leuven (2022)
10. Beale, C., Schultz, R., Smith, C., Walsh, T.: Degree of freedom selection approaches for MIMO vibration test design. In: Proceedings of IMAC-XL, the 40th International Modal Analysis Conference, Orlando (2022)
11. Wernsen, M.W.F., Maarten, v.d.S.V., de Klerk, D.: An indicator sensor criterion for in-situ characterisation of source vibrations. In: Proceeding of IMAC-XXXV (2017)
12. Aucejo, M., De Smet, O.: Bayesian source Identificatyion using local priors. Mech. Syst. Signal Process. **66–67**, 120–136 (2016)
13. Aucejo, M., De Smet, O.: On a full Bayesian inference for force reconstruction problems. Mech. Syst. Signal Process. **104**, 36–59 (2018)
14. Voormeeren, S., de Klerk, D., Rixen, D.J.: Uncertainty quantification in experimental frequency based substructuring. Mech. Syst. Signal Process. **24**(1), 106–118 (2010)
15. Meggit, J.W., Moorhouse, A.T., Elliott, A.S.: A covariance based framework for the propagation of uncertainty through inverse problems with an application to force identification. Mech. Syst. Signal Process. **124**, 275–297 (2019)
16. Acri, A., Nijman, E., Acri, A., Offner, G.: Influences of system uncertainties on the numerical transfer path analysis of engine systems. Mech. Syst. Signal Process. **95**, 106–121 (2017)
17. Kammer, D.C., Blelloch, P., Sills, J.: Variational coupled loads analysis using the hybrid parametric variation method. In: Model Validation and Uncertainty Quantification Conference Proceeding of the Society for Experimental Mechanics, vol. 3. Springer, Cham (2020)

Chapter 8
How Virtual Points, Component TPA, and Frequency-Based Substructuring Disrupted the Vehicle Suspension Development Process

Ron Reichart, Munhwan Cho, David P. Song, and Steven W. B. Klaassen

Abstract The high competition in the automotive industry has led to ever-shorter development cycles and the introduction of modular vehicle designs. To succeed in this environment, engineers need to be able to make quantitative design suggestions as early as possible. For NVH engineers, this means, for example, making an optimal choice for the suspension bushings to compromise between driving dynamics, ride comfort, noise, and durability. This is a task wherein decisions involve many stakeholders, design parameters, and targets, and these need to be made before the first physical prototype exists. Thus, early-phase insights are crucial.

In this chapter, we show how NVH engineers conquer these challenges by applying state-of-the-art methods from structural dynamics: first, the source excitation and noise propagation are separated using component TPA. Then, a model of the car suspension, including all the bushing degrees of freedom, is measured using the virtual points. The bushing stiffnesses are virtually modified using a frequency-based substructuring method called stiffness injection (SI). The bushing parameters are optimized using the genetic algorithm. Our results show how the combination of these technologies allows us to efficiently produce optimal design choices considering various driving conditions, target quantities, and design constraints. It furthermore shows how modern software design easily allows this to become an integral part of the standard vehicle development process.

Keywords NVH · Blocked force TPA · Frequency-based substructuring · Stiffness injection · Virtual points

8.1 Introduction

The daily challenges of a noise vibration harshness (NVH) engineer have changed drastically over the last decades. Not just is the shift to electric vehicles causing a complete makeover of the design and sound of the cars, but also is the high competition within the field forcing the manufacturers to decrease the development cycles. The engineers at OEMs thus must understand and integrate new components into the nowadays modular vehicle designs with less time for testing. Especially, in the field of vehicle NVH, where the complexity of the systems makes it impossible to solely rely on simulation data, the analysis of experimental data is still of high importance. Many problems cannot be anticipated in the early design stages but need to be discovered, understood, and solved quickly once the first prototype arrives. The best engineers in the field manage to do so thanks to their great feeling for the cars, and their experience. Once they emerge after many hours on the probing grounds and test labs, the development process is very close to the final design freeze. Hence, they need to think of good arguments for the expensive late-stage changes that they need to solve the problem at hand.

Besides this dilemma, NVH engineers are usually not the only ones who would like to make some alterations to the vehicle design. There are a couple of stakeholders from different departments involved in the development process. In the case of the suspension design, the system integration engineers need to consider driving dynamics, robustness, ride comfort, and tire noise (Fig. 8.1). It is obvious how late-stage trial-and-error is not the most cost- and resource-efficient strategy to

R. Reichart (✉) · S. W. B. Klaassen
VIBES.technology, Delft, The Netherlands
e-mail: rreichart@vibestechnology.com

M. Cho · D. P. Song
Hyundai Motor Company – NVH Research Lab, Hwaseong-si, Gyeonggi-do, South Korea

M. Allen et al. (eds.), *Dynamic Substructures, Volume 4*, Conference Proceedings of the Society for Experimental Mechanics Series, https://doi.org/10.1007/978-3-031-36694-9_8

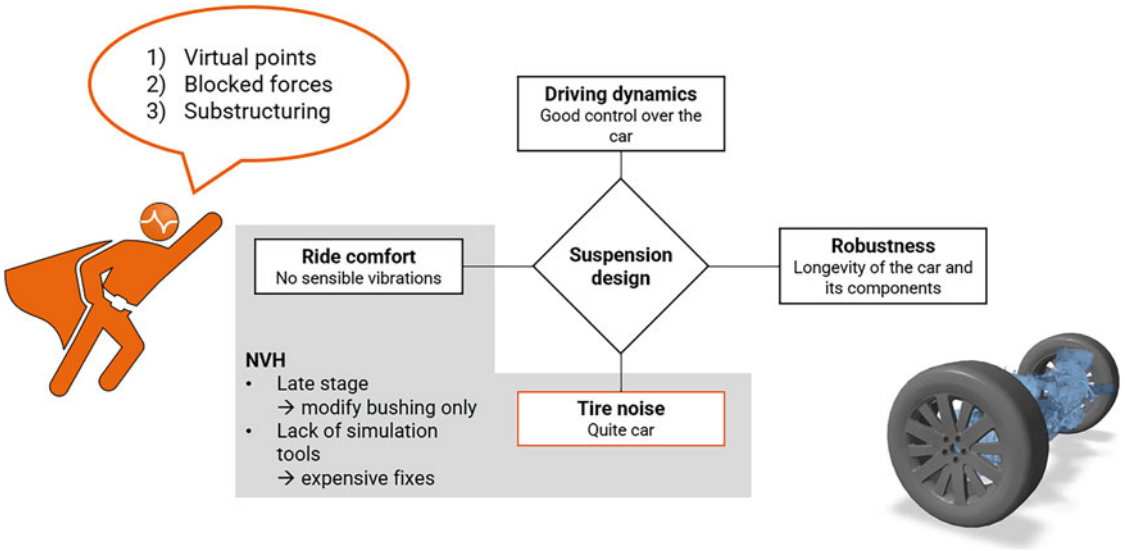

Fig. 8.1 The different stakeholders and the role of NVH in the suspension design process

solve the challenges in the development of complex systems like the suspension of a modern vehicle. Therefore, research departments in the automotive industry have been working hard to come up with technologies that allow NVH engineers to identify and solve design problems at an early stage in the development process.

Over the past years, in our collaboration with HMC, we have identified key technologies and established procedures that allow NVH engineers to solve tire noise challenges using virtual points, component-based blocked force TPA, and frequency-based substructuring [1–3]. In this chapter, we present the workflow that combines these technologies in an optimization of the tire noise while respecting the boundary conditions of other stakeholders. The following sections describe the workflow and the technologies used within.

8.2 Approach

Road noise can be very unpleasant and tiring for the driver and passengers if not considered in the vehicle design process. It contains low booming noise (50–200 Hz), the cavity noise (200–250 Hz), and the rumble (200–500 Hz). Any of these components can become troublesome for certain driving conditions (e.g., specific road conditions and driving speeds). The goal of NVH engineers is thus to identify the weaknesses of the suspension design for all relevant scenarios and tune the system parameters to remedy them. As the final cabin noise is a result of the complex vehicle design, it is important to cascade the targets from full vehicle level (cabin noise) to the different systems (suspension and car body) and to the parts that it is composed of (e.g., subframe, suspension arms, bushings, tire). Like this, problems can be attributed and tackled effectively by the development groups at OEMs or suppliers in the modular vehicle development process.

Our workflow was designed to fit the needs of this modular vehicle development process (see Fig. 8.2). It optimizes targets on system or vehicle level, uses inputs on part level, and creates optimized targets on part level. All of these can be adapted to the available data of the different design stages and the constraints and modifications by other stakeholders throughout the whole development cycle. Models could first use simple numerical data combined with benchmark vehicle data and later be replaced by test-based models of prototypes. Tire excitation data can be updated once suppliers release new versions. The ranges of the bushing stiffnesses can be updated to the target ranges set by other groups. And cost functions can be designed in a wholistic approach to balance the interests of all stakeholders. These flexibilities make it perfectly suitable for the high-speed development process in the automotive industry.

The first step is the system modeling based on the principles of substructuring. The suspension system is divided into substructures that are described through their dynamics at the interface points using virtual points. The second step is the measurement of the test-based VP-FRF model. This is the initial configuration of the system. Next is the source characterization of the tire/road excitation with blocked forces. These will provide the equivalent input excitation for the simulation of the system responses. Then the system modifications using the stiffness injection at the various bushing degrees of freedom are defined. And the genetic algorithm is used to compute the bushing configuration that optimizes the tire noise for the given suspension. All these steps are explained and discussed in more detail in the following sections.

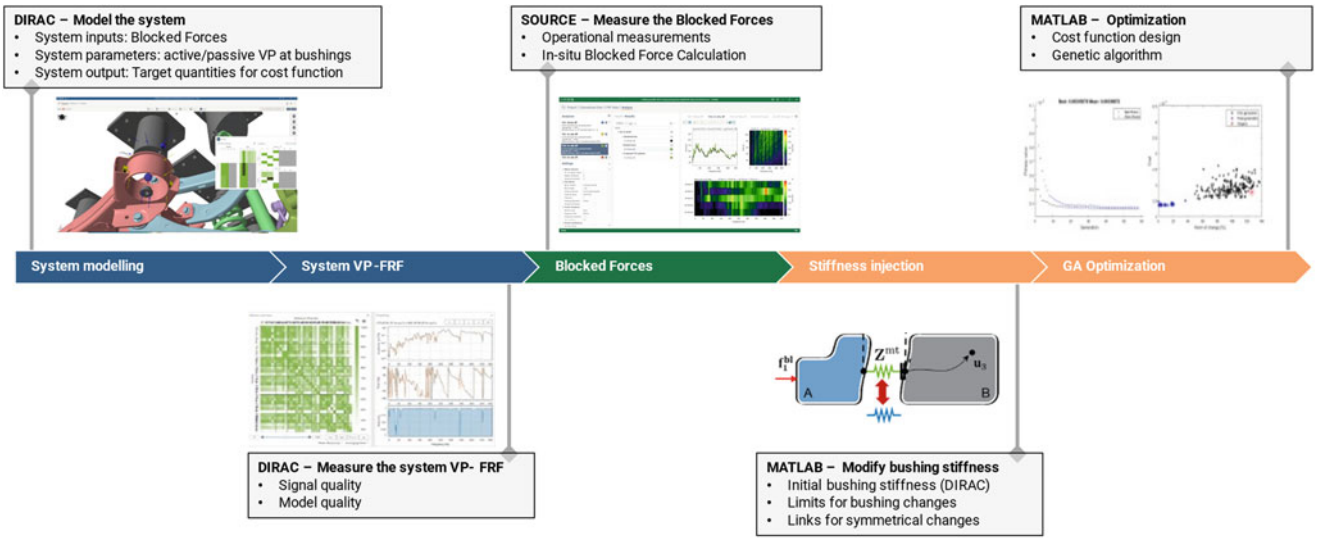

Fig. 8.2 The workflow for optimizing the suspension design

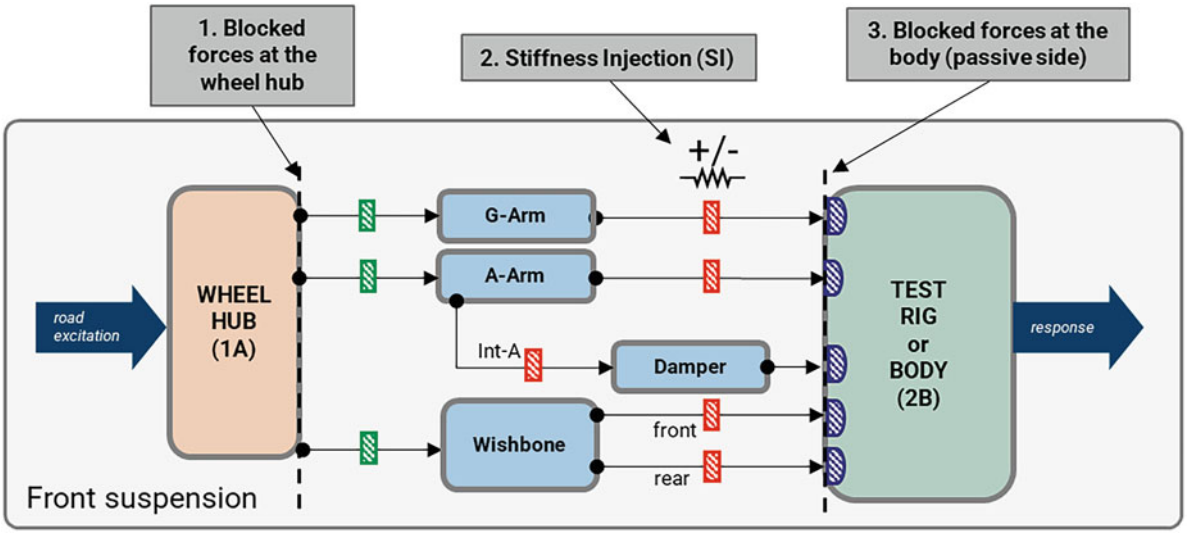

Fig. 8.3 The workflow for optimizing the suspension design

8.2.1 System Modeling

From the system engineering point of view, it is thus essential to differentiate sound phenomena into the source excitation and the sound transmission through the vehicle to the driver's ear. Problems can occur due to particularly high excitations or due to resonances in the transfer path. The system modeling needs to be able to display both. Hence, a clear definition of the substructures of the system and their interfaces is the first step in the workflow.

Figure 8.3 shows the modeling of a front suspension. The system input is the road excitation. It is modeled using blocked forces at the wheel hub (see respective section below). Note that the system excitation is modeled upstream of the design alterations. This is a relevant and necessary requirement for the validity of the response predictions of the modified systems.

The stiffnesses of the suspension bushings are the system parameters that are used to optimize the tire noise performance. They are modified using stiffness injection between the active and passive side of the bushing (see respective section below). The system output can be defined on the level of the suspension system or on the vehicle level. When working with a suspension test bench [4], the target quantities are the blocked forces at the body. They can be measured on the rigid rig and used to predict the tire noise in the vehicle and thus are a possible choice for the target quantity [1]. When working on a vehicle setup or soft rig setup, a possible target quantity could also be the power input to the body [5]. For troubleshooting in the late design stage of a prototype vehicle, the obvious target quantity is the sound pressure level in the cabin.

During the different design stages, the most accurate data of the substructures can be numerical and/or experimental. To create high-quality system models, it is important to ensure compatibility of all datasets at the interfaces. Modeling the interfaces with virtual points ensures compatibility of all setups and describes all relevant interface dynamics in test-based models [6].

8.2.2 System VP-FRF

The system FRF model used in the workflow can be updated and replaced by more refined ones throughout the whole development process. Engineers can use early-stage numerical models for first estimates, then improve their predictions with first suspension prototypes, and do quick late-stage troubleshooting with vehicle prototypes. The models can also be hybrid models using experimental and numerical data.

A key to high model quality is that its compatibility is ensured at the interface degrees of freedom (especially when data from different test setups are merged). For test-based modeling, this can be achieved by describing the interfaces with virtual points. This technology is implemented in the DIRAC software that we used to further ensure signal quality and data consistency.

8.2.3 Blocked Forces

Component TPA allows us to characterize the road excitation with blocked forces in different test setups. The blocked forces can then be applied to the corresponding virtual point of the system model to predict the response of the target quantity [7, 8]. Since the goal of this workflow is to find an optimal modification of the system parameters, it is important to consider the point of application of the blocked force inputs. In order to remain representative of the source excitation, the clocked forces must be before the modified parts. Here, we model them at the wheel hub interface between the tire and the knuckle. The wheel hub is upstream of all suspension bushing in the transfer path that allows for the changes using stiffness injection. Modeling the blocked forces at the wheel hub is also favorable since the tires are produced by suppliers and thus provide a good basis for communication and target setting.

The choice of the blocked forces is very relevant to the optimization results. It is important to include all relevant operational conditions in the combined set of blocked forces. These can be obtained from tire test benches or vehicle test drives at various speeds and surfaces for all the different tire options. Our calculations of the big blocked-force datasets were performed in SOURCE.

8.2.4 Stiffness Injection

In the classical sense, frequency-based substructuring is used to couple two substructures at their interface. This technique can, however, also be used to modify the dynamics of an already assembled system. The stiffness injection method uses this to introduce additional stiffness and/or damping between the virtual points of the active and passive side of bushings:

$$\mathbf{Y_{mod}} = \mathbf{Y} - \mathbf{YB^T}\left(\mathbf{BYB^T} + \mathbf{Y_{SI}}\right)^{-1}\mathbf{BY}, \tag{8.1}$$

where $\mathbf{Y_{mod}}$ is the modified system FRF, $\mathbf{Y}$ is the original system FRF, $\mathbf{B}$ is the Boolean matrix of the active and passive bushing dofs, and $\mathbf{Y_{SI}}$ the additional stiffness and damping FRF, which is placed in parallel to the bushing [9]. Component TPA allows then to apply the blocked forces to the new system dynamics to compute the new response at the target points. All these computations can be done in the software COUPLE.

Stiffness injection can be used to increase and decrease the stiffness between the virtual points of the suspension bushings. The changes can lead to significant system alterations and instabilities if chosen too high. Thus, it makes sense to set limits to the design alterations based on the initial stiffness of the bushings. These initial values can be obtained from supplier test data or through inverse substructuring [10].

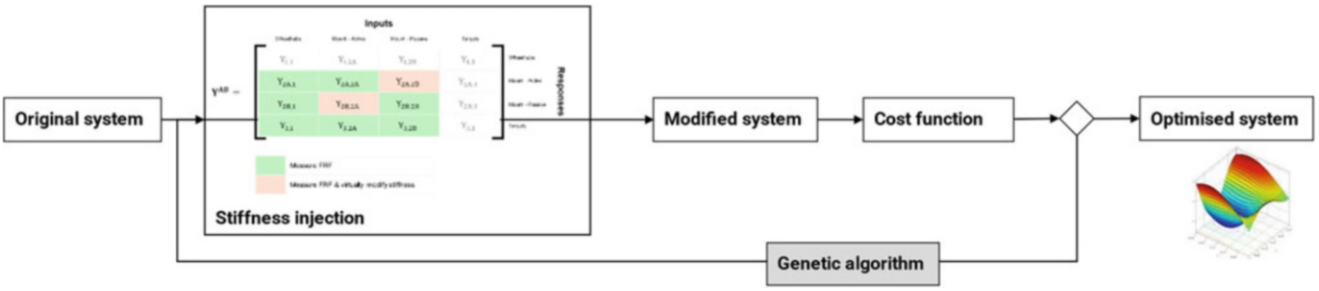

Fig. 8.4 System optimization using stiffness injection and the genetic algorithm

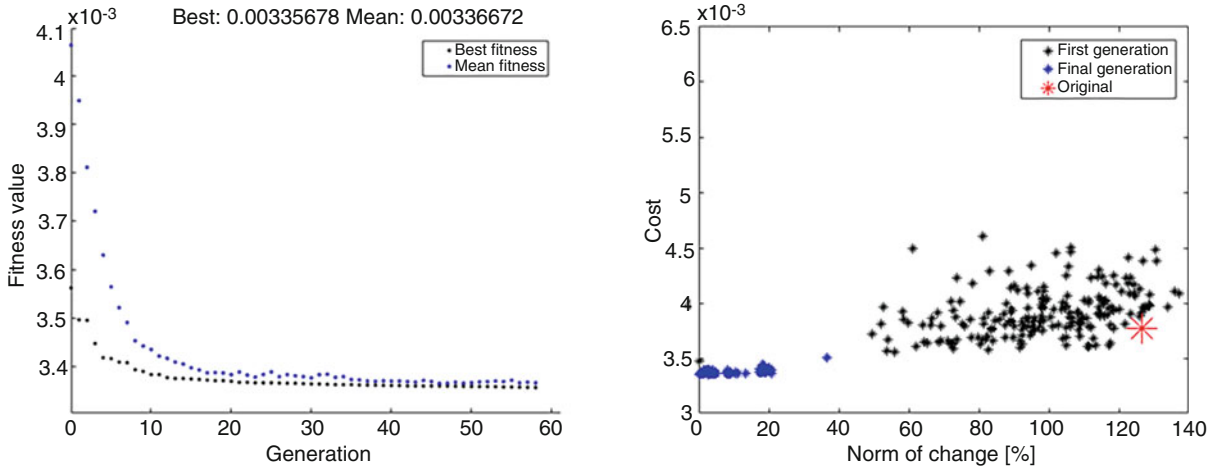

Fig. 8.5 Convergence of the genetic algorithm over the generations (left). Convergence of the population in the solution space (right)

8.2.5 Genetic Algorithm Optimization

The number of bushing design parameters can be higher than 20 for some suspension designs. This would result in a myriad of possible different bushing configurations. Hence, an algorithmic approach is required to solve the optimization problem. The high cross-coupling between the different suspension bushings leads to a high complexity of the system: making one bushing stiffer changes the energy flow through the whole system – like water taking the path of least resistance. This results in many local optima, which makes line search optimizers useless. A better way to solve this problem is to use global optimization algorithms like the genetic algorithm (see Fig. 8.4). This allows us to converge to the optimal bushing target stiffnesses within less than an hour. Such high-speed creation of early-stage development insights is game changing in NVH engineering.

The results in Fig. 8.5 show how the genetic algorithm converges over the iterations of the generations and how the populations converge in the solution space indicating that a global minimum is achieved (using MATLAB). The response of optimized system shows an improvement of the target quantity (see Fig. 8.6). The precise cost function design (the reduction of the multidimensional target response to a scalar value) can be shaped so that specific regions are improved more than others or peaks are focused on more than broadband noise. Note that some areas outside the optimized frequency range can also become worse. Hence, it is important to include the interests of tire noise and all other stakeholders in the design of the cost function for an optimal suspension design.

8.3 Conclusion

It was shown how the combined technologies of virtual points, blocked force TPA, stiffness injection, and the genetic algorithm allow NVH engineers to approach in a completely different way. While common practices rely heavily on late-stage trial-and-error testing and the experience of the engineers, we presented a workflow that allows us to optimize the design

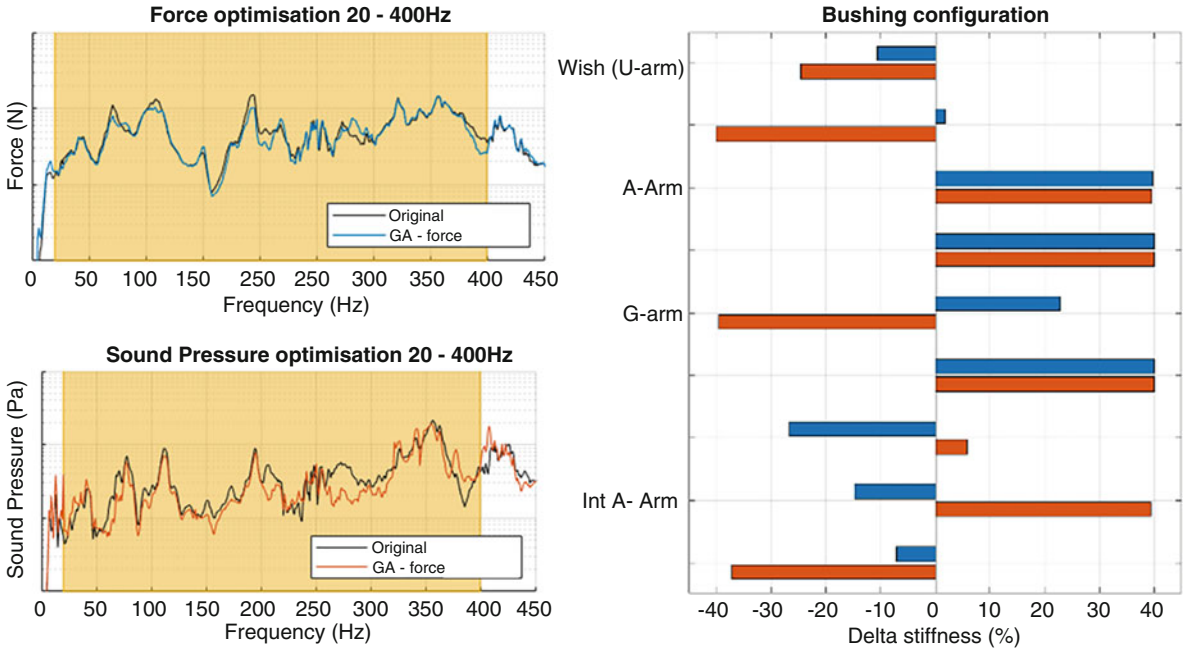

Fig. 8.6 Target response of the original and optimized system when optimizing for forces (top left, blue) and sound pressure (bottom left, orange). Suggested changes for the respective optimized bushing configurations (right)

of vehicle suspension systems in a highly cost-efficient way. It can be used in many design stages using the most accurate numerical and/or experimental model data available. Furthermore, it approaches the challenges of the design process in a holistic way by incorporating the interests of all stakeholders in global cost functions.

Acknowledgments We acknowledge the NVH Research Lab of Hyundai Motor Company for funding this research. We thank Müller-BBM VibroAkustik Systeme Korea for their support in the measurement campaigns and coordination.

References

1. van der Seijs, M.V., Harvie, J.M., Song, D.P.: Road noise: embedding suspension test benches in sound & vibration design using virtual points and the transfer path analysis framework. In: Dynamic Substructures, vol. 4, pp. 99–106. Springer, Cham (2022)
2. Harvie, J.M., van der Seijs, M.V., Song, D.P., Cho, M.: Road noise NVH part 2: exploring the capabilities of the TPA framework with interface forces. In: Dynamic Substructures, vol. 4, pp. 19–28. Springer, Cham (2023)
3. Cho, M., Song, D.P., Lee, M., Lee, J., et al.: Prediction and optimization of blocked force changes of a suspension system using bush stiffness injection method. SAE Technical Paper, 2022-01-0956 (2022). https://doi.org/10.4271/2022-01-0956
4. Song, D.P., Min, D., Kang, Y.J., Cho, M., Kim, H.G., Ih, K.D.: A methodolgy for evaluating the structure-borne road noise prior to a prototype vehicle using direct force measured on a suspension rig. Noise Control Eng. J. **64**(3), 295–304 (2016)
5. Pasma, E.A., Klaassen, S.W.B., Passanesi, A.V.V., Westlund, J.: Advanced complex power TPA studies for road noise NVH performance on a rear axle. In: ISMA2022: International Conference on Noise and Vibration Engineering, Leuven (2022)
6. van der Seijs, M.V., van den Bosch, D.D., Rixen, D.J., de Klerk, D.: An improved methodology for the virtual point transformation of measured frequency response functions in dynamic substructuring. In: COMPDYN 2013: 4th ECCOMAS Thematic Conference on Computational Methods in Structural Dynamics and Earthquake Engineering, Kos (2013)
7. Moorhouse, A.T., Elliott, A.S., Evans, T.A.: In situ measurement of the blocked force of structure-borne sound. J. Sound Vib. **325**(4–5), 679–685 (2009)
8. van der Seijs, M.V., Rixen, D.J., de Klerk, D.: General framework for transfer path analysis: history, theory and classification of techniques. Mech. Syst. Signal Process. **68**, 217–244 (2016)
9. Gagliardini, L., de Klerk, D. Stiffness injection: a tool for vehicle NVH performance optimization. SAE Technical Paper, 2022-01-0976 (2022). https://doi.org/10.4271/2022-01-0976
10. Haeussler, M., Klaassen, S.W.B., Rixen, D.J.: Experimental twelve degree of freedom rubber isolator models for use in substructuring assemblies. J. Sound Vib. **474**, 115253 (2020)

Chapter 9
In-Situ Component-Based TPA for Time-Variant Dynamic Systems: A State-Space Formulation

R. S. O. Dias, M. Martarelli, and P. Chiariotti

Abstract In this chapter, a methodology to calculate equivalent forces by taking into account the possible time-varying dynamic behavior of the components under analysis is presented. This methodology is based on the use of the state-space realization of the in-situ component-based TPA method. To take into account possible time-varying dynamic behavior of the systems under study, a local linear parameter varying (LPV) model identification approach is used. This approach enables the computation of state-space models representative of the components at each time instant by interpolating a given set of linear time-invariant (LTI) state-space models representative of the dynamics of the components under study for fixed operating conditions. By exploiting a numerical example, it is found that when dealing with structures presenting time-varying behavior, accurate equivalent forces can be computed in time domain by using the approaches presented in this chapter. Furthermore, it is clearly demonstrated that ignoring the time dependency of the dynamic behavior of mechanical systems can lead to an important deterioration of the results.

Keywords Transfer path analysis · State-space substructuring · Linear parameter-varying (LPV) systems · System identification · State-space models

9.1 Introduction

Transfer path analysis (TPA) is a well-established technique in the noise, vibration, and harshness (NVH) field. During the last years, TPA has been exploited to study the transmission paths of noise and vibration from active components (i.e., sources) to the connected passive components (e.g., see [1–3]). As far as the automotive field is concerned, it should be reported that the current TPA applications mainly exploit the frequency-domain formulation. However, applications involving transient phenomena, such as ride comfort analysis while driving over bumps and the characterization of injector noise, would definitely benefit from the use of a TPA time-domain formulation. This chapter points to those TPA applications targeted to the identification of loads in NVH (see [4]). Namely, the family of component-based TPA methods, whose aim is the characterization of sources by a set of forces (also known as equivalent forces) that are an inherent property of the source itself. Several methods enabling time-domain force reconstruction are available in the literature, for example, based on adaptive algorithms [5] and on state-space models [6, 7]. However, less attention has been given to the time-domain computation of equivalent forces by taking into account the possible time variations on the dynamic behavior of the components under study. Nevertheless, many mechanical systems are made of components that might present important dynamic time-dependent variations under operating conditions. A well-known example is represented by rubber mounts, whose mechanical behavior depends on several parameters, like preload applied and temperature (see [8]).

To take into account time variations on the dynamics of the components under analysis, while computing equivalent forces, we aim at introducing a methodology based on the use of the state-space formulation. The benefit of using state-space models to deal with this kind of applications is justified by three main reasons. Firstly, the state-space models have an intrinsic suitability to deal with problems posed in time domain, hence approaching these problems is easier by exploiting

R. S. O. Dias · M. Martarelli
Department of Industrial Engineering and Mathematical Sciences, Università Politecnica delle Marche, Ancona, Marche, Italy
e-mail: r.dasilva@staff.univpm.it; m.martarelli@staff.univpm.it

P. Chiariotti (✉)
Department of Mechanical Engineering, Politecnico di Milano, Lombardia, Milan, Italy
e-mail: paolo.chiariotti@polimi.it

M. Allen et al. (eds.), *Dynamic Substructures, Volume 4*, Conference Proceedings of the Society for Experimental Mechanics Series, https://doi.org/10.1007/978-3-031-36694-9_9

the state-space formulation. Secondly, by using this kind of models, the performance of time-domain simulations, which take into account variations on the dynamic behavior of the components under study, is simplified. Thirdly, it is widely known that the state-space formulation is one of the best choices for real-time applications.

The methodology here presented is based on the use of the state-space realization of the in situ component-based TPA method. To account for time variations on the dynamic behavior of the components under analysis, we propose the use of local Linear Parameter-Varying (LPV) model identification approaches (see [9–11]). These approaches enable the interpolation of linear time-invariant (LTI) state-space models representative of the dynamics of the components under study for constant values of the scheduling parameters, that is, for fixed operating conditions. Thereby, it becomes possible to estimate state-space models representative of the operating conditions of the target component at each time sample, without the need to experimentally characterize the component for each individual operating condition.

The state-space realization of the in-situ component-based TPA method is presented in Sect. 9.2. Then, guidelines on how to implement a local LPV model identification approach are provided in Sect. 9.3. In Sect. 9.4 the approaches discussed in this chapter are validated by using a numerical example. Finally, in Sect. 9.5 the conclusion is presented.

9.2 In-Situ Component-Based TPA

In this section, the in-situ method of the component-based TPA family (see [4]) will be extended into the state-space domain. It is worth mentioning that the state-space realization of this method will be presented by assuming an estimation of the forces in a linear least-squares sense (perhaps the most straightforward way to compute the intended forces). Nevertheless, it is well known from the literature that the force identification problem is ill-posed. Moreover, in an experimental scenario, estimating forces in a linear least-squares sense does not lead in general to useful results as it generally amplifies the noise in the used operational outputs to estimate the forces (see, for instance, [7, 12]). More robust methodologies to solve the force identification problem are available in the literature (see, for instance, [6, 7, 13]). However, these approaches will not be investigated here because the sole aim of this chapter is to theoretically introduce a methodology to account for time variations on the dynamic behavior of components when calculating equivalent forces. For this reason, a discussion on the most suitable methods to estimate time-domain forces is out of the scope of this chapter.

To start approaching the in-situ component-based TPA method, let us consider the assembled structure of Fig. 9.1, where a source and a passive component are connected together. By using component-based TPA methods, we aim at characterizing the source by a set of forces that are an inherent property of the source itself. These forces are commonly tagged as equivalent forces and, when applied on the active component A at rest, the operational responses (i.e., when the source is turned on) at the passive component can be simulated (see Fig. 9.1b). Moreover, as the equivalent forces are only a property of the source, they can be used to determine the operational responses at any passive system connected with the source [4, 14].

At this point, we may compute the operational acceleration responses at the indicator's location of the structure given in Fig. 9.1 by either using the internal forces generated by the internal mechanisms of the source or applying the set of equivalent forces at the interface between the source and the passive system. By computing those operational responses by following both mentioned approaches, we obtain the following identity:

$$\left[\bar{H}_{TJ}(j\omega)\right]\left\{U_{J,eq}(j\omega)\right\} = \left[\bar{H}_{TS}(j\omega)\right]\{U_S(j\omega)\} \tag{9.1}$$

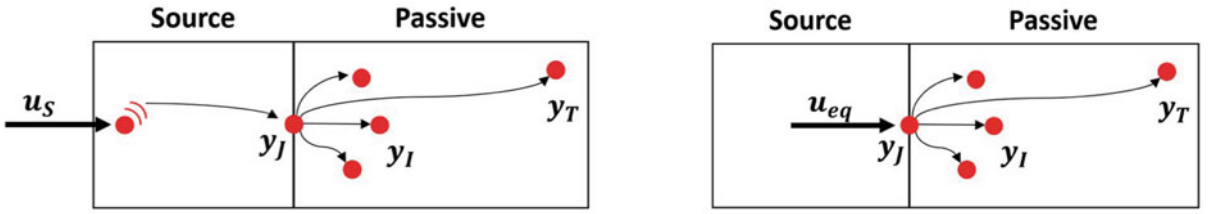

(a) Operational responses originated by the internal forces generated by the internal mechanisms of the source.

(b) Operational responses originated by the equivalent forces determined with component-based TPA.

Fig. 9.1 Assembled structure composed by a source and a passive substructure

where $\{U_{J,eq}(j\omega)\} \in \mathbb{C}^{n_J \times 1}$ is the vector of equivalent forces in frequency domain, $[H(j\omega)] \in \mathbb{C}^{n_o \times n_i}$ denotes an acceleration FRF matrix, and overbar variables denote variables associated with the assembled structure. Variables n_i and n_o represent the number of inputs and outputs, respectively, whereas n_J represents the number of interface DOFs. Subscripts S and J denote variables associated with internal DOFs belonging to the source and with the interface DOFs, respectively, while subscripts I and T denote variables associated with indicators and targets DOFs, respectively (see Fig. 9.1). From expression (9.1), we may establish a relation between the internal forces generated on the source and the set of equivalent forces as given below.

$$\{U_{J,eq}(j\omega)\} = \left[\bar{H}_{TJ}(j\omega)\right]^{-1}\left[\bar{H}_{TS}(j\omega)\right]\{U_S(j\omega)\} \tag{9.2}$$

It can be proven that the following relation holds (see [4]):

$$\left[\bar{H}_{TJ}(j\omega)\right]^{-1}\left[\bar{H}_{TS}(j\omega)\right] = \left[H^S_{JJ}(j\omega)\right]^{-1}\left[H^S_{JS}(j\omega)\right] \tag{9.3}$$

where superscript S denotes variables associated with the source. Expression (9.2) can be rewritten as follows:

$$\{U_{J,eq}(j\omega)\} = \left[H^S_{JJ}(j\omega)\right]^{-1}\left[H^S_{JS}(j\omega)\right]\{U_S(j\omega)\} \tag{9.4}$$

or by using state-space matrices:

$$\begin{aligned}\{U_{J,eq}(j\omega)\} = &\left(\left[C^S_{J,accel}\right](j\omega[I] - [A^S])^{-1}\left[B^S_J\right] + \left[D^S_{JJ,accel}\right]\right)^{-1}\left(\left[C^S_{J,accel}\right]\left(j\omega[I] - \left[A^S\right]\right)^{-1}\left[B^S_S\right]\right.\\ &\left.+\left[D^S_{JS,accel}\right]\right)\{U_S(j\omega)\}\end{aligned} \tag{9.5}$$

where subscript *accel* denotes matrices of an acceleration state-space model. Expressions (9.4) and (9.5) prove that the equivalent forces are a property of the source. The set of equivalent forces may also be computed in time domain. It is worth mentioning that as we are using state-space models possible changes on the dynamic properties of both source and passive components over time can be taken into account to compute the equivalent forces. Hence in the following, when working in the time domain, the state-space matrices will be assumed to be time dependent. In this way, we may calculate the equivalent forces in time domain as follows:

$$\begin{aligned}\{\dot{x}^{S,inv}(t)\} &= \left[A^{S,inv}(t)\right]\left\{x^{S,inv}(t)\right\} + \left[B^{S,inv}_J(t)\right]\left\{\ddot{y}^S_J(t)\right\}\\ \left\{u_{J,eq}(t)\right\} &= \left[C^{S,inv}_J(t)\right]\{x^{S,inv}(t)\} + \left[D^{S,inv}_{JJ}(t)\right]\left\{\ddot{y}^S_J(t)\right\}\end{aligned} \tag{9.6}$$

where $\{x(t)\} \in \mathbb{R}^{n\times 1}$ is the state vector, $\{u(t)\} \in \mathbb{R}^{n_i \times 1}$ is the input vector. Variable n represents the number of states, and matrices $[A^{S,inv}(t)]$, $[B^{S,inv}(t)]$, $[C^{S,inv}(t)]$ and $[D^{S,inv}(t)]$ are given as follows:

$$\begin{aligned}[A^{S,inv}(t)] &= [A^S(t)] - [B^S_J(t)][D^S_{JJ,accel}(t)]^{-1}[C^S_{J,accel}(t)],\quad [B^{S,inv}_J(t)] = [B^S_J(t)][D^S_{JJ,accel}(t)]^{-1}\\ [C^{S,inv}_J(t)] &= -[D^S_{JJ,accel}(t)]^{-1}[C^S_{J,accel}(t)],\quad [D^{S,inv}_{JJ}(t)] = [D^S_{JJ,accel}(t)]^{-1}\end{aligned} \tag{9.7}$$

while the acceleration responses $\{\ddot{y}^S_J(t)\}$ must be computed by exploiting the state-space model given below:

$$\begin{aligned}\{\dot{x}^S(t)\} &= \left[A^S(t)\right]\left\{x^S(t)\right\} + \left[B^S_S(t)\right]\left\{u_S(t)\right\}\\ \left\{\ddot{y}^S_J(t)\right\} &= \left[C^S_{J,accel}(t)\right]\{x^S(t)\} + \left[D^S_{JS,accel}(t)\right]\left\{u_S(t)\right\}\end{aligned} \tag{9.8}$$

Even though by using expression (9.5) it is possible to compute the set of equivalent forces, we are required to know the internal forces caused by the internal mechanism of the source. In practice, these forces are generally impossible to measure. To circumvent this requirement, we may calculate the set of equivalent forces by following the in-situ method proposed by Moorhouse and Elliott (see [15, 16]). This method holds the advantage of avoiding the use of special test rigs and the need

of dismounting any component. By exploiting this approach, we may calculate the equivalent forces at the interface of the assembly given in Fig. 9.1 as follows:

$$\left\{U_{J,eq}(j\omega)\right\} = \begin{bmatrix} \bar{H}_{JJ}(j\omega) \\ \bar{H}_{IJ}(j\omega) \\ \bar{H}_{TJ}(j\omega) \end{bmatrix}^{\dagger} \begin{Bmatrix} \ddot{\bar{Y}}_J(j\omega) \\ \ddot{\bar{Y}}_I(j\omega) \\ \ddot{\bar{Y}}_T(j\omega) \end{Bmatrix} \tag{9.9}$$

where superscript † denotes the Moore–Penrose pseudoinverse of a matrix. By using state-space matrices, expression (9.9) can be rewritten as given below.

$$\left\{U_{J,eq}(j\omega)\right\} = \begin{bmatrix} [\bar{C}_{J,accel}](j\omega[I] - [\bar{A}])^{-1}[\bar{B}_J] + [\bar{D}_{JJ,accel}] \\ [\bar{C}_{I,accel}](j\omega[I] - [\bar{A}])^{-1}[\bar{B}_J] + [\bar{D}_{IJ,accel}] \\ [\bar{C}_{T,accel}](j\omega[I] - [\bar{A}])^{-1}[\bar{B}_J] + [\bar{D}_{TJ,accel}] \end{bmatrix}^{\dagger} \begin{Bmatrix} \ddot{\bar{Y}}_J(j\omega) \\ \ddot{\bar{Y}}_I(j\omega) \\ \ddot{\bar{Y}}_T(j\omega) \end{Bmatrix} \tag{9.10}$$

The equivalent forces can also be computed in time domain by using the in-situ method as follows:

$$\begin{aligned} \{\dot{x}(t)\} &= \left[\bar{A}^{inv}(t)\right]\{x(t)\} + \left[\bar{B}_J^{inv}(t)\right] \begin{Bmatrix} \ddot{\bar{y}}_J(t) \\ \ddot{\bar{y}}_I(t) \\ \ddot{\bar{y}}_T(t) \end{Bmatrix} \\ \left\{u_{J,eq}(t)\right\} &= \left[\bar{C}_{JIT}^{inv}(t)\right]\{x(t)\} + \left[\bar{D}_{JIT,J}^{inv}(t)\right] \begin{Bmatrix} \ddot{\bar{y}}_J(t) \\ \ddot{\bar{y}}_I(t) \\ \ddot{\bar{y}}_T(t) \end{Bmatrix} \end{aligned} \tag{9.11}$$

where

$$\begin{aligned} [\bar{A}^{inv}(t)] &= [\bar{A}(t)] - [\bar{B}_J(t)][\bar{D}_{JIT,J}(t)]^{\dagger}[\bar{C}_{JIT}(t)], \quad [\bar{B}_J^{inv}(t)] = [\bar{B}_J(t)][\bar{D}_{JIT,J}(t)]^{\dagger} \\ [\bar{C}_{JIT}^{inv}(t)] &= -[\bar{D}_{JIT,J}(t)]^{\dagger}[\bar{C}_{JIT}(t)], \quad [\bar{D}_{JIT,J}^{inv}(t)] = [\bar{D}_{JIT,J}(t)]^{\dagger} \end{aligned} \tag{9.12}$$

matrices $[\bar{C}_{JIT}(t)]$ and $[\bar{D}_{JIT,J}(t)]$ are given below:

$$\left[\bar{C}_{JIT}(t)\right] = \begin{bmatrix} \bar{C}_{J,accel}(t) \\ \bar{C}_{I,accel}(t) \\ \bar{C}_{T,accel}(t) \end{bmatrix}, \quad \left[\bar{D}_{JIT.J}(t)\right] = \begin{bmatrix} \bar{D}_{JJ,accel}(t) \\ \bar{D}_{IJ,accel}(t) \\ \bar{D}_{TJ,accel}(t) \end{bmatrix} \tag{9.13}$$

Note that for the sake of completeness, in expressions (9.9), (9.10), and (9.11), we presented how to calculate the equivalent forces from measured operational responses at the interface, indicators, and targets locations. Nevertheless, in practice, the equivalent forces are solely determined from operational responses measured at the indicators (see [4]). In fact, the responses acquired at the target DOFs are usually not used, because they are many times small in number and placed far away from the interface. Consequently, they do not properly observe the interface between the source and the passive system. On the other hand, the responses at the interface DOFs are usually difficult to measure as it requires the placement of sensors at the interface, which implies practical difficulties. Conversely, the location of the indicator DOFs is specially chosen to be accessible and close to the interface to properly observe it. Furthermore, the number of these DOFs is typically at least two times higher than the number of equivalent forces to be determined in order to guarantee overdetermination and, hence, better matrix conditioning [4].

Note also that, as proven above, the equivalent forces are a property of the source; hence, the equivalent forces computed by using the in-situ method continue to be valid to simulate the operational responses at any passive component to which the source is coupled. However, to successfully compute the equivalent forces by exploiting the in-situ method, we must guarantee that the operational excitation only comes from the source and that the measured operational responses used to compute the equivalent forces are acquired at the passive component or at the interface between the source and the passive system [4].

9.3 Linear Parameter-Varying models

In this section, we will present how to estimate linear parameter-varying models by using a local approach. The local approaches enable the interpolation of LTI state-space models representative of the dynamics of the component under study for constant values of the scheduling parameters, that is, for fixed operating conditions, thus making the identification of the state-space model representations of the operating conditions of the target components possible, with no need to experimentally characterize the component for each individual operating condition. We will assume that the LTI state-space models used to construct the LPV model are displacement state-space models. The use of displacement models is indeed advantageous because by definition these models present null feed-through matrices; thus, the number of variables involved on the computation of the LPV model decreases. Consequently, the computational cost for computing the LPV models and the cost of computing the interpolated state-space models for each of the intermediate operational conditions also decreases.

To start, we must define the operating conditions for which a set of LTI models will be estimated. There are no strict rules on which operating conditions to choose. Nevertheless, for a system depending on a scheduling parameter β, whose value varies from a minimum value of $\underline{\beta}$ to a maximum value of $\bar{\beta}$, it is recommended that one of the chosen operating conditions be characterized by a β slightly lower or equal to $\underline{\beta}$; in addiction, one of the chosen operating conditions must be characterized by a β equal or slightly higher than $\bar{\beta}$. In this way, we make sure that there is no need of performing extrapolation to characterize the dynamic behavior of the target component. It is also suggested to choose operating conditions characterized by an equidistant value of the scheduling parameter. Moreover, the number of used LTI models must be as small as possible (to reduce the number of state-space models to be identified), but large enough to well-capture the influence of the scheduling parameter over the target component dynamics [10].

To successfully compute an LPV model from a given set of LTI models, we must firstly transform the models into a coherent representation. When the set of state-space models is directly constructed from the mechanical properties of the component under analysis (in an analytical or numerical scenario), they are already obtained in a coherent representation. However, in an experimental context the state-space models are in general computed from experimentally acquired data by using system identification algorithms, for instance, by using the well-known n4sid methods (see [17, 18]) or the procedures presented in [19, 20], which rely on a previous modal identification step by using PolyMAX [21] and ML-MM methods [22]. In this scenario, the estimated set of state-space models is generally not obtained in a coherent representation. In the literature, several approaches to transform the estimated set of state-space models into a coherent representation have been proposed (e.g., see [11, 23]). Here, to transform the set of estimated state-space models into a coherent representation, we will start by transforming each of the state-space models into modal form as follows:

$$\begin{aligned} \{\dot{x}_{mf}(t)\} &= [A_{mf}]\{x_{mf}(t)\} + [B_{mf}]\{u_{mf}(t)\} \\ \{y_{mf}(t)\} &= [C_{mf}]\{x_{mf}(t)\} \end{aligned} \tag{9.14}$$

where subscript mf denotes matrices/vectors associated with a state-space model transformed into modal form, whereas matrices $[A_{mf}]$, $[B_{mf}]$, and $[C_{mf}]$ are given in (9.15).

$$[A_{mf}] = [\Lambda] = [T_{mf}]^{-1}[A][T_{mf}], \quad [B_{mf}] = [T_{mf}]^{-1}[B], \quad [C_{mf}] = [C][T_{mf}] \tag{9.15}$$

In Eq. (9.15), $[\Lambda]$ is a diagonal matrix containing the eigenvalues of matrix $[A]$ (which are also the poles of the system) and $[T_{mf}]$ is a modal matrix containing all system eigenvectors as columns and can be computed by solving the eigenvalue problem given below:

$$[A][T_{mf}] = [T_{mf}][\Lambda]. \tag{9.16}$$

As next step, we must ensure that the poles of each state-space model of the set of identified models (which are present in the diagonal of the state matrices) are sorted in a coherent way. Each pole has an associated natural frequency and damping ratio; hence, to take into account both values, we will sort the poles in ascending damped natural frequency. The damped natural frequency of a pole can be simply computed as follows:

$$\omega_d^r = \omega_n^r \sqrt{1 - (\xi^r)^2} \tag{9.17}$$

where ω_d^r and ω_n^r are the damped natural frequency of the rth pole, respectively, while ξ^r is the damping ratio of the rth pole. Note that eventual ties when sorting pairs of complex conjugate poles are broken by firstly including the pole presenting positive imaginary part and by including afterward the pole presenting negative imaginary part. The rows of the input matrix and the columns of the output matrix must be sorted in accordance with the poles.

Then, we must coherently scale the matrices $[B_{mf}]$ and $[C_{mf}]$ of each state-space model of the estimated set of models. The need for scaling both input and output matrices arises because the modal domain representation of a state-space model is not unique with respect to these scalings. Thus, to ensure a smooth variation of the coefficients of both input and output matrices a coherent scaling is mandatory [23]. In this way, we may define the scaling of both input and output matrices as follows:

$$[B_{mf,sc}] = [W]^{-1}[B_{mf}] \tag{9.18}$$

$$[C_{mf,sc}] = [C_{mf}][W] \tag{9.19}$$

where subscript sc denotes a coherently scaled state-space matrix, while $[W] \in \mathbb{C}^{n \times n}$ is the scaling matrix. A straightforward approach to coherently scale all the estimated state-space models is, for instance, to normalize each row of the $[B_{mf}]$ matrix associated to each of the poles of the system with respect to one of its elements [23]. Assuming that a normalization with respect to the first element of each row of $[B_{mf}]$ is chosen, the $[W]$ matrix must be constructed as follows:

$$[W] = \begin{bmatrix} B_{11,mf} & & \\ & B_{21,mf} & \\ & & \ddots \end{bmatrix} \tag{9.20}$$

where the first and second subscripts denote the number of the row and column of the input matrix element, respectively. It is worth mentioning that by using the scaling matrix given in expression (9.20), the input–output properties of the state-space models are unchanged. To demonstrate this, we may compute the FRFs of the scaled state-space model as given below.

$$[H_{mf,sc}(j\omega)] = [C_{mf}][W](j\omega[I] - [\Lambda])^{-1}[W]^{-1}[B_{mf}] = [C_{mf}](j\omega[I] - [\Lambda])^{-1}[B_{mf}] \tag{9.21}$$

By observing expression (9.21) and having in mind that matrices $[W]$ and $[\Lambda]$ are diagonal matrices, we may conclude that by scaling state-space models with $[W]$ the FRFs of the state-space model are not changed, and hence, the input–output properties of the model remain unchanged. The scaling approach just presented will be exploited in the numerical example discussed in Sect. 9.4.

After having represented the set of state-space models coherently, an LPV model can be constructed. To define the LPV model, we will follow the procedure proposed by De Caigny et al. in [10]. This approach assumes that the interpolating LPV model to be constructed presents a homogeneous polynomial dependency on the parameterized values that the scheduling parameters take in a multisimplex Λ.

Let us assume that by using an interpolating LPV model, we aim at estimating a state-space model representative of the dynamics of a structure for a fixed operating condition l that is characterized by a single scheduling parameter β. A parameterization of β in the multisimplex Λ of dimension $N = 2$ (common choice in practice [10]) can be defined as follows:

$$\alpha_{l,1} = \frac{\beta_l - \underline{\beta}}{\bar{\beta} - \underline{\beta}}, \quad \alpha_{l,2} = 1 - \alpha_{l,1} \tag{9.22}$$

where $\bar{\beta}$ and $\underline{\beta}$ are the maximum and minimum values of the scheduling parameter associated with the set of state-space models used to define the LPV model, respectively.

After having parameterized the scheduling parameter, we may define the interpolated state-space matrices representative of the fixed operating condition l by using a LPV model as follows:

$$diag[A(\alpha_l)] = \sum_{k=1}^{J_N(g)} \alpha_l^k \{\tilde{A}^k\} \tag{9.23a}$$

$$[B(\alpha_l)] = \sum_{k=1}^{J_N(g)} \alpha_l^k [\tilde{B}^k] \tag{9.23b}$$

$$[C(\alpha_l)] = \sum_{k=1}^{J_N(g)} \alpha_l^k [\tilde{C}^k] \tag{9.23c}$$

where $diag[\bullet]$ is a column vector containing the diagonal elements of matrix $[\bullet]$, α_l^k represents the element placed on the k^{th} column of $\{\alpha_l\}$, which assuming an homogeneous polynomial dependency of degree g must be computed as given below:

$$\{\alpha_l\} = \left[\alpha_{l,1}^g \alpha_{l,2}^0 \; \alpha_{l,1}^{g-1} \alpha_{l,2}^1 \; \ldots \; \alpha_{l,1}^0 \alpha_{l,2}^g\right] \tag{9.24}$$

It is worth mentioning that all the coefficients of the vector $\{\alpha_l\}$ must present the same degree g, because by exploiting the approach proposed in [10], we assume that the LPV model to be set-up presents an homogeneous polynomial dependency on the parameterized values of the scheduling parameter. Moreover, $\{\alpha_l\}$ should be composed by a number of elements given by the expression presented below.

$$J_N(g) = \frac{(N+g-1)!}{g!(N-1)!} \tag{9.25}$$

The variables $\{\tilde{A}^k\} \in \mathbb{C}^{n\times 1}$, $[\tilde{B}^k] \in \mathbb{C}^{n\times n_i}$, and $[\tilde{C}^k] \in \mathbb{C}^{n_o\times n}$ in expression (9.23) are unknown vectors/matrices associated with the monomial positioned on the k^{th} column of $\{\alpha_l\}$. These variables must be determined in order to define the interpolating LPV model. A straightforward approach is determining those unknown vectors/matrices in a linear least-squares sense. In this way, we must define our problem as follows:

$$[a]\{q\} = \{b\} \tag{9.26}$$

where

$$[a] = \begin{bmatrix} \alpha_1 \bigotimes I_{A,A} & & & \\ \vdots & & & \\ \alpha_m \bigotimes I_{A,A} & & & \\ & \alpha_1 \bigotimes I_{B,B} & & \\ & \vdots & & \\ & \alpha_m \bigotimes I_{B,B} & & \\ & & \alpha_1 \bigotimes I_{C,C} & \\ & & \vdots & \\ & & \alpha_m \bigotimes I_{C,C} & \end{bmatrix} \tag{9.27a}$$

$$\{q\} = \left\{\{\tilde{A}^1\}^T \; \ldots \; \{\tilde{A}^{J_N(g)}\}^T\right\} \left(vec[\tilde{B}^1]\right)^T \; \ldots \; \left(vec[\tilde{B}^{J_N(g)}]\right)^T \; \left(vec[\tilde{C}^1]\right)^T \; \ldots \; \left(vec[\tilde{C}^{J_N(g)}]\right)^T \Big\} \tag{9.27b}$$

$$\{b\} = \Big\{(diag[\Lambda^1])^T \; \ldots \; (diag[\Lambda^m])^T \; \left(vec[B_{mf,sc}^1]\right)^T \; \ldots \; \left(vec[B_{mf,sc}^m]\right)^T \; \left(vec[C_{mf,sc}^1]\right)^T \; \ldots \; \left(vec[C_{mf,sc}^m]\right)^T \Big\} \tag{9.27c}$$

where $\bigotimes$ denotes the Kronecker matrix product, matrices $[I_{A,A}]$, $[I_{B,B}]$, and $[I_{C,C}]$ are identity matrices of dimension n, nn_i, and nn_o, respectively, $vec[\bullet]$ is the vector obtained by stacking all columns of matrix $[\bullet]$, and m is the number of state-space models included in the set of estimated state-space models. Note that, as the state-space models used to construct the LPV model are transformed in modal form, their state matrix is a diagonal matrix. This is the reason why to construct the vector $\{b\}$, we only use the diagonal elements of the state matrices of each state-space model. Indeed, the construction of an LPV model by using state-space models transformed into modal form is interesting in the sense that the state matrix of each of the estimated LTI models becomes a diagonal matrix. Thus, to define the partition of the interpolating LPV model

responsible for calculating the state matrices of the interpolated models, we are only required to determine unknown vectors composed by n elements instead of unknown matrices composed by n^2 elements.

At this point, to compute vector $\{q\}$ in a linear least-squares sense, we may use the following expression.

$$\{q\} = [a]^{\dagger}\{b\} \tag{9.28}$$

Obviously, by calculating the unknown parameters as presented above, we aim at minimizing the squared 2-norm of the error vector given below.

$$\{F(q)\} = -\begin{bmatrix} \sum_{k=1}^{J_N(g)} \alpha_1^k \{\tilde{A}^k\} - diag[\Lambda^1] \\ \vdots \\ \sum_{k=1}^{J_N(g)} \alpha_m^k \{\tilde{A}^k\} - diag[\Lambda^m] \\ \sum_{k=1}^{J_N(g)} \alpha_1^k vec[\tilde{B}^k] - vec[B_{mf,sc}^1] \\ \vdots \\ \sum_{k=1}^{J_N(g)} \alpha_m^k vec[\tilde{B}^k] - vec[B_{mf,sc}^m] \\ \sum_{k=1}^{J_N(g)} \alpha_1^k vec[\tilde{C}^k] - vec[C_{mf,sc}^1] \\ \vdots \\ \sum_{k=1}^{J_N(g)} \alpha_m^k vec[\tilde{C}^k] - vec[C_{mf,sc}^m] \end{bmatrix} \tag{9.29}$$

9.4 Numerical Example

In this section, a numerical example will be studied to validate the approaches discussed in this chapter. The numerical example to be analyzed involves three different components, from now on labeled as components A, B, and C (see Fig. 9.2). Moreover, two assembled structures will be analyzed, one of the assemblies is originated from the coupling of components A and B (from now on tagged as assembly AB), while the other one is originated from the coupling of components A and C (from now on denoted as assembly AC). Both assemblies are depicted in Fig. 9.3, whereas the value of the physical parameters labeled in Figs. 9.2 and 9.3 is provided in Table 9.1.

To start approaching the numerical example, analytical state-space models representative of the three components and of the two assemblies were directly defined from their correspondent mass, stiffness and damping matrices. For simplicity, the damping matrix of each system was constructed from the stiffness one by replacing the stiffness terms by damping ones. Moreover, one stiffness and one damping parameter associated with components A, B, and C present a nonlinear variation

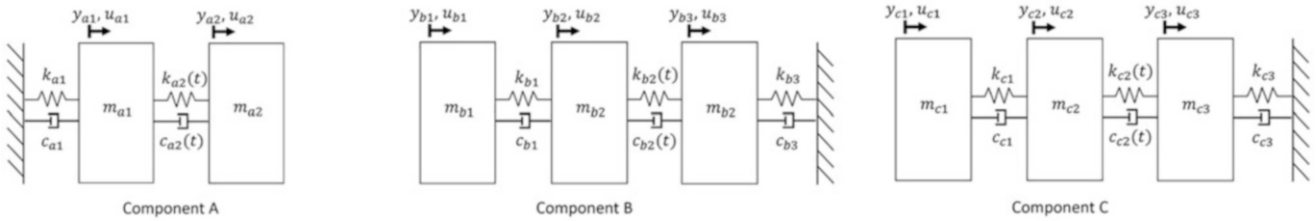

Fig. 9.2 Components

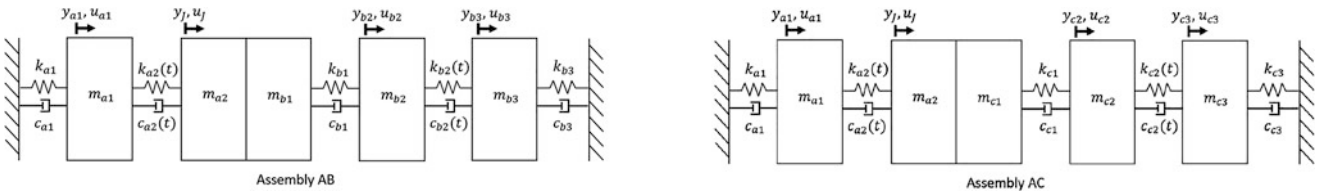

Fig. 9.3 Assemblies

Table 9.1 Physical parameter values

i	m_i (kg)	c_i (N s m^{-1})	k_i (N m^{-1})
$a1$	6	10	4×10^3
$a2$	4	$(5)^{n_1(t)}$	$(2 \times 10^3)^{n_1(t)}$
$b1$	5	20	1×10^3
$b2$	3	$(15)^{n_2(t)}$	$(3.5 \times 10^3)^{n_2(t)}$
$b3$	1.5	5	4×10^3
$c1$	7	10	5×10^3
$c2$	3.5	$(20)^{n_3(t)}$	$(7.5 \times 10^3)^{n_3(t)}$
$c3$	5	12	1×10^3

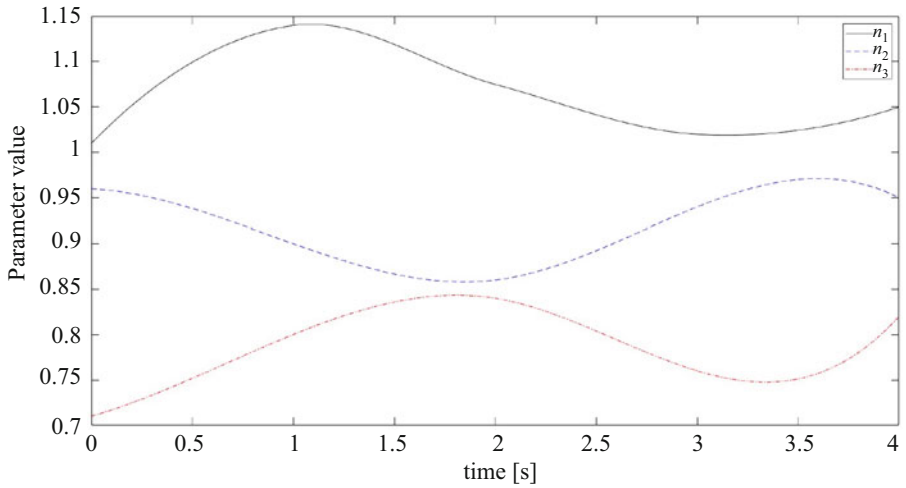

Fig. 9.4 Variation of the value of parameters n_1, n_2, and n_3 over time

Table 9.2 Parameter values at the fixed operating conditions used to define the LPV models

Parameter	Fixed condition 1	Fixed condition 2	Fixed condition 3	Fixed condition 4
n_1	1	1.05	1.1	1.15
n_2	0.85	0.9	0.95	1
n_3	0.7	0.75	0.8	0.85

with respect to the value of variables n_1, n_2, and n_3, respectively. The value of these variables is assumed to vary over time as depicted in Fig. 9.4. Each of the curves shown in this figure was discretized with a sampling frequency of 2×10^4 Hz. Then, for each mechanical system, analytical state-space models were computed at each time sample.

After having computed the analytical state-space models, an LPV model for each of the three components must be defined. It was found that four different state-space models representative of the dynamics of each component for four different operating conditions is enough to capture the influence of parameters n_1, n_2, and n_3 on the dynamics of components A, B, and C, respectively. The value of the time-dependent parameters associated with the set of state-space models used to define each of the LPV models is shown in Table 9.2. The state-space models used to define the LPV models representative of components A, B, and C were obtained analytically and then were transformed into modal form (see expression (9.15)). In this way, the sets of state-space models used to construct each of the LPV models were not directly represented in a coherent form (which is the common situation in practice). Thus, the procedures discussed in Sect. 9.3 were applied to coherently represent each set of state-space models. To scale both output and input matrices of each state-space model, a normalization of each row of the input matrix with respect to the first input was performed. Figures 9.5, 9.6, and 9.7 show the comparison of some FRFs of the set of analytical state-space models with the FRFs of the correspondent coherent representation used to set up the LPV models for components A, B, and C, respectively. By observing these figures, we may verify that by scaling both output and input matrices as discussed in Sect. 9.3 the FRFs of the state-space models remain unchanged. Therefore, the input–output properties of the models are also not affected by the scaling procedure.

From the coherent sets of state-space models, LPV models representative of the dynamics of components A, B, and C were constructed. The construction of these models was performed by parameterizing the associated time-dependent variable in the multisimplex Λ of dimension $N = 2$. Moreover, each of the LPV models was assumed to present a homogeneous

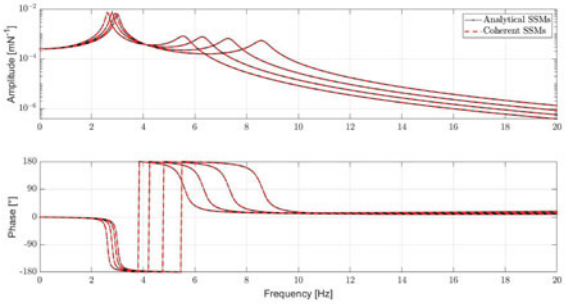

(a) Displacement FRFs, whose output is the DOF a_1 and the input is the DOF a_2.

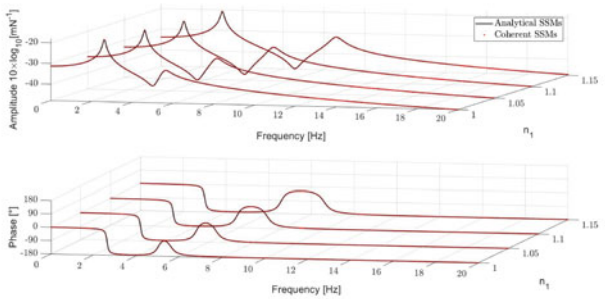

(b) Driving point displacement FRFs, whose output and input is the DOF a_2.

Fig. 9.5 Comparison of some displacement FRFs of the set of analytical state-space models with the same displacement FRFs of their correspondent coherent representation used to set up an LPV model representative of the dynamics of component A

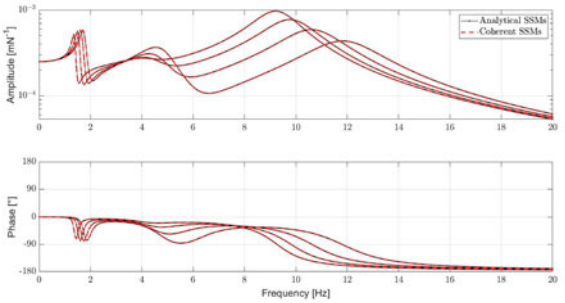

(a) Driving point displacement FRFs, whose output and input is the DOF b_3.

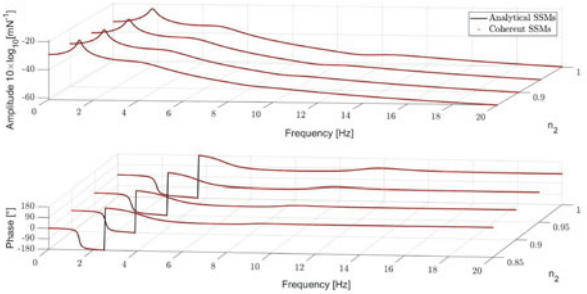

(b) Displacement FRFs, whose output is the DOF b_1 and the input is the DOF b_2.

Fig. 9.6 Comparison of some displacement FRFs of the set of analytical state-space models with the same displacement FRFs of their correspondent coherent representation used to set up an LPV model representative of the dynamics of component B

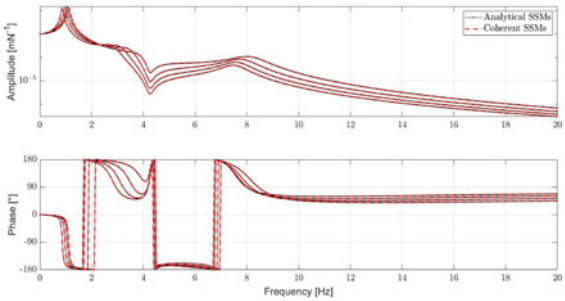

(a) Displacement FRFs, whose output is the DOF c_2 and the input is the DOF c_3.

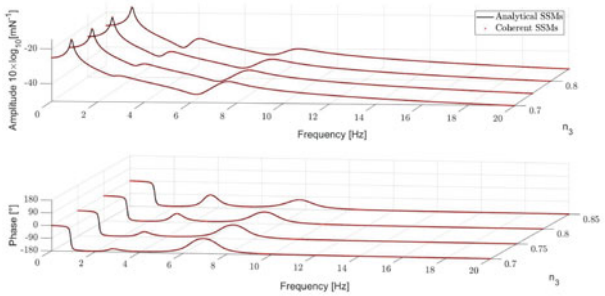

(b) Driving point displacement FRFs, whose output and input is the DOF c_1.

Fig. 9.7 Comparison of some displacement FRFs of the set of analytical state-space models with the same displacement FRFs of their correspondent coherent representation used to set up an LPV model representative of the dynamics of component C

polynomial dependency on the correspondent time-dependent variable of degree $g = 3$, because it was found that this choice leads to the computation of LPV models with associated error vectors presenting the lowest 2-norms (see equation (9.29)). By solving the linear least-squares problem described in Sect. 9.3 the system matrices of each of the LPV models were computed. As validation, state-space models for operating fixed conditions in between the fixed conditions associated with the set of models used to define the LPV models were calculated (see Table 9.3). Figures 9.8, 9.9 and 9.10 show the comparison of the FRFs of the analytical state-space models with the FRFs of the interpolated state-space models calculated by using the defined LPV models.

Table 9.3 Parameter values at the fixed operating conditions used to validate the LPV models

Parameter	Fixed condition 1	Fixed condition 2	Fixed condition 3	Fixed condition 4
n_1	1.025	1.075	1.115	1.135
n_2	0.875	0.915	0.935	0.97
n_3	0.715	0.735	0.775	0.825

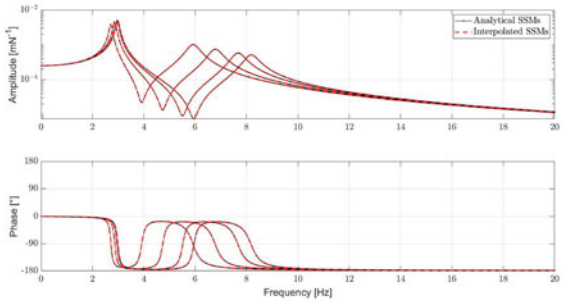

(a) Driving point displacement FRFs, whose output and input is the DOF a_1.

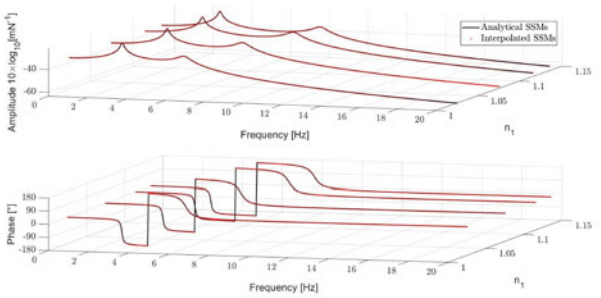

(b) Displacement FRFs, whose output is the DOF a_2 and the input is the DOF a_1.

Fig. 9.8 Comparison of some displacement FRFs of the analytical state-space models of component A associated with the fixed conditions given in Table 9.3 with the same FRFs of the interpolated state-space models obtained by using the computed LPV model representative of the dynamics of system A

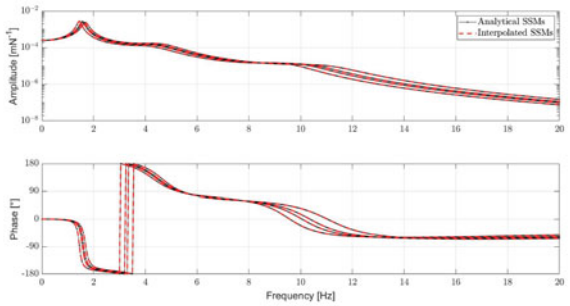

(a) Displacement FRFs, whose output is the DOF b_3 and the input is the DOF b_1.

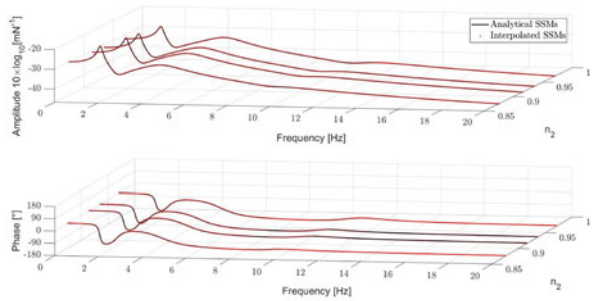

(b) Driving point displacement FRFs, whose output and input is the DOF b_2.

Fig. 9.9 Comparison of some displacement FRFs of the analytical state-space models of component B associated with the fixed conditions given in Table 9.3 with the same FRFs of the interpolated state-space models obtained by using the computed LPV model representative of the dynamics of system B

By observing Figs. 9.8, 9.9, and 9.10, we may conclude that the FRFs of the interpolated models obtained from the established LPV models very well match the FRFs of the correspondent analytical state-space models. Therefore, we may claim that the constructed LPV models are reliable to represent the dynamics of components A, B, and C when submitted to fixed operating conditions characterized by a value of the time-varying parameter in $1 \leq n_1 \leq 1.15$, $0.85 \leq n_2 \leq 1$ and $0.7 \leq n_3 \leq 0.85$, respectively.

At this point, the assembly AB (see Fig. 9.2) will be studied by assuming that the component A is a source. The analysis will be performed for a time period of 4 s. It will be assumed that the source is switched on during 1 s generating a constant load of 10 N acting at DOF a_1. After this period, the source is switched off and the load acting in DOF a_1 vanishes.

To validate the state-space realization of the in-situ component-based TPA method presented in Sect. 9.2 an equivalent force acting at the interface between components A and B will be determined in time domain. Before implementing the state-space realization of the in-situ component-based TPA method, the operational response of the assembly AB must be calculated. To determine the operational responses of assembly AB, we have discretized each of the analytical state-space models representative of the dynamics of assembly AB at each time sample by using a sampling frequency of 2×10^4 Hz and the first-order-hold method (see [24]). Then, the operational responses of assembly AB were computed by using the discretized state-space models as follows:

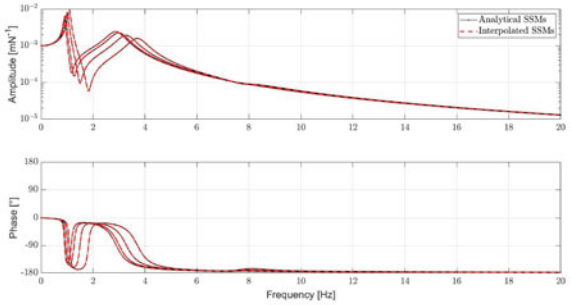

(a) Driving point displacement FRFs, whose output and input is the DOF c_3.

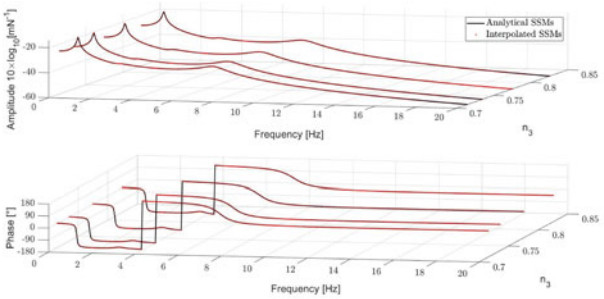

(b) Displacement FRFs, whose output is the DOF c_2 and the input is the DOF c_1.

Fig. 9.10 Comparison of some displacement FRFs of the analytical state-space models of component C associated with the fixed conditions given in Table 9.3 with the same FRFs of the interpolated state-space models obtained by using the computed LPV model representative of the dynamics of system C

$$\begin{aligned}
\{x^{AB}(k+1)\} &= \left[A^{AB}(k)\right]\left\{x^{AB}(k)\right\} + \left[B^{AB}(k)\right]\begin{Bmatrix} u_{a_1}^{AB}(k) \\ u_{J}^{AB}(k) \\ u_{b_2}^{AB}(k) \\ u_{b_3}^{AB}(k) \end{Bmatrix} \\
\begin{Bmatrix} \ddot{y}_{a_1}^{AB}(k) \\ \ddot{y}_{J}^{AB}(k) \\ \ddot{y}_{b_2}^{AB}(k) \\ \ddot{y}_{b_3}^{AB}(k) \end{Bmatrix} &= \left[\, C_{accel}^{AB}(k) \,\right]\{x^{AB}(k)\} + \left[\, D_{accel}^{AB}(k) \,\right]\begin{Bmatrix} u_{a_1}^{AB}(k) \\ u_{J}^{AB}(k) \\ u_{b_2}^{AB}(k) \\ u_{b_3}^{AB}(k) \end{Bmatrix}
\end{aligned} \tag{9.30}$$

where k denotes the sample under analysis and superscript AB denotes variables associated with a state-space model representative of assembly AB. The same approach was exploited to compute the operational responses of assembly AC. It is worth mentioning that even though the responses computed by using expression (9.30) are denoted as analytical from now on, when dealing with structures presenting a nonlinear mechanical behavior, they will in fact represent linearized responses of the system. Obviously, as the used sampling frequency to discretize the state-space models is increased, better will be the match between the exact and the linearized responses.

By using the state-space realization of the in-situ component-based TPA method and the operating acceleration responses at the interface DOF and at DOFs b_2 and b_3 of assembly AB, we aim at characterizing the source by determining an equivalent force. However, to compute the equivalent force by following this approach, acceleration state-space models representative of the assembly AB at each time sample must be available. These state-space models will be computed by exploiting two different strategies. In the first strategy, the intended state-space models will be obtained by coupling with LM-SSS the analytical displacement models (see, [25]) representative of the dynamics of systems A and B at each sample. The redundant states originating from each coupling operation will be eliminated by following the postprocessing procedure presented in [26] that relies on the use of a Boolean localization matrix. In the second methodology, the coupled state-space models will be computed by coupling the displacement models of substructures A and B obtained at each sample from the interpolating LPV models. Note that, as the state-space models obtained from the interpolating LPV models are represented in the modal domain, before being coupled, they were transformed into unconstrained coupling form (UCF) (see, [25]) in order to enable the elimination of the redundant states originating from the coupling operations. Once again, the elimination of the redundant states was performed by following the postprocessing procedure presented in [26] that relies on the use of a Boolean localization matrix. Both described methodologies lead to the computation of displacement coupled state-space models; hence, we are required to double-differentiate them (see, [27]) in order to obtain the coupled acceleration state-space models of assembly AB required by the state-space realization of the in-situ component-based TPA method presented in Sect. 9.2.

Figure 9.11a shows the comparison of (a) the analytical equivalent force in time domain (see expression (9.6)), (b) the equivalent forces estimated by using the state-space realization of the in-situ component-based TPA method with the coupled state-space models obtained at each sample from the analytical models of components A and B, and (c) the equivalent forces estimated by using the state-space realization of the in-situ component-based TPA method with the coupled state-

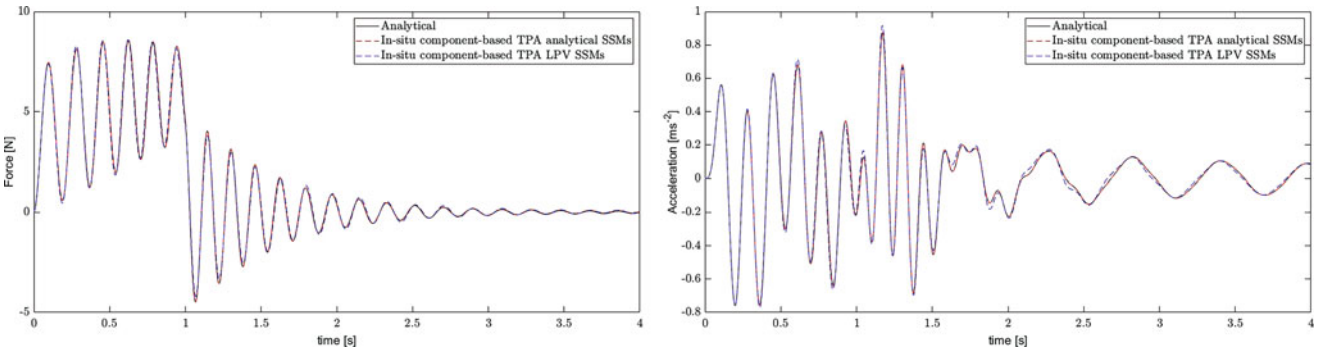

Fig. 9.11 Comparison of the computed equivalent force and of the operational acceleration response at the DOF c_2 of assembly AC by following three different methodologies

space models obtained at each sample from the state-space models of components A and B computed with the defined interpolating LPV models. Figure 9.11b presents the comparison of (i) the reference operational acceleration response at DOF c_2 of the assembly AC, (ii) the estimated operational acceleration response at the same DOF computed by using the equivalent forces obtained with approach (b) and the acceleration coupled state-space models representative of assembly AC computed by coupling at each sample the analytical models of components A and C; and (iii) the estimated operational acceleration response at DOF c_2 of assembly AC by exploiting the equivalent force computed with methodology (c) and the coupled state-space models representative of assembly AC obtained by coupling at each sample the models representative of components A and C determined from the respective LPV models.

Figure 9.11a suggests that the estimated equivalent force by following approach (b) perfectly matches the analytical equivalent force. More importantly, the operational responses at the passive side of assembly AC (which is composed of the same source as assembly AB, but by a different passive component) estimated with this equivalent force perfectly match the analytical operational responses of this assembly. Hence, proving that the equivalent force computed by the state-space realization of the in-situ component-based TPA method is an inherent property of the source itself and, thus, transferable to structures composed of the same source linked to any other passive component.

As far as the equivalent force estimated with the methodology (c) is concerned, we may conclude that it is well-matching the analytical equivalent force, leading to a well-matching reconstruction of the operational response at the DOF c_2 of assembly AC (see Fig. 9.11). Thus, we may claim that the joint use of the state-space realization of the in-situ component-based TPA with coupled state-space models computed by coupling models estimated from LPV models represents a reliable approach to compute equivalent forces in time domain, when dealing with systems presenting time-varying dynamic behavior.

To demonstrate the benefit of taking into account the time-varying dynamic behavior of assembly AB, the equivalent force was recomputed by only using the coupled state-space model representative of AB for $n_1 = n_2 = 1$, hence by neglecting the time variation of the dynamics of assembly AB. Figure 9.12a shows the comparison of this equivalent force with the analytical equivalent force and with the equivalent force obtained from methodology (c). By using the equivalent force computed by assuming that the dynamics of assembly AB remain unchanged over time and by using the analytical state-space model representative of assembly AC for $n_1 = 1$ and $n_3 = 0.7$, the operating acceleration response at DOF c_2 of assembly AC was predicted. Figure 9.12b reports the comparison between the predicted operational response at DOF c_2 of assembly AC without taking into account the time variation of the dynamics of both assemblies AB and AC with the reference operational acceleration response and with the same operational response computed by following approach (iii).

By observing Fig. 9.12a, it is straightforward to conclude that the computed equivalent force without taking into account the time-varying dynamical behavior of the assembly AB is not representative of the analytical solution. Moreover, the quality of the reconstructed operational response at the DOF c_2 of assembly AC is poor (see Fig. 9.12b). The poor results are a direct consequence of neglecting the time variation of the mechanical properties of several components. Hence, we may conclude that it is worth using interpolating LPV models to take into account the time-varying behavior of the systems under analysis. Indeed, even though the interpolating LPV models are not capable of perfectly estimating state-space models for intermediate operating conditions, the time-varying mechanical behavior can still be accurately described, leading to good quality solutions (see Fig. 9.12). Conversely, neglecting important variations of the dynamics of the structures under analysis can lead to poor solutions as demonstrated in Fig. 9.12.

As a final note, it is worth mentioning that in practice it is not common to compute equivalent forces by using operational responses collected at the interface of the source with the passive system. Nevertheless, as in this section we dealt with a

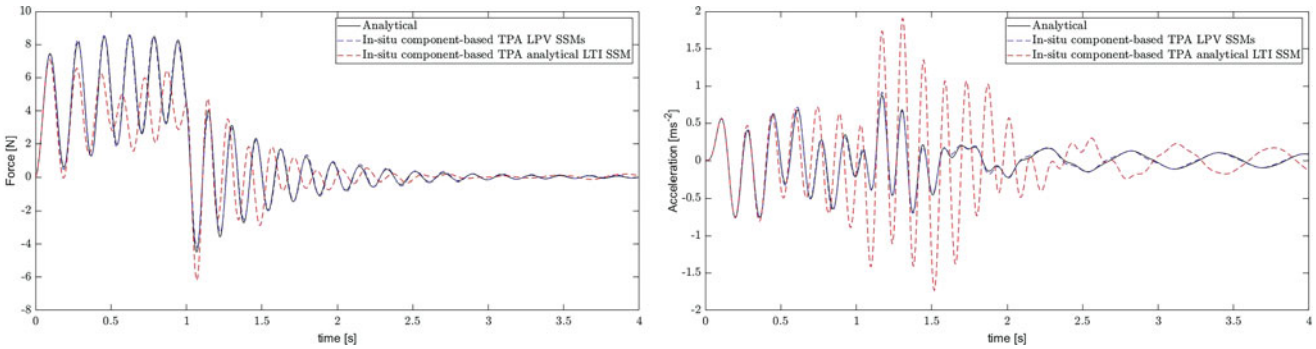

Fig. 9.12 Comparison of the computed equivalent force (Fig. 9.12a) and operational acceleration response at the DOF c_2 of assembly AC (Fig. 9.12b) by following two different methodologies that take into account the time-varying dynamical behavior of the assemblies AB and AC with the computed equivalent force and operational acceleration response at the DOF c_2 of assembly AC by using an approach that neglects the time-varying behavior of the assemblies AB and AC

numerical example, we were forced to use interface operational responses to estimate the equivalent forces by using the state-space realization of the in-situ component-based TPA method; otherwise, we would be required to invert a null matrix. In an experimental scenario, this issue will in general not be faced because state-space models estimated from experimental data do not present a diagonal feed-through matrix.

9.5 Conclusion

The state-space realization of the in-situ component-based TPA presented in this chapter demonstrated to be valid to compute time-domain equivalent forces when dealing with structures presenting time-varying dynamic behavior (see Sect. 9.4). Furthermore, the use of interpolating LPV models to take into account time variations on the dynamic properties of the systems under analysis showed to be promising, enabling good estimations of equivalent forces. Thereby, opening perspectives to apply the methodologies here described in real-case scenarios.

Acknowledgments This project received funding from the European Union's Framework Programme for Research and Innovation Horizon 2020 (2014–2020) under the Marie Sklodowska-Curie Grant Agreement n° 858018.

References

1. Penne, F.: Shaping the sound of the next-generation BMW. In: Proceedings of the International Conference on Noise and Vibration Engineering (ISMA), Leuven, pp. 25–39 (2004)
2. van der Auweraer, H., Mas, P., Dom, S., Vecchio, A., Janssens, K., van de Ponseele, P.: Transfer path analysis in the critical path of vehicle refinement: the role of fast, hybrid and operational path analysis. SAE Technical Paper 2007-01-2352 (2007)
3. Wagner, P., Bianciardi, F., Corbeels, P., Hülsmann, A.: High frequency source characterization of an e-motor using component-based TPA. SIA NVH Comfort 2021 (2021)
4. van der Seijs, M.V., de Klerk, D., Rixen, D.J.: General framework for transfer path analysis: history, theory and classification of techniques. Mech. Syst. Sig. Proces. **68–69**, 217–244 (2016)
5. Sturm, M., Moorhouse, A.: Robust calculation of simultaneous multichannel blocked force signatures from measurements made in-situ using an adaptive algorithm in time domain. In: Proceedings of the 20th InInternational Congress on Sound and Vibration (ICSV), Bangkok, vol. 2, pp. 1610–1617 (2013)
6. Allen, M.S., Carne, T.G.: Delayed, multi-step inverse structural filter for robust force identification. Mech. Syst. Sig. Proces. **22**(5), 1036–1054 (2008)
7. Mao, Y.M., Guo, X.L., Zhao, Y.: A state space force identification method based on Markov parameters precise computation and regularization technique. J. Sound Vib. **329**, 3008–3019 (2010)
8. Haeussler, M., Klaassen, S.W.B., Rixen, D.J.: Experimental twelve degree of freedom rubber isolator models for use in substructuring assemblies. J. Sound Vib. **474**, 115253 (2020)
9. De Caigny, J., Camino, J.F., Swevers, J.: Interpolating model identification for siso linear parameter-varying systems. Mech. Syst. Sig. Proces. **23**, 2395–2417 (2009)

10. De Caigny, J., Camino, J.F., Swevers, J.: Interpolation-based modeling of MIMO LPV systems. IEEE Trans. Control Syst. Technol. **19**(1), 46–63 (2011)
11. De Caigny, J., Pintelon, R., Camino, J.F., Swevers, J.: Interpolated modeling of LPV systems. IEEE Trans. Control Syst. Technol. **22**(6), 2232–2246 (2014)
12. Steltzner, A., Kammer, D.: Input force estimation using an inverse structural filter. In: 17th InInternational Modal Analysis Conference, Kissimmee, FL, pp. 954–960 (1999)
13. Vettori, S., Di Lorenzo, E., Peeters, B., Luczak, M.M., Chatzi, E.: An adaptive-noise augmented kalman filter approach for input-state estimation in structural dynamics. Mech. Syst. Sig. Proces. **184**, 109654 (2023)
14. Almirón, J.O., Bianciardi, F., Corbeels, P., Ullmann, R., Desmet, W.: Mount characterization analysis in the context of FBS for component-based TPA on a wiper system. Forum Acusticum 2020, Lyon (2020)
15. Elliott, A.S., Moorhouse, A.T.: Characterisation of structure borne sound sources from measurement in-situ. J. Acoust. Society Am. **123**, 3176–3176 (2008)
16. Moorhouse, A.T., Elliott, A.S., Evans, T.A.: In situ measurement of the blocked force of structure-borne sound sources. Mech. Syst. Sig. Proces. **325**, 679–685 (2009)
17. McKelvey, T., Akcay, H., Ljung, L.: Subspace-based multivariable system identification from frequency response data. IEEE Trans. Autom. Control **41**, 960–979 (1996)
18. Ljung, L.: System Identification Theory for the User, 2nd ed. Prentice Hall, Upper Saddle River (1999)
19. El-Kafafy, M., Peeters, B.: A Robust Identification of Stable MIMO Modal State Space Models. In: Dilworth, B.J., Marinone, T., Mains, M. (eds.) Topics in Modal Analysis & Parameter Identification, vol. 8. Conference Proceedings of the Society for Experimental Mechanics Series, pp. 81–95. Springer, Cham (2023)
20. Dias, R.S.O., Martarelli, M., Chiariotti, P.: State-space domain virtual point transformation for state-space identification in dynamic substructuring. In: Proceedings of ISMA 2022 – International Conference on Noise and Vibration Engineering and USD 2022 – International Conference on Uncertainty in Structural Dynamics (2022)
21. Peeters, B., Van der Auweraer, H., Guillaume, P., Leuridan, J.: The polymax frequency-domain method: a new standard for modal parameter estimation? Schock Vib. **11**, 395–409 (2004)
22. El-Kafafy, M., Peeters, B., Guillaume, P., De Troyer, T.: Constrained maximum likelihood modal parameter identification applied to structural dynamics. Mech. Syst. Sig. Proces. **72–73**, 567–589 (2016)
23. Yung, J.H.: Gain scheduling for geometrically nonlinear flexible space structures (PhD dissertation). Massachusetts Institute of Technology, Cambridge (2002)
24. Franklin, G.F., Powell, D.J., Workman, M.L.: Digital Control of Dynamic Systems, 3rd edn. Prentice Hall, Hoboken (1997)
25. Dias, R.S.O., Martarelli, M., Chiariotti, P.: On the use of lagrange multiplier state-space substructuring in dynamic substructuring analysis. Mech. Syst. Sig. Proces. **180** (2022)
26. Dias, R.S.O., Martarelli, M., Chiariotti, P.: Lagrange Multiplier State-Space Substructuring. J. Phys. Conf. Ser. **2041**(1), 012016 (2021)
27. Lembregts, F., Leuridan, J., Van Brussel, H.: Frequency domain direct parameter identification for modal analysis: state space formulation. Mech. Syst. Sig. Proces. **4**, 65–75 (1990)

Chapter 10
Isolation and Expansion of Gyroscopic Effects Using Frequency-Based Substructuring

Michael Kreutz and Daniel J. Rixen

Abstract Due to gyroscopic effects, the dynamics of rotating machinery depend on the rotational speed. In order to experimentally determine a machine's dynamics, measurements for each rotational speed are required. A method using frequency-based substructuring to extrapolate the speed-dependent dynamics is presented for a system with gyroscopic forces. In an isolation step, the dynamics of the rotating system are decoupled from the dynamics of the nonrotating system, which yields the gyroscopic terms. In an expansion step, the isolated gyroscopic terms can be extrapolated to an arbitrary speed. This is coupled with the dynamics of the nonrotating system for the dynamics of the rotating system at an arbitrary speed. Here, the frequency response function must only be measured for the rotor at standstill and at one rotational speed. The FBS method gives good results as long as the interface is rigid enough. Also, another method that divides the dynamic stiffness into symmetric and skew-symmetric parts is presented, which only needs FRFs at one rotational speed. It gives slightly worse results than the FBS method in the current implementation.

Keywords Substructuring · FRF · Rotor · Gyroscopic · VPT

10.1 Gyroscopic Terms

The dynamics of rotor systems depend on the rotational speed. Most important are gyroscopic effects that arise due to the titling of rotating discs (see Fig. 10.1).

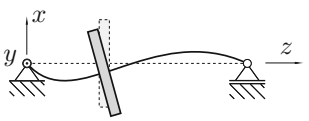

Fig. 10.1 Rotor with tilting disc

The linearized dynamic equations of a rotor system observed from an inertial position can be written as, cf. [1, 2],

$$\boldsymbol{M}\ddot{\boldsymbol{q}} + \left(\boldsymbol{C} + \Omega\tilde{\boldsymbol{G}}\right)\dot{\boldsymbol{q}} + \boldsymbol{K}\boldsymbol{q} = \boldsymbol{f}, \tag{10.1}$$

with the mass $\boldsymbol{M}$, damping $\boldsymbol{C}$, stiffness matrix $\boldsymbol{K}$, and the gyroscopic matrix $\boldsymbol{G} = \Omega\tilde{\boldsymbol{G}}$ with the rotational speed Ω and the external forcing $\boldsymbol{f}$. The generalized gyroscopic matrix $\tilde{\boldsymbol{G}}$ is constant, skew-symmetric, and has entries only in degrees of freedom corresponding to angles. For a *Laval* rotor with a tilting rigid disc, the gyroscopic matrix can be written as

M. Kreutz (✉) · D. J. Rixen
Chair of Applied Mechanics, TUM School of Engineering and Design, Technical University of Munich, Garching, Germany
e-mail: m.kreutz@tum.de; rixen@tum.de

M. Allen et al. (eds.), *Dynamic Substructures, Volume 4*, Conference Proceedings of the Society for Experimental Mechanics Series, https://doi.org/10.1007/978-3-031-36694-9_10

$$\boldsymbol{G} = \Omega\tilde{\boldsymbol{G}} = \Omega \begin{bmatrix} 0 & 0 & 0 & 0 \\ 0 & 0 & 0 & 0 \\ 0 & 0 & 0 & J_p \\ 0 & 0 & -J_p & 0 \end{bmatrix}, \qquad \text{with } \boldsymbol{q} = \begin{bmatrix} x \\ y \\ \varphi_x \\ \varphi_y \end{bmatrix} \tag{10.2}$$

where J_p is the polar moment of inertia of the disc. The polar moment of inertia can be computed from a 3D model of the disc for numerical simulations. The inertia can also be obtained experimentally by doing pendulum experiments and weighing the system; cf. [3]. In this contribution, a method using frequency-based substructuring (FBS) is shown to obtain the gyroscopic matrix of a system through frequency response measurements.

10.2 Isolation and Expansion Using Frequency-Based Substructuring

Frequency-based substructuring is used in structural dynamics to couple and decouple the dynamics of subsystems using FRFs. Here, it is used to isolate and expand the effect of gyroscopic effects from experimental measurements. For an overview of FBS, see [4–6].

The method to extrapolate the gyroscopic effects using FBS is divided in two steps: an isolation step to obtain the gyroscopic matrix and an expansion step to extrapolate the dynamics for a different rotation speed. The extrapolation step is very similar to the method presented in [7].

10.2.1 Isolation

In the isolation step, the dynamics of the rotating system are decoupled from the dynamics of the nonrotating system, which yields the gyroscopic terms. This step is shown schematically in Fig. 10.2.

Frequency response functions of the nonrotating system $\boldsymbol{Y}^0_{uf}$ and of the rotating system $\boldsymbol{Y}^{\mathrm{op1}}_{uf}$ with rotational speed Ω_1 are measured for many points, close to the disc with the main gyroscopic effect. FRFs that are directly measured in the space of the sensors and impacts are indicated by the subscript $_{uf}$.

10.2.1.1 Virtual Point Transformation

Using a virtual point transformation, the measured FRFs are transformed in the space of $\boldsymbol{q} = \left[x,\ y,\ \varphi_x,\ \varphi_y\right]^T$, which is indicated by the subscript $_q$.

$$\boldsymbol{Y}_q = \boldsymbol{T}_u \boldsymbol{Y}_{uf} \boldsymbol{T}_f^T.$$

Rigidity is assumed for the virtual point transformation. So, the transformation matrices $\boldsymbol{T}_u$, $\boldsymbol{T}_f$ are found from geometry; see [4].

Specifically, for the given space of $\boldsymbol{q}$, the transformation matrices $\boldsymbol{R}_u$ and $\boldsymbol{R}_f$ can be obtained from

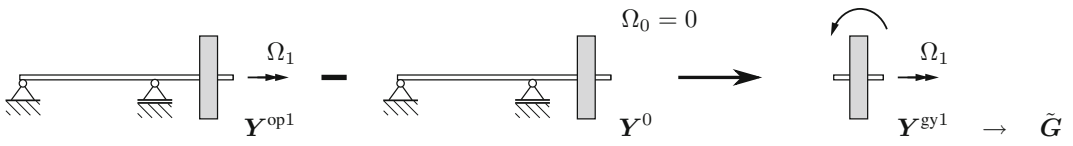

Fig. 10.2 Scheme of the isolation step

$$u^k = \underbrace{\begin{bmatrix} e_x^k, & e_y^k, & e_z^k \end{bmatrix} \begin{bmatrix} 1 & 0 & 0 & r_z^k \\ 0 & 1 & -r_z^k & 0 \\ 0 & 0 & r_y^k & -r_x^k \end{bmatrix}}_{\boldsymbol{R}^k} \underbrace{\begin{bmatrix} x \\ y \\ \varphi_x \\ \varphi_y \end{bmatrix}}_{\boldsymbol{q}}, \qquad k = 1 \dots N \quad (N \text{ sensor channels})$$

where $\begin{bmatrix} r_x^k, & r_y^k, & r_z^k \end{bmatrix}^T$ is the vector from the virtual point to the sensor location and $\begin{bmatrix} e_x^k, & e_y^k, & e_z^k \end{bmatrix}^T$ is the direction vector of the sensor channel; both are expressed in the virtual point coordinate system. The matrices for each sensor channel are stacked to obtain $\boldsymbol{R}$. In general, the resulting matrices $\boldsymbol{R}_u, \boldsymbol{R}_f$ are overdetermined, so the transformation matrices $\boldsymbol{T}_u, \boldsymbol{T}_f$ are obtained from a pseudo-inverse.

10.2.1.2 Decoupling

Now the matrices can be decoupled by Lagrange multiplier frequency-based substructuring (LM-FBS) resulting in an FRF $\boldsymbol{Y}_q^{\mathrm{gy1}}$ or by primal decoupling resulting in a dynamic stiffness $\boldsymbol{Z}_q^{\mathrm{gy1}}$; cf. [4].

Primal Decoupling

Primal decoupling is easy to write and understand because it is so similar to the assembly process in finite element models. For primal decoupling, all degrees of freedom (dofs) q can be used to decouple the matrices. Here, we only use interface degrees of freedom, that is, no internal dofs of the system. The procedure of primal decoupling can be written as

$$\boldsymbol{Z}_q^{\mathrm{gy1}} = \boldsymbol{Z}_q^{\mathrm{op1}} - \boldsymbol{Z}_q^0 \qquad \text{with } \boldsymbol{Z}_q^0 = \left(\boldsymbol{Y}_q^0\right)^{-1}, \quad \boldsymbol{Z}_q^{\mathrm{op1}} = \left(\boldsymbol{Y}_q^{\mathrm{op1}}\right)^{-1}.$$

The resulting dynamic stiffness $\boldsymbol{Z}_q^{\mathrm{gy1}}$ is then partitioned to extract the angle dofs $\boldsymbol{q}_p = \begin{bmatrix} \varphi_x, & \varphi_y \end{bmatrix}^T$,

$$\boldsymbol{Z}_{q_p}^{\mathrm{gy1}} = \begin{bmatrix} \boldsymbol{0}_{2\times 2}, & \boldsymbol{I}_{2\times 2} \end{bmatrix} \boldsymbol{Z}_q^{\mathrm{gy1}} \begin{bmatrix} \boldsymbol{0}_{2\times 2} \\ \boldsymbol{I}_{2\times 2} \end{bmatrix},$$

with the 2-by-2 zero matrix $\boldsymbol{0}_{2\times 2}$ and the identity matrix $\boldsymbol{I}_{2\times 2}$.

Lagrange Multiplier Frequency-Based Substructuring

The LM-FBS procedure in matrix form can be written as

$$\boldsymbol{Y}_q^{\mathrm{op1-0}} = \boldsymbol{Y}_q^{\mathrm{op1|-0}} - \boldsymbol{Y}_q^{\mathrm{op1|-0}} \boldsymbol{B}^T \left(\boldsymbol{B} \boldsymbol{Y}_q^{\mathrm{op1|-0}} \boldsymbol{B}^T\right)^{-1} \boldsymbol{B} \boldsymbol{Y}_q^{\mathrm{op1|-0}}$$

$$\text{with} \quad \boldsymbol{Y}_q^{\mathrm{op1|-0}} = \begin{bmatrix} \boldsymbol{Y}_q^{\mathrm{op1}} & \boldsymbol{0} \\ \boldsymbol{0} & -\boldsymbol{Y}_q^0 \end{bmatrix} \quad \text{and} \quad \boldsymbol{B} = \left[\boldsymbol{0}_{2\times 2} \; \boldsymbol{I}_{2\times 2} \,\middle|\, \boldsymbol{0}_{2\times 2} \; -\boldsymbol{I}_{2\times 2}\right]$$

Similarly to primal decoupling, the resulting FRF-matrix is partitioned to only keep the angle dofs.

$$\boldsymbol{Y}_{q_p}^{\mathrm{gy1}} = \begin{bmatrix} \boldsymbol{0}_{2\times 2}, & \boldsymbol{I}_{2\times 2}, & \boldsymbol{0}_{2\times 4} \end{bmatrix} \boldsymbol{Y}_q^{\mathrm{gy1}} \begin{bmatrix} \boldsymbol{0}_{2\times 2} \\ \boldsymbol{I}_{2\times 2} \\ \boldsymbol{0}_{4\times 2} \end{bmatrix}.$$

In LM-FBS, only the angle dofs are decoupled, which can be seen by the matrix $\boldsymbol{B}$, as using the whole space of $\boldsymbol{q}$ results in singular matrices in the LM-FBS decoupling procedure. Theoretically, the remainder of the decoupling procedure is only

$\boldsymbol{Y}_q^{\mathrm{gy1}} = (i\omega \boldsymbol{G})^{-1}$, which is a singular matrix, as can be seen in eq. (10.2). In appendix A, it is shown in detail where the problems in the LM-FBS decoupling arise.

10.2.1.3 Parameterization

From $\boldsymbol{Z}_{q_p}^{\mathrm{gy1}} = \left(\boldsymbol{Y}_{q_p}^{\mathrm{gy1}}\right)^{-1}$, the entries of the partitioned generalized gyroscopic matrix $\tilde{\boldsymbol{G}}_{q_p}$ are identified. The speed dependence and the frequency dependence are removed from $\boldsymbol{Z}_{q_p}^{\mathrm{gy1}}$, see eqs. (10.1) and (10.2), by

$$\tilde{\boldsymbol{G}}_{q_p}(\omega) = -\frac{i}{\omega \Omega_1} \boldsymbol{Z}_{q_p}^{\mathrm{gy1}}.$$

The generalized gyroscopic matrix $\tilde{\boldsymbol{G}}_{q_p}$ should be purely real, skew-symmetric, and independent of the frequency ω to agree with the model

$$\tilde{\boldsymbol{G}}_{q_p,\mathrm{model}} = \begin{bmatrix} 0 & J_p \\ -J_p & 0 \end{bmatrix}.$$

The model matrix is identified from the experimental $\tilde{\boldsymbol{G}}_{q_p}(\omega)$ by the following steps:

1. A frequency region with good results is chosen. In general, this can be a region of low frequency, where the rigidity assumption of the virtual point holds. However, in practice, problems can arise due to measurement noise in the low-frequency region.
2. Take the mean for each entry in the matrix for the chosen frequency region: $\tilde{\boldsymbol{G}}_{q_p,\mathrm{mean}} = \mathrm{mean}\left(\tilde{\boldsymbol{G}}_{q_p}(\omega_{\mathrm{selected}})\right)$.
3. One keep the real parts of the matrix: $\tilde{\boldsymbol{G}}_{q_p,\mathrm{real}} = \mathrm{Re}\left(\tilde{\boldsymbol{G}}_{q_p,\mathrm{mean}}\right)$.
4. Force the matrix to be skew-symmetric: $\tilde{\boldsymbol{G}}_{q_p,\mathrm{identified}} = \frac{1}{2}\left(\tilde{\boldsymbol{G}}_{q_p,\mathrm{real}} - \tilde{\boldsymbol{G}}_{q_p,\mathrm{real}}^T\right)$.

More advanced methods for the identification of the generalized gyroscopic matrix can be applied, for example, by applying a least-squares curve fit to the results from the experiment. In the example presented in this contribution, the very simple procedure was enough to identify realistic gyroscopic terms.

10.2.2 Expansion

In the expansion step, the isolated gyroscopic terms can be extrapolated to an arbitrary speed. The procedure is given schematically in Fig. 10.3. This is coupled with the dynamics of the nonrotating system to obtain the dynamics of the rotating system at an arbitrary speed. The expansion step for gyroscopic matrices is similar to the method in [7].

The gyroscopic matrix of the new configuration is extrapolated from the generalized partitioned gyroscopic matrix with the new rotation speed Ω_2

$$\boldsymbol{Z}_{q_p}^{\mathrm{gy2}} = i\omega\Omega_2 \tilde{\boldsymbol{G}}_{q_p}.$$

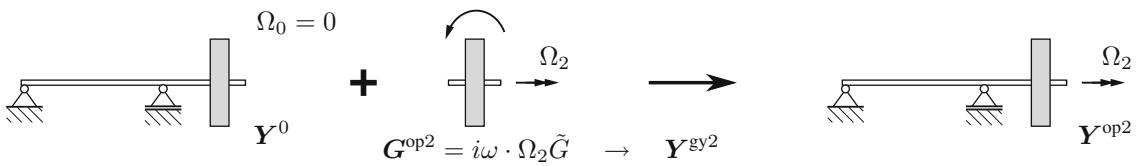

Fig. 10.3 Scheme of the expansion step

This gyroscopic matrix is then coupled with the system at standstill via primal decoupling or LM-FBS to obtain the FRF matrix of the rotating system at the new rotation speed $\boldsymbol{Y}_q^{\mathrm{op2}}$. For primal coupling, this can be written as

$$\boldsymbol{Z}_q^{\mathrm{op2}} = \boldsymbol{Z}_q^0 + \boldsymbol{Z}_q^{\mathrm{gy2}}, \qquad \text{with } \boldsymbol{Z}_q^{\mathrm{gy2}} = \begin{bmatrix} \boldsymbol{0}_{2\times 2} \\ \boldsymbol{I}_{2\times 2} \end{bmatrix} \boldsymbol{Z}_{q_p}^{\mathrm{gy2}} \left[\boldsymbol{0}_{2\times 2},\ \boldsymbol{I}_{2\times 2}\right],$$

giving the dynamic stiffness of the dynamic system at Ω_2.

10.3 Isolation and Expansion by Using Symmetry

Another idea that does not use frequency-based substructuring is to identify the gyroscopic effects by using the symmetry of the dynamic stiffness.

This can be applied when the only source of skew-symmetry comes from gyroscopic effects. When there are rotor components with asymmetric dynamic matrices, it is hard to distinguish the source. Also, some components may have speed-dependent dynamics that arise in the symmetric part.

As an isolation step, the system matrices are divided into a symmetric and skew-symmetric part:

$$\boldsymbol{Z}_{\mathrm{sym}} = \frac{1}{2}\left(\boldsymbol{Z} + \boldsymbol{Z}^T\right) = -\omega^2 \boldsymbol{M} + j\omega \boldsymbol{C} + \boldsymbol{K}$$
$$\boldsymbol{Z}_{\mathrm{skew}} = \frac{1}{2}\left(\boldsymbol{Z} - \boldsymbol{Z}^T\right) = j\omega \boldsymbol{G}.$$

The symmetric part only includes nonspeed-dependent dynamics. The skew-symmetric part contains the speed-dependent gyroscopic matrix.

For an expansion of the gyroscopic matrix, we can apply

$$\boldsymbol{Z}^{\mathrm{op2}} = \boldsymbol{Z}_{\mathrm{sym}}^{\mathrm{op1}} + \boldsymbol{Z}_{\mathrm{skew}}^{\mathrm{op1}} \cdot \frac{\Omega_2}{\Omega_1},$$

which gives the dynamics of the rotor system at the rotational speed Ω_2. It is interesting that this method only needs FRFs at one rotational speed and does not need FRFs at standstill.

The presented procedure can be performed directly in the uf-space, the space of the sensor channels. A virtual point transformation is not needed. Still, a VPT could be performed if the value of J_p should be found analytically.

In this contribution, the method is used directly in the uf-space, without a parameterization step. The obtained $\boldsymbol{Z}_{\mathrm{skew}}^{\mathrm{op1}}(\omega)$ is used directly.

10.4 Simulation Results

The methods outlined above are applied on simulation results for simple rotor systems. The rotor systems are modeled with the open-source MATLAB rotor simulation toolbox AMrotor, see [8, 9], from finite elements using Timoshenko beam theory.

In a first step, the methods were applied to a system with a rigid interface to verify the correct implementation of the method. The results are not shown here because in that case the FBS results are very close to the exact results, as expected. This was used as a validation of the code.

A more realistic case, with a flexible rotor is considered. The system consists of a slender steel beam with length $\ell = 500\,\mathrm{mm}$, diameter $d = 8\,\mathrm{mm}$. The bearings are modeled as springs and the disc is modeled as discrete mass and inertias. The system is depicted in Fig. 10.4.

The FRFs of the system are obtained for force and response in x and y at the sensor positions. This is the minimal set of measurements to be able to reconstruct $\boldsymbol{q}$. In an experimental application, measurements at more positions should be used. An overdetermination of the virtual point transformation can filter out random measurement errors; cf. [4].

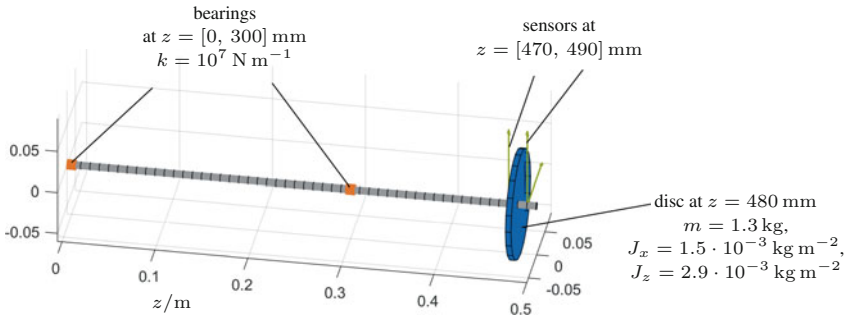

Fig. 10.4 Model of the rotor system

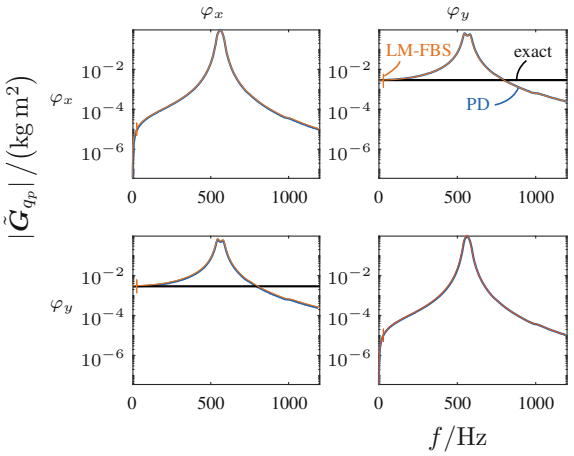

Fig. 10.5 Result of isolation step: generalized partitioned gyroscopic matrix $\tilde{\boldsymbol{G}}_{q_p}$

Results at standstill $\Omega = 0$ and at a rotational speed $\Omega_1 = 1200$ min^{-1} are used for the isolation step. The obtained gyroscopic matrix is then expanded for a very large rotational speed $\Omega_2 = 8\Omega_1 = 9600$ min^{-1}. A very large speed Ω_2 is chosen to show the limitations of the method.

The results from the isolation step are shown in Fig. 10.5, where the matrix $\tilde{\boldsymbol{G}}_{q_p}$ is given and compared to the exact values. The results of isolation using symmetry are not shown here because in this study it is performed directly in the space of uf and thus does not give values for $\tilde{\boldsymbol{G}}_{q_p}$.

Results of primal decoupling (PD) and LM-FBS are the same, except at a spurious peak around 29 Hz. This is most likely due to a bad conditioning of the inversion in the LM-FBS at this point.

The diagonal entries are expected to be zero and the off-diagonal entries to be constant $|J_p|$. It can be seen that results for low frequencies agree with the expected values. For higher frequencies, there are unwanted dynamics in the isolated generalized gyroscopic matrix. These result from local flexibility of the system between the measurement points and the disc, thus violating the rigidity assumption in the applied virtual point transformation. A constant gyroscopic matrix is identified from the results using low frequency, which gives almost the exact values of the generalized gyroscopic matrix.

The identified real, constant, skew-symmetric generalized gyroscopic matrix is used for the expansion step. Results of the expansion step are shown in Fig. 10.6. For the FBS methods, the curves of primal decoupling are shown because it looks identical to the LM-FBS curves. Figure 10.5a shows the resulting FRF back-transformed to the coordinates of sensor 1. It can be seen here that for higher frequencies, the FBS results deviate from the exact FRFs. The results using symmetry (symm), that is, $\boldsymbol{Z}_{\text{skew}}$, gives worse results. This is due to the direct usage of the frequency-dependent matrix $\boldsymbol{Z}^{\text{op1}}_{\text{skew}} \cdot \Omega_2/\Omega_1$. The identification step is beneficial for the correct expansion.

Figure 10.6b shows a Campbell diagram. This is obtained by performing the expansion for different rotational speeds and reading the eigenfrequencies from the resulting FRFs. The results agree well with exact values for low frequencies. Similar to Fig. 10.6a the prediction becomes worse for high frequencies. The results with using symmetry (symm), that is, $\boldsymbol{Z}_{\text{skew}}$, gives worse results.

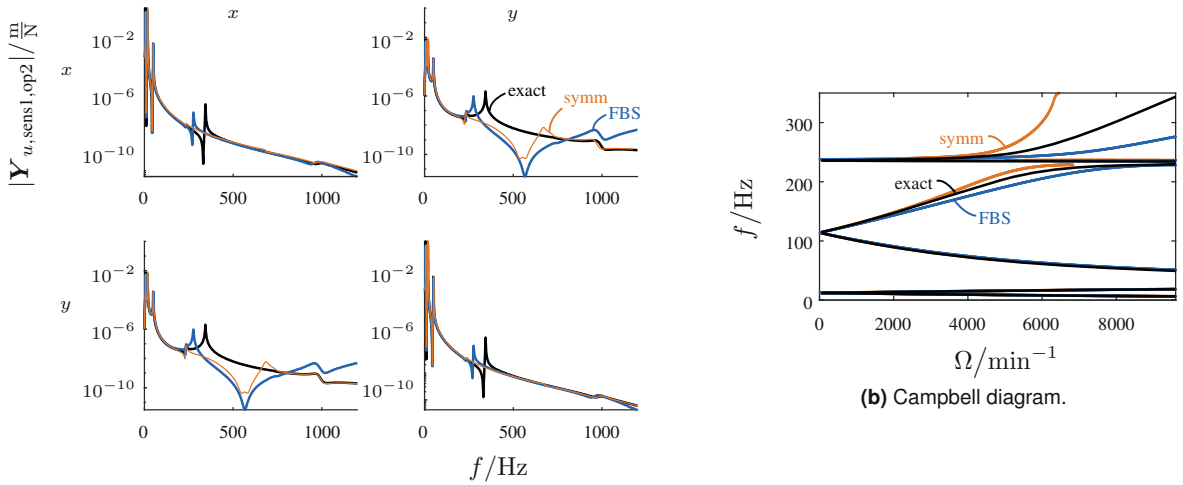

(a) FRFs at position of sensor 1.

(b) Campbell diagram.

Fig. 10.6 Results of expansion step: comparison of exact results with frequency-based substructuring

The good results of FBS for low frequencies confirm the method and also show the limitations for flexible systems and high frequencies for which the rigidity assumption of the applied virtual point transformation does not hold anymore. There seems to be no problem in extrapolating the dynamics for very high rotational speeds Ω, but results for high excitation frequencies f deteriorate. Using primal decoupling or LM-FBS gives the same results except for a spurious peak. Using the symmetry of the system matrices can be interesting, but here it gives worse results due to the missing parameterization step in the procedure applied here.

10.5 Conclusion and Outlook

An FBS method to isolate and expand the gyroscopic effects was shown. It uses FRF measurements at standstill and at one rotation speed. The method was validated by a simulation example. The expanded FRFs are good for low frequencies but show deviations to exact results for higher frequencies, where the virtual point rigidity is violated.

A method taking advantage of the symmetry of the system matrices was shown, which only needs FRFs at one rotational speed and not at standstill. However, in the current implementation, the results were worse than with the FBS-methods. Also, the method cannot distinguish different surces of asymmetry in the system matrices. Still, this method should be investigated further. Using a parameterization step like the FBS method seems beneficial to the results.

It should also be investigated how all the presented methods can handle additional components with speed-dependent behavior as, for example, additional discs or journal bearings.

A next step is the application of the presented method to an experimental system. A special challenge is in measuring the FRFs of a rotor system during rotation.

Appendix

Note on Singularity in LM-FBS

To show the singularity, when decoupling in all dofs with LM-FBS, the dofs are reordered to $\hat{\boldsymbol{q}} = \left[x,\, \varphi_y,\, y,\, \varphi_x\right]^T$. The first two dofs describe the bending of the rotor in the x-z-plane and the last two dofs describe bending in y-z-plane. This is done so that $\hat{\boldsymbol{Z}}^0$, $\hat{\boldsymbol{Z}}^{\mathrm{op1}}$ can be written in the form of block matrices. All matrices have to be reordered as well, the reordered matrices for $\hat{\boldsymbol{q}}$ are indicated by the hat-symbol $\hat{}$.

$$\hat{\boldsymbol{Z}}^0 = \begin{bmatrix} -\omega^2 \hat{\boldsymbol{M}}_x + i\omega \boldsymbol{C} + \hat{\boldsymbol{K}}_x & \boldsymbol{0}_{2\times 2} \\ \boldsymbol{0}_{2\times 2} & -\omega^2 \hat{\boldsymbol{M}}_x + i\omega \boldsymbol{C} + \hat{\boldsymbol{K}}_x \end{bmatrix} = \begin{bmatrix} \hat{\boldsymbol{Z}}_x^0 & \boldsymbol{0}_{2\times 2} \\ \boldsymbol{0}_{2\times 2} & \hat{\boldsymbol{Z}}_x^0 \end{bmatrix},$$

$$\hat{\boldsymbol{Z}}^{\mathrm{op1}} = \begin{bmatrix} \hat{\boldsymbol{Z}}_x^0 & i\omega \hat{\boldsymbol{G}}_{xy}^{\mathrm{op1}} \\ -i\omega \hat{\boldsymbol{G}}_{xy}^{\mathrm{op1}} & \hat{\boldsymbol{Z}}_x^0 \end{bmatrix}$$

The dynamic stiffness matrix $\hat{\boldsymbol{Z}}_x^0$ is symmetric because of the symmetry of $\hat{\boldsymbol{M}}, \hat{\boldsymbol{C}}, \hat{\boldsymbol{K}}$ for a symmetric rotor. The submatrix of the gyroscopic matrix $\hat{\boldsymbol{G}}_{xy}^{\mathrm{op1}}$ is also symmetric and for a rigid tilitng disc according to eq. (10.2) can be given as

$$\hat{\boldsymbol{G}}_{xy}^{\mathrm{op1}} = \begin{bmatrix} 0 & 0 \\ 0 & -\Omega J_p \end{bmatrix}$$

The LM-FBS decoupling, when decoupling in all dofs, yields

$$\begin{aligned} \hat{\boldsymbol{Y}}^{\mathrm{gy1}} &= \hat{\boldsymbol{Y}}^{\mathrm{op1}} - \hat{\boldsymbol{Y}}^{\mathrm{op1}} \left(\hat{\boldsymbol{Y}}^{\mathrm{op1}} - \hat{\boldsymbol{Y}}^0 \right)^{-1} \hat{\boldsymbol{Y}}^{\mathrm{op1}} \\ &= \Big(\boldsymbol{I} - \underbrace{\hat{\boldsymbol{Y}}^{\mathrm{op1}} \left(\hat{\boldsymbol{Y}}^{\mathrm{op1}} - \hat{\boldsymbol{Y}}^0 \right)^{-1}}_{\left(\boldsymbol{I} - \hat{\boldsymbol{Y}}^0 \left(\hat{\boldsymbol{Y}}^{\mathrm{op1}} \right)^{-1} \right)^{-1}} \Big) \hat{\boldsymbol{Y}}^{\mathrm{op1}}, \end{aligned}$$

for the last line, see also [7]. The expression in brackets is evaluated, which is easy with the chosen ordering of the dofs.

$$\begin{aligned} \left[\boldsymbol{I}_{4\times 4} - \hat{\boldsymbol{Y}}^0 \left[\hat{\boldsymbol{Y}}^{\mathrm{op1}} \right]^{-1} \right]^{-1} &= \left[\boldsymbol{I}_{4\times 4} - \begin{bmatrix} \hat{\boldsymbol{Y}}_x^0 & \boldsymbol{0}_{2\times 2} \\ \boldsymbol{0}_{2\times 2} & \hat{\boldsymbol{Y}}_x^0 \end{bmatrix} \begin{bmatrix} \hat{\boldsymbol{Z}}_x^0 & i\omega \hat{\boldsymbol{G}}_{xy}^{\mathrm{op1}} \\ -i\omega \hat{\boldsymbol{G}}_{xy}^{\mathrm{op1}} & \hat{\boldsymbol{Z}}_x^0 \end{bmatrix} \right]^{-1} \\ &= \left[\boldsymbol{I}_{4\times 4} - \begin{bmatrix} \hat{\boldsymbol{Y}}_x^0 \hat{\boldsymbol{Z}}_x^0 & i\omega \hat{\boldsymbol{Y}}_x^0 \hat{\boldsymbol{G}}_{xy}^{\mathrm{op1}} \\ -i\omega \hat{\boldsymbol{Y}}_x^0 \hat{\boldsymbol{G}}_{xy}^{\mathrm{op1}} & \hat{\boldsymbol{Y}}_x^0 \hat{\boldsymbol{Z}}_x^0 \end{bmatrix} \right]^{-1} \\ &= \begin{bmatrix} \boldsymbol{0}_{2\times 2} & -i\omega \hat{\boldsymbol{Y}}_x^0 \hat{\boldsymbol{G}}_{xy}^{\mathrm{op1}} \\ i\omega \hat{\boldsymbol{Y}}_x^0 \hat{\boldsymbol{G}}_{xy}^{\mathrm{op1}} & \boldsymbol{0}_{2\times 2} \end{bmatrix}^{-1} \\ &= \underbrace{\begin{bmatrix} -i\omega \begin{bmatrix} \hat{\boldsymbol{Y}}_x^0 & 0 \\ 0 & \hat{\boldsymbol{Y}}_x^0 \end{bmatrix} \end{bmatrix}}_{\boldsymbol{A}_1} \underbrace{\begin{bmatrix} \boldsymbol{0}_{2\times 2} & \hat{\boldsymbol{G}}_{xy}^{\mathrm{op1}} \\ -\hat{\boldsymbol{G}}_{xy}^{\mathrm{op1}} & \boldsymbol{0}_{2\times 2} \end{bmatrix}}_{\boldsymbol{A}_2}^{-1} = \boldsymbol{A}^{-1} \end{aligned}$$

The matrix $\boldsymbol{A}$ is now investigated in terms of its rank. We use the rule

$$\mathrm{rank}\left(\boldsymbol{A}_1 \boldsymbol{A}_2\right) \leq \min\left(\mathrm{rank}\left(\boldsymbol{A}_1\right), \mathrm{rank}\left(\boldsymbol{A}_2\right)\right).$$

$$\mathrm{rank}\left(A_2\right) = \mathrm{rank} \begin{bmatrix} \boldsymbol{0}_{2\times 2} & \hat{\boldsymbol{G}}_{xy}^{\mathrm{op1}} \\ -\hat{\boldsymbol{G}}_{xy}^{\mathrm{op1}} & \boldsymbol{0}_{2\times 2} \end{bmatrix} = \mathrm{rank} \begin{bmatrix} 0 & 0 & 0 & 0 \\ 0 & 0 & 0 & -\Omega J_p \\ 0 & 0 & 0 & 0 \\ 0 & 0 & \Omega J_p & 0 \end{bmatrix} = 2$$

It can be seen that the matrix $\boldsymbol{A}$ does not have full rank, thus being singular. The inversion of $\boldsymbol{A}$ fails. If the LM-FBS decoupling is only performed in the angle dofs as shown in the contribution, the singularity can be avoided.

References

1. Gasch, R., Nordmann, R., Pfützner, H.: Rotordynamik, 2nd edn. Springer, Berlin (2006)
2. Genta, G.: Dynamics of Rotating Systems. Mechanical Engineering Series, p. 660. Springer US, New York (2005). https://doi.org/10.1007/0-387-28687-X
3. Dresig, H., Holzweißig, F.: Dynamics of Machinery. Springer, Berlin (2010). https://doi.org/10.1007/978-3-540-89940-2
4. Allen, M.S., Rixen, D., Seijs, van der, M., Tiso, P., Abrahamsson, T., Mayes, R.L.: Substructuring in Engineering Dynamics. CISM International Centre for Mechanical Sciences. Springer International Publishing, Cham (2020). https://doi.org/10.1007/978-3-030-25532-9
5. Seijs, M.V., de van der Klerk, D., Rixen, D.J.: General framework for transfer path analysis: history, theory and classification of techniques. Mech. Syst. Sig. Proces. **68–69**, 217–244 (2016). https://doi.org/10.1016/j.ymssp.2015.08.004
6. De Klerk, D., Rixen, D.J., Voormeeren, S.N.: General framework for dynamic substructuring: history, review, and classification of techniques. AIAA J. **46**(5), 1169–1181 (2008). https://doi.org/10.2514/1.33274
7. Häußler, M., Reichart, R., Bartl, A., Rixen, D.J.: Post correcting for gyroscopic effects via dynamic substructuring.In: 24th International Congress on Sound and Vibration, ICSV 2017, London (2017)
8. GitHub: AMrotor – A MATLAB toolbox for the Simulation of Rotating Machinery. https://github.com/AppliedMechanics/AMrotor
9. Maierhofer, J., Kreutz, M., Mulser, T., Thümmel, T., Rixen, D.J.: AMrotor – a MATLAB ®toolbox for the simulation of rotating machinery. In: 12th International Conference on Vibrations in Rotating Machinery. Ed. by Institute of Mechanical Engineers. CRC Press, Liverpool (2020). https://doi.org/10.1201/9781003132639

Chapter 11
Development of Power Flow Sensitivity Analysis for Experimental Data Using Virtual Point Transformation

Jon Young and Kyle Myers

Abstract The equations for a power flow sensitivity analysis are developed by means of describing the coupling interface between substructures with virtual points. This analysis describes how power flow between source and receiver structures changes with respect to modifications made to the real and imaginary components of the receiver impedance; termed the real and imaginary sensitivities, respectively. Previously developed power flow sensitivity equations have been applied to analytical and numerical models, but assume source and receiver interfaces have identical meshes, and both translational and rotational dynamics are accounted for. In an experimental setting, translational dynamics can easily be measured by use of accelerometers, but rotational measurements are more difficult to make as an array of accelerometers is often needed. However, the equations derived for numerical models are cast onto a domain in which physical and virtual coordinates are accounted for, where the virtual coordinates define the coupling interface with three translational and three rotational degrees of freedom (DOFs). It is shown that the properties of the real and imaginary sensitivity still hold after this coordinate transformation. Finally, retaining internal DOFs, and the need for defining a "synthetic impedance" in the derivation of the sensitivity equations, is discussed.

Keywords Substructuring · Virtual point · Power flow sensitivity

11.1 Introduction

For the past several decades, power flow analysis has been used to quantify the vibratory response of structures. It can be used to determine energy transmission paths within an assembly of structures and allow for design changes to be made to the structure so as to reduce vibration amplitude. Several studies address calculating power flow from experimental measurements [1–6] or numerical data output from finite element models [7–12]. However, these studies focus on the calculation of power flow, not how it responds to structural modifications. Understanding how power flow changes in response to structural modifications is useful in the context of vibration reduction, particularly in an experimental setting where frequency response functions (FRFs) can readily be measured.

Previous analyses have been proposed for calculating the sensitivity of power flow to changes made in the impedance matrix of a passive receiver structure [13]. This was done by considering the source and receiver as independent substructures that were coupled using the Lagrange multiplier frequency-based substructuring (LMFBS) method and differentiating the power flow equation with respect to the receiver impedance. This approach is valid for numerically modeled structures where the translational and rotational interface degrees of freedom (DOFs) are fully defined, and the meshes on the two interfaces are compatible. In the context of experimental substructuring, where measurement of the rotational DOFs can be difficult, they must be obtained using some approximation. The virtual point transformation (VPT) has been a topic of recent research in the experimental substructuring community [14–17] and will be used here to extend the general power flow sensitivity equations to equations that can be applied to experimental data.

The VPT accounts for rotational DOFs on the interface of a substructure by using a first-order approximation from measured responses using a set of non-collinear triaxial accelerometers placed in the vicinity of the coupling interface [14]. The interface dynamics are determined in a least-squares sense by projecting a large number of force and response measurements onto a virtual point containing three translational and three rotational DOFs. Larger sets of virtual point coordinates can be obtained, such as shear and torsion deformations, so as to relax the condition of assuming a locally rigid

J. Young (✉) · K. Myers
Applied Research Laboratory, Structural Acoustics Department, Pennsylvania State University, State College, PA, USA

M. Allen et al. (eds.), *Dynamic Substructures, Volume 4*, Conference Proceedings of the Society for Experimental Mechanics Series, https://doi.org/10.1007/978-3-031-36694-9_11

interface [18]. The equations presented here are not dependent on the number of virtual point coordinates that are present. Rather, the number of measurements required to accurately estimate those coordinates changes while the mathematics remains the same.

A quick summary of the VPT is first presented with its underlying assumptions. The experimental power flow sensitivity equations are then derived starting from the virtual point power flow equation. Several assumptions regarding the symmetry of the mobility matrices are made, and the ramifications of these assumptions are discussed. Quality indicators relevant to the assumptions are then presented, and the validity of the sensitivity equations is demonstrated on a numerical model so as to be free of potential experimental measurement errors.

11.2 Virtual Point Transformation

A vast literature pertaining to the VPT exists, but its basic properties will be discussed here as they are required for the derivation of the experimental power flow sensitivity equations. Defining the interface dynamics of a substructure is difficult in an experimental setting because making direct measurements of rotational DOFs is either impractical or impossible. As such, FRFs can be measured in the vicinity of the interface of a substructure and projected onto a virtual point containing three translational and three rotational DOFs. The measured forces and responses used for constructing the FRF matrix do not need to be collocated. That is, the forces and responses do not need to be measured at the same locations or in the same directions near the coupling interface. In fact, to accurately model the interface dynamics using the VPT, the interface must only be locally rigid, and more than six responses and forces must be measured on the structure. The reason for this becomes apparent when looking at the projection from physical to virtual coordinates:

$$\mathbf{u} = \mathbf{R_u}\mathbf{q} + \boldsymbol{\mu} \tag{11.1a}$$

$$\mathbf{m} = \mathbf{R_f}^T\mathbf{f} \tag{11.1b}$$

where $\mathbf{u}$ and $\mathbf{f}$ are the physical response and force vectors, $\mathbf{q}$ and $\mathbf{m}$ are the virtual point responses and forces, $\mathbf{R_u}$ and $\mathbf{R_f}$ are the virtual point response and force projection matrices, and $\boldsymbol{\mu}$ is a vector containing information regarding the flexibility of the interface. The interface is perfectly rigid when $\boldsymbol{\mu} = \mathbf{0}$. If N_u responses and N_f forces are measured near the interface with a single virtual point containing 6 DOFs, the sizes of $\mathbf{R_u}$ and $\mathbf{R_f}$ are $N_\mathrm{u} \times 6$ and $N_\mathrm{f} \times 6$, respectively. So long as N_u and N_u are both greater than 6, Eqs. 11.1a and 11.1b can be solved in a least-squares sense. The transpose of the force projection matrix is used because the virtual point forces cannot be uniquely defined from an arbitrary set of physical forces. Information regarding the structure of these matrices can be found in [14]. Transforming from physical to virtual coordinates requires solving Eqs. 11.1a and 11.1b for $\mathbf{q}$ and $\mathbf{f}$. Doing so results in

$$\mathbf{q} = \left(\mathbf{R_u}^T\mathbf{R}_\mathrm{u}\right)^{-1}\mathbf{R_u}^T\mathbf{u} \tag{11.2a}$$

$$\mathbf{f} = \mathbf{R_f}\left(\mathbf{R_f}^T\mathbf{R_f}\right)^{-1}\mathbf{m} \tag{11.2b}$$

where the residual $\boldsymbol{\mu}$ is no longer present because it is orthogonal to $\mathbf{R_u}^T$. These matrices only act on the interface DOFs, but physical internal DOFs can be retained as well by augmenting the pseudo-inverses with identify matrices equal to the size of the number of measured internal responses and forces given by

$$\mathbf{T_u} = \begin{bmatrix} \mathbf{I_u} & \mathbf{0} \\ \mathbf{0} & \left(\mathbf{R_u}^T\mathbf{R_u}\right)^{-1}\mathbf{R_u}^T \end{bmatrix} \tag{11.3a}$$

$$\mathbf{T_f}^T = \begin{bmatrix} \mathbf{I_f} & \mathbf{0} \\ \mathbf{0} & \mathbf{R_f}\left(\mathbf{R_f}^T\mathbf{R_f}\right)^{-1} \end{bmatrix} \tag{11.3b}$$

which can now be applied to the experimentally obtained FRF matrices. Since power is most easily calculated with the mobility matrix, the FRFs considered in this work are mobilities, and the terms will be used interchangeably.

Unlike numerical data, the experimental mobility matrix is not guaranteed to be square and symmetric because it is often infeasible to measure forces and responses at the same locations on the structure. As such, the rectangular mobility matrix

$$\mathbf{Y}_{\text{exp}} = \begin{bmatrix} \mathbf{Y}_{\text{ii}} & \mathbf{Y}_{\text{ic}} \\ \mathbf{Y}_{\text{ci}} & \mathbf{Y}_{\text{cc}} \end{bmatrix} \tag{11.4}$$

is available where the subscripts i and c denote internal and coupling interface DOFs, respectively, $\mathbf{Y}_{\text{ii}}$ and $\mathbf{Y}_{\text{cc}}$ are not required to be square and symmetric, and as a result $\mathbf{Y}_{\text{ic}} \neq \mathbf{Y}_{\text{ci}}^T$. The coupling interface FRFs can be made square and (possibly) symmetric by applying the VPT matrices

$$\mathbf{Y} = \mathbf{T}_{\mathbf{u}} \mathbf{Y}_{\text{exp}} \mathbf{T}_{\mathbf{f}}^T = \begin{bmatrix} \mathbf{Y}_{\text{ii}} & \mathbf{Y}_{\text{iv}} \\ \mathbf{Y}_{\text{vi}} & \mathbf{Y}_{\text{vv}} \end{bmatrix} \tag{11.5}$$

where the subscript v denotes a quantity pertaining to the virtual point coordinates. The resulting mobility matrix $\mathbf{Y}$ is still not required to be square and symmetric, but the virtual points enforce displacement compatibility between substructure interfaces automatically, and the coupling force can be predicted easily using the LMFBS. The LMFBS method couples FRFs obtained from independent structures using their respective interface FRFs. This is achieved by using a Boolean interface mapping matrix, which identifies the interface DOFs in the global FRF matrix, and calculates the coupling forces between structures explicitly. As only the coupling force is needed for the sensitivity equations, the discussion of the LMFBS will conclude here. However, information on this method can be found in [19, 20], and it is recommended the unfamiliar reader review these references before continuing. Assuming no external forces are applied to the receiver aside from those imparted on it by the source, the coupling force is given by

$$\boldsymbol{\lambda}_{\text{v}} = \left(\mathbf{Y}_{\text{vv}}^{(\text{s})} + \mathbf{Y}_{\text{vv}}^{(\text{r})} \right)^{-1} \mathbf{B}_{\mathbf{u}}^{(\text{s})} \mathbf{Y}^{(\text{s})} \mathbf{m} \tag{11.6}$$

where the superscripts (s) and (r) denote source and receiver properties, respectively, and $\mathbf{B}_{\mathbf{u}}^{(\text{s})}$ is a Boolean interface mapping matrix that identifies the interface (virtual) DOFs on the source based on measured internal responses. Another interface mapping matrix exists for forces. In an arbitrary structure, the response and force interface mapping matrices take the form

$$\mathbf{B}_{\mathbf{u}} = [\mathbf{0}_{\mathbf{u}} \quad \pm \mathbf{I}] \tag{11.7a}$$

$$\mathbf{B}_{\mathbf{f}} = \left[\mathbf{0}_{\mathbf{f}} \pm \mathbf{I} \right] \tag{11.7b}$$

where $\mathbf{I}$ is the identity matrix of size $6N_{\text{v}}$ for N_{v} virtual points, $\mathbf{0}_{\mathbf{u}}$ and $\mathbf{0}_{\mathbf{f}}$ are (in general) rectangular zero matrices where the number of columns in each matrix is determined by the number of internally measured responses or forces, respectively. The positive and negative identity matrices are required to enforce compatibility at the substructure interfaces. That is, if the source interface mapping matrix uses $\mathbf{I}$, then the receiver interface mapping matrix must use $-\mathbf{I}$.

11.3 Experimental Power Flow Sensitivity

Using the quantities derived in the previous section, power flow through an interface whose dynamics are defined by a virtual point can now be calculated as

$$Q = \frac{1}{2} \boldsymbol{\lambda}_{\text{v}}^H \mathbf{Y}_{\text{vv}}^{(\text{r})} \boldsymbol{\lambda}_v \tag{11.8}$$

The power flow sensitivity equations are derived by differentiating Eq. 11.8 with respect to the receiver impedance. This allows one to determine how power flow from source to receiver will change due to small modifications made to the receiver structure. This can be done using the chain rule

$$\frac{\partial Q}{\partial \grave{\mathbf{Z}}^{(\mathrm{r})}} = \frac{\partial Q}{\partial \mathbf{Y}_{\mathrm{vv}}^{(\mathrm{r})}} \frac{\partial \mathbf{Y}_{\mathrm{vv}}^{(\mathrm{r})}}{\partial \grave{\mathbf{Z}}^{(\mathrm{r})}} \tag{11.9a}$$

$$\frac{\partial Q}{\partial \grave{\mathbf{Z}}^{(\mathrm{r})^H}} = \frac{\partial Q}{\partial \mathbf{Y}_{\mathrm{vv}}^{(\mathrm{r})^H}} \frac{\partial \mathbf{Y}_{\mathrm{vv}}^{(r)^H}}{\partial \grave{\mathbf{Z}}^{(\mathrm{r})^H}} \tag{11.9b}$$

where $\grave{\mathbf{Z}}^{(\mathrm{r})}$ is the receiver impedance. The ò notation is used because the actual receiver impedance is not known as it cannot be determined by inverting the experimentally determined mobility matrix due to the possibility of non-collocated internal DOF measurements $\mathbf{Y}_{\mathrm{ii}}$. It will be shown that these measurements are not actually needed in the calculation of the sensitivity equations, and as a result power is instead differentiated with respect to a "synthetic" impedance where internal FRFs are assumed to be collocated. This will become more apparent later in the derivation. First, evaluating the derivatives of power with respect to the virtual point mobility and its complex conjugate is done by applying the chain and product rule to Eq. 11.8. Doing so results in

$$\frac{\partial Q}{\partial \mathbf{Y}_{\mathrm{vv}}^{(\mathrm{r})}} = -\frac{1}{2}\left(\mathbf{I} - \mathbf{Z}_{\mathrm{vv}}^{(\mathrm{c})}\mathbf{Y}_{\mathrm{vv}}^{(\mathrm{r})}\right)\mathbf{G}_{\lambda_{\mathrm{v}}\lambda_{\mathrm{v}}}^{T} \tag{11.10a}$$

$$\frac{\partial Q}{\partial \mathbf{Y}_{\mathrm{vv}}^{(\mathrm{r})^H}} = \frac{1}{2}\mathbf{G}_{\lambda_{\mathrm{v}}\lambda_{\mathrm{v}}}^{T}\mathbf{Y}_{\mathrm{vv}}^{(\mathrm{r})}\mathbf{Z}_{\mathrm{vv}}^{(\mathrm{c})^H} \tag{11.10b}$$

where $\mathbf{Z}_{\mathrm{vv}}^{(\mathrm{c})} = \left(\mathbf{Y}_{\mathrm{vv}}^{(\mathrm{s})} + \mathbf{Y}_{\mathrm{vv}}^{(\mathrm{r})}\right)^{-1}$ is the coupling impedance, and $\mathbf{G}_{\lambda_{\mathrm{v}}\lambda_{\mathrm{v}}} = \boldsymbol{\lambda}_{\mathrm{v}}\boldsymbol{\lambda}_{\mathrm{v}}^{H}$ is the one-sided coupling force cross-spectral density matrix. Again, it was assumed that the virtual point mobilities were symmetric in this calculation. The task at hand now is to calculate the second set of derivatives in Eqs. 11.9a and 11.9b. Doing so requires defining an analytical relationship between the interface mobility and global impedance matrix of the receiver. Fortunately, this can be done using

$$\mathbf{Y}_{\mathrm{vv}}^{(\mathrm{r})} = \mathbf{B}_{\mathbf{u}}^{(\mathrm{r})}\mathbf{Y}^{(\mathrm{r})}\mathbf{B}_{\mathbf{f}}^{(\mathrm{r})^T} \tag{11.11}$$

where the structure of the mobility matrix $\mathbf{Y}^{(\mathrm{r})}$ is given in Eq. 11.5. The internal mobility $\mathbf{Y}_{\mathrm{ii}}$ matrix has not yet been constrained to be square and symmetric, and as a result equating the impedance matrix to be the inverse of the mobility matrix cannot be done because the experimental mobility matrix could be singular. However, consider for a moment an experimental mobility matrix in which the interface DOFs have been projected onto virtual coordinates, and the internally measured FRFs *were* collocated, making $\mathbf{Y}_{\mathrm{ii}}$ square and symmetric. To distinguish between this hypothetical set of internal FRFs and the actual measured ones, the following notation will be adopted:

$$\grave{\boldsymbol{Y}}^{(\mathrm{r})} = \begin{bmatrix} \grave{\boldsymbol{Y}}_{\mathrm{ii}} & \mathbf{Y}_{\mathrm{iv}} \\ \mathbf{Y}_{\mathrm{vi}} & \mathbf{Y}_{\mathrm{vv}} \end{bmatrix} \tag{11.12}$$

where $\grave{\boldsymbol{Y}}_{\mathrm{ii}}$ is set of hypothetically collocated internal FRFs, and due to the assumed symmetry of $\mathbf{Y}_{\mathrm{vv}}$, $\mathbf{Y}_{\mathrm{iv}} = \mathbf{Y}_{\mathrm{vi}}^{T}$. The implication of this is that (1) the force and response interface mapping matrices are identical, and (2) the mobility matrix is invertible – the receiver impedance matrix mathematically exists. That is,

$$\mathbf{B}^{(\mathrm{r})} = \mathbf{B}_{\mathbf{u}}^{(\mathrm{r})} = \mathbf{B}_{\mathbf{f}}^{(\mathrm{r})} = \begin{bmatrix} \mathbf{0} & \pm\mathbf{I} \end{bmatrix} \tag{11.13}$$

and

$$\grave{\boldsymbol{Z}}^{(\mathrm{r})} = \grave{\boldsymbol{Y}}^{(\mathrm{r})^{-1}} \tag{11.14}$$

is the "synthetic" impedance. From these two statements, Eq. 11.11 can be rewritten as

$$\mathbf{Y}_{\mathrm{vv}}^{(\mathrm{r})} = \mathbf{B}^{(\mathrm{r})}\grave{\mathbf{Z}}^{(\mathrm{r})^{-1}}\mathbf{B}^{(\mathrm{r})^T} \tag{11.15}$$

where $\grave{\boldsymbol{Z}}^{(\mathrm{r})}$ exists only in a mathematical sense and is not a matrix that is obtained from experimental measurements. While this may seem troublesome at first, it will be shown that the internal mobility matrix does not explicitly appear in the sensitivity equations, and are therefore not needed. Now that a relationship between the interface mobility and impedance matrix of the receiver exists, differentiation gives

$$\frac{\partial \mathbf{Y}_{\mathrm{vv}}^{(\mathrm{r})}}{\partial \grave{\boldsymbol{Z}}^{(r)}} = -\overline{\grave{\boldsymbol{Y}}} \otimes \overline{\grave{\boldsymbol{Y}}}^{T} \tag{11.16a}$$

$$\frac{\partial \mathbf{Y}_{\mathrm{vv}}^{(\mathrm{r})^{H}}}{\partial \grave{\boldsymbol{Z}}^{(\mathrm{r})^{H}}} = -\overline{\grave{\boldsymbol{Y}}}^{*} \otimes \overline{\grave{\boldsymbol{Y}}}^{H} \tag{11.16b}$$

where $\overline{\grave{\boldsymbol{Y}}} = \mathbf{B}^{(\mathrm{r})}\grave{\boldsymbol{Y}}^{(\mathrm{r})} = \left[\mathbf{Y}_{\mathrm{vi}}\ \mathbf{Y}_{\mathrm{vv}}\right]$, and $\otimes$ is the Kronecker product. As such, Eqs. 11.16a and 11.16b are fourth-order tensors. The hypothetical internal FRF matrix $\grave{\boldsymbol{Y}}_{\mathrm{ii}}$ is not present in this derivative, and therefore does not actually need to be measured experimentally to calculate the power flow sensitivities. The only FRFs that need to be measured are the interface mobilities to be projected onto a virtual point, and the mobilities that couple the internal and interface dynamics $\mathbf{Y}_{\mathrm{vi}}$. This matrix is determined by applying forces to the internal DOFs and measuring the response at the interface. Alternatively, due to reciprocity in Eq. 11.12, $\mathbf{Y}_{\mathrm{iv}}$ can be determined by applying forces to the interface and measuring the response at several internal DOFs, and its transpose can be used in place of $\mathbf{Y}_{\mathrm{vi}}$. The derivatives of power with respect to the receiver impedance are then written as

$$\frac{\partial Q}{\partial \grave{\boldsymbol{Z}}^{(\mathrm{r})}} = \frac{1}{2}\left(\mathbf{I} - \mathbf{Z}_{\mathrm{vv}}^{(\mathrm{c})}\mathbf{Y}_{\mathrm{vv}}^{(\mathrm{r})}\right)\mathbf{G}_{\lambda_{\mathrm{v}}\lambda_{\mathrm{v}}}^{T}\left[\overline{\grave{\boldsymbol{Y}}} \otimes \overline{\grave{\boldsymbol{Y}}}^{T}\right] \tag{11.17a}$$

$$\frac{\partial Q}{\partial \grave{\boldsymbol{Z}}^{(\mathrm{r})^{H}}} = -\frac{1}{2}\mathbf{G}_{\lambda_{\mathrm{v}}\lambda_{\mathrm{v}}}^{T}\mathbf{Y}_{\mathrm{vv}}^{(\mathrm{r})}\mathbf{Z}_{\mathrm{vv}}^{(\mathrm{c})}\left[\overline{\grave{\boldsymbol{Y}}}^{*} \otimes \overline{\grave{\boldsymbol{Y}}}^{H}\right] \tag{11.17b}$$

where the derivatives of Q are given with respect to the synthetic receiver impedance $\grave{\boldsymbol{Z}}^{(\mathrm{r})}$ using the LTI assumption of a reciprocal mobility matrix. This means that information about how power flow will change due to modifications made to the internal DOFs of the receiver is known, even without measuring the internal mobility matrix directly. All that is needed is a set of FRFs from the interface to a desired number of internal DOFs to calculate Eqs. 11.17a and 11.17b. One final step is needed to calculate the power flow sensitivities. As is, Eqs. 11.17a and 11.17b are complex valued matrices, which is not of much use when trying to determine how the real part of power flow changes with respect to the real (dissipative) and imaginary (elastic and inertial) components of the receiver impedance. Additionally, active power (the real component of power) is usually of interest because it describes the energy that is moving within the structure. Derivatives relating the real component of Q to the real and imaginary components of the receiver impedance can be obtained by applying the properties of the Wirtinger derivatives to Eqs. 11.17a and 11.17b [21]. Doing so results in

$$\mathbf{S}_{\mathrm{R}} = \frac{\partial\,\mathrm{Re}\{Q\}}{\partial\,\mathrm{Re}\left\{\grave{\boldsymbol{Z}}^{(\mathrm{r})}\right\}} = \mathrm{Re}\left\{\frac{\partial Q}{\partial \grave{\boldsymbol{Z}}^{(\mathrm{r})}}\right\} + \mathrm{Re}\left\{\frac{\partial Q}{\partial \grave{\boldsymbol{Z}}^{(\mathrm{r})^{H}}}\right\} \tag{11.18a}$$

$$\mathbf{S}_{\mathrm{I}} = \frac{\partial\,\mathrm{Re}\{Q\}}{\partial\,\mathrm{Im}\left\{\grave{\boldsymbol{Z}}^{(\mathrm{r})}\right\}} = -\,\mathrm{Im}\left\{\frac{\partial Q}{\partial \grave{\boldsymbol{Z}}^{(\mathrm{r})}}\right\} + \mathrm{Im}\left\{\frac{\partial Q}{\partial \grave{\boldsymbol{Z}}^{(\mathrm{r})^{H}}}\right\} \tag{11.18b}$$

where Re{∘} and Im{∘} denote the real and imaginary components of the argument, respectively. The resulting matrices, termed the real and imaginary sensitivities, are both real valued, square, and symmetric. They describe how power flow changes with respect to small modifications made to the real and imaginary components of the receiver's impedance at a single DOF (diagonal elements) or the coupling between two DOFs (off-diagonal elements).

11.4 Quality Indicators

One quality indicator will be used to determine the accuracy of the VPT. Numerical data is used here to avoid measurement error in the projection matrices and FRFs. Since the sensitivity equations assume a symmetric mobility matrix, particularly the virtual point partition of the mobility matrix, the first indicator of measurement quality is the coherence function. It is defined as

$$\chi_{mn} = \frac{(Y_{mn} + Y_{nm})\left(Y^*_{mn} + Y^*_{nm}\right)}{2\left(Y_{mn}Y^*_{mn} + Y_{nm}Y^*_{nm}\right)} \tag{11.19}$$

which compares how similar the FRFs Y_{mn} and Y_{nm} are. It outputs a real valued number χ_{mn} between 0 and 1, with 0 indicating the two FRFs are dissimilar, and 1 indicating the two FRFs are identical. The diagonal elements of the matrix are guaranteed to have a value of 1. A Hermitian matrix, for example, would be the identity matrix. If the matrix of FRFs is symmetric, the resulting coherence matrix would be a matrix containing all ones.

Another quality indicator to describe how well the VPT estimates the interface dynamics is passivity. Since a mobility matrix is being used in the sensitivity equations, the phase of the drive-point FRFs should be between $\pm 90°$. This indicator is used to verify that the structure does not generate its own energy. Other quality indicators exist, such as force and response consistency, which describe the rigidity of the coupling interface. While it is important to calculate these quantities to ensure the VPT is a valid coupling procedure in a specific frequency range, it will not be further discussed here. The reason for this is because it has been verified in a previous study that the model considered in the case study presented here has a consistency of 1 over the entire frequency range tested and was verified by the authors to be passive [22]. More information on this quality indicator can be found in [14, 15].

11.5 Case Study: Complex Conjugate Impedance

To demonstrate that the virtual point sensitivity equations are valid, and do in fact calculate the rate of change of power flow with respect to the receiver impedance, a source structure coupled to a receiver whose impedance is complex conjugate to that of the source is considered. This example was chosen because it is known that power flow is maximized when a source is connected to its complex conjugate [23] – the quantity being aptly named the maximum available power (MAP) in the literature. Therefore, given that $\mathbf{S}_R$ and $\mathbf{S}_I$ are derivatives of power with respect to the receiver impedance, both should be equal to the zero matrix at all frequencies when the receiver impedance is the complex conjugate of the source impedance. A simple beam structure is considered with one coupling interface, requiring a single virtual point, shown in Fig. 11.1. Several FRFs from the virtual point to internal DOFs are shown as well.

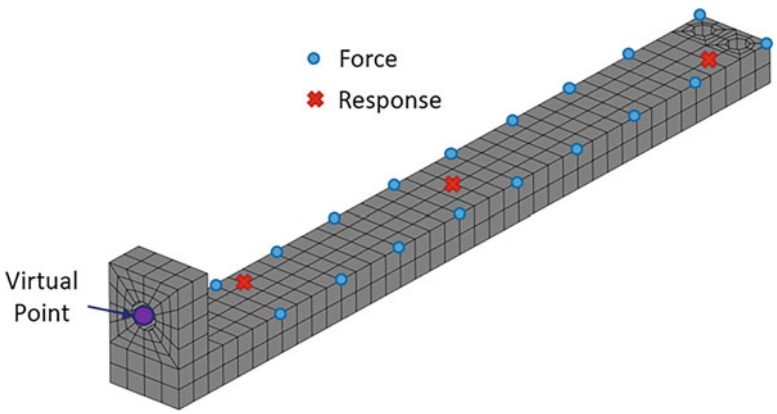

Fig. 11.1 Virtual point location and measurement locations for constructing $\overline{\grave{Y}}$ using internal force and response measurements, resulting in interface mapping matrices $\boldsymbol{B_f}$ and $\boldsymbol{B_u}$, respectively

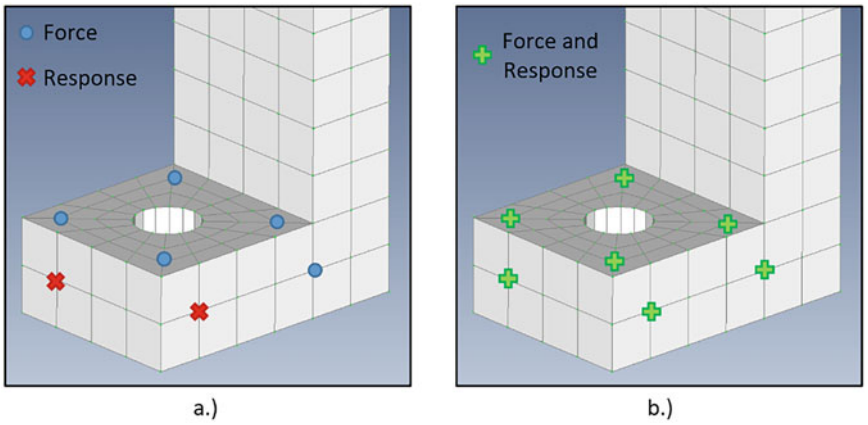

Fig. 11.2 Applied forces and measured responses on interface of beam structure for (**a**) non-collocated force and response measurements and (**b**) collocated force and response measurements

Figure 11.1 provides a visual intuition of how the matrix $\overline{\grave{\boldsymbol{Y}}}$ can be obtained based on internally measured forces or responses. The purpose of including internal DOFs in the analysis is to provide information to the analyst regarding which locations on the structure, specifically those away from the interface, to modify in an effort to reduce power flow. These internal DOFs can be measured by means of forces or responses, as all that is needed for the sensitivity equations are the transfer mobilities from the virtual point to the desired internal DOFs. Practically speaking, if the sensitivity at a few locations internal to the structure is of interest, measuring the response at these internal locations with accelerometers due to excitations at the interface is a feasible task. When a higher spatial resolution of the sensitivity on the internal DOFs is desired, it becomes more practical to apply forces to the DOFs of interest and measure the response at the interface.

Analysis was performed over the range of 60–1600 Hz. The beam being analyzed was made out of aluminum with a modulus of elasticity of 69 GPa, density of 2700 kg/m^3, and Poisson's ratio of 0.33. It had a nominal length of 38.1 cm (15 in.), width of 3.81 cm (1.5 in.), and thickness of 1.9 cm (0.75 in.). The base of the beam was flanged to allow for it to be bolted to another structure. The depth of this flange was 3.81 cm with a thickness of 1.9 cm, and there was a bolt hole at the center with a diameter of 1.33 cm. This is where the virtual point was located for substructure coupling. These dimensions provided sufficient stiffness in the vicinity of the coupling interface (flange) to yield a consistency of 1 over the frequency range of interest.

This example is not physical as coupling a source to its complex conjugate is not realizable. However, it does serve to demonstrate that Eqs. 11.17a and 11.17b are the analytical derivatives of power flow with respect to the receiver impedance, as well as the fact that they are indifferent to using internal force or response measurements. Additionally, the assumption of a reciprocal virtual point mobility, and its effect on the resulting sensitivities, can be examined through this demonstration. This was done by projecting FRFs obtained from a numerical model onto the virtual point in two ways. The first is more representative of an experimental setup, in which the forces applied and responses measured on the interface are not collocated – the forces and responses are not measured at the same location. The second guarantees symmetry of the virtual point mobility matrix by collocating for forces and responses on the interface, resulting in identical transformation matrices $\mathbf{T_u}$ and $\mathbf{T_f}$. Non-collocated virtual point interface force and response measurements are shown in Fig. 11.2a, and collocated interface measurements are shown in Fig. 11.2b.

11.6 Results

The symmetry of the virtual point mobility for non-collocated and collocated interface measurements is first compared as the symmetry will affect the resulting calculation of power flow sensitivity. The frequency-averaged coherence of $\mathbf{Y}_{vv}^{(r)}$ is shown in Fig. 11.3. It is clear from the low coherence on the off-diagonal terms that the virtual point interface mobility matrix is not symmetric over most of the frequency range. In other words, the virtual point does not behave reciprocally as would a node in a typical linear finite element model. Based on the data shown in Fig. 11.3a, applying a force in the x direction and measuring the velocity in the θ_x direction is not the same applying a force in the θ_x direction and measuring the velocity in the x direction. This is an issue particularly when substituting these results into Eqs. 11.17a and 11.17b because of the

symmetry that was assumed in deriving the equations. Symmetry of the virtual point mobility is preserved for the collocated interface measurements, which is indicated by a coherence of 1 for all FRFs.

Now that it is known that the non-collocated interface measurements result in an asymmetric virtual point mobility, a comparison between the calculated power flow and its corresponding sensitivities is shown in Fig. 11.4. More specifically, the sensitivity of the z component of the virtual point mobility matrix is shown. This value describes how power flow would respond to the changes made to the receiver impedance in the vicinity of the coupling interface in the z direction. Knowing that the values of $\boldsymbol{S}_{\mathrm{R}}$ and $\boldsymbol{S}_{\mathrm{I}}$ should be zero for all frequencies in this coupling configuration, there is clearly an issue with the sensitivity calculated from the non-collocated interface measurements. At 60 Hz, the magnitude of the real sensitivity is on the order of 10^2 and the imaginary sensitivity is on the order of 10^3. As frequency increases, the values of the sensitivities decrease, but only to a magnitude of approximately 10^{-7}. Lastly, there is a discrepancy between the predictions in the real and imaginary sensitivities using internal response and internal force measurements. This again is due to the asymmetry in the virtual point mobility matrix.

The collocated interface measurements result in a real and imaginary sensitivity that are much smaller than the ones predicted from the non-collocated measurements. At 60 Hz, the values of the real and imaginary sensitivities are on the order of 10^{-13} and 10^{-9}, respectively – much closer to zero than for the non-collocated measurements. Numerically, given that the

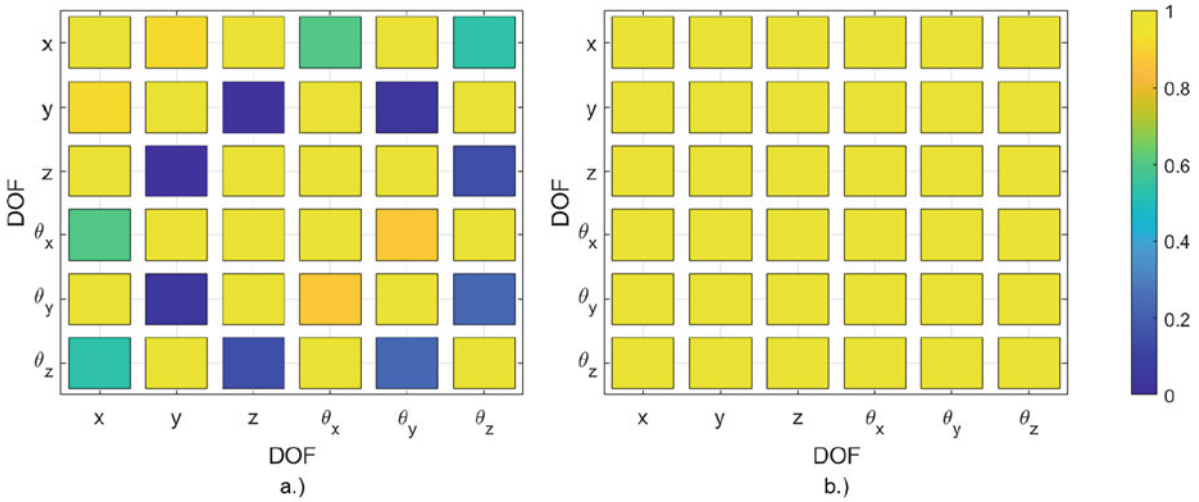

Fig. 11.3 Frequency-averaged coherence of virtual point mobility $\boldsymbol{Y}_{\mathrm{vv}}^{(\mathrm{s})}$ for (**a**) non-collocated force and response measurements and (**b**) collocated force and response measurements

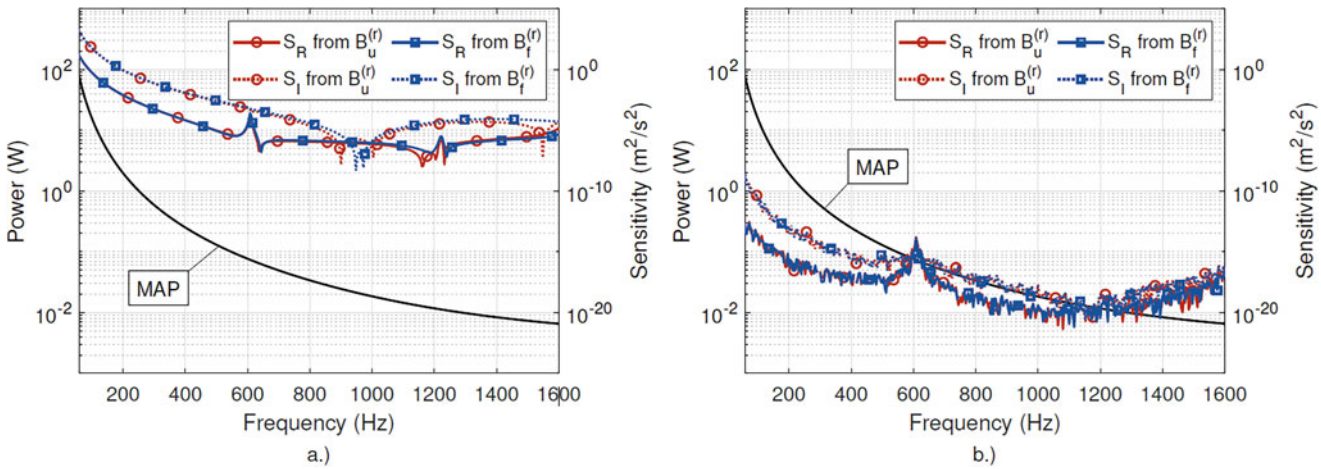

Fig. 11.4 Power flow and real and imaginary sensitivities of z coordinate of virtual point with different sets of internal DOFs for (**a**) non-collocated force and response measurements, and (**b**) collocated force and response measurements

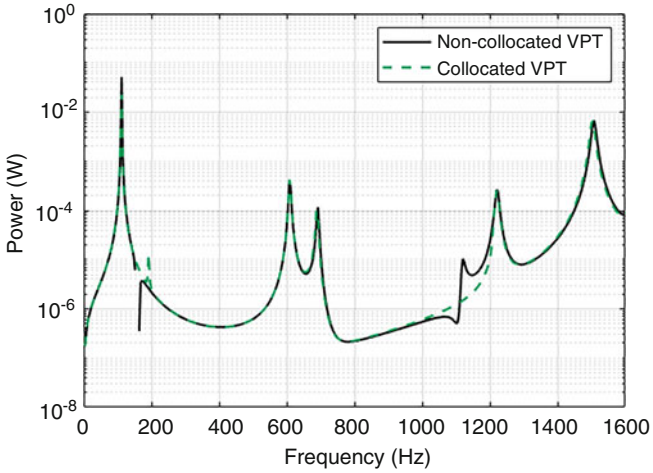

Fig. 11.5 Power flow for non-collocated and collocated interface measurements for coupling case when $\grave{\mathbf{Z}}^{(\mathrm{r})} = \grave{\mathbf{Z}}^{(\mathrm{s})}$

sensitivities represent the rate of change in power flow with respect to the real and imaginary impedances, these magnitudes are essentially zero, thus verifying Eqs. 11.17a and 11.17b are the analytical derivatives of power with respect to the receiver impedance. The sensitivities calculated using internal responses and internal forces are approximately identical, though given how close to machine precision the values are it is difficult to compare the two quantities. The spectrum appears noisy due to the small magnitude of the real and imaginary sensitivities. One interesting feature that appears is the apparent resonance at 600 Hz. This coincides with a natural frequency of the source structure when it is uncoupled from any receiver.

One final observation from Fig. 11.4 is that power flow appears to be unaffected by the asymmetry in the virtual point mobility matrix as the frequency dependence of power flow is identical for the non-collocated and collocated interface measurement cases. This is most likely due to the type of coupling considered, where the receiver impedance is complex conjugate that of the source. The resulting coupling interface impedance $\mathbf{Z}_{\mathrm{vv}}^{(\mathrm{c})}$ is purely real and does not display resonant behavior as a function of frequency. If a different coupling case were considered, for example, when the receiver impedance is equal to that of the source, the power flow spectrum for the non-collocated and collocated interface measurements should be different. This is shown in Fig. 11.5.

There are some clear discrepancies between power flow calculated with non-collocated and collocated interface measurements when performing the VPT. Capturing resonant frequencies does not appear to be an issue. This is expected as the imaginary component of impedance is fairly small here and the real component dominates similar to what happens when calculating the MAP in Fig. 11.4. The most notable differences in the spectra occur around 200 Hz and 1100 Hz. At 200 Hz, the non-collocated interface measurements dictate that power flow will be negative. This is physically impossible as the interface mobility matrix should be positive semi-definite. At 1100 Hz, the non-collocated VPT appears to create an additional resonant frequency of the assembled structures. This is important to note as power flow is also heavily dependent on the symmetry of the virtual point mobility matrix. Given that there are more matrix multiplication operations in the sensitivity equations, any deviations from a symmetric interface mobility matrix will be further amplified in the calculation of the real and imaginary sensitivities. As is, more research should be done on how to obtain a more symmetric interface mobility matrix so power flow, and the real and imaginary sensitivities, can be more accurately calculated for experimentally obtained mobility data.

11.7 Conclusion

The analytical derivatives of complex power flow from source to passive receiver were derived for experimental data using the VPT to model the dynamics of the coupling interface between substructures. It was shown that the power flow sensitivity can be calculated at internal DOFs using either internally measured forces or responses under the assumption that the receiver mobility matrix is symmetric, without actually measuring the full mobility matrix. This creates a "synthetic" impedances, whose power flow is differentiated with respect to. The equations were tested on a beam structure such that the source was

coupled to a receiver whose impedance was the complex conjugate of the source's. Due to maximum power flow occurring in this coupling configuration, the real and imaginary sensitivities were verified to be zero. However, both power flow and the sensitivities were shown to be dependent on the symmetric mobility assumption as an asymmetric virtual point mobility matrix can lead to spurious resonances in the power flow response and lead to further errors in the calculation of the real and imaginary sensitivities. Future work should apply these equations to experimental data and focus on finding methods to obtain a more symmetric virtual point mobility matrix.

Acknowledgments The authors thank the Walker Graduate Assistantship and the Pennsylvania State University Applied Research Laboratory for funding this research.

References

1. Noiseux, D.: Measurement of power flow in uniform beams and plates. J. Acoust. Soc. Am. **47**(1B), 238–247 (1970)
2. Pavic, G.: Measurement of structure borne wave intensity, part I: formulation of the methods. J. Sound Vib. **49**(2), 221–230 (1976)
3. Pinnington, R., White, R.: Power flow through machine isolators to resonant and non-resonant beams. J. Sound Vib. **75**(2), 179–197 (1981)
4. Szwerc, R.P., Burroughs, C.B., Hambric, S.A., McDevitt, T.E.: Power flow in coupled bending and longitudinal waves in beams. J. Acoust. Soc. Am. **107**(6), 3186–3195 (2000)
5. Mace, B.: Wave reflection and transmission in beams. J. Sound Vib. **97**(2), 237–246 (1984)
6. Hambric, S.A., Barnard, A.R., Conlon, S.C.: Power transmission coefficients based on wavenumber processing of experimental modal analysis data for bolted honeycomb sandwich panels. In: 39th International Congress on Noise Control Engineering 2010, INTER-NOISE 2010, pp. 7022–7031 (2010)
7. Hambric, S.A.: A mechanical power flow capability for the finite element code NASTRAN. Tech. rep., David Taylor Research Center Bethesda, MD Computational Mathematics/Logistics Department (1989)
8. Hambric, S.A.: Power flow and mechanical intensity calculations in structural finite element analysis. J. Vib. Acoust. **112**(4) (1990)
9. Hambric, S.A., Taylor, P.: Comparison of experimental and finite element structure-borne flexural power measurements for a straight beam. J. Sound Vib. **170**(5), 595–605 (1994)
10. Hambric, S.A., Szwerc, R.P.: Predictions of structural intensity fields using solid finite elements. Noise Control Eng. J. **47**(6), 209–217 (1999)
11. Cuschieri, J.: Power flow as a complement to statistical energy analysis and finite element analysis. Tech. rep., Florida State University (1987)
12. Nefske, D., Sung, S.: Power flow finite element analysis of dynamic systems: basic theory and application to beams. J. Vib. Acoust. Stress. Reliab. Des. **111**, 94–100 (1989)
13. Young, J., Myers, K.: Structure-borne power flow sensitivity analysis for general structural modifications. In: ASME 2021 International Mechanical Engineering Congress and Exposition. American Society of Mechanical Engineers Digital Collection (2021)
14. Allen, M.S., et al.: Substructuring in Engineering Dynamics. Springer International Publishing, New York (2020)
15. van der Seijs, M.V., et al.: An improved methodology for the virtual point transformation of measured frequency response functions in dynamic substructuring. In: 4th ECCOMAS Thematic Conference on Computational Methods in Structural Dynamics and Earthquake Engineering. No. 4 (2013)
16. van der Seijs, M.: Experimental dynamic substructuring: analysis and design strategies for vehicle development (2016)
17. Trainotti, F., Berninger, T.F.C., Rixen, D.J.: Using laser vibrometry for precise FRF measurements in experimental substructuring. In: Dynamic Substructures, vol. 4, pp. 1–11. Springer, Cham (2020)
18. Pasma, E.A., et al.: Frequency based substructuring with the virtual point transformation, flexible interface modes and a transmission simulator. In: Dynamics of Coupled Structures, vol. 4, pp. 205–213. Springer, Cham (2018)
19. de Klerk, D., Rixen, D.J., de Jong, J.: The frequency based substructuring (FBS) method reformulated according to the dual domain decomposition method. In: Proceedings of the 24th International Modal Analysis Conference, a Conference on Structural Dynamics (2006)
20. de Klerk, D., Rixen, D.J., Voormeeren, S.N.: General framework for dynamic substructuring: history, review and classification of techniques. AIAA J. **46**(5), 1169–1181 (2008)
21. Bouboulis, P.: Wirtinger's calculus in general Hilbert spaces. arXiv preprint arXiv:1005.5170 (2010)
22. Young, J., Myers, K.: Uncertainty in power flow due to measurement errors in virtual point transformation for frequency-based substructuring. In: Dynamic Substructures, Proceedings of the 40th IMAC, A Conference and Exposition on Structural Dynamics, vol. 4, pp. 1–9. Springer, New York (2023)
23. Moorhouse, A.: On the characteristic power of structure-borne sound sources. J. Sound Vib. **248**(3), 441–459 (2001)

Chapter 12
An Experimental Exercise as Part of the Substructuring Benchmark Structure Challenge

A. Linderholt

Abstract Some years ago, the Society for Experimental Mechanics' (SEM) Dynamic Substructuring Technical Division (TD) recognized a need for a simpler, yet challenging benchmark structure for experimental–numerical substructuring exercises. That structure should replace the modified version of an Ampair 600 wind turbine as the common test object within the TD. Representatives from several research institutes formed a group that defined several desirable properties for the new benchmark structure. The outcome is a frame structure together with different plates. Together, they can represent various structures such as automotive frames, wing-fuselage structures, and building floors. The frame is made as a one-piece structure with many 10/32 tapped holes that can be used to attach other components, sensors, or excitation devices.

Sandia National Labs has manufactured the benchmark structure's components, an aluminum frame together with two aluminum rectangular wings. An exercise/challenge has been formulated. The components have been shipped to the ones that have shown interest in participating in the exercise. The idea of the exercise is to compare different strategies to tackle an experimental substructuring task, containing both decoupling and coupling, thereby learning from each other.

In the exercise, the participants start with an assembly built up by the frame and the thinner of the rectangular wings. That wing should then be numerically decoupled from the fuselage. To that numerical representation of the fuselage, the thicker wing should be coupled numerically. These decoupling and coupling operations render a numerical representation of the thicker wing attached to the fuselage; a representation whose output is compared with test data stemming from the real structure counterpart.

Here, virtual points are used in the decoupling and coupling operations. Four attachment points, for example, four screws, are used. In addition, washers between the fuselage and the wings are used in the connections. The purpose is to avoid too challenging nonlinearities to start with. The component mode synthesis (CMS) technique is used.

Keywords Benchmark structure · Experimental dynamic substructuring · Component mode synthesis · Transmission simulator · Decoupling

12.1 Introduction

Research on experimental dynamic substructuring has grown in the last years; both in academy and industry. Methods to couple and decouple in the modal domain, that is, using component mode synthesis (CMS), the frequency domain, that is,. frequency-based substructuring (FBS) and in the state-space domain have been developed. In addition, the use of virtual points has enabled new strategies in experimental substructuring.

The Society for Experimental Mechanics' (SEM) Dynamic Substructuring Technical Division recognized a need for a simple, yet challenging benchmark structure for experimental–analytical substructuring collaborations compared to previous benchmark structures [1, 2]. A team with members from many research institutes set out from several desirable properties and a unit-frame structure was designed as a benchmark for current collaborative efforts. The benchmark structure was presented at the IMAC XXXVIII [3]. The benchmark structure is built up by a frame with threaded inserts that are bolted to plates of varying thickness and materials. Together, they can represent structures from a variety of fields; automotive frames, wing-

A. Linderholt (✉)
Department of Mechanical Engineering, Linnaeus University, Växjö, Sweden
e-mail: andreas.linderholt@lnu.se

M. Allen et al. (eds.), *Dynamic Substructures, Volume 4*, Conference Proceedings of the Society for Experimental Mechanics Series, https://doi.org/10.1007/978-3-031-36694-9_12

fuselage structure, as well as building floors are examples of assemblies possible to represent by the benchmark structure. The frame is made as a one-piece structure, consists of four units cells, and includes 10/32 tapped holes that can be used to attach other components. In addition, 10/32 tapped holes are made on the side of the frame to attach impedance heads or force transducers.

In experimental substructuring, test and finite element (FE)-based subassembly models are used in decoupling and coupling exercises. FE models contain high-fidelity spatial information, whereas experimental models capture the dynamics of components that are difficult to model. Here, the assembly consisting of the fuselage and the thin wing is represented by test data, whereas the two wings are represented by finite element data.

12.2 Substructuring Exercise

In Fig. 12.1, the decoupling of the thin wing from the fuselage is shown schematically. Simultaneously, a coupling of a thicker wing is made.

The substructuring exercise sets out from the well-known three-field formulation in block diagonal form:

$$\begin{cases} M \cdot \ddot{u}(t) + C \cdot \dot{u}(t) + Ku(t) = f(t) + g(t) \\ B \cdot u(t) = 0 \\ L^T \cdot g(t) = 0 \end{cases}$$

The effect of subtracting a substructure can be achieved by simply adding the negative of that structure. That is, adding a substructure that has negative mass, damping, and stiffness terms to the coupled system.

By substituting the physical displacements with a combination of modal contributors, $u = \phi \bullet \eta$, and premultiplying with ϕ^T

$$\phi^T M\phi\ddot{\eta} + \phi^T C\phi\dot{\eta} + \phi^T K\phi\eta = \phi^T f + \phi^T g + \phi^T r \text{ and } B\phi\eta = 0$$

in which the last component of the governing equation of motion vanishes due to the orthogonal properties of the modes. Here, there are three components: the fuselage, the thicker wing to be coupled, and the thinner wing to be uncoupled. Let them have the indices f (fuselage), T (thick), and t (thin), respectively, and note the negative sign of the thinner wing. Then, with mass normalized mode shapes, the uncoupled form becomes

$$\begin{bmatrix} I_\mathrm{f} & 0 & 0 \\ 0 & I_\mathrm{T} & 0 \\ 0 & 0 & -I_\mathrm{t} \end{bmatrix} \begin{Bmatrix} \ddot{\eta}_\mathrm{f} \\ \ddot{\eta}_\mathrm{T} \\ \ddot{\eta}_\mathrm{t} \end{Bmatrix} + \begin{bmatrix} 2\varsigma_\mathrm{r}\omega_{r\,\mathrm{f}} & 0 & 0 \\ 0 & 2\varsigma_\mathrm{r}\omega_{r\,\mathrm{T}} & 0 \\ 0 & 0 & -2\varsigma_\mathrm{r}\omega_{r\,\mathrm{t}} \end{bmatrix} \begin{Bmatrix} \dot{\eta}_\mathrm{f} \\ \dot{\eta}_\mathrm{T} \\ \dot{\eta}_\mathrm{t} \end{Bmatrix}$$

$$+ \begin{bmatrix} \omega_{r\,\mathrm{f}}^2 & 0 & 0 \\ 0 & \omega_{r\,\mathrm{T}}^2 & 0 \\ 0 & 0 & -\omega_{r\,\mathrm{t}}^2 \end{bmatrix} \begin{Bmatrix} \eta_\mathrm{f} \\ \eta_\mathrm{T} \\ \eta_\mathrm{t} \end{Bmatrix} = \begin{Bmatrix} \phi_\mathrm{f}^T f_\mathrm{f} \\ \phi_\mathrm{T}^T f_\mathrm{T} \\ \phi_\mathrm{t}^T f_\mathrm{t} \end{Bmatrix} + \begin{Bmatrix} \phi_\mathrm{f}^T g_\mathrm{f} \\ \phi_\mathrm{T}^T g_\mathrm{T} \\ \phi_\mathrm{t}^T g_\mathrm{t} \end{Bmatrix}$$

Fig. 12.1 From the assembly consisting of the fuselage and the thin wing (f and t), the thin wing (t) is decoupled giving a representation of the fuselage (f). Simultaneously, a ticker rectangular wing (T) is coupled

which can be expressed as

$$M_{\mathrm{m}} \cdot \ddot{\eta} + C_{\mathrm{m}} \cdot \dot{\eta} + K_{\mathrm{m}} \cdot \eta = f_{\mathrm{m}} + g_{\mathrm{m}}$$

Mode shapes representing the motion at the connection points of the thin wing, that is, $\phi_{\mathrm{t,\,c}}$ are used as a basis to span the connection motion for each component. Its pseudo-inverse, $\phi^{+}_{\mathrm{t,c}}$, is premultiplied with the compatibility constraint expressed at the connection degrees of freedom:

$$\begin{bmatrix} \phi^{+}_{\mathrm{t,c}} & 0 \\ 0 & \phi^{+}_{\mathrm{t,c}} \end{bmatrix} \cdot \begin{bmatrix} \phi_{\mathrm{f}} & 0 & -\phi_{\mathrm{t}} \\ 0 & \phi_{\mathrm{T}} & -\phi_{\mathrm{t}} \end{bmatrix} \cdot \begin{Bmatrix} \eta_{\mathrm{f}} \\ \eta_{\mathrm{T}} \\ \eta_{\mathrm{t}} \end{Bmatrix} = \tilde{B} \cdot \eta = \begin{Bmatrix} 0 \\ 0 \\ 0 \end{Bmatrix}$$

Let $\eta = \tilde{L} \cdot q$ and choose $\tilde{L}$ to be the null space of $\tilde{B}$, then the compatibility requirement is automatically fulfilled. Furthermore, $\tilde{L}^{T}\phi = 0$, so making the variable change and premultiplying the governing equation of motion with $\tilde{L}^{T}$ renders in

$$\tilde{M}_{\mathrm{m}} \cdot \ddot{q} + \tilde{C}_{\mathrm{m}} \cdot \dot{q} + \tilde{K}_{\mathrm{m}} \cdot q = \tilde{f}_{\mathrm{m}}$$

The equations are treated rigorously in Allen et al. [4]. More information about the structure and the exercise can be found at the Dynamic Substructures Wiki – Round Robin Frame Structure.

12.3 Vibrational Testing

The study sets out from the assembly consisting of the frame and the rectangular wing. The rectangular wing was numerically decoupled from the fuselage using an FE model representing the wing. Four connection points, that is, four screws, were used. In addition, washers were used between the fuselage and the wings in the connections. The purpose was to avoid too challenging nonlinearities to start with. The component mode synthesis (CMS), together with the transmission simulator technique [5], was used. The thicker rectangular wing was numerically and simultaneously coupled to the representation of the frame, from the decoupling, using an FE model according to an engineer's best knowledge. The result was compared with results from measurements on the assembly.

The structures tested were hanging in fishing lines and were excited by an automatic Wavehit Max modal hammer. The responses were measured by a 3D Polytec scanning laser Doppler vibrometer (see Fig. 12.2). Connection points at the surface of the fuselage were defined as the four virtual points. The motion at several points surrounding each screw on the wings was measured. From them, the motions at the virtual points were estimated. In addition, the motion at several points on the wings and on the fuselage was measured to visualize mode shapes. The assembled structures were excited in three perpendicular directions, one at a time. The three columns of FRFs were used for modal extraction. A tightening torque of 3 Nm was used for the four screws.

12.4 Conclusion

The exercise set out from an assembly built up by the fuselage and the thinner rectangular wings. Four attachment points were used, and washers were used between the fuselage and the wings at the connections. Noncontact measurements using an automatic modal hammer for excitation and a 3D scanning laser Doppler vibrometer were made. Four virtual points represented the attachment. Finite element models were utilized to decouple the thinner wing from the assembly and, at the same time, couple the thicker one. Component mode synthesis, together with the transmission simulation technique, was used for that.

Fig. 12.2 (**a**) The three Polytec scanning laser Doppler vibrometer heads are shown. (**b**) The automatic hammer exciting the structure. (**c**) The test object. The red circles are used to calibrate the lasers positions. (**d**) The Polytec software showing decaying velocity signals

References

1. Mayes, R.L.: An introduction to the sem substructures focus group test bed - the ampair 600 wind turbine. In: 30th IMAC, A Conference on Structural Dynamics Conference Proceedings of the Society for Experimental Mechanics Series (2012)
2. Harvie, J., Avitabile, P.: Comparison of some wind turbine blade tests in various configurations. In: 30th IMAC, A Conference on Structural Dynamics Conference Proceedings of the Society for Experimental Mechanics Series, pp. 73–79 (2012)
3. Roettgen, D., et al.: Technical division benchmark structure for dynamic substructuring. In: IMAC XXXVIII, Houston (2020)
4. Allen, M.S., et al.: Substructuring in engineering dynamics. In: Emerging Numerical and Experimental Techniques, vol. 594. CISM International Centre for Mechanical Sciences, Udine (2020)
5. Allen, M.S., Mayes, R.L., Bergman, E.J.: Experimental modal sub- structuring to couple and uncouple substructures with flexible fixtures and multi-point connections. J. Sound Vib. **329**, 4891–4906 (2010)
6. Dynamic Substructures Wiki - Round Robin Frame Structure.: https://sem.mywikis.wiki/wiki/Round_Robin_Frame_Structure

Chapter 13
Using Component-Based TPA to Translate Vibration Environments Between Versions of the Round-Robin Structure with FRFs Derived from Analytical Models

Steven Carter and Brian Owens

Abstract This chapter will show the results of a study where component-based transfer path analysis was used to translate vibration environments between versions of the round-robin structure. This was done to evaluate a hybrid approach where the responses were measured experimentally, but the frequency response functions were derived analytically. This work will describe the test setup, force estimation process, response prediction (on the new system), and show comparisons between the predicted and measured responses. Observations will also be made on the applicability of this hybrid approach in more complex systems.

Keywords Transfer path analysis · Round-robin structure · Vibration environments

13.1 Introduction and Motivation

Component-based transfer path analysis (TPA) shows significant promise for generating virtual field data to develop multi-axis vibration test specifications [1]. This is because the estimated forces are a property of the source system and can be applied to any version of the coupled source–receiver system, assuming the source system (loads and structural dynamics) remains the same. The reader is referred to [2] for a complete derivation of the method.

In this case, inverse force estimation from Eq. 13.1 was used, based on the equation of motion in Eq. 13.2, where $[F(\omega)]$ is the cross-power spectral density (CPSD) matrix of the forces, $[X(\omega)]$ is the CPSD matrix of the system responses, and $[H(\omega)]$ is the frequency response function (FRF) matrix of the coupled source–receiver system. Note that the "+" indicates a pseudo-inverse and the "*" indicates a conjugate transpose:

$$[F(\omega)] = [H(\omega)]^{+}[X(\omega)][H(\omega)]^{+*} \tag{13.1}$$

$$[X(\omega)] = [H(\omega)][F(\omega)][H(\omega)]^{*} \tag{13.2}$$

The sketch in Fig. 13.1 shows a picture of a source–path–receiver system that is described in the above equations. In this case, the responses on the payload are the receivers ($X(\omega)$), the forces acting on the payload are the sources ($F(\omega)$), and the frequency response functions (FRFs) between the forces and responses are the paths ($H(\omega)$). Virtual field data can be generated for a new payload assuming the following: the new payload is coupled to the same propulsion system as the

S. Carter (✉) · B. Owens
Sandia National Laboratories, Albuquerque, NM, USA
e-mail: spcarter@mtu.edu

M. Allen et al. (eds.), *Dynamic Substructures, Volume 4*, Conference Proceedings of the Society for Experimental Mechanics Series, https://doi.org/10.1007/978-3-031-36694-9_13

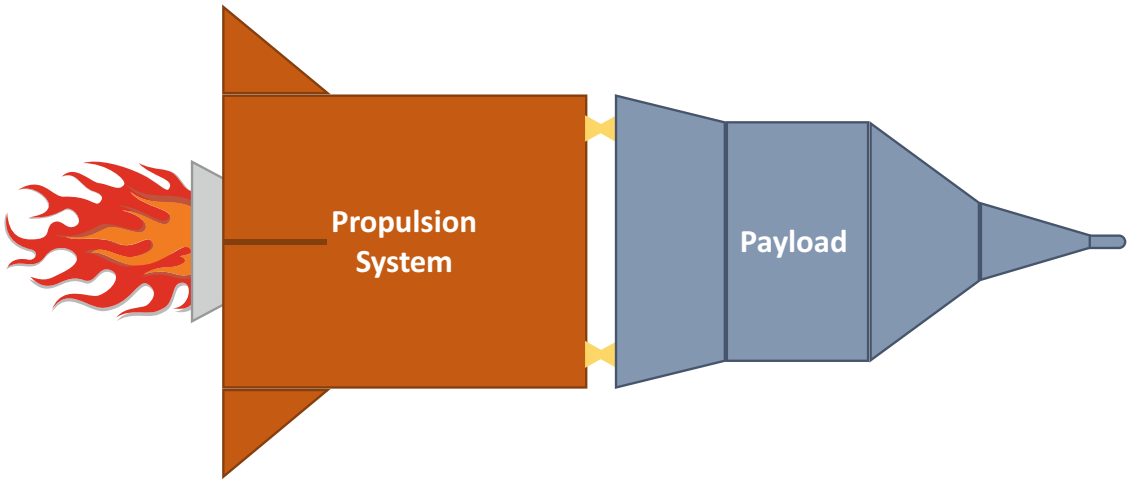

Fig. 13.1 Sketch of a system showing clear delineations between the source and the receiver

original payload, the FRFs are gathered from the coupled source–receiver system, and field data exists from an original version of the system to perform the inverse force estimation. The process for generating virtual field data is as follows:

1. Collect field data and FRFs on an original version of the system
2. Estimate the forces on the source (propulsion) system via FRF matrix inversion
3. Collect FRFs on a new version of the system, where only the payload is changed (this is a requirement for component-based TPA)
4. Propagate the forces through the new system FRFs to generate the virtual field data on the new receiver (payload)

This process obviously requires accurate FRFs as any errors in those will propagate into the force and response estimates. The FRFs are typically acquired via a test on the exact device under test (DUT) to reduce these types of errors. However, it can be difficult or impossible to collect this data when the DUT is unavailable (e.g., when using legacy data) or when it is extremely valuable, limiting test access (which is common in the aerospace community). As such, it would be beneficial if a finite element (FE) model could be used to derive the FRFs.

The use of an FE model introduces additional uncertainties into the TPA process, given the modeling errors (and resulting errors in the FRFs). This work is a first attempt to gain an understanding of how the modeling errors will propagate into force and response estimates. It will exercise the full "hybrid TPA" process, where the response data is gathered experimentally and the FRFs are derived from an FE model. This will be done for two versions of the round-robin system [3, 4], where the forces are estimated on an "original" version of the system and then applied to a "new" version of the system to "translate" the vibration environment between the systems. The goal of this work is to determine the most significant sources of error in the hybrid TPA process to guide future research efforts. It should be noted that this work may not result in accurate estimates of the new system response (since the goal is to find the sources of error, *not* to fix the sources of error).

Note that this chapter only presents the initial findings from this study. Further work is underway and will be presented at the conference.

13.2 Description of the System Under Study

This work is being performed on the round-robin system of the Society for Experimental Mechanics' (SEM) Dynamic Substructures Technical Division. This system is shown in Fig. 13.2 and is the aluminum copy of the system with the thick (0.25″) and thin (0.125″) straight wings. This figure also shows the attachment points that are being used. The FE model makes these connections using JOINGT2G elements, which are a native element in the Sandia in-house FE analysis software, Sierra/SD (they are analogous to Nastran CBUSH elements). See [5] for a more complete description of the model. However, some of these parameters may change in an FE model updating process. Also note that the "single-point attachments" are being made in the physical version of the system by putting washers between the wing and frame at the bolt locations.

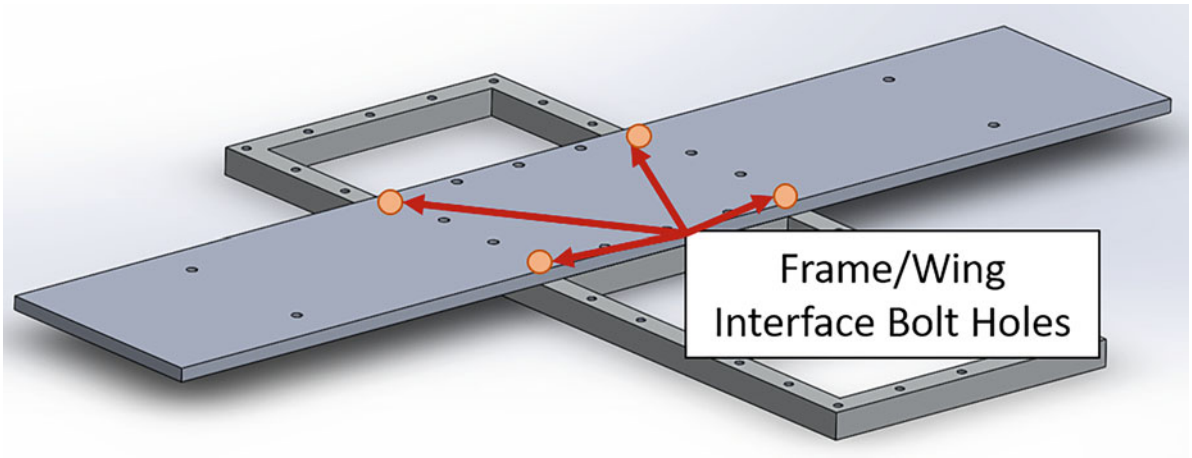

Fig. 13.2 Computer-aided design model of the round-robin system

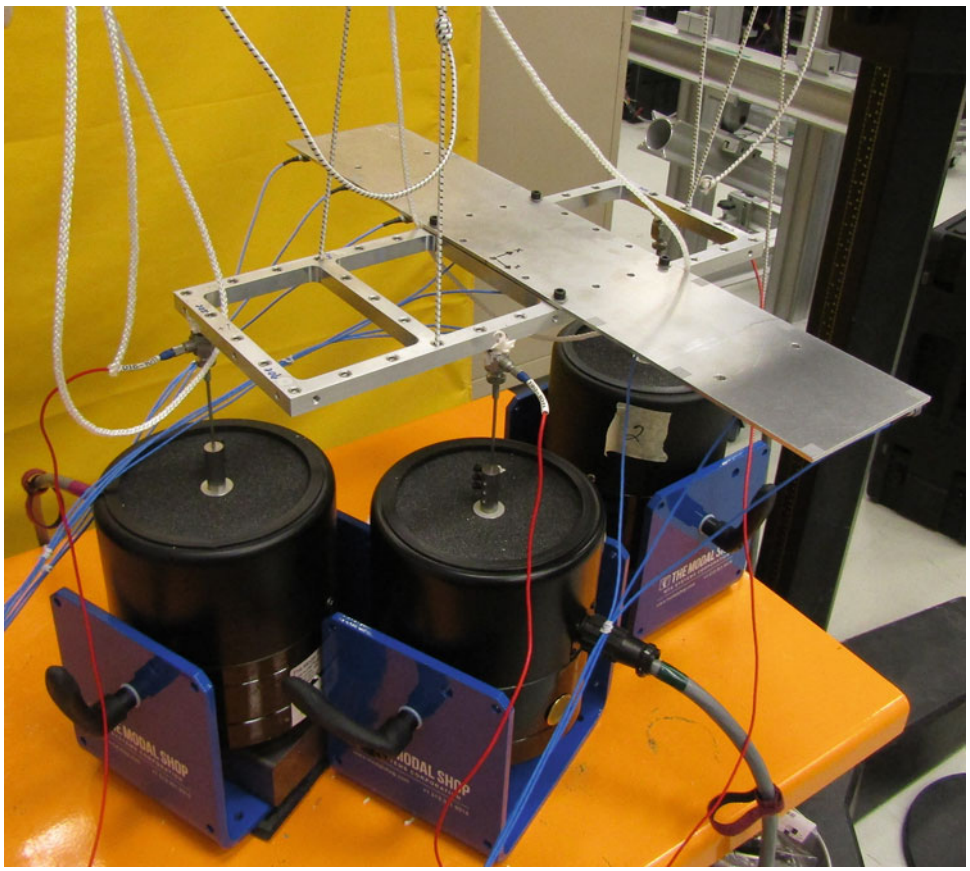

Fig. 13.3 Setup for the "field test"

13.3 Description of the Performed Experiments

A variety of tests were performed on both (thick and thin wing) versions of the system. These tests included a "field test," where the systems were excited by electrodynamic shakers that were connected to the frame. Modal tests were also performed on the assembled systems and system components to enable model updating in case this was deemed to be necessary. Figure 13.3 shows an image of the field test, and Fig. 13.4 shows a picture of the modal test on the assembled system.

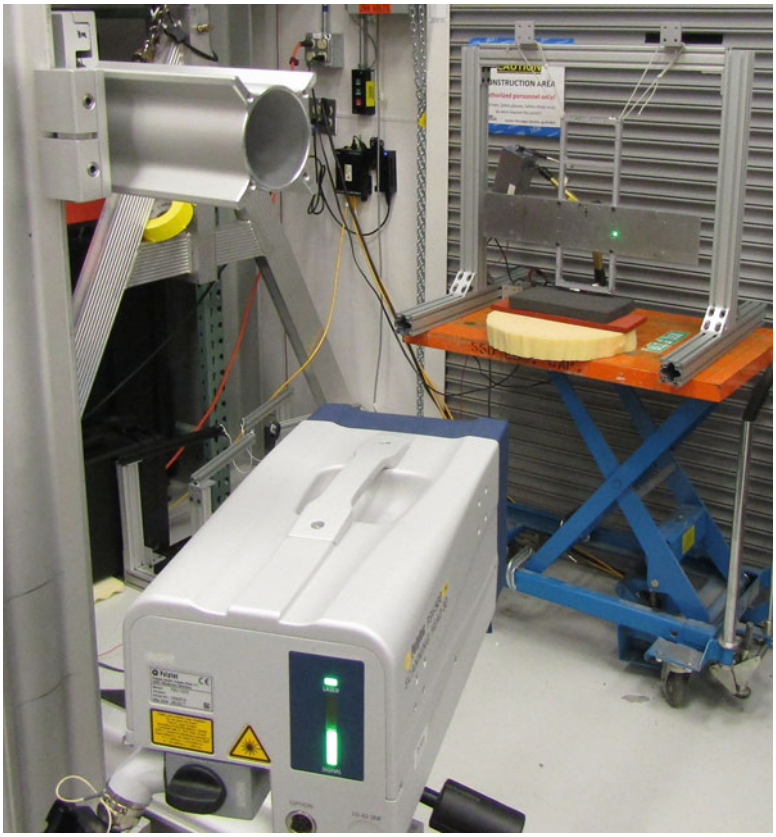

Fig. 13.4 Setup for the modal test

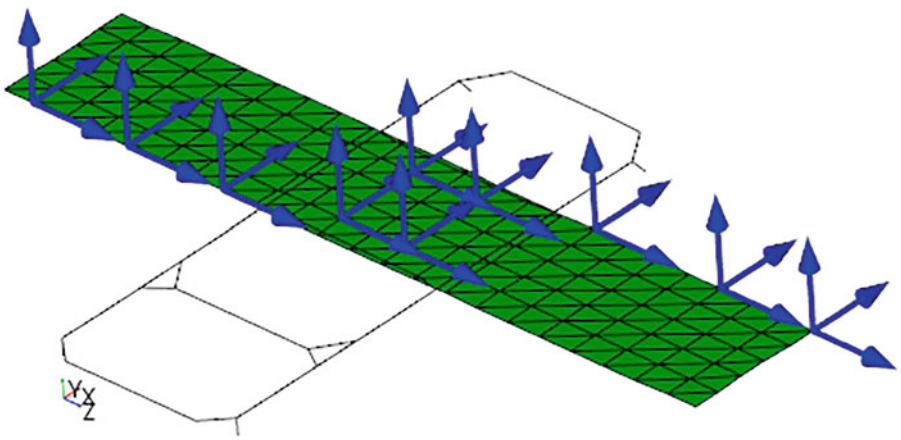

Fig. 13.5 Field data response measurement locations on stick model of the round-robin system

The field test was performed by playing controlled forces into the system at three locations using electrodynamic shakers and the Rattlesnake vibration controller [6]. Note that these forces were initially generated on the original (thick wing) system by playing flat voltages through each of the shakers (i.e., the measured force CPSDs from the first test became the control specification for the following tests). The responses were measured at 10 locations with triaxial accelerometers, as shown in Fig. 13.5 on a stick model of the system.

These measurement locations were chosen subjectively based on experience and some numerical studies into the accuracy of component-based TPA. Additionally, the test was intentionally limited to 30 response degrees of freedom (DOFs) to replicate what is typically seen in flight testing, where the minimum number of transducers is used. Lastly, Figs. 13.6, 13.7,

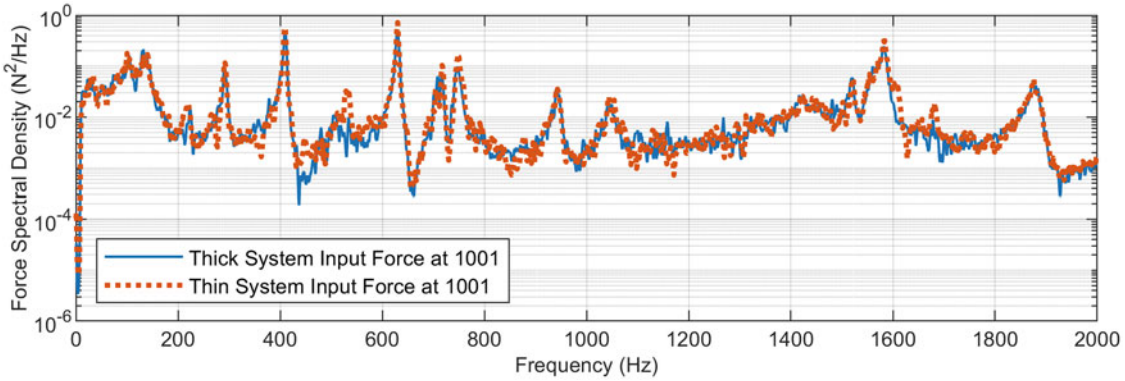

Fig. 13.6 Comparison of the input forces for both versions of the system at point 1001 (aft)

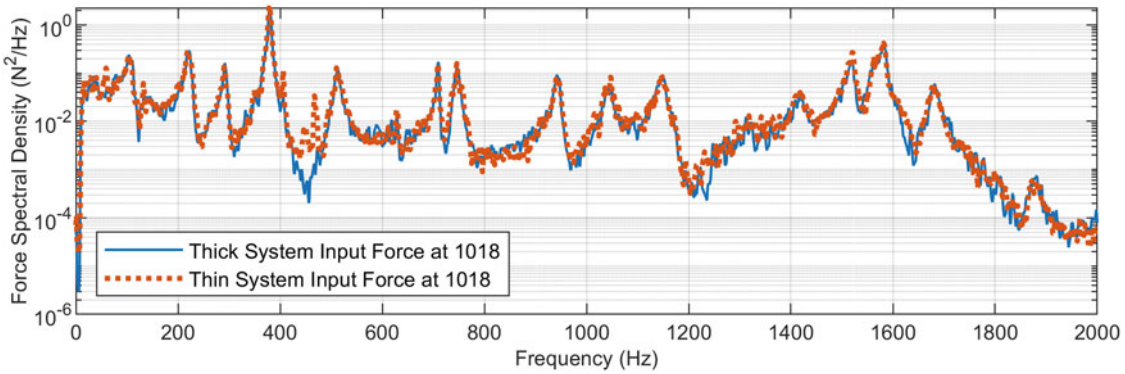

Fig. 13.7 Comparison of the input forces for both versions of the system at point 1018 (forward)

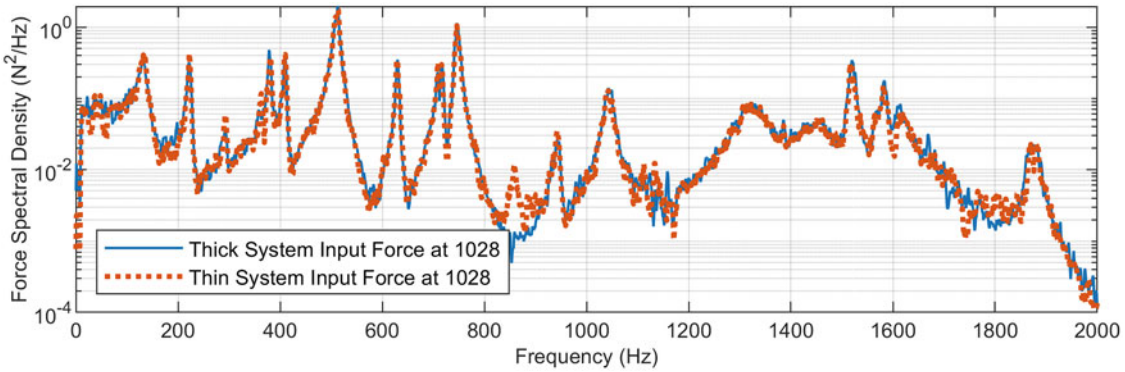

Fig. 13.8 Comparison of the input forces for both versions of the system at point 1028 (right side)

and 13.8 show the force autopower spectral densities (APSDs) that were applied to both versions of the system, indicating the similarity of the source environments for each system.

The modal test was performed using a scanning laser Doppler vibrometer (SLDV) and an automatic impact hammer, which excited the system at multiple locations and directions. The (triaxial) response measurement locations matched a reduced set of nodes from the FE model. There were 164 response nodes for the assembled system tests, 138 response nodes for the wing tests, and 42 response nodes for the frame test. It should be noted that the modal tests were performed with the accelerometers removed from the wings but with the load cells left on. This change could be significant since removing the accelerometers is expected to influence the system damping (due to the influence of the cables).

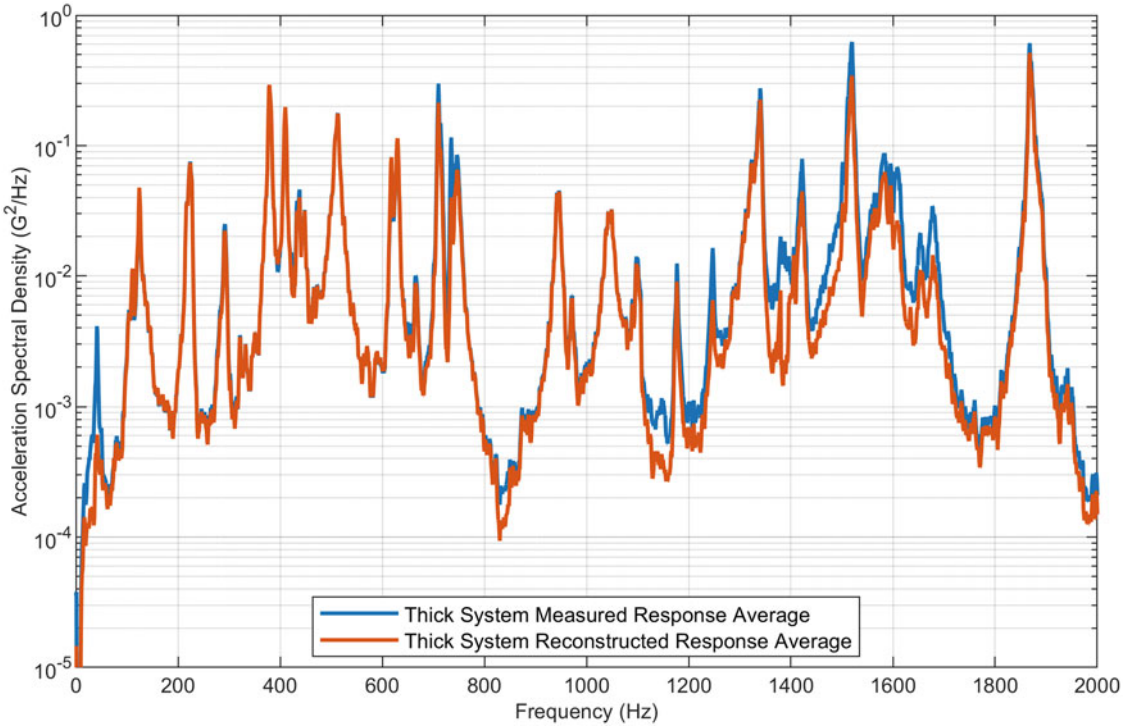

Fig. 13.9 Comparison of the DOF averaged measured and reconstructed responses on the thick wing system

13.4 Initial TPA Efforts and Results

The initial efforts attempted to estimate the interface forces on the thick wing system and then apply them to the thin wing system to predict its response. This procedure was done using noncalibrated models of the systems to generate the necessary FRFs. The damping ratios were determined from the field test and were set to 0.266% for all the thick wing system modes and 0.417% for all the thin wing system modes. The forces were estimated at the frame side (JOINT2G) interface node between the frame and wing in the vertical direction (perpendicular to wing) only.

A first attempt used 3DOF (X, Y, Z) forces at each interface, but this clearly resulted in an overfit solution like the one that was seen in [5]. The reasons for this overfit solution are unclear, but it is likely related to the small number of true sources acting on the system limiting the possible number equivalent sources (that are estimated in the inversion process). However, numerical studies have shown that there is no 1:1 relationship between the number of true sources and possible equivalent sources, making it difficult to choose appropriate FRF reference DOFs. Improved regression methods, such as Bayesian inference [7, 8], could reduce the possibility of an overfit solution while still including 3DOF forces in the estimate, and this is a topic of current study.

The DOF averaged spectrum results for the initial work are shown in Figs. 13.9 and 13.10 for thick and thin wing systems, respectively. The dB error spectra for each response DOF (as well as the average dB error) on the thin wing are also shown in Fig. 13.11. As expected, there is a very good match between the measured and reconstructed responses on the thick wing system. This match may indicate that it is appropriate to only use the vertical forces at the interface, but further study would be needed to confirm this conclusion. Additionally, it is important to note that this check only provides a minor validation of the forces as it is a check on the least-square solution and *not* the accuracy of the forces.

The thin wing estimated responses show a reasonable match to the measured data, especially below ~600 Hz. The estimated responses would provide useful “virtual field data” (over the whole frequency range) if measured data was not available, but there is obvious room for improvement. The reasons for the mismatch between the estimated and measured response are unknown. It is suspected that the errors are due to both model inaccuracies and poor conditioning/setup in the inverse solution. Work is currently underway to better understand the causes of these errors.

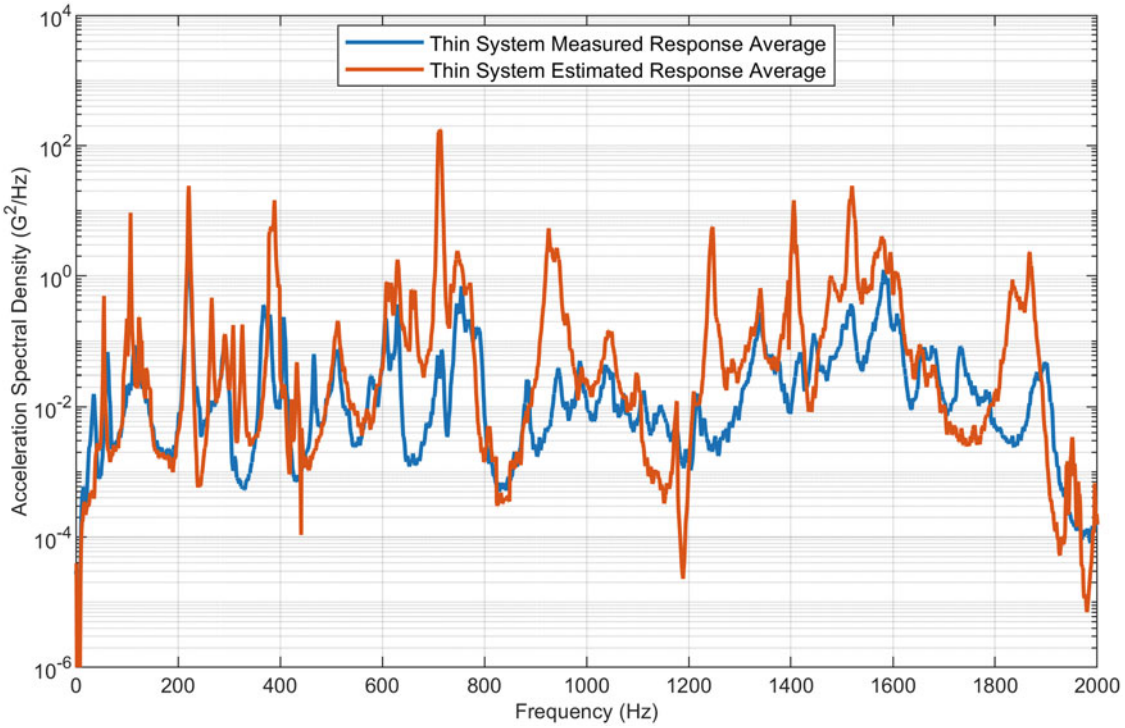

Fig. 13.10 Comparison of the DOF averaged measured and estimated (from the thick wing interface forces) responses on the thin wing system

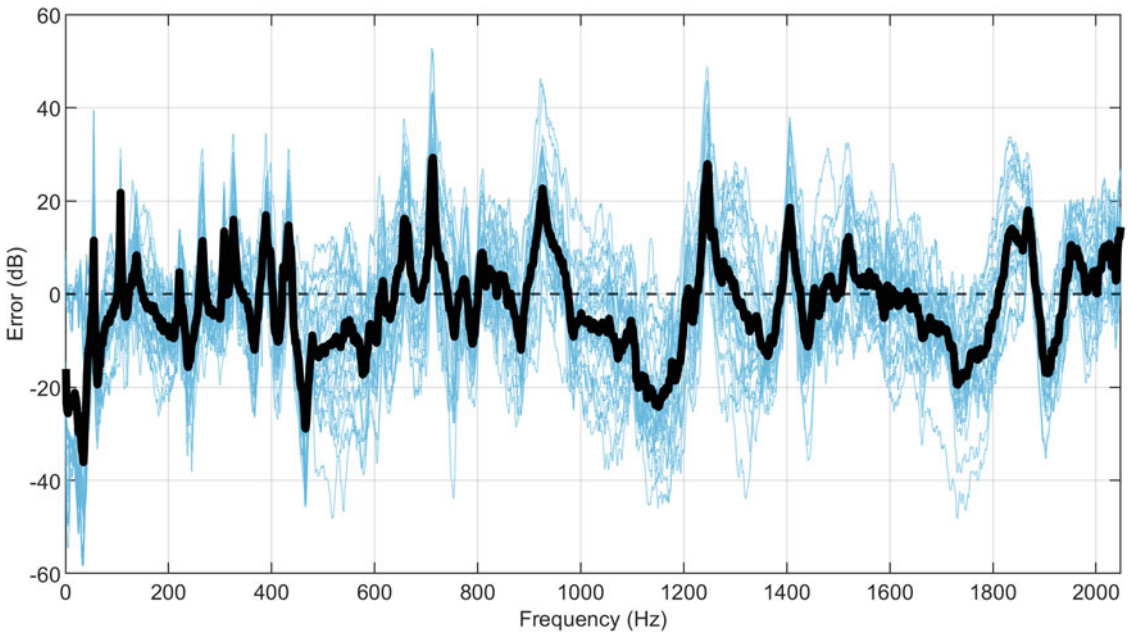

Fig. 13.11 Per DOF dB spectrum error for the thin wing system. The dashed black line is the zero axis, the solid black curve is the mean dB error, and the blue curves are the dB error for each response DOF

13.5 Conclusions

This chapter showed the initial attempts at using component-based TPA to translate vibration environments between versions of the round-robin structure. In this case, forces were estimated at the frame/wing interface on the thick wing system and then applied to the thin wing system to generate response estimates. The initial results showed reasonable comparisons to

the measured data, but there is obvious room for improvement. Work is currently underway to better understand and mitigate the sources of error, with the goal to present updated results at the conference.

References

1. Carter, S.: A review of using transfer path analysis methods to derive multi-axis vibration environments. In: Proceedings of IMAC-XLI - Forthcoming, Austin (2023)
2. van der Seijs, M.V., de Klerk, D., Rixen, D.J.: General framework for transfer path analysis: history, theory, and classification of techniques. Mech. Syst. Signal Process. **68–69**, 217–244 (2016)
3. Roettgen, D., Lopp, G., Jaramillo, A., Moldenhauer, B.: Experimental substructuring of the dynamic substructures round Robin testbed. In: Proceedings of IMAC-XL, the 40th International Modal Analysis Conference, Orlando (2022)
4. Linderholt, A., Roettgen, D.: Substructuring on combinations of steel and aluminum components of the benchmark structure of the technical division on dynamic substructures. In: Proceedings of IMAC-XL, the 40th International Modal Analysis Conference, Orlando (2022)
5. Carter, S.P., Owens, B.C.: Errors using six degree of freedom force estimates to translate environments system-to-system. In: ISMA 2022, Leuven (2022)
6. Rohe, D.P., Schultz, R.: Rattlesnake: an open-source multi-axis and combined evironments vibration controller. In: Proceedings of IMAC-XL, the 40th International Modal Analysis Conference, Orlando (2022)
7. Aucejo, M., De Smet, O.: Bayesian source identification using local priors. Mech. Syst. Signal Process. **66–67**, 120–136 (2016)
8. Aucejo, M., De Smet, O.: On a full Bayesian inference for force reconstruction problems. Mech. Syst. Signal Process. **104**, 36–59 (2018)

Chapter 14
Fixture Design and Analysis for Multi-axis Mechanical Shock Testing

Adam J. Bouma, Tyler F. Schoenherr, and David E. Soine

Abstract Resonant plate shock testing techniques have been used for mechanical shock testing at Sandia for several decades. A mechanical shock qualification test is often done by performing three separate uniaxial tests on a resonant plate to simulate one shock event. Multi-axis mechanical shock activities, in which shock specifications are simultaneously met in different directions during a single shock test event performed in the lab, are not always repeatable and greatly depend on the fixture used during testing. This chapter provides insights into various designs of a concept fixture that includes both resonant plate and angle bracket used for multi-axis shock testing from a modeling and simulation point of view based on the results of finite element modal analysis. Initial model validation and testing performed show substantial excitation of the system under test as the fundamental modes drive the response in all three directions. The response also shows that higher order modes are influencing the system, the axial and transverse response are highly coupled, and tunability is difficult to achieve. By varying the material properties, changing thicknesses, adding masses, and moving the location of the fixture on the resonant plate, the response can be changed significantly. The goal of this work is to identify the parameters that have the greatest influence on the response of the system when using the angle bracket fixture for a mechanical shock test for the intent of tunability of the system.

Keywords Mechanical shock · Fixture design · Resonant plate · Modal analysis

14.1 Introduction

Simulations of pyroshock events have been performed in the laboratory for many years using resonant structures. Resonant structure techniques using plates or beams are an accepted method for simulating high-frequency pyroshock-type environments at the component and assembly level. For resonant plate shock testing, a test article is attached to the front side of a tuned resonant plate with free boundary conditions while a projectile is fired into the back of the plate using an air gun. The impact of the projectile against the plate causes the plate to respond, consequently exciting the test article. Many factors are considered when planning a pyroshock test, including the size of the resonant plate, type of test fixture, location of the unit under test, and location of impact by the projectile, to name a few. Figure 14.1 depicts a typical resonant plate shock test machine in the laboratory. If the unit under test or the location of impact by the projectile is at an off-center location, a larger multi-axis response can be achieved by a single-axis input in one direction, but significant component over-test in one direction may occur. Multi-axis response during mechanical shock testing has been studied recently by investigating the response of the system when the component under test was positioned at the plate's center and the impact was located offset toward one corner of the plate [1, 2]. The measured responses indicated generally good agreement with the test specifications

A. J. Bouma (✉) · T. F. Schoenherr · D. E. Soine
Sandia National Laboratories, Albuquerque, NM, USA
e-mail: abouma@sandia.gov

M. Allen et al. (eds.), *Dynamic Substructures, Volume 4*, Conference Proceedings of the Society for Experimental Mechanics Series, https://doi.org/10.1007/978-3-031-36694-9_14

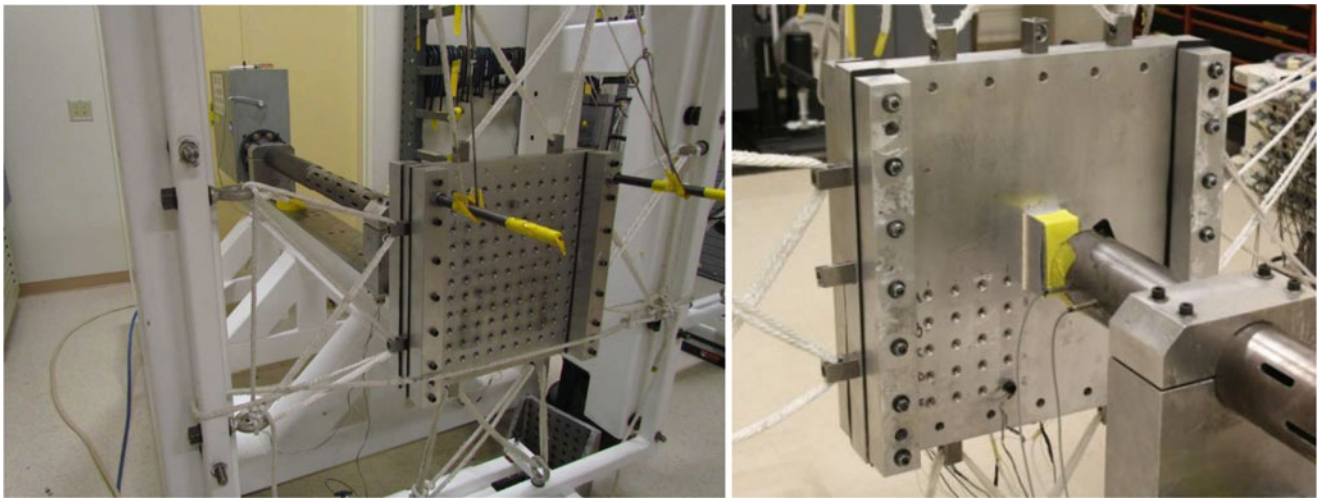

Fig. 14.1 Typical resonant plate test setup

in two directions and slightly high inputs to the component in the third axis. Although this study by Hopkins and Sisemore [1] was considered a success, further tests are needed to bring the off-axis responses into closer agreement with test specification. The output response is a coupled response of the transverse plate vibration and the rotational motion of the component on the plate. Recent efforts in modeling and simulation as well as testing of the resonant plate with and without a component under test have been able to provide insight into the mode shapes of the plate itself and help understand the true test environment [3, 4]. Model-driven test design should be developed and validated for a single test that excites the multi-axis environment simultaneously without over-testing in a single direction. This report aims to use the model-driven test design method to design an angle bracket test fixture for multi-axis mechanical shock testing.

14.2 Angle Bracket Fixture Design

For this study, an angle bracket fixture is used. The fixture consists of an 8 × 8 inch platform with 0.5-inch-thick ribs along the bottom for support normal to the angle bracket. The base and angle plates each have a thickness of 0.25 inches. Only the mounting location of the fixture, along with the impact location, is varied for this study. This angle bracket design is seen in Fig. 14.2, both by itself and mounted off-center on the resonant plate with a test mass, including the response axes as well. The configurations for the location of the angle bracket fixture and test mass are seen in Table 14.1, where the impact location changes from the middle of the plate to one of the corners, and the fixture location changes from the middle of the plate to the opposite corner of the impact location. The impact force used for these simulations is based on previous multi-axis pyroshock test data with similar configurations [4].

14.3 Simulation Results

The following results are based on the configurations of Table 14.1, where a comparison is made between response of the angle bracket fixture when changing the impact and mounting locations on the resonant plate. Figures 14.3, 14.4, and 14.5 show the frequency response and shock response spectra and are based on a tri-axis measurement point located on the platform of the angle bracket as highlighted in Fig. 14.2a. From Fig. 14.3, the response normal to the plate (z-direction) is much higher than the off-axis (x- and y-direction) responses. When the impact location is moved off-center, the off-axis responses are considerably increased, as seen in Fig. 14.4. Figure 14.5 shows that moving the impact location and the fixture opposite of each other increases the off-axis responses even more, with results similar to the response normal to the resonant plate.

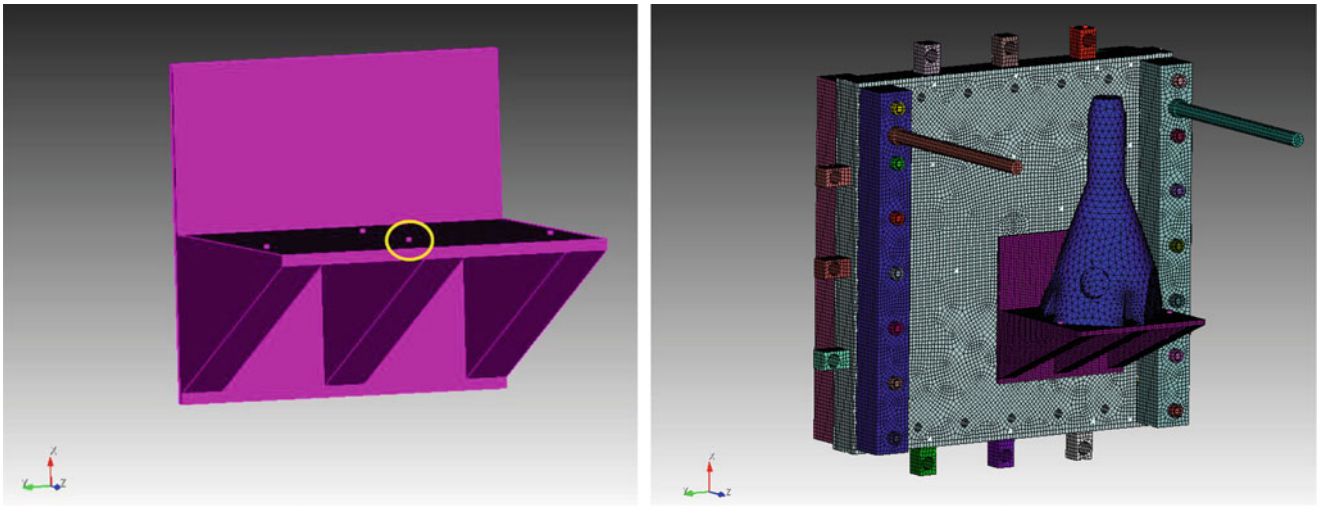

Fig. 14.2 (**a**) Angle bracket design and (**b**) angle bracket mounted on the resonant plate along with testing mass

Table 14.1 Configurations for the angle bracket for resonant plate testing

Configuration type	Impact and fixture location (inches)	Case #
3 rib configuration	(0, 0) & (0, 0)	1
	(3.0, 3.0) & (0, 0)	2
	(3.0, 3.0) & (−3.0, −3.0)	3

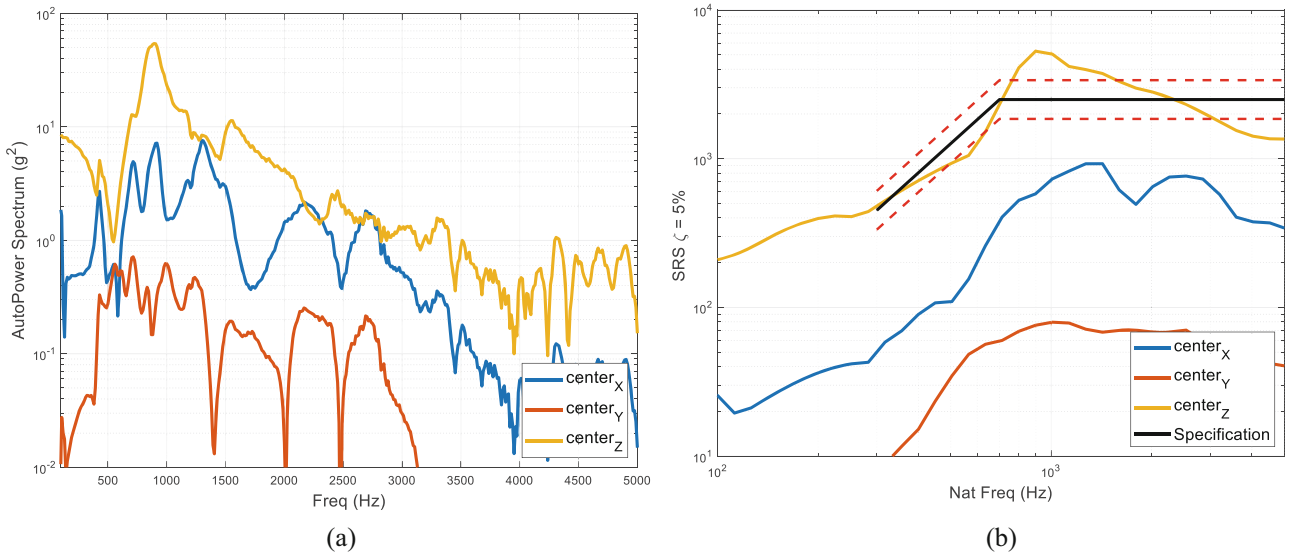

Fig. 14.3 (**a**) Frequency response spectra and (**b**) shock response spectra of the angle bracket for case 1

14.4 Conclusions

This chapter presents results of simulations of an angle bracket fixture for multi-axis pyroshock testing. Model-driven test design is a valuable tool for understanding the preliminary response of fixtures before using them in the laboratory in an actual test. The results presented show that the off-axis responses will increase to levels similar to the response normal to the plate when moving the impact and fixture location opposite of each other. Further work should be pursued to develop an angle bracket that provides a true multi-axis response from a single-axis input in a laboratory environment.

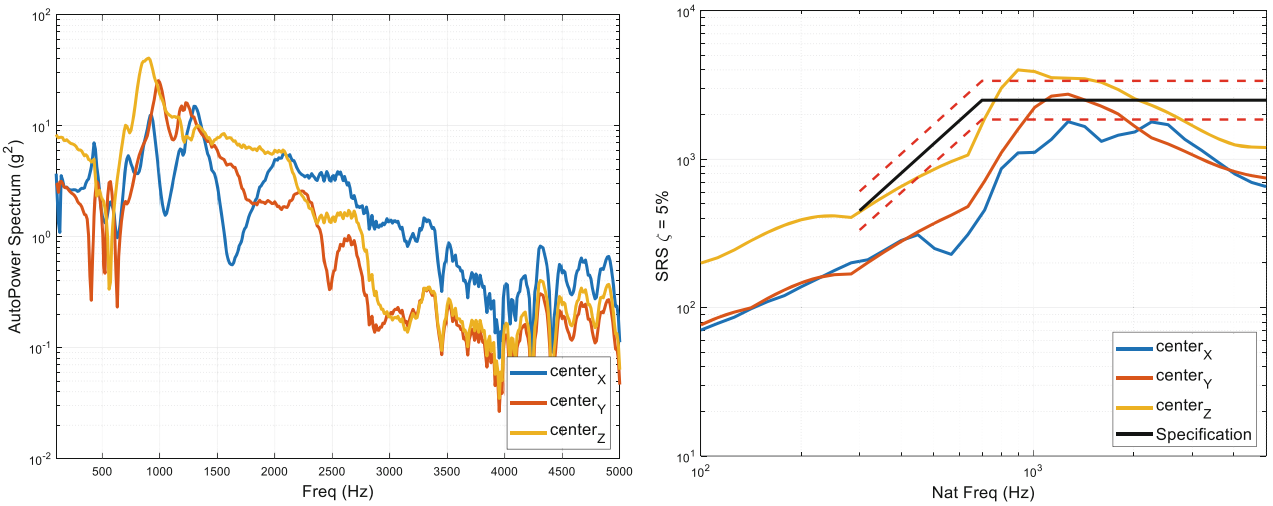

Fig. 14.4 (**a**) Frequency response spectra and (**b**) shock response spectra of the angle bracket for case 2

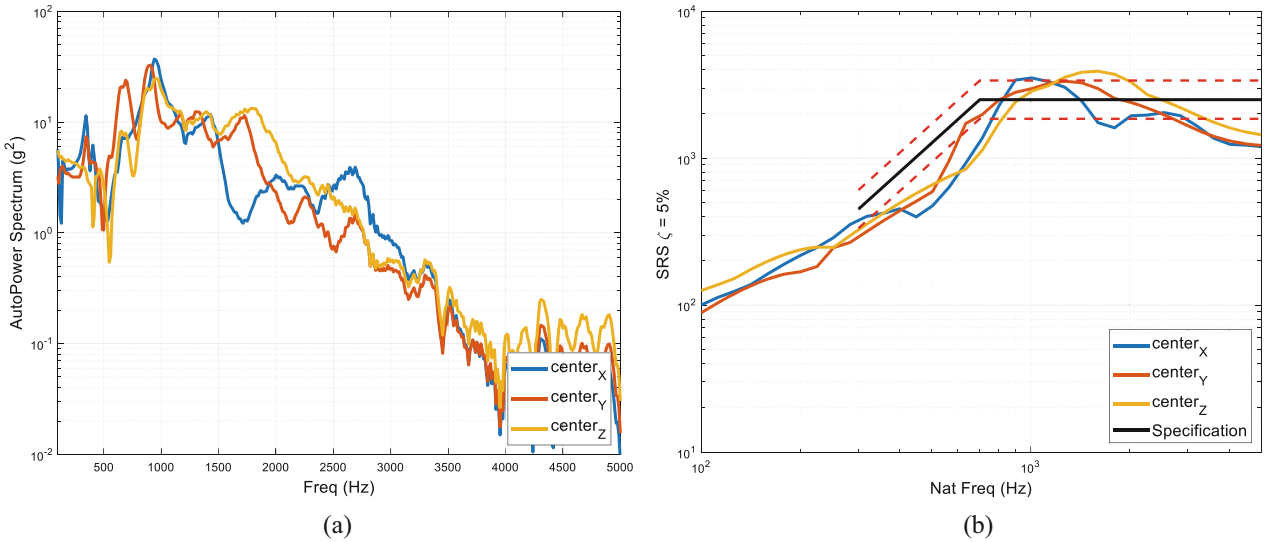

Fig. 14.5 (**a**) Frequency response spectra and (**b**) shock response spectra of the angle bracket for case 3

References

1. Hopkins, R., Sisemore, C.: Design of a Resonant Plate Shock Test for Simultaneous Multi-Axis Excitation. SAND2019-0777C, Sandia National Laboratories (SNL-NM), Albuquerque (2019)
2. Sisemore, C., Babuska, V., Flores, R.: Multi-axis resonant plate shock testing evaluation and test specification development. Report SAND2020–10224, Sandia National Laboratories (SNL-NM), Albuquerque (2020)
3. Schoenherr, T.F., Soine, D.E., Witt, B.L.: Experimental modal analysis of a resonant plate during a mid-field pyroshock replication test. In: Sensors and Instrumentation, Aircraft/Aerospace Dynamic Environments Testing, vol. 7, pp. 41–52. Springer, NY (2023)
4. Schoenherr, T.F., Soine, D.E., Witt, B.L.: Testing, characterization, and modeling of the resonant plate test environment. Report SAND2022–0780, Sandia National Laboratories (SNL-NM), Albuquerque (2022)